AFRL-OSR-VA-TR-2014-0257

CHARACTERIZATION AND LOW-DIMENSIONAL MODELING OF URBAN FLUID FLOW

DIETMAR REMPFER
ILLINOIS INSTITUTE OF TECHNOLOGY

10/06/2014
Final Report

Air Force Research Laboratory
AF Office Of Scientific Research (AFOSR)/RTA
Arlington, Virginia 22203
Air Force Materiel Command

REPORT DOCUMENTATION PAGE

The public reporting burden for this collection of information is estimated to average 1 hour per response, including the time for reviewing instructions, searching existing data sources, gathering and maintaining the data needed, and completing and reviewing the collection of information. Send comments regarding this burden estimate or any other aspect of this collection of information, including suggestions for reducing the burden, to the Department of Defense, Executive Service Directorate (0704-0188). Respondents should be aware that notwithstanding any other provision of law, no person shall be subject to any penalty for failing to comply with a collection of information if it does not display a currently valid OMB control number.
PLEASE DO NOT RETURN YOUR FORM TO THE ABOVE ORGANIZATION.

1. REPORT DATE (DD-MM-YYYY)	2. REPORT TYPE	3. DATES COVERED (From - To)
01-10-2014	Final Report	05-2011 - 04-2014

4. TITLE AND SUBTITLE	5a. CONTRACT NUMBER
Characterization and Low-Dimensional Modeling of Urban Fluid Flow	FA9550-11-1-0056

5b. GRANT NUMBER

5c. PROGRAM ELEMENT NUMBER

6. AUTHOR(S)
Dietmar Rempfer
Candace Wark
Bruno Monnier
Sriharsha Kandala

5d. PROJECT NUMBER

5e. TASK NUMBER

5f. WORK UNIT NUMBER

7. PERFORMING ORGANIZATION NAME(S) AND ADDRESS(ES)	8. PERFORMING ORGANIZATION REPORT NUMBER
Illinois Institute of Technology 3300 South Federal Street Chicago, IL 60616	

9. SPONSORING/MONITORING AGENCY NAME(S) AND ADDRESS(ES)	10. SPONSOR/MONITOR'S ACRONYM(S)
AF OFFICE OF SCIENTIFIC RESEARCH 875 N. RANDOLPH ST. ROOM 3112 ARLINGTON VA 22203	
	11. SPONSOR/MONITOR'S REPORT NUMBER(S)

12. DISTRIBUTION/AVAILABILITY STATEMENT
Distribution A - Approved for Public Release

13. SUPPLEMENTARY NOTES

14. ABSTRACT

This report describes work studying the structure of a model urban boundary layer flow. The flow around this geometry was studied both experimentally as well as computationally. For the experiment, a Stereoscopic Particle Image Velocimetry (SPIV) method was developed that allows for a three-dimensional description of this urban flow. On the computational side, a new spectral-element code was developed that was demonstrated to produce accurate results, and can scale to thousands of processors on large high-performance computing systems. Wind tunnel experiments were performed at a number of different angles of incidence, providing for the first time a detailed overview of the effect of wind direction on the flow structure. The effects of incidence angles from 0 to 45 degrees of the incoming flow with respect to the urban array were investigated. A strong channeling effect is observed for all incidence angles and is in agreement with that observed in other investigations for as little as 4 degrees. This channeling significantly affects the turbulence distribution within the array, the correlations between the various gust components and and the structures responsible for contaminant transport.

15. SUBJECT TERMS
Urban fluid flow, Spectral element method, Particle Image Velocitmetry

16. SECURITY CLASSIFICATION OF:			17. LIMITATION OF ABSTRACT	18. NUMBER OF PAGES	19a. NAME OF RESPONSIBLE PERSON
a. REPORT	b. ABSTRACT	c. THIS PAGE			Dietmar Rempfer
			SAR	152	19b. TELEPHONE NUMBER (Include area code) 312-567-3189

Reset

Standard Form 298 (Rev. 8/98)
Prescribed by ANSI Std. Z39.18
Adobe Professional 7.0

INSTRUCTIONS FOR COMPLETING SF 298

1. REPORT DATE. Full publication date, including day, month, if available. Must cite at least the year and be Year 2000 compliant, e.g. 30-06-1998; xx-06-1998; xx-xx-1998.

2. REPORT TYPE. State the type of report, such as final, technical, interim, memorandum, master's thesis, progress, quarterly, research, special, group study, etc.

3. DATES COVERED. Indicate the time during which the work was performed and the report was written, e.g., Jun 1997 - Jun 1998; 1-10 Jun 1996; May - Nov 1998; Nov 1998.

4. TITLE. Enter title and subtitle with volume number and part number, if applicable. On classified documents, enter the title classification in parentheses.

5a. CONTRACT NUMBER. Enter all contract numbers as they appear in the report, e.g. F33615-86-C-5169.

5b. GRANT NUMBER. Enter all grant numbers as they appear in the report, e.g. AFOSR-82-1234.

5c. PROGRAM ELEMENT NUMBER. Enter all program element numbers as they appear in the report, e.g. 61101A.

5d. PROJECT NUMBER. Enter all project numbers as they appear in the report, e.g. 1F665702D1257; ILIR.

5e. TASK NUMBER. Enter all task numbers as they appear in the report, e.g. 05; RF0330201; T4112.

5f. WORK UNIT NUMBER. Enter all work unit numbers as they appear in the report, e.g. 001; AFAPL30480105.

6. AUTHOR(S). Enter name(s) of person(s) responsible for writing the report, performing the research, or credited with the content of the report. The form of entry is the last name, first name, middle initial, and additional qualifiers separated by commas, e.g. Smith, Richard, J, Jr.

7. PERFORMING ORGANIZATION NAME(S) AND ADDRESS(ES). Self-explanatory.

8. PERFORMING ORGANIZATION REPORT NUMBER. Enter all unique alphanumeric report numbers assigned by the performing organization, e.g. BRL-1234; AFWL-TR-85-4017-Vol-21-PT-2.

9. SPONSORING/MONITORING AGENCY NAME(S) AND ADDRESS(ES). Enter the name and address of the organization(s) financially responsible for and monitoring the work.

10. SPONSOR/MONITOR'S ACRONYM(S). Enter, if available, e.g. BRL, ARDEC, NADC.

11. SPONSOR/MONITOR'S REPORT NUMBER(S). Enter report number as assigned by the sponsoring/ monitoring agency, if available, e.g. BRL-TR-829; -215.

12. DISTRIBUTION/AVAILABILITY STATEMENT. Use agency-mandated availability statements to indicate the public availability or distribution limitations of the report. If additional limitations/ restrictions or special markings are indicated, follow agency authorization procedures, e.g. RD/FRD, PROPIN, ITAR, etc. Include copyright information.

13. SUPPLEMENTARY NOTES. Enter information not included elsewhere such as: prepared in cooperation with; translation of; report supersedes; old edition number, etc.

14. ABSTRACT. A brief (approximately 200 words) factual summary of the most significant information.

15. SUBJECT TERMS. Key words or phrases identifying major concepts in the report.

16. SECURITY CLASSIFICATION. Enter security classification in accordance with security classification regulations, e.g. U, C, S, etc. If this form contains classified information, stamp classification level on the top and bottom of this page.

17. LIMITATION OF ABSTRACT. This block must be completed to assign a distribution limitation to the abstract. Enter UU (Unclassified Unlimited) or SAR (Same as Report). An entry in this block is necessary if the abstract is to be limited.

Final Report

Characterization and Low-Dimensional Modeling of Urban Fluid Flow

Contract Number: FA9550-11-1-0056

Authors: D. Rempfer, C. Wark, B. Monnier, S. Kandala

Cognizant Program Officer: Douglas R. Smith

October 1, 2014

Contents

List of Tables

List of Figures

Abstract

This report describes work that was done under AFOSR Contract Number FA9550-11-1-0056, studying the structure of a model urban boundary layer flow. The model geometry consisted of a set of plexiglass blocks, and the flow around this geometry was studied both experimentally as well as computationally. For the experiment, a Stereoscopic Particle Image Velocimetry (SPIV) method was developed that allows for a three-dimensional description of this urban flow, and helps gain insight into the characteristic flow structures in the streets and canyons of our model urban geometry. On the computational side, a new spectral-element code was developed that was demonstrated to produce accurate results, and can scale to thousands of processors on large high-performance computing systems. Good agreement between the experiment and computation was demonstrated.

Most notably, wind tunnel experiments were performed at a number of different angles of incidence, providing for the first time a detailed overview of the effect of wind direction on the flow structures in the urban geometry. Valuable information about the flow structures are presented. The effects of incidence angles from 0 to 45 degrees of the incoming flow with respect to the urban array are investigated. A major observation from this work is that a strong channeling effect is observed for all incidence angles and is in agreement with that observed in other investigations for as little as 4 degrees. This channeling significantly affects the turbulence distribution within the array, the correlations between the various gust components and the structures responsible for contaminant transport.

Chapter 1

Introduction

1.1 Introductory comments

Urban flows have been increasingly studied during the past decade. Many challenges are yet to be fully addressed, with the understanding of contaminant dispersion being one of the critical issues. In the context of pollution dispersion in densely populated areas and the fear of chemical or biological attacks, more studies are addressing this type of flow. The physics involved are very complex since the flow is often strongly three-dimensional and dependent upon the temperature distribution, the turbulence induced by moving cars, the presence of obstacles such as trees in the streets, etc. Remote flow sensing, in particular, has become a very important field of research. Through the use of sparse sensors optimally distributed in an urban environment, the desire is to estimate the characteristics of the flow field and predict its evolution. This is especially important in the context of predicting the displacement of a plume of contaminants.

Another relatively recent area of interest relevant to this type of study is the desire to fly Micro Aerial Vehicles (MAVs) in urban areas. These MAVs, which are unmanned aerial vehicles with relatively small dimensions (10-20 cm wingspan), can be used for surveillance, data collection (remote sensing), and can be flown in areas that are hazardous to people. However, they are often still limited to flying in relatively calm wind conditions (Watkins et al. [2009, 2010]). Therefore, there is a growing need to characterize wind gusts and both the intensity and spatial distribution of turbulence at the urban scale so as to provide the flow fundamentals to design new generations of MAVs with enhanced maneuverability.

Turbulent fluid flows in complex domains occur in nature and in many industrial applications. A good understanding of flow physics as well as the ability to accurately predict these flows play an important role in many applications ranging from weather prediction to efficient design of engineering equipment. Traditionally, given the exorbitant number of grid points required for accurate resolution of all flow features, experimental measurements supplemented with theory were the only feasible choice for understanding these flows. Experiments are expensive and often provide data only in a limited region of the flow field. However with rapid increase in computing power and advances in numerical algorithms, numerical simulations are increasingly becoming feasible for higher Reynolds number flows. While resolving all scales of interest is still intractable for flows of engineering interest, large eddy simulations, which resolve the large scales and model small scales, are becoming increasingly feasible.

Accurate numerical simulations of turbulent flows in domains of engineering interest require algorithms which have low dispersion and diffusion errors, support complex geometries and are highly scalable. While spectral methods do an excellent job, their application is limited to simple geometries. Second-order finite

volume and finite element codes can handle complex geometries and are currently the standard tools of choice in the CFD industry. However, they have high diffusion and dispersion errors and need more degrees of freedom for the same accuracy, making them very expensive for long term integration. Spectral elements (Deville et al. [2002], Karniadakis and Sherwin [2005]) combine the high-order accuracy of spectral methods with the geometric flexibility of finite element methods. They have very low dispersion errors which make them very efficient for long term integration. Weak C^0 coupling between adjacent elements increases the computation to communication ratio which facilitates highly scalable algorithms.

The computational work for this project focused on the development and optimization of a parallel spectral element solver, *Specsolve*, for simulating turbulent flows in complex geometries. The code uses the $\mathcal{P}_N$-$\mathcal{P}_{N-2}$ formulation for the spatial discretization of velocity and pressure. Velocity is represented within each spectral element using a tensor product of Lagrangian basis functions based on GLL (Gauss-Lobatto-Legendre) nodes, and C^0 continuity is enforced between adjacent spectral elements. Pressure within each spectral element is represented using a tensor product of one-dimensional Legendre polynomials of appropriate order and inter-element continuity is not explicitly enforced. The code is built in C++ and uses the Message Passing Interface (MPI) for communication. One of the principal bottlenecks in the numerical solution of the Navier-Stokes equations is the pressure solve. A multilevel strategy is implemented to build a scalable solver for pressure. A state-of-the-art algebraic multigrid (AMG) solver is implemented to solve the coarse pressure problem. An FDM (fast diagonalization method) based block-Jacobi preconditioner is used for efficient solution of the fine pressure problem. The code uses filter-based stabilization for simulating high Reynolds number flows. A novel turbulent outflow boundary condition is implemented in order to stabilize flow at the outflow boundary in the presence of localized regions of reverse flow. This parallel spectral element solver is used for simulation of incompressible flows in model urban street canyons.

1.2   Advantages and limitations of field experiments and numerical simulations

While they are essential to verify results obtained both from numerical and wind tunnel experiments, direct field studies are extremely difficult and expensive to conduct. Many parameters are influencing the flow field and results are often difficult to interpret. In terms of practicality, the most common tools used to measure velocity in field experiments are sodars and anemometers installed on tall towers which usually results in a rather coarse spatial resolution. As a result, turbulence characterization is mostly carried out in 1D, usually along a vertical axis, see Nielsen [2000] and Christen et al. [2003] for example. Therefore, no direct information on the spatial structure of the flow in the directions normal to the line of measurement is available. Few field experiments have considered spatial variation of turbulence at the street level (Rotach [1995], Eliasson et al. [2006]). Other types of work in simplified field experiments can be found in Louka et al. [1998], who worked toward a better understanding of the ventilation of pollution from a street formed of two long buildings and its dependence on the shape of the roofs of the obstacles. They focused on the coupling of the turbulent airflow in a street canyon with the turbulent airflow above the roofs. Within the same field setting, Louka et al. [2000] performed experiments to study the air flow within the street and found that the recirculation region is highly unsteady and that the shear layer from the upstream roof is very unstable due to a Kelvin-Helmholtz instability. In a more realistic environment, Louka et al. [2002] looked at the thermal effects on the flow field in a street in Nantes, France, and compared their results to a 2D numerical simulation using a standard k-ϵ model. They found that the numerical simulations overestimate the thermal effects on the flow field. Dobre et al. [2005] showed the flow behavior in a few streets in London, UK. More specifically, their work illustrated the effect of the wind incidence angle with respect to the streets

2

and the role of the street intersections on the wind direction switching phenomenon. Their measurements showed that the flow within the street can be viewed as the vector sum of a channeling in the streets and a recirculation vortex.

The work by Xie et al. [2003] is very interesting in the sense that it would be extremely difficult to reproduce in a wind tunnel. They performed field tests with the measurements of the concentration of car exhaust in Guangzhou, China. They found that in the street, pollutants are carried from the windward to the leeward side of the street by a large recirculation region. One part of the pollutants gets trapped in the recirculation region, while the other is flushed out of the street at the roof level. One major finding is that photochemical reactions involving O_3 take place at the roof level and is therefore less of a threat to pedestrians.

Recently, there has been an increased effort in developing and improving computational and numerical models. Camelli et al. [2006] have used very large-eddy simulation (VLES) to study the release of a passive scalar contaminant in realistic urban areas. This technique is equivalent to standard large-eddy simulation (LES), but the largest scales are on the order of a few kilometers. Krajnovic and Davidson [2000] have used LES on a single cube while Baik and Kim [1999] have used a 2D k-ϵ turbulence model for a 2D street.

Kim and Baik [2004] used a 3D numerical simulation, renormalized group k-ϵ scheme, to solve the flow within an array of cubes. They investigated the dependence of the vortical structures on the wind incidence angle and then classifed the flow in three regimes depending on this incidence angle.

More recently, Coceal et al. [2006] performed a direct numerical simulation of the turbulent flow within an array of cubes and found very good agreement with experimental data. Only numerical studies can provide information with excellent spatio-temporal resolution, but unless DNS is used, the main drawback is their limited ability to capture accurately the range of turbulence scales. The use of DNS is however computationally prohibitive. Even with recent progress in computing, numerical simulations need validation through experimental studies for such complex flow fields. Therefore, there is a very specific need for reliable 3D data in a more realistic urban model.

The study of Kim and Baik [2003] is interesting in the sense that by using a 2D numerical model to solve the flow within a single street, it allowed them to vary the inflow turbulence intensity easily. Such a study in an experimental setting would be more challenging. They found that as the inflow turbulence increases, both turbulent kinetic energy and turbulent diffusivity increase. Similarly, the magnitude of the mean speed increases and the vortical regions are strengthened. An increase in turbulent intensity is directly linked to an enhanced pollutant dispersion within the street.

As mentioned previously, thermal stratification of the atmospheric boundary layer is very difficult to simulate in a wind tunnel although some have been successful in doing so as will be seen in the following section. However, there is no such constraint for numerical simulations, and researchers have started looking into the effects of solar radiation on the flow field at the street level. By simulating ground-level heating through various numerical models, Xie et al. [2006] were able to show that thermal effects could enhance vertical diffusion especially for low mean wind speeds. In another work by Xie et al. [2005], the study of step-up and step-down configurations for the street geometry was carried out as well as the heating of either the windward or leeward side of the street. The thermal effects in these cases could then either strengthen or weaken the main vortex within the street. Similar results were obtained independently by Mestayer et al. [1995]. Uehara et al. [2000] looked at the effect of flow stratification on the flow field within the street over a range of Richardson numbers (defining stable, neutral, or unstable atmospheres). Kim and Baik [2001] performed a numerical simulation of a street with bottom heating. They were able to observe significant changes in the flow structure for large temperature gradients with the generation of a second vortical structure within the street, located directly underneath the vortical structure found for no temperature gradients.

Hang et al. [2012] also used CFD methods to clarify the role of building layouts and height variability

in ground-level pollutant dispersion. They could distinguish between the roles of the mean flow and the turbulent diffusion in pollutant dispersion for each of their building geometries. They also partially used wind tunnel hot-wire data to verify their CFD results.

1.3   Wind tunnel experiments

Unlike field experiments, wind tunnel experiments allow for good control over the parameters driving the flow field of interest. It also allows for independently investigating the effect of the key parameters.

Most past wind tunnel studies have focused their interest on two-dimensional (2D) configurations (i.e. spanning the width of the wind tunnel) and have considered the neutrally stratified atmospheric boundary layer since it is extremely difficult to simulate a temperature distribution in a wind tunnel. A seminal study of flow patterns in an urban environment was performed by Oke [1988]. This work, which is relevant to street design and contaminant dispersion, described the effect of streamwise spacing on street canyons. Although his results were 2D, he identified three different regimes directly dependent on the streamwise spacing of the street canyon. Li et al. [2008] performed experiments in a water channel, investigating the different flow regimes using Laser Doppler Anemometry. Similar regimes have been found in 3D configurations (i.e. finite size of the streets). Martinuzzi and Havel [2000] investigated the effect of the streamwise spacing between two cubic blocks mounted in tandem in a thin boundary layer and found three distinct regimes for different streamwise spacings. Other parameters such as the span-to-width ratio of the obstacles or the spanwise spacing for obstacle arrays are believed to have an effect on the transition between regimes. Few wind tunnel experiments have investigated more realistic geometries (Rafailidis [1997], Kastner-Klein and Rotach [2004]). While these studies are considering more complex geometries, the amount of information about the mean flow field and the turbulence within the model is limited spatially.

Recently, researchers have begun investigating the effect of three-dimensionality; but again, there are very few measurements offering full 3D sets of data. Becker et al. [2002] with Laser Doppler Anemometry (LDA) and Sousa [2002] with 2D - three component particle image velocimetry (2D-3C PIV) measurements were among the first to have looked at three-dimensional flow fields around a single cuboid obstacle. Becker et al. [2002] described the effect of the angle of attack, the aspect ratio, the Reynolds number and the boundary-layer type on the flow structures around a single obstacle. They found no fundamental changes in the vortex structure for the various boundary layers investigated, and determined that an increase in the power-law coefficient n in

$$\frac{U}{U(h)} = \left(\frac{z}{h}\right)^n \tag{1.1}$$

caused a reduction in the size of the recirculation region downstream of the obstacle. Here, U is the time-averaged velocity at the wall-normal coordinate z, and h is a wall-normal location in the upper part of the inertial sublayer at which the velocity $U(h)$ is known. They also found that increasing the incidence angle created and subsequently amplified a dislocation of one leg of the arch vortex behind the single block until it attached to its top for incidence angles larger than $60°$. Sousa [2002], using conservation of mass to extract the third velocity component from 2D PIV data around a cube, focused his interest on the identification and localization of large-scale vortical structures. He found that swirling strength and normalized angular momentum techniques were more advantageous for identifying coherent structures as compared with a vorticity-based method. Similarly, Martinuzzi and Tropea [1993], using various flow visualization techniques as well as static pressure measurements on the surface of the obstacle, showed the effect of the width-to-height ratio on the three-dimensionality of the flow past a single 3D obstacle. They found that, for an obstacle with a width-to-height ratio $W/H > 6$, the flow downstream of the block is largely 2D

with alternating saddle and nodal points on the windward face of the obstacle. They concluded that cellular structures were created upstream of the obstacle and that the flow was following preferred paths over the top.

Hussein and Martinuzzi [1996] investigated the turbulence dissipation rate, the production, convection and transport terms and the balance of the turbulent kinetic energy transport equation for a three-dimensional flow around a cube mounted in a channel using LDA. They identified various scales relevant to different features of the flow around the cube (e. g. wake, shear layer, horseshoe vortex). These different scales characterizing the turbulence production and dissipation are a good indication that the flow field within an urban area is a multi-scale problem.

Belcher and Coceal [2001] and Coceal and Belcher [2004] developed an urban canopy model for mean winds in urban areas that compares well with data from wind tunnel experiments. Interestingly, they could model the minimal distance within an array of buildings that is required to reach an adjustment to the inhomogeneous canopies.

Many researchers have investigated the flow within an array of obstacles, for example, regular and staggered arrays of cubes (Castro et al. [2006], Cheng and Castro [2002], Reynolds and Castro [2008]). Their primary goal was to understand the features of urban-like boundary layers, what influenced them and how to parameterize them. With the same objective in mind, MacDonald et al. [2002] performed experiments with a regular array of cubes and measured characteristic mean flow and turbulence statistics for urban areas.

Robins and Castro [1977] investigated the plume dispersion in the vicinity of a wall mounted cube by releasing propane for different configurations (porous cube, release from a point source at different locations, release from a stack, etc...) The concentration of propane was measured downstream of the cube and it was found that an effective source height concept could be applied to estimate the concentration field beyond two cube heights. A fundamental difference was found in the behavior of the flow dispersion phenomenon between high and low level release with the authors underlining a possible effect of surface geometry on dispersion.

Castro and Robins [1977] investigated the pressure distribution on the surface of a wall-mounted cube in a turbulent boundary layer and the flow field in its wake. Two incidence angles of the incoming flow were studied. They showed that an increase of turbulence intensity and shear would reduce the size of the recirculation region downstream of the cube. Reattachment on the top surface of the obstacle is observed for the urban type boundary layer (as opposed to the cube being placed in a uniform flow). This reattachment occurs for different cube sizes, but may be intermittent for the larger obstacles (as the height approaches the boundary layer thickness). For a 45° incidence angle, the cube placed in a uniform flow sheds vortices from its top edges, similar to a delta wing, that have a strong effect on the axial velocity for a distance of about six times the cube length, then this effect diminishes quickly. When turbulence intensity is raised in the case of the urban type boundary layer, this effect tends to disappear. Garbero et al. [2010] performed an experimental study of pollutant dispersion within a street network, measuring the mass exchange between the streets and the flow above the roofs for various geometrical configurations as well as various wind directions.

While the majority of investigations concentrate on street canyons in the middle row of a full array of buildings, Princevac et al. [2010] used PIV measurements in a water channel to focus on the flow distribution for a general array of mock up buildings, they discovered a new flow feature called 'lateral channeling' which explains the inward and outward mean flow distribution on pathways on the boundaries of the urban array model.

An interesting experimental study at a larger scale was carried out by Richards et al. [2001] where they measured the surface pressure on a 6 m cube sitting on the ground in an open country. They found good agreement with wind tunnel data for the windward face of the cube, but the pressure distribution in the field experiment was more sensitive to incoming velocity profiles, turbulence and Reynolds number on the other

faces than the pressure distribution obtained in the wind tunnel experiment. Richards et al. [2007] carried out a 1:40 scaled-down wind tunnel experiment of this cube and compared their results to the field experiments. They found similar behavior but identified various sources of discrepancies between the wind tunnel and field experiments. These included a Reynolds number effect and the difficulty of reproducing varying wind directions to match the field experiment, affecting the mean and amplitude of pressure observed during the measurements.

Takimoto et al. [2011] applied PIV in an outdoor field experiment on an array of 1.5 m-sized cuboid obstacles. In spite of several differences compared to the wind tunnel test, they suggested valuable information regarding turbulent flow structures by proposing dominant eddy modes and the shear layer behavior at the canopy roof level. A thorough study about the effect of the array geometry parameters such as array layout, buildings heights, and wind direction on aerodynamic parameters of buildings, such as drag coefficient (C_d) was carried out by Hagishima et al. [2009] in the wind tunnel using floating pressure gauges.

Kellnerova et al. [2012] used PIV to investigate the turbulent flow in street canyons. POD methods were used to analyze the velocity field and extract coherent modes. They studied the effect of roof top shape (pitched and flat) on turbulent flow characteristics in streets. Even with valuable improvements in urban flow studies, extracting three-dimensional shape and distribution of the vortical structures was still a weak aspect of most investigations. Monnier et al. [2010] for the first time used stereoscopic PIV (SPIV) methods to generate fully three-dimensional velocity data of street canyons in wind tunnel tests. They used a scaled model of the MUST field experiment (Biltoft [2001]), investigated the effects of streamwise spacing, ambient boundary layer regimes (wake interference and skimming flow), and small wind direction angles ($0°$, $4.5°$ and $15°$). Representation of mean streamlines, turbulent kinetic energy (TKE) contours and coherent structures were used in the investigation. Using proper orthogonal decomposition (POD) methods to refine statistical data provided them with advanced three-dimensional iso-surfaces of coherent structures of vortical motions. Arch vortices were clearly detected and depicted in streets. The effect of wind direction on the flow characteristics, dispersion, TKE and the mean flow was studied by Kim and Baik [2004] using CFD. Angles of $0°$ to $45°$ in increment of $5°$ were studied. The evolution of the portal vortex (arch vortex) was studied in three main categories of wind direction angle of $0°$, $5°$ to $20°$ and $25°$ to $45°$.

Mostly during the last decade, researchers have begun to investigate other effects on the flow field within urban-like environments. The addition of thermal effects, presence of obstacles such as trees, and extra turbulence generated by moving cars are more and more investigated experimentally. In a first study, Kovar-Panskus et al. [2002b] looked at the streamwise aspect ratio effect of the street on the flow pattern, followed by a study where Kovar-Panskus et al. [2002a] investigated thermal effects in a wind tunnel experiment. They investigated the flow field within a street for conditions where a single recirculation region is the dominant flow structure. Under low speed wind conditions, as the heating of the windward wall is increased, the reverse flow speed magnitude is reduced. Upon further heating, the flow pattern significantly changed.

Some researchers have started to look into added turbulence generated by moving cars. For example, Eskridge and Rao [1986] focused specifically on the turbulence levels created by moving objects. More recently, Kastner-Klein et al. [2001] studied the high concentration levels of car exhaust encountered when the incoming flow was normal to the street, and looked at the effects of one-way and two-way traffic on this concentration. In another study, Kastner-Klein et al. [2000] found that dispersion of pollutants could be enhanced by the motion of vehicles, especially at low wind speeds. Ahmad et al. [2002] implemented multi-lane traffic for simulating road traffic and concluded that pollutant concentrations could be reduced significantly by moving cars, once again at low wind speeds.

In the last few years, the effect of still obstacles on the dispersion of pollutants has been investigated. More specifically, the effect of trees was highlighted in the work by Gromke and Ruck [2009], Gromke and Ruck [2007] and Gromke et al. [2008]. It was found that in some cases the presence of trees lowers the

6

dispersion of pollutants from the leeward side of the street, by weakening the large recirculation region. On the windward side of the street, pollutant concentrations were less than in the baseline case (with no trees), due to a larger amount of clean air moving into the street from the top. Gayev and Savory [1999] focused on trying to model the roughness associated with stationary obstacles in a single street-canyon model.

Chapter 2

Wind Tunnel, Apparatus and Data Processing

2.1 Modelling of the Atmospheric Boundary Layer

2.1.1 Definition

The first step in this investigation was to experimentally model the atmospheric boundary layer (ABL) for the conditions of interest Stull [1988]. The wind velocity profile of the ABL is often characterized by a log-law in the inertial sublayer. However, using a power law, see Equation 1.1, provides a simpler characterization of a neutrally stratified boundary layer Plate [1971] since only one parameter (the exponent) is needed to describe the wind velocity profile in the inertial sublayer. Typical exponents for various types of terrains can be found in the work by Davenport [1965], and range from 0.4 for large high-rises to 0.16 over a flat surface such as a lake. An ABL with a power-law exponent of 0.17, corresponds to flow over lower suburban buildings and was used for this investigation.

2.1.2 Wind-Tunnel Modeling

The boundary layers are modeled in a closed-loop wind tunnel at IIT, based on the work done by Nagib et al. [1974] and Gunnarsson [1974]. The experiment is carried out in the low speed test section that is capable of mean free-stream speeds, U_0, up to 8 m/s. The test section is 1.2 m in span by 1.7 m in height and 0.635 m in length. For larger test sections such as this one, it is very important to consider the spanwise uniformity of the incoming boundary layer. Nagib et al. [1974] and Gunnarsson [1974] used roughness elements and a counter jet upstream of the test section to tune the characteristic parameters of the approaching boundary layer and ensure spanwise uniformity. The counter jet, discussed both in Nagib et al. [1974] and Gunnarsson [1974], proved to be very useful in ensuring spanwise uniformity for the free-stream flow speeds of interest here. The configurations we chose for roughness elements and counter jet settings provide a spanwise uniform neutrally stratified atmospheric boundary layer for free-stream speeds ranging from $U_0 = 2.2$ m/s to 3.4 m/s.

The counter jet consists of a 60-mm diameter steel tube placed on the floor of the wind tunnel and spanning the entire width. The counter jet is placed at the upstream location of the roughness fetch (Figure 2.1) which is 3.48 m upstream of the test section. There are 38, 6.35-mm diameter holes drilled along the

span of the steel tube, with the tube itself being connected to a compressed air supply. The orientation, θ_j, of the 38 jets can be varied from $-20°$ to $+20°$ with respect to the oncoming free stream by rotating the tube. The magnitude of the jet velocity, U_j, can also be varied by controlling the compressed air supply pressure. For our study, we found that $U_j/U_0 = 15$ with an upstream flow angle, θ_j of $+10°$ (see Fig. 2.1 for definition of θ_j) provides a spanwise uniform boundary layer in the test section. The reader is referred to Gunnarsson [1974] for a more comprehensive discussion of the counter jet technique. Directly downstream
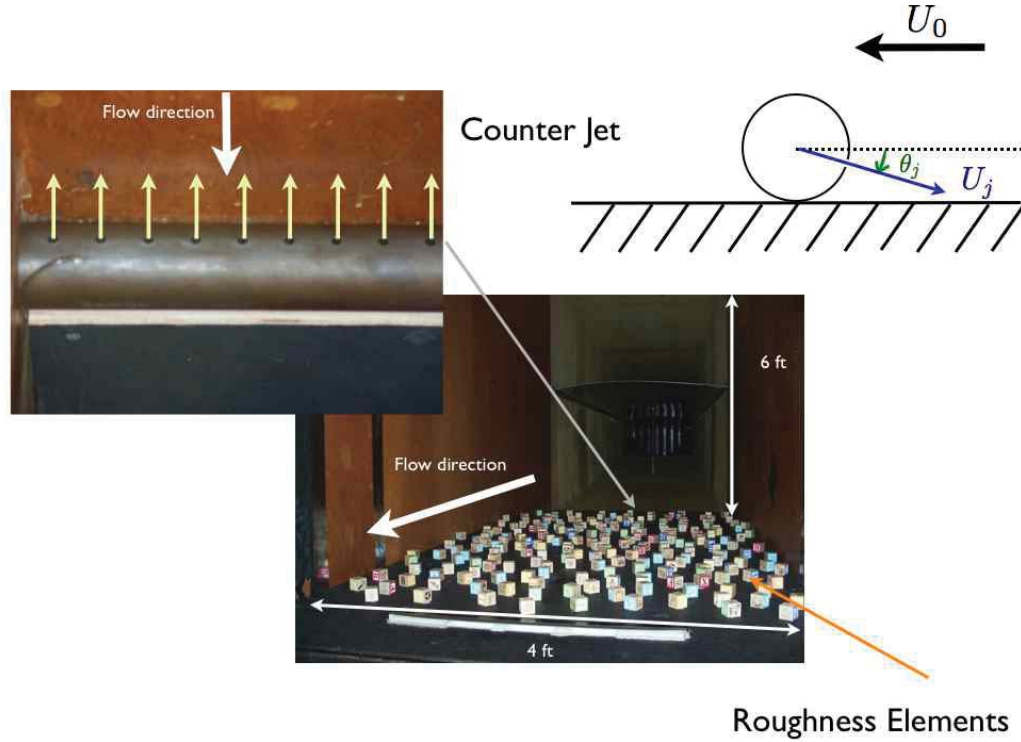
Figure 2.1: Photograph of counter jet and roughness elements upstream of the test section. Note: the test section is not shown here and is downstream of this image.

of the counter jet is the roughness element fetch. The roughness elements used are 30 mm cubes placed randomly on the floor (see Figure 2.1). The end of the roughness fetch is 2.08 m from the counter jet and 1.40 m from the upstream edge of the 1.22 m $\times$ 1.93 m test section. The roughness elements occupy 8% of the planform area of the entire roughness fetch. The test section, which begins 1.40 m after the downstream end of the roughness fetch, can be seen in Figure 2.2.

2.1.3 Characteristics of the modelled ABL

The approach boundary layer is documented using a spanwise array of three hot wires and its characteristics are summarized in Table 2.1.. The rack is mounted on a vertical traverse system enabling measurement of the velocity profiles starting from a position in close proximity to the floor ($\approx$ 1 mm) and extending
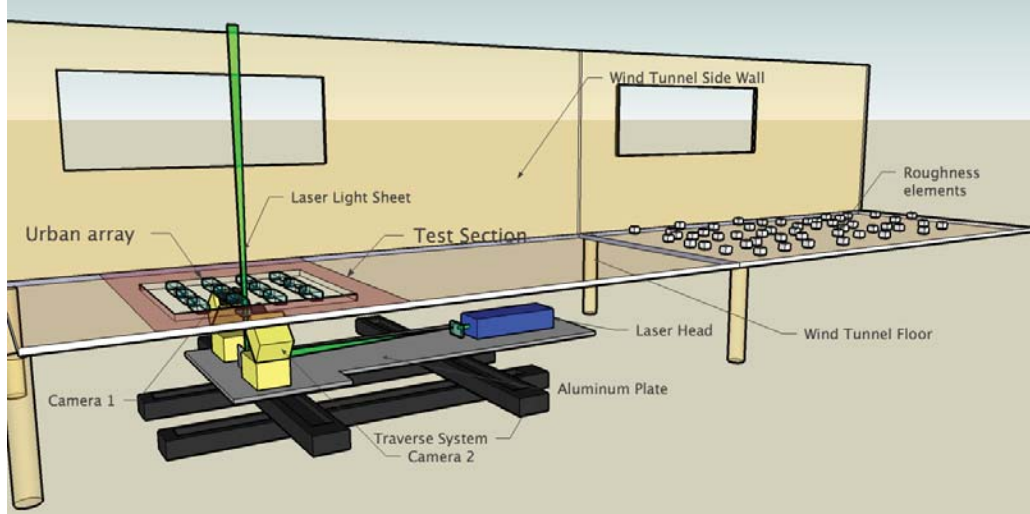
Figure 2.2: Schematic of the stereoscopic PIV setup, the roughness fetch and the test section.

Table 2.1: Boundary layer test matrix

ABL #	U_0	δ	θ	Re_θ	n
ABL	3.4 m/s	≈ 450 mm	≈ 50 mm	≈ 10800	0.17

approximately 400 mm above it. The middle hot wire is located along the centerline of the wind tunnel while the two other hot wires are located 127 mm apart from the centerline. Note that for meteorological studies, x, y and z are the streamwise, spanwise and wall-normal coordinates, respectively. Since the hot-wire traverse is limited to 400 mm, a Pitot-static tube traverse is used to estimate the boundary-layer thickness δ, where δ is defined as the wall-normal (z) location where $U/U_0 = 0.99$. The momentum thickness θ is obtained from the profiles ($\theta \approx 50$ mm) and is computed as:

$$\theta = \int_0^{0.8m} \frac{U(z)}{U_0} \left(1 - \frac{U(z)}{U_0}\right) dz \tag{2.1}$$

where the integration is performed over the interval 0 to 0.8 m.

Figure 2.3 presents the velocity profile for our ABL. The velocity profile was obtained 100 mm upstream of the test section and the values for δ, θ and the power-law coefficient n are presented in Table 2.1.
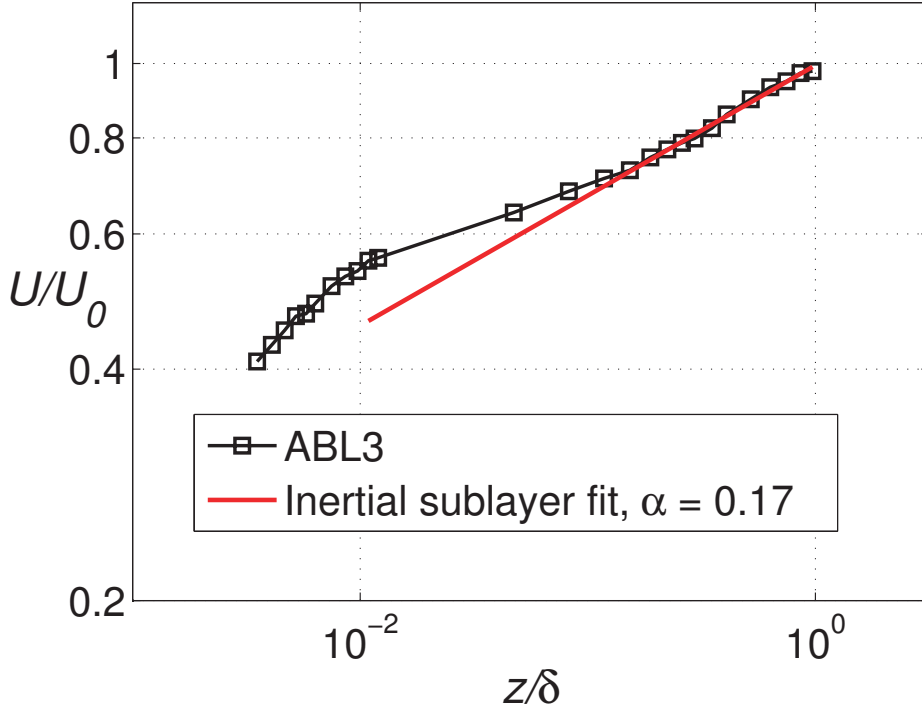
Figure 2.3: Logarithmic representation of normalized velocity profiles for ABL upwind of the beginning of the urban array.

2.2   Urban model

The canopy array used in this study consists of 7 rows of blocks in span and 5 in the streamwise direction, which makes 6 parallel streets in span and 4 intersecting streets in the streamwise direction. The data were taken in the region behind the mid-span column of the blocks, so the data were acquired in the four streets shown in Figure 2.4. The three intersecting streets on each side in span were aimed to provide geometrical symmetry and spanwise flow uniformity. The geometrical information of the urban model is shown in Figure 2.5. The Cartesian coordinate system and cardinal directions are used to better address the locations and directions in the array. Note that the coordinate system is attached to the urban array in cases of various wind directions. The model dimensions are described as: building height, $H = 50$ mm, building width, $W = L = 25$ mm, and street length, $S = 37.5$ mm.
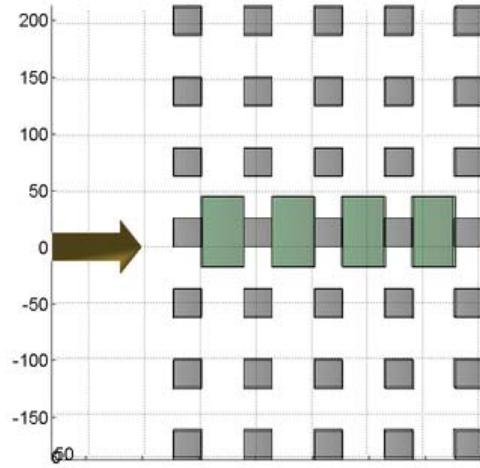
Figure 2.4: Array structure (5×7) and data acquisition regions, top view.

The other parameters which describe the array geometry are packing density and dimensionless frontal area. Packing density (λ_p) is the ratio of the total plan area of the buildings (A_p) to the total underlying surface area (A_T). Dimensionless frontal area (λ_f) is defined as the ratio of the frontal area of the buildings facing the wind (A_f) over A_T. Dimensionless frontal area (λ_f) is important in the drag calculations, since it represents the surface facing the wind flow. Typical ranges of λ_f, are from 0.1 for areas with a moderate density of buildings up to 0.3 in downtown areas. For the current investigation $\lambda_f = 0.4$ and $\lambda_p = 19.9$ % which is considered a relatively medium dense array compared to typical urban array models. Zaki et al. [2011] used packing densities of 7.7% up to 39% for their experiments, and Pillai et al. (2012) used packing densities of 6% up to 25%, where they were studying the effect of the packing density on pollutant dispersion.

The desired region of study in each street, shown in Figure 2.6(a), is a volume of $38 \times 62.5 \times 71$ mm, in the $x \times y \times z$ directions respectively. This region is centered at the middle of each street in span and covers half-length of intersecting streets on each side. In order to attain a full data matrix of this region, a set of data planes is accumulated. Each data plane is a volume of $38 \times 2 \times 71$ mm, in $x \times y \times z$ respectively (Figure 2.6(a)). Each plane contains a 38×71 grid of data points. 27 data planes are in span with one located at the center (as shown in Figure 2.6(b)) and 13 on each side. The spanwise distances of these 13 planes from the
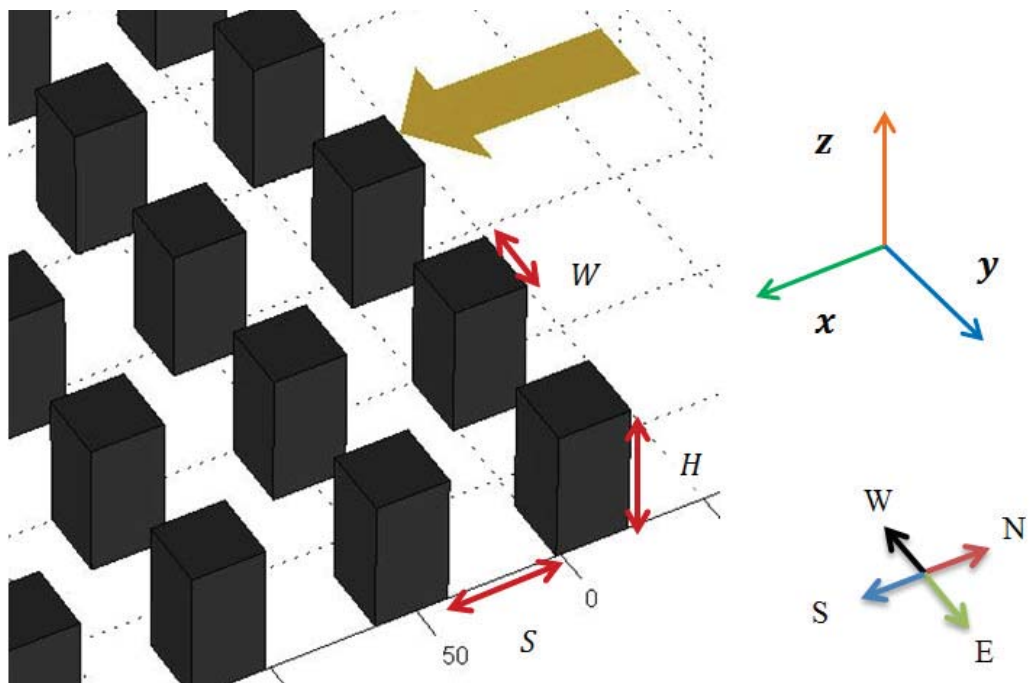
Figure 2.5: Geometrical information of the urban model.

center on each side are shown in Table 2.2.

Table 2.2: Spanwise data acquisition positions.

Plane #	1	2	3	4	5	6	7	8	9	10	11	12	13
Distance from center (mm)	2.5	4.5	6.5	8.5	10.5	12.5	14.5	16.5	18.5	20	23.5	27.5	31.25

(a) Region of interest in a single street   (b) Single SPIV plane
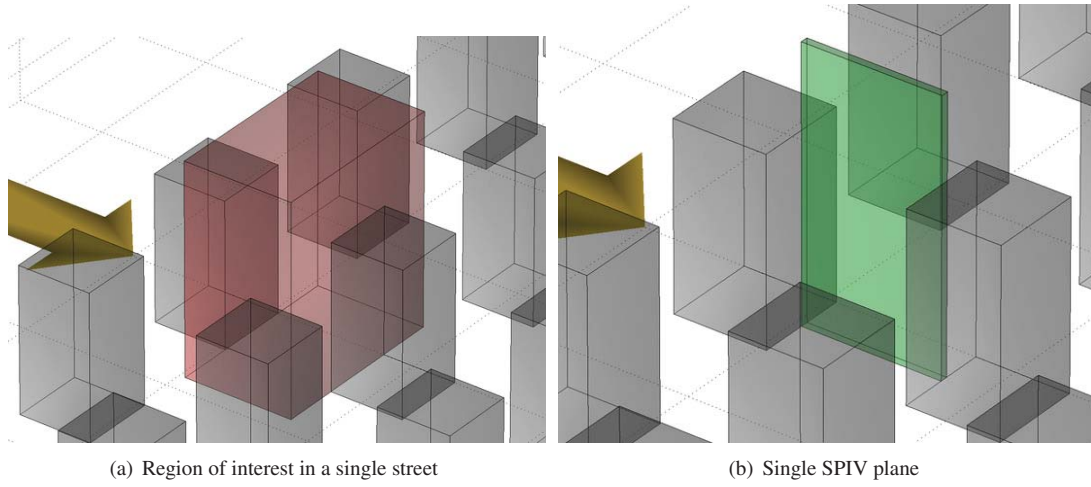
Figure 2.6: Data acquisition regions.

In each acquisition plane, a set of 1218 pairs of images are taken by each camera. The camera shooting exposure time is set to be 182 μs. Laser shooting frequency and camera capturing frequency are both 15 Hz. The detailed SPIV specifications are summarized in Table 2.3.

2.3 Hot-wire anemometry

The hot-wire probes used to characterize the three atmospheric boundary layers described earlier were operated by a Constant Temperature Anemometer, CTA, custom-made at IIT. The hot wires were built using 3.8-μm diameter tungsten wire (Sigmund Cohn Co.). The sensing length of the wire was about 1 mm to ensure a length-to-diameter ratio of $l/d > 200$. The non-dimensional sensing length, $l^+ = lu_\tau/\nu$, is less than 20 as advised by Blackwelder and Haritonidis [1983] to satisfy the spatial resolution of the small-scale turbulence structures found in wall-bounded flows. The overheat ratio was set at 1.7. The hot wires were calibrated in situ against a Pitot static probe. Fourth-order polynomial curves were used to fit the calibration data. The temperature was also monitored using a thermocouple so as to correct for any drift in the measured

14

Table 2.3: Spanwise data acquisition positions.

Feature	Specification
Laser type	pulsed dual-head Nd-Yag
Pulse separation	130 μs
Q-switch	180 μs
Laser frequency	15 Hz
Camera resolution	1280 $\times$ 1024 pixels
Interrogation area	32 $\times$ 32 pixels
Illumination thickness	2 mm
Camera capturing rate	15 fps
Camera exposure time	182 μs
Image contrast	0.05
Number of image pairs/ data set	1218
Number of data sets/ street	27

signals of the hot wires according to the temperature correction formula provided by Drubka et al. [1977]. The output signals were low-pass filtered using an Ithaco filter with a 2 kHz cut-off frequency. The sampling frequency was set at 4 kHz and the acquisition time was set at 30 s per wall-normal position of the hot wire. A National Instruments data acquisition board (PCI-6251) was used to acquire the hot-wires measurements along with the LabVIEW interface.

2.4   Stereoscopic PIV system

Particle Image Velocimetry (PIV) is a measurement technique that was introduced in the early 80's, see Adrian and Yao [1985]. Adrian [2005] defines PIV as "the accurate, quantitative measurement of fluid velocity vectors at a very large number of points simultaneously." An extension to this technique called Stereoscopic PIV (SPIV) introduced by Soloff et al. [1997] is used in this study. Essentially, the addition of a second camera allows for determining the third component of the velocity field in the out-of-plane direction. Figure 2.7 presents a simple sketch of the two cameras pointing at the region of interest from different positions. The displacement of a particle is therefore seen differently from the two cameras. Through a calibration procedure that records known out-of-plane displacements of a calibration target from both cameras, the 3D velocity field can be estimated in the laser plane. The Scheimpflug condition (image plane, lens plane and object plane intersecting in one line, see Louhichi et al. [2006]) is also satisfied so as to improve the image quality when looking at the laser plane at an angle.

Figure 2.8 presents a photograph of the SPIV setup with the laser firing. In order to make SPIV measurements possible over a large domain, it is necessary to move the measurement system quickly and accurately. The calibration process for SPIV is tedious because a new calibration is usually required for each independent plane of data if any of the SPIV components are moved. However, in this work, a solution to overcome this limitation is implemented, where we set the entire SPIV system on a single plate sitting on a two-axis traverse system located under the wind tunnel. As can be seen in Figures 2.2 and 2.8, the laser head, the light sheet optics, and the two cameras are secured to that plate. The stereo configuration chosen is also shown in Figures 2.2 and 2.8, with the two cameras viewing the laser light sheet from opposite spanwise
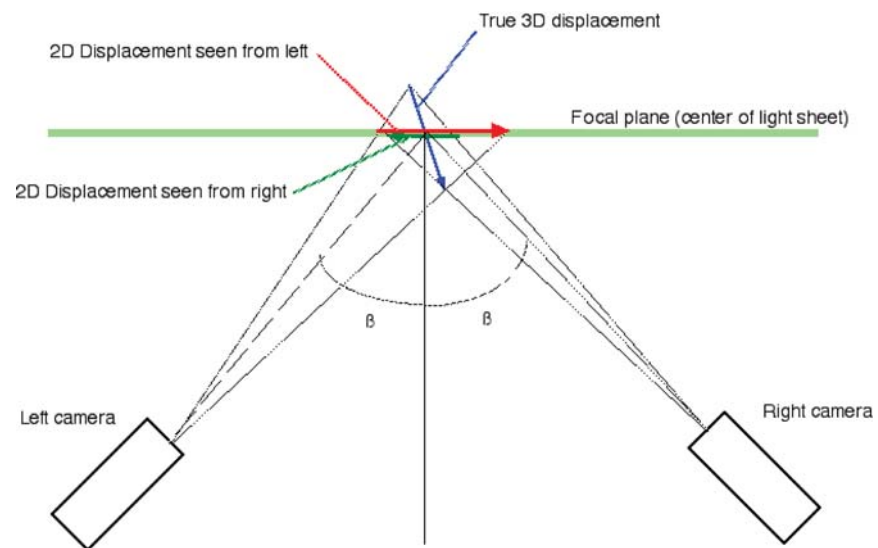
Figure 2.7: Stereoscopic principle.
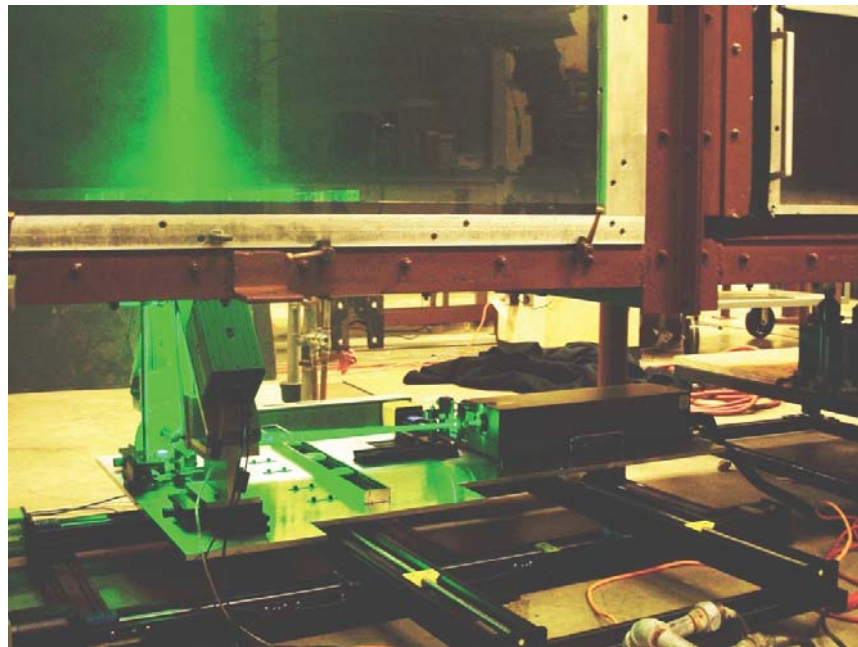
Figure 2.8: Picture of the Stereoscopic Particle Image Velocimetry system.

sides at an angle β of about 50° as defined in Figure 2.7. The light sheet enters the test section through a thin (3.18 mm) glass section of the floor. The advantages of this setup include the high accuracy of the computer-controlled two-axis traverse system, the ease of rotation of the entire PIV system to study different approach flow incidence angles, and most importantly, this system requires a single calibration per dataset (up to 224 planes). In addition, the calibration process is greatly simplified by keeping the calibration target immobile and instead displacing the SPIV setup at various out-of-plane positions using the traverse system.

The traverse system is a two-axis traverse system manufactured by Velmex, and has a large traveling distance (635 mm along both axes) so that the entire test section can be covered if needed. The repeatability is typically 4 μm, which means that when the laser plane is returned to its initial position, there is no more than 4 μm of discrepancy due to backlash. The straight line accuracy is 0.076 mm over the entire travel distance and the screw lead accuracy is 0.076 mm per 250 mm (data provided by Velmex).

The SPIV system is from Integrated Design Tools, Inc (IDT); the laser is a pulsed dual-head Nd-Yag New Wave Research (200 mJ per pulse). The two cameras are X-Stream 5 with 1280x1024 pixels and IDT ProVision-XS software is used to acquire and process the raw images. The frequency of acquisition is always set at its maximum value of 15 Hz.

The seeding is done via three Trust Science Innovation (TSI) atomizers and consists of a mixture of polyethylene glycol (PEG) and distilled water. The atomizers produce a mean droplet diameter of 0.3 μm with a geometric standard deviation of less than 2.0 μm so that the particles will follow the flow accurately (see Raffel et al. [1998]). The seeding particles are injected into the wind tunnel through three inlets at the floor just downstream of the roughness fetch. The injection speed is low enough so that it does not generate additional disturbances in the flow. This was confirmed by acquiring hot-wire velocity profiles just upstream of the urban array. The atomizers were emptied from the water and PEG mixture and run at the same compressed air pressure value as that used in the SPIV study to simulate the seeding. These velocity profiles agreed very well with those for no injection; therefore, the effect of the seeding on the boundary layer is considered to be negligible.

2.5   SPIV data processing

The commercial software used to process the raw SPIV images is ProVision-XS by Integrated Design Tools (IDT) and lets us store a "flag matrix" that contains the status of each computed velocity vector. Namely, we know if the computation of the vector is successful; which means, a valid vector is one where all conditions to obtain an accurate estimation of the velocity are met. Conversely, a spurious vector is one where all conditions are not met. A common approach is to replace the spurious vectors with interpolated vectors using a least square estimation based on the nearest neighbors approximation. This is not the approach used for the current study. When considering turbulent flows such as the urban flow, it is very difficult to obtain a uniform seeding. Often, PIV images will present regions without any particles, and depending on the size of these regions, the nearest neighbors approximation can be highly inaccurate.

A more efficient way of recovering the missing information is to use gappy-POD (Gunes et al. [2006]), which was successfully implemented by Murray and Ukeiley [2007] on PIV data. The amount of spurious velocity vectors in our data sets is on average 2% and the large amount of SPIV snapshots available to us for each vertical plane make gappy-POD an excellent alternative to standard interpolation Gunes et al. [2006].

2.6 Notes on accuracy and calibration of the SPIV setup

2.6.1 Accuracy of out-of-plane velocity component

For typical SPIV investigations, the accuracy for the in-plane components is usually given as 1-2%. Recently, many have looked into various techniques to improve the accuracy of the out-of-plane velocity component Calluaud and David [2004], Lecerf et al. [1999], **?**.

Prior to the collection of the SPIV data in the urban environment, a separate experiment was carried out to estimate the accuracy of our SPIV system. In order to estimate the accuracy of the out-of-plane component of the velocity field, SPIV measurements were taken in an axisymmetric jet. Figure 2.9 presents a photograph of the setup. The jet is shown on the right hand side in the picture and the cameras are mounted on the side and pointed at a calibration target, which is mounted perpendicular to the jet axis. In this configuration, the out-of-plane component captures the streamwise velocity of the jet. Several data sets were collected in this configuration by varying the calibration target type and the number of calibration images. The calibration target providing the best results for this jet flow is shown in Figure 2.10, as seen from both cameras. The target is made of aluminum to ensure its flatness. The grid nodes (with a 5-mm spacing in both the horizontal and vertical directions) are holes through the plate. In this example, the white mesh displayed on top of both views of the target is covering a 50×35-mm region. Each mesh node is aligned with a target grid node. The calibration process tracks the displacement of these grid nodes as the target is moved by a small amount in the out-of-plane direction. The best results in accuracy of the mean velocity measurements were obtained for 11 calibration images spanning the thickness of the laser light sheet (≈ 2 mm). These calibration parameters were therefore used in the collection of the SPIV measurements in the urban environment.

The same velocity measurements were performed for a configuration where the calibration target was mounted parallel to the jet. As a result, the streamwise component of the jet was captured by an in-plane component of the SPIV data. Figure 2.11 illustrates the results for the streamwise velocity profile of the axisymmetric jet as measured using both configurations. It can be seen that the agreement in the mean velocity profile is very good in the core of the jet ($-0.4 < r/D < 0.4$). In this region, the difference in magnitude between the in- and out-of-plane configurations does not exceed 2% as shown in Figure 2.12 and is comparable to the accuracy obtained by Lecerf et al. [1999]. Larger differences are observed in the shear layer where the seeding was non-uniform.

Since several manual steps are needed for the calibration process in the urban array study, seven sets of calibrations are collected and compared for each setup, in order to reduce the human errors. The most accurate calibration should meet two criteria on the out-of-plane (y direction) component of the velocity field. The candidate should show a relatively low level of variance, and also reveal a good agreement with other calibrations at the same time. These different calibrations were applied to street data in order to compare variance levels. Root mean squares (rms) of spanwise velocities (v_{rms}) were compared on a vertical line of data located at the centroid of the 2nd street. Furthermore spanwise mean velocities (V_m) were compared on the same line of data. Samples of these comparisons for the case of AOI = 45° are shown in Figure 2.13. In this sample, calibration number 7 (purple line) meets these two criteria better than others. As discussed earlier, the out-of-plane velocity is measured in a 2 mm thick layer which increases the measurement sensitivity. This issue is especially critical for greater incidence angles such as AOI = 45°.
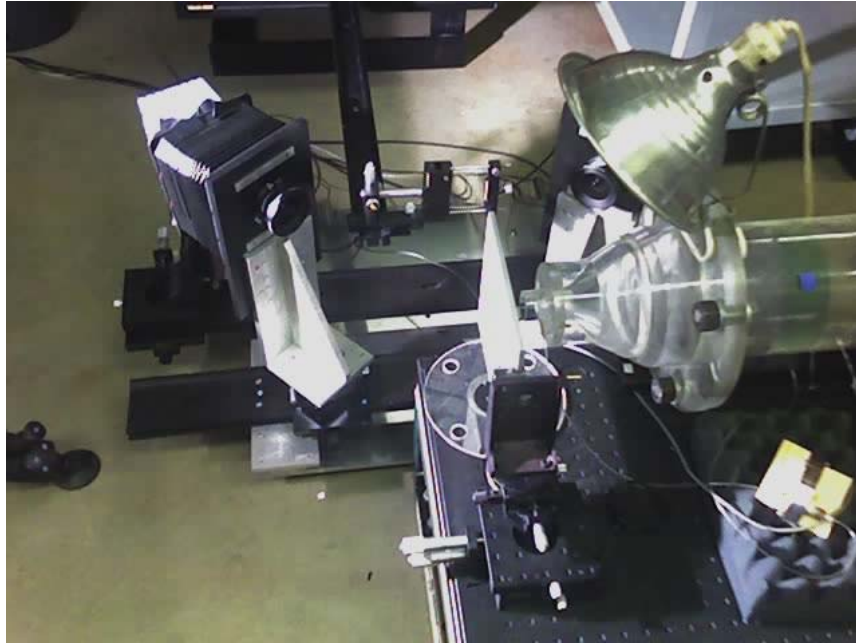
Figure 2.9: Picture of the axisymmetric jet and SPIV cameras.
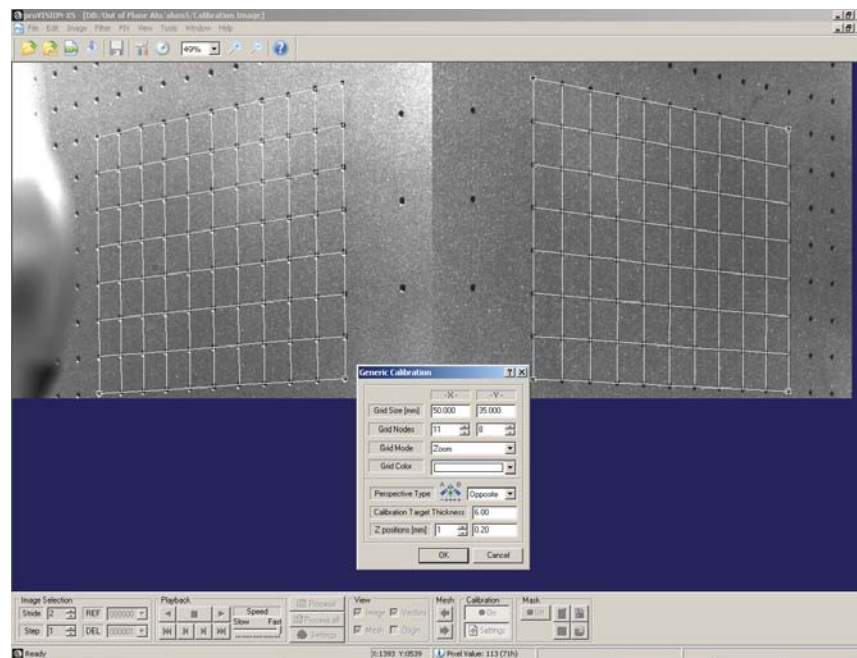
Figure 2.10: Calibration target as seen from both cameras.
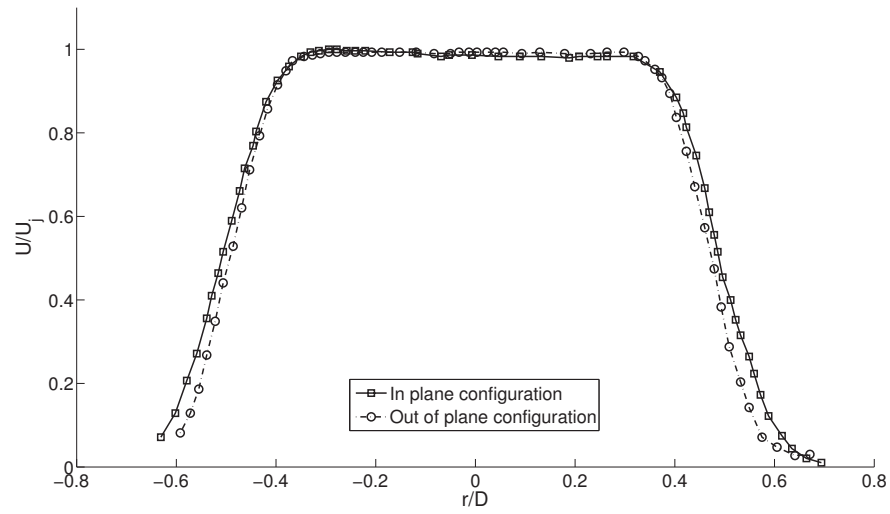
Figure 2.11: Comparison of streamwise velocity profiles for both measurement configurations.
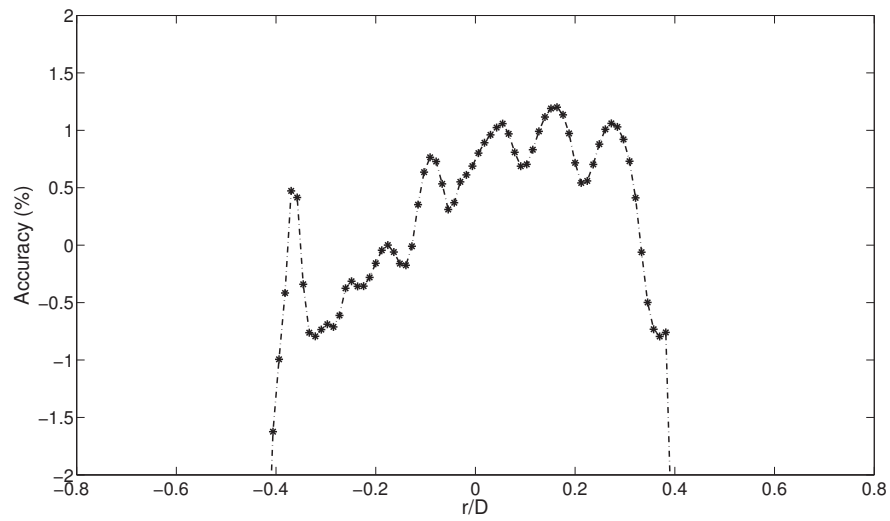
Figure 2.12: Deviation in % between the mean streamwise velocity measured in in-plane and out-of-plane configurations.
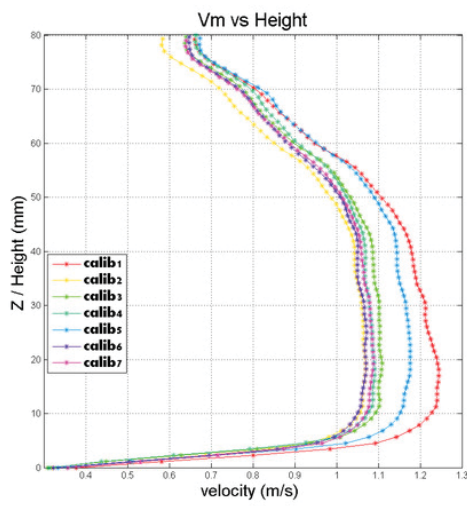
(a) V_m
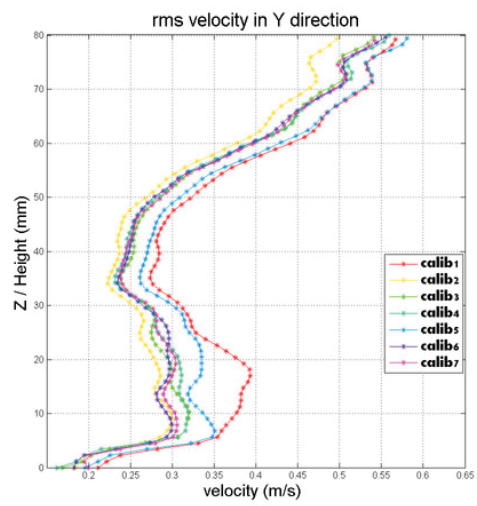
(b) v_{rms}

Figure 2.13: Seven calibrations, for AOI=45° case.

Chapter 3

Numerical method

In this chapter, the basics of the spectral element method are presented. The spectral element discretization is discussed in the context of the Poisson and incompressible Navier-Stokes equations.

3.1 Spectral element method

The Spectral element method, introduced in a 1984 paper by Patera [1984], combines the high-order accuracy of spectral methods with the geometric flexibility of the finite element methods. The simulation domain (Ω) is subdivided into spectral elements (Ω^k) and the solution within each spectral element is expressed as a linear combination of orthogonal polynomial basis functions. We define $\mathcal{P}_\mathbf{N}(\Omega^k)$ as the space of all polynomials of degree $\leq N$ in each direction on domain Ω^k. We will restrict ourselves to quadrilateral and hexahedral spectral elements.

A $\mathcal{P}_\mathbf{N}$ approximation of the solution $u(\xi_1, \xi_2, \xi_3)$ within the standard hexahedral region is represented as follows:

$$u(\xi_1, \xi_2, \xi_3) = \sum_{k=0}^{N} \sum_{j=0}^{N} \sum_{i=0}^{N} \hat{u}_{ijk} \pi_{N,i}^{GLL}(\xi_1) \pi_{N,j}^{GLL}(\xi_2) \pi_{N,k}^{GLL}(\xi_3). \tag{3.1}$$

Here, ξ_1, ξ_2 and ξ_3 are the local Cartesian coordinates, $\pi_N^{GLL}(\xi)$ are the one-dimensional Lagrangian polynomials of order N based on Gauss-Lobatto-Legendre (GLL) nodes and $\hat{u}_{ijk}$ are the basis coefficients. In this case, the total number of basis functions is $N_b = (N+1)^3$.

3.2 Spectral element discretization of the Poisson equation

We first describe the spectral element discretization in the context of the Poisson equation. The Poisson equation in the domain Ω with homogeneous Dirichlet boundary conditions is given by

$$\mathcal{L}(u) = \Delta^2 u - f = 0 \text{ in } \Omega \tag{3.2}$$
$$u = 0 \text{ on } \delta\Omega. \tag{3.3}$$

A typical spectral element mesh consisting of four spectral elements is shown in figure 3.1. The spectral
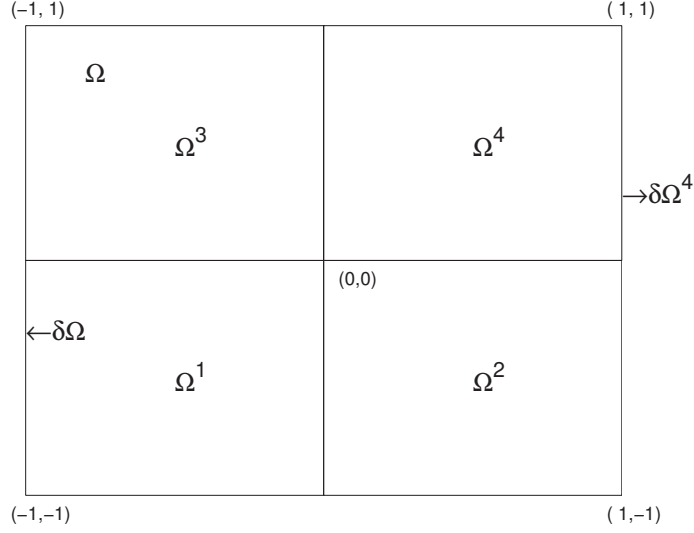
Figure 3.1: A typical spectral element mesh consisting of 4 subdomains.

element discretization is characterized by $\delta = (K, N)$ where K is the number of spectral elements and N the degree of polynomial approximation within each spectral element. We choose a function space X_δ as

$$X_\delta = \{\phi|_{\Omega^k} \in \mathcal{P}_{\mathbf{N}}(\Omega^k)\} \cap \mathcal{H}_0^1, \tag{3.4}$$

where $\mathcal{H}_0^1(\Omega)$ is is the space of all functions which are zero on the boundary and whose derivatives are square integrable over the domain Ω.

We assume that the solution and the forcing function can be accurately represented by a linear combination of basis functions

$$u^\delta(\mathbf{x}) = \sum_{i=0}^{N_b} \hat{u}_i \phi_i(\mathbf{x}), \tag{3.5}$$

$$f^\delta(\mathbf{x}) = \sum_{i=0}^{N_b} \hat{f}_i \phi_i(\mathbf{x}), \tag{3.6}$$

where $\phi_i(\mathbf{x})$ are the basis (or trial) functions and $\hat{u}_i$, $\hat{f}_i$ are the expansion coefficients. Substituting the approximation (3.5) into equation (3.2) produces the residual R such that

$$\mathcal{L}(u^\delta) = R(u^\delta). \tag{3.7}$$

We introduce the Legendre inner product (f, g) over the domain Ω as

$$(f, g) = \int_\Omega f(\boldsymbol{x})g(\boldsymbol{x})d\boldsymbol{x}. \tag{3.8}$$

The Method of Weighted Residuals (MWR) computes the unknown coefficients in equation (3.5) by restricting the residual to be orthogonal to a set of test functions $v_j(\boldsymbol{x})$ i.e.,

$$(v_j(\boldsymbol{x}), R) = 0. \tag{3.9}$$

23

For our case of the Galerkin method, we choose the trial functions to be the same as test functions. From equations (3.2), (3.5) and (3.7) we have the variational form of the Poisson equation

$$-\int_\Omega \nabla u.\nabla v d\mathbf{x} = \int_\Omega f v d\mathbf{x}. \tag{3.10}$$

Defining the stiffness matrix K as

$$\mathbf{K} = \int_\Omega \nabla\phi_i(\mathbf{x})\nabla\phi_j(\mathbf{x})d\mathbf{x} \tag{3.11}$$

and the mass matrix $\mathbf{M}$

$$\mathbf{M} = \int_\Omega \phi_i(\mathbf{x})\phi_j(\mathbf{x})d\mathbf{x}. \tag{3.12}$$

the expansion coefficients for the solution can be obtained by solving the linear system

$$\mathbf{K}\hat{u} = \mathbf{M}\hat{f} \tag{3.13}$$

3.3   Spectral element discretization of the Navier-Stokes equations

In this section, we present the spectral element discretization of the unsteady incompressible Navier-Stokes equations. The function spaces chosen for velocity and pressure basis functions are given. We then describe the spatial discretization and temporal integration algorithm for the unsteady Navier-Stokes equations. The velocity pressure decoupling algorithm is discussed. Finally, the multilevel algorithm used for computation of pressure is described.

3.3.1   Navier-Stokes equations

The Navier-Stokes equations governing incompressible fluid flow in a domain Ω with boundary $\delta\Omega$ are given by

$$\partial_t u_i + u_j\partial_j u_i = \partial_j \tau_{ij} + f_i \qquad \text{on } \Omega \times [0\ T], , \qquad (3.14a)$$

$$\partial_i u_i = 0 \qquad \text{on } \Omega \times [0\ T], , \qquad (3.14b)$$

$$u_i(t=0) = u_i^0 \qquad \text{on } \Omega, , \qquad (3.14c)$$

$$u_i = g_i^{\mathcal{D}} \qquad \text{on } \delta\Omega_{\mathcal{D}}, , \qquad (3.14d)$$

$$n_j\tau_{ij} = \left(-p\delta_{ij} + \frac{1}{Re}(\partial_j u_i + \partial_i u_j)\right)n_j = 0 \qquad \text{on } \delta\Omega_{\mathcal{O}}, , \qquad (3.14e)$$

$$u_i(x_k) = u_i(x_k') \text{ for } x_k, x_k' \qquad \text{on } \delta\Omega_{\mathcal{P}}, \qquad (3.14f)$$

where $u_i(x_j)$, $p(x_j)$ and $f_i(x_j)$ are velocity, pressure and body force at each point x_j in domain Ω. The Reynolds number is $Re = UL/\nu$, where U and L are the characteristic velocity and length scales and ν is the kinematic viscosity. Equations (3.14a) and (3.14b) present the momentum and continuity equations respectively. Equations (3.14c), (3.14d), (3.14e) and (3.14f) present the initial condition, Dirichlet boundary condtion, outflow boundary conditions and periodic boundary conditions respectively. $\delta\Omega_{\mathcal{D}}$, $\delta\Omega_{\mathcal{O}}$ and $\delta\Omega_{\mathcal{P}}$ represent the Dirichlet, outflow and periodic boundaries respectively. In equation (3.14f), x_k' represents a shadow point corresponding to the point x_k on the periodic boundary.

3.3.2 Function spaces

Before proceeding with the spatial discretization, it is important to choose consistent function spaces for velocity ($X_\mathbf{N}$) and pressure ($Y_\mathbf{N}$) so that the resulting system is stable. Here, we use the $\mathcal{P}_\mathbf{N} - \mathcal{P}_{\mathbf{N-2}}$ formulation for velocity and pressure. This satisfies the inf-sup (Babuska-Brezzi-Ladyzenskaya) condition for stability. Tensor products of one dimensional Lagrangian polynomials based on GLL nodes,

$$u_i(\xi_1, \xi_2, \xi_3) = \sum_{l=0}^{N} \sum_{m=0}^{N} \sum_{n=0}^{N} \hat{u}_{i,lmn} \pi_{N,l}^{GLL}(\xi_1) \pi_{N,m}^{GLL}(\xi_2) \pi_{N,n}^{GLL}(\xi_3) = \sum_{j=0}^{NV_b} \hat{u}_{i,j} \phi_j(\xi_1, \xi_2, \xi_3). \tag{3.15}$$

are used as basis functions for velocity within each spectral element and C^0 continuity is enforced between adjacent spectral elements. Here, $NV_b = (N+1)^3$ is the total number of velocity basis functions. This has certain important advantages. Since the interior basis functions are zero on the boundary GLL nodes, enforcement of Dirichlet boundary conditions and inter-element continuity only involves boundary nodes. This simplifies the implementation of Dirichlet boundary conditions and offers significant reduction in communication costs. We use $\Phi_i(x_j)$ to denote the global velocity basis functions.

The $\mathcal{P}_{\mathbf{N-2}}$ function space is chosen for pressure. Since inter-element continuity is not explicitly enforced for pressure between adjacent spectral elements, a modal basis consisting of tensor products of one-dimensional Lagrangian polynomials

$$p(\xi_1, \xi_2, \xi_3) = \sum_{l=0}^{N-2} \sum_{m=0}^{N-2} \sum_{n=0}^{N-2} \hat{p}_{lmn} L_{N,l}(\xi_1) L_{N,m}(\xi_2) L_{N,n}(\xi_3) = \sum_{j=0}^{NP_b} \hat{p}_j \psi_j(\xi_1, \xi_2, \xi_3), \tag{3.16}$$

are used as basis functions within each spectral element. Here, $NP_b = (N-1)^3$ is the total number of pressure basis functions. We use $\Psi_i(x_j)$ to denote the global pressure basis functions.

3.3.3 Galerkin projection

We now proceed to derive the weak form of the Navier-Stokes equation using the Galerkin projection method. The velocity, pressure and body force are represented by a linear combination of their global basis functions as

$$u_i(x_k) = \sum_{j=0}^{NGV_b} \hat{u}_{i,j} \Phi_j(x_k), p(x_k) = \sum_{j=0}^{NGP_b} \hat{p}_j \Psi_j(x_k) \text{ and } f_i(x_k) = \sum_{j=0}^{NGV_b} \hat{f}_{i,j} \Phi_j(x_k). \tag{3.17}$$

The Galerkin method computes the unknown coefficients in (3.14) by restricting the residual to be orthogonal to the function space used for approximating the solution. Thus the test functions are the same as the basis functions. Following the variational procedure outlined in the earlier section, we obtain

$$\int_\Omega \Phi_k \Phi_l \frac{d\hat{u}_{i,l}}{dt} dV + \int_\Omega \hat{u}_{j,m} \left(\Phi_m \Phi_k \partial_j \Phi_l \right) \hat{u}_{i,l} dV = \oint_{\delta\Omega} \Phi_k (\tau_{ij} n_j) dS - \int_\Omega \partial_j \Phi_k \tau_{ij} dV$$

$$+ \int_\Omega \Phi_k \Phi_l \hat{f}_{i,l} dV, \tag{3.18a}$$

$$\int_\Omega \Psi_k \partial_i \Phi_l \hat{u}_{i,l} dV = 0. \tag{3.18b}$$

We use the convective form for discretizing the nonlinear term. The Dirichlet boundary conditions are enforced using the lifting technique, $\hat{u}_i = \hat{u}_i^{int} + \hat{u}_i^{\mathcal{D}}$. We can see that the first term on the right-hand side is zero on Dirichlet and outflow boundaries and can be dropped. These equations can be rewritten as

$$M\frac{d\hat{u}_i}{dt} + \hat{u}_j C\hat{u}_i = M\hat{f}_i - \frac{1}{Re}A\hat{u}_i + D_i^T\hat{p}, \tag{3.19a}$$

$$D_i\hat{u}_i = 0, \tag{3.19b}$$

where

$$M = \int_\Omega \phi_k\phi_k dV, C = \int_\Omega \phi_m\phi_k\partial_j\phi_l dV, A = \int_\Omega \partial_k\phi_i\partial_k\phi_j dV, \text{ and } D_i = \int_\Omega \psi_k\partial_i\phi_l dV. \tag{3.20}$$

Here M, C and A are the mass matrix, convective matrix and Laplacian matrix respectively. The matrix D_i contains the projection of the derivatives of the velocity basis functions in the ith direction on the pressure basis function.

3.3.4 Temporal discretization

We use a semi-explicit scheme for temporal discretization. The Stokes operator, which places a severe restriction on time step size if treated explicitly, is treated implicitly using a backward difference (BDF) scheme. The nonlinear convective term is treated explicitly using the extrapolation (EX) scheme. Discretizing equation (3.19) using a second-order backward difference (BDF2) scheme for the Stokes operator and second-order extrapolation scheme (EX2) we get

$$M\left[\alpha_0\hat{u}_i^{n+2} - \alpha_1\hat{u}_i^{n+1} - \alpha_2\hat{u}_i^n\right] = M\hat{f}_i^{n+2} - \frac{1}{Re}A\hat{u}_i^{n+2} + D_i^T p^{n+2}$$
$$- \left[\beta_0\hat{u}_j^{n+1}C\hat{u}_i^{n+1} + \beta_1\hat{u}_j^n C\hat{u}_i^n\right], \tag{3.21a}$$

$$D_i\hat{u}_i = 0, \tag{3.21b}$$

where,

$$\alpha_0 = \frac{3}{2\Delta t}, \ \alpha_1 = \frac{2}{\Delta t}, \ \alpha_2 = \frac{-1}{2\Delta t}, \ \beta_0 = 2, \ \beta_1 = -1. \tag{3.21c}$$

Using the notation

$$\hat{u} = \begin{bmatrix} \hat{u}_1 \\ \hat{u}_2 \\ \hat{u}_3 \end{bmatrix}, \hat{r} = \begin{bmatrix} \hat{r}_1 \\ \hat{r}_2 \\ \hat{r}_3 \end{bmatrix}, \hat{D} = \begin{bmatrix} \hat{D}_1 \\ \hat{D}_2 \\ \hat{D}_3 \end{bmatrix},$$

$$\hat{A} = \begin{bmatrix} A_1 & & \\ & A_2 & \\ & & A_3 \end{bmatrix}, \hat{M} = \begin{bmatrix} M_1 & & \\ & M_2 & \\ & & M_3 \end{bmatrix} \text{ and } \hat{H} = \frac{1}{Re}\hat{A} + \alpha_0\hat{M}.$$

equation (3.21) can be rewritten as

$$\begin{bmatrix} \hat{H} & -\hat{D}^T \\ -\hat{D} & 0 \end{bmatrix}\begin{bmatrix} \hat{u}^{n+2} \\ \hat{p}^{n+2} \end{bmatrix} = \begin{bmatrix} \hat{r} \\ 0 \end{bmatrix}. \tag{3.22}$$

Here $\hat{A}$, $\hat{M}$ and $\hat{H}$ are the global Laplacian, mass and Helmholtz matrices respectively.

26

3.3.5 Pressure velocity decoupling

In principle, the system of equations (3.21) can solved directly for pressure using the Uzawa algorithm. We have

$$\hat{S}\hat{p} = -\hat{D}\hat{H}^{-1}\hat{r}, \tag{3.23}$$

where

$$\hat{S} = \hat{D}\hat{H}^{-1}\hat{D}^T. \tag{3.24}$$

For steady problems, the $\hat{S}$ matrix is well conditioned and can be solved very efficiently using an iterative method like the preconditioned conjugate gradient method when preconditioned by the mass matrix. In this case, while the number of outer solves are small, the $\hat{H}$ system (in this case the $\hat{A}$ system) needs to be solved in each iteration.

However, for the unsteady Navier-Stokes equations, while the $\hat{H}$ system is well conditioned and can be solved quickly using the diagonally preconditioned conjugate gradient method, the $\hat{S}$ matrix is very ill-conditioned. This significantly increases the number of outer iterations. This necessitates the use of a more efficient decoupling algorithm for solving problems of engineering interest.

In this code, we use a numerical fractional step method for decoupling pressure and velocity. This is discussed in detail in Couzy [1995], Perot [1993] and Fischer [1997]. The basic idea is to compute the pressure update only instead of the full pressure. The system of equations (3.21) can be rewritten as

$$\begin{bmatrix} \hat{H} & -\hat{H}\hat{Q}\hat{D}^T \\ -\hat{D} & 0 \end{bmatrix} \begin{bmatrix} \hat{u}^{n+2} \\ \hat{p}^{n+2} - \hat{p}^{n+1} \end{bmatrix} = \begin{bmatrix} \hat{r} + \hat{D}^T\hat{p}^{n+1} + res \\ 0 \end{bmatrix}. \tag{3.25}$$

where the splitting error is given by

$$res = (I - \hat{H}\hat{Q})\hat{D}^T(\hat{p}^{n+2} - \hat{p}^{n+1}). \tag{3.26}$$

Following Couzy [1995] and Fischer [1997], we choose $\hat{Q} = \frac{1}{\alpha_0}\hat{M}^{-1}$ which yields a splitting error

$$res = \frac{1}{\alpha_0 Re}(\hat{A}\hat{M}^{-1})\hat{D}^T(\hat{p}^{n+2} - \hat{p}^{n+1}). \tag{3.27}$$

which is second order in time. In general, this fractional step method can be tuned for higher order of accuracy. Using Gaussian elimination, equation (3.25) can be reduced to

$$\begin{bmatrix} \hat{H} & -\frac{1}{\alpha_0}\hat{H}\hat{M}^{-1}\hat{D}^T \\ 0 & E \end{bmatrix} \begin{bmatrix} \hat{u}^{n+2} \\ \hat{p}^{n+2} - \hat{p}^{n+1} \end{bmatrix} = \begin{bmatrix} \hat{r} + \hat{D}^T\hat{p}^{n+1} + res \\ \hat{g} \end{bmatrix},$$

where

$$\hat{E} = \frac{1}{\alpha_0}\hat{D}\hat{M}^{-1}\hat{D}^T, \tag{3.28a}$$

$$\hat{g} = -\hat{D}\hat{H}^{-1}(\hat{r} + \hat{D}^T\hat{p}^{n+1}). \tag{3.28b}$$

The system E is called the consistent Poisson operator.

3.3.6 Solution strategy for pressure

The solution of the Navier-Stokes equations requires two system solves at each time step. The first one is the solution of the Helmholtz system. At high Reynolds number, the Helmholtz operator is diagonally dominant and can be solved in a computationally efficient way using a Jacobi-preconditioned conjugate gradient algorithm. The most expensive step is the solution of consistent Poisson equation for pressure given by

$$\hat{E}\hat{p} = \hat{g}. \tag{3.29}$$

We use a two level solution strategy Fischer [1996] for solving the consistent Poisson equation. We decompose the pressure into fine (p_f) and coarse (p_c) components. Figure 3.2 illustrates a typical decomposition of pressure modes into fine and coarse components. Slowly varying pressure modes are chosen as coarse
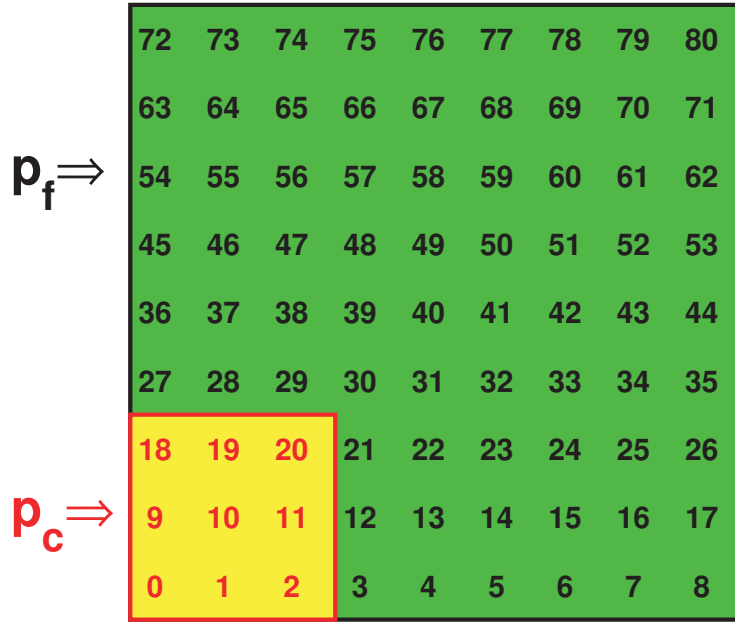
Figure 3.2: Schematic illustrating the decomposition of pressure into fine (p_f) and coarse (p_c) modes for a quadrilateral spectral element. In this case, an eighth-order approximation is used for the fine pressure, and a second-degree approximation is used for the coarse pressure.

modes. The degree of coarse space can be chosen at runtime. Using the decomposition $\hat{p} = \hat{p}_c + \hat{p}_f$, equation (3.29) can be rewritten as

$$\begin{bmatrix} \hat{E}_{ff} & \hat{E}_{fc} \\ \hat{E}_{cf} & \hat{E}_{cc} \end{bmatrix} \begin{bmatrix} \hat{p}_f \\ \hat{p}^c \end{bmatrix} = \begin{bmatrix} \hat{g}_f \\ \hat{g}_c \end{bmatrix}.$$

The fine and coarse systems for pressure are given by

$$\hat{E}_f \hat{p}_f = \hat{g}_f - \hat{E}_{fc}\hat{E}_{cc}^{-1}\hat{g}_c, \tag{3.30a}$$

$$\hat{E}_{cc}\hat{p}_c = \hat{g}_c - \hat{E}_{cf}\hat{p}_f, \tag{3.30b}$$

respectively where $\hat{E}_f = \hat{E}_{ff} - \hat{E}_{fc}\hat{E}_{cc}^{-1}\hat{E}_{cf}$. This system is first solved for $\hat{p}_f$ and then for $\hat{p}_c$.

3.3.7 Solution of the fine pressure system

The fine pressure system is solved using a block-Jacobi preconditioned conjugate gradient method. This is described in the work of Couzy [1995]. We first assume that the spectral element is a rectangle or a rectangular parallelepiped in three dimensions. The local consistent Poisson operator $\hat{E}_k$ can be written as

$$\hat{E}_k = D_x M^{-1} D_x^T + D_y M^{-1} D_y^T + D_z M^{-1} D_z^T \tag{3.31}$$

where

$$D_x = \frac{l_y l_z}{2.2} \left[\psi_t w_t \phi_t \otimes \psi_s w_s \phi_s \otimes \psi_r w_r \phi_r' \right], \tag{3.32a}$$

$$D_y = \frac{l_x l_z}{2.2} \left[\psi_t w_t \phi_t \otimes \psi_s w_s \phi_s' \otimes \psi_r w_r \phi_r \right], \tag{3.32b}$$

$$D_z = \frac{l_x l_y}{2.2} \left[\psi_t w_t \phi_t' \otimes \psi_s w_s \phi_s \otimes \psi_r w_r \phi_r \right], \tag{3.32c}$$

$$M^{-1} = \frac{2.2.2}{l_x l_y l_z} \left[\hat{w}_t^{-1} \otimes \hat{w}_s^{-1} \otimes \hat{w}_r^{-1} \right]. \tag{3.32d}$$

Here ψ is the matrix containing the one-dimensional pressure basis functions, ϕ is the matrix containing the one-dimensional velocity basis functions and ϕ' is the matrix containing the derivatives of one dimensional velocity basis functions. These are all evaluated on the Gauss-Legendre mesh. w is the diagonal matrix containing Gauss-Legendre weights and $\hat{w}$ is the diagonal matrix containing the Gauss-Lobatto-Legendre weights.

$$\hat{E}_k = \left[\frac{l_y l_z}{2l_x} J_t \otimes J_s \otimes E_r + \frac{l_x l_z}{2l_y} J_t \otimes E_s \otimes J_r + \frac{l_x l_y}{2l_z} E_t \otimes J_s \otimes J_r \right], \tag{3.33}$$

where

$$J_r = J_s = J_t = \psi w \phi \hat{w}^{-1} \phi^T w^T \psi^T, \tag{3.34a}$$

$$E_r = E_s = E_t = \psi w \phi' \hat{w}^{-1} \phi'^T w^T \psi^T. \tag{3.34b}$$

In this form, $\hat{E}_k$ can be inverted using a fast diagonalization method (FDM).

$$\hat{E}_k^{-1} = (S_z \otimes S_y \otimes S_x)(\frac{l_y l_z}{2l_x} I_z \otimes I_y \otimes \Lambda_x + \frac{l_x l_z}{2l_y} I_z \otimes \Lambda_y \otimes I_x + \frac{l_x l_y}{2l_z} \Lambda_z \otimes I_y \otimes I_x)^{-1}(S_z^T \otimes S_y^T \otimes S_x^T) \tag{3.35}$$

where $S_x, S_y, S_z, \Lambda_x, \Lambda_y$ and Λ_z are the solutions of generalized eigenvalue problems

$$E_x S_x = J_x S_x \Lambda_x, \quad E_y S_y = J_y S_y \Lambda_y \text{ and } E_z S_z = J_z S_z \Lambda_z. \tag{3.36}$$

The matrix in the middle is diagonal and can be trivially inverted. Hence, the block Jacobi preconditioner is given by

$$E_f^{prec} = \begin{bmatrix} \hat{E}_1^{-1} & & & \\ & \hat{E}_2^{-1} & & \\ & & \ddots & \\ & & & \hat{E}_K^{-1} \end{bmatrix}. \tag{3.37}$$

29
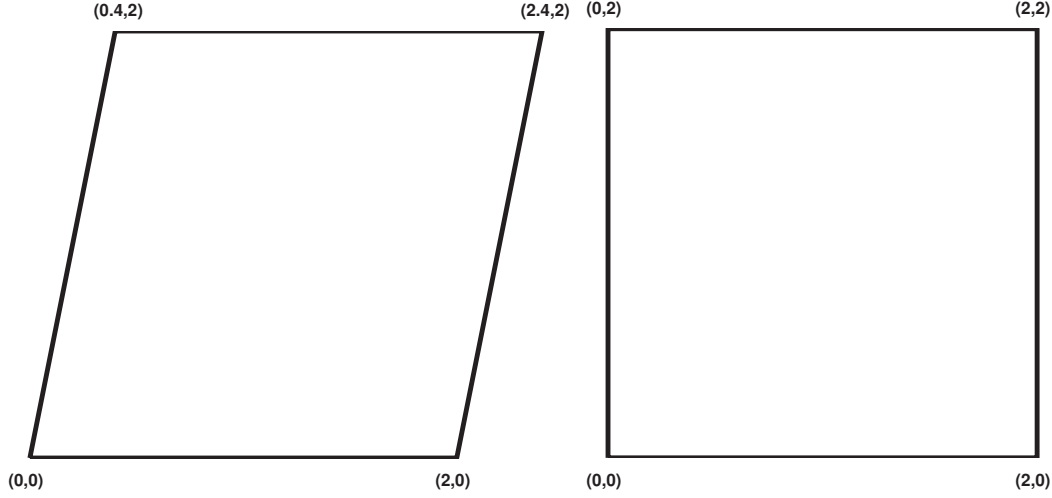
Figure 3.3: Schematic of a "deformed" element (left) and the corresponding "undeformed" element (right) used for constructing the block preconditioner for pressure

In the general case, the individual spectral elements are "deformed" and the local $\hat{E}_k$ matrix cannot be inverted using FDM. In those cases, we first construct a corresponding "undeformed" element with average dimensions of the "deformed" element. Figure 3.3 shows a typical "deformed" element and the corresponding "undeformed". For example, in a deformed hexahedral spectral element the average seperation between faces can be computed using

$$l_r^k = \left[\frac{\sum_{m,n} \rho_m \rho_n [(x_{Nmn}^k - x_{0mn}^k)^2 + (y_{Nmn}^k - y_{0mn}^k)^2 + (z_{Nmn}^k - z_{0mn}^k)^2]}{\sum_{m,n} \rho_m \rho_n} \right]^{0.5}, \qquad (3.38a)$$

$$l_s^k = \left[\frac{\sum_{l,n} \rho_l \rho_n [(x_{lNn}^k - x_{l0n}^k)^2 + (y_{lNn}^k - y_{l0n}^k)^2 + (z_{lNn}^k - z_{l0n}^k)^2]}{\sum_{l,n} \rho_l \rho_n} \right]^{0.5}, \qquad (3.38b)$$

$$l_t^k = \left[\frac{\sum_{l,m} \rho_l \rho_m [(x_{lmN}^k - x_{lm0}^k)^2 + (y_{lmN}^k - y_{lm0}^k)^2 + (z_{lmN}^k - z_{lm0}^k)^2]}{\sum_{l,m} \rho_l \rho_m} \right]^{0.5}. \qquad (3.38c)$$

Here, l_r, l_s and l_t are the average lengths in principal directions, N is the order of polynomial approximation in each direction, ρ are the one dimensional GLL weights and x, y and z are the cartesian coordinates of mesh points.

3.3.8 Solution of the coarse pressure system

Efficient solution of the coarse grid problem plays an important part in the scalability of the spectral element solver. In this code, we implement two coarse grid solvers. The first is a fast parallel direct solver described in detail in the work of Tufo [2001]. The second is an algebraic multigrid (AMG) solver described in the work of Lottes [2011]. We make two important improvements. The parallel direct solver is modified to

support partition counts that are not an integral power of two. The code for setting up the AMG solver is multi-threaded which helps in reducing setup time. The parallel direct solver is used for mesh sizes less than 10^5 and the AMG solver is used for larger mesh sizes.

3.3.9 Outflow boundary condition for turbulent flows

For high Reynolds number flows, energy influx into the domain caused by strong vortices exiting at the outflow boundary can create numerical instability. If we look at the equation governing the evolution of kinetic energy,

$$\frac{\partial}{\partial t} \int_\Omega \frac{1}{2}(u_k u_k) dV = \nu \int_\Omega (\partial_j u_k \partial_j u_k) dV + \int_\Omega (f_i u_i) dV$$
$$+ \int_{\partial\Omega_\mathcal{D}} (n_j \tau_{ij} - \frac{1}{2} u_k u_k n_i) u_i dS + \int_{\partial\Omega_\mathcal{O}} (n_j \tau_{ij} - \frac{1}{2} u_k u_k n_i) u_i dS, \quad (3.39)$$

we can see that the last term on the right hand side describing the surface integral over $\partial\Omega_\mathcal{O}$ can cause numerical instability if $n_j u_j < 0$ anywhere on $\partial\Omega_\mathcal{O}$.

We implement the outflow boundary condition described in the work of Dong et al. [2014]. The idea is to impose the boundary condition

$$n_j \tau_{ij} = \frac{1}{2}(u_k u_k) S_0(n_k u_k) n_i \text{ on } \Omega_\mathcal{O}, \quad (3.40)$$

so that energy influx through the outflow boundary will not create numerical instability. Here

$$S_0(n_k u_k) = \frac{1}{2}\left(1 - tanh\left(\frac{n_k u_k}{U_0 \delta}\right)\right), \quad (3.41)$$

where U_0 is the characteristic velocity scale and δ is a small non-dimensional positive constant.

3.3.10 Filter-based stabilization

At high Reynolds numbers a stabilization method is generally needed in absence of a LES model. Here, we use the filter-based stabilization method developed by Fischer and Mullen [2001]. The basic idea is to interpolate the flow field onto a coarser mesh and interpolate the data back from the coarse mesh back to the fine mesh. For velocity u in $\mathcal{P}_N$, the filtered velocity $\hat{u}_\alpha$ is given by

$$\hat{u}_\alpha = (1 - \alpha)u + I_{N-1}u, \quad (3.42)$$

where α is the filter coefficient. Here, $I_{N-1}u$ is generated by interpolating u onto GLL points for $\mathcal{P}_{N-1}$ and interpolating it back onto GLL points for $\mathcal{P}_N$. In general, multi-level filters can be used. This procedure has the advantage that inter-element continuity is preserved and so is spectral accuracy. In general, the filter is applied to the flow field after each time step.

3.4 Implementation details

In this section, we present some implementation details related to the spectral element solver *Specsolve*. The code is developed in C++ and uses the Message Passing Interface (MPI) for communication. It exploits the

object-oriented features of C++ and uses dynamic memory allocation for optimal memory usage. The code is relatively self-contained and the only external dependencies are the LAPACK and BLAS libraries. We present below a brief description of some important components of the code.

The CUBIT mesh generator is used for generating the spectral element meshes. Currently only quadrilateral and hexahedral meshes are supported.

The program `mesh.c` contains components for reading and processing the spectral element mesh. The function `read_mesh()` reads the spectral element mesh generated by CUBIT. The mesh is then scanned for presence of periodic zones. If periodic zones are present, each face in a periodic zone is matched with appropriate face in the corresponding shadow zone. It also makes sure that the periodic and shadow faces are properly aligned. It then matches periodic nodes and edges with corresponding shadow nodes and edges. It then assigns nodes, edges and faces to corresponding cells. The data structures used for nodes, faces, edges, cells and zones are defined in geom.h. It then proceeds to assign global id (*gid*) to each degree of freedom. Figure 3.4 shows the spectral element mesh for a typical quadrilateral spectral element. It numbers
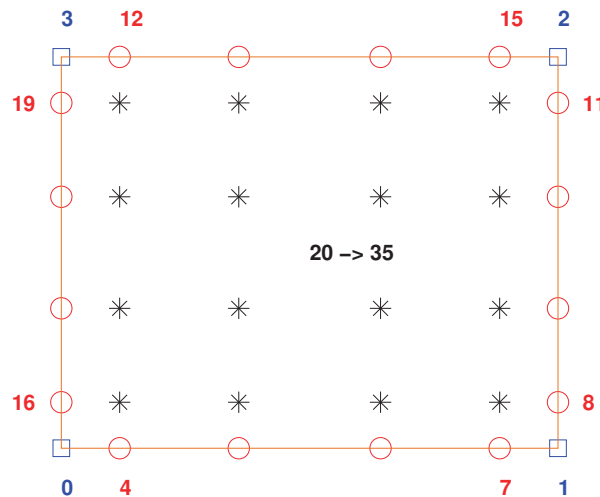

Figure 3.4: Numbering node ($\square$), face ($\circ$) and interior ($*$) degrees of freedom for a quadrilateral spectral element.

nodes, edges (in three dimensions) and faces in that order. The interior cell points are numbered in the end after the entire skeleton is numbered. For edges, faces and cells only the *gid* range ($[gid_{first}, gid_{last} + 1]$) needs to be stored. A weighted graph is then built based on node connectivity information. The graph is then partitioned using our parallel recursive spectral bisection algorithm. The graph partitioning algorithm is written in `graph.c`. Figure 3.5 shows partitioning of a typical spectral element mesh into 5 partitions. This partitioner does not require the number of partitions to be an integral power of two. This partition information is also used during the setup stage by the parallel direct solver, which is used to solve the coarse grid problem. Master processors are assigned to each node, edge, face and cell. It then assigns boundary conditions to each degree of freedom.

The program `solver.c` initializes the "Solver" object. The Solver class is defined in solver.h. This program distributes mesh data to each processor based on partition information. In addition, mesh information related to cells on processor boundaries are distributed redundantly to all processors involved.

The program `basis.c` generates the one-dimensional basis functions, quadrature points and quadrature
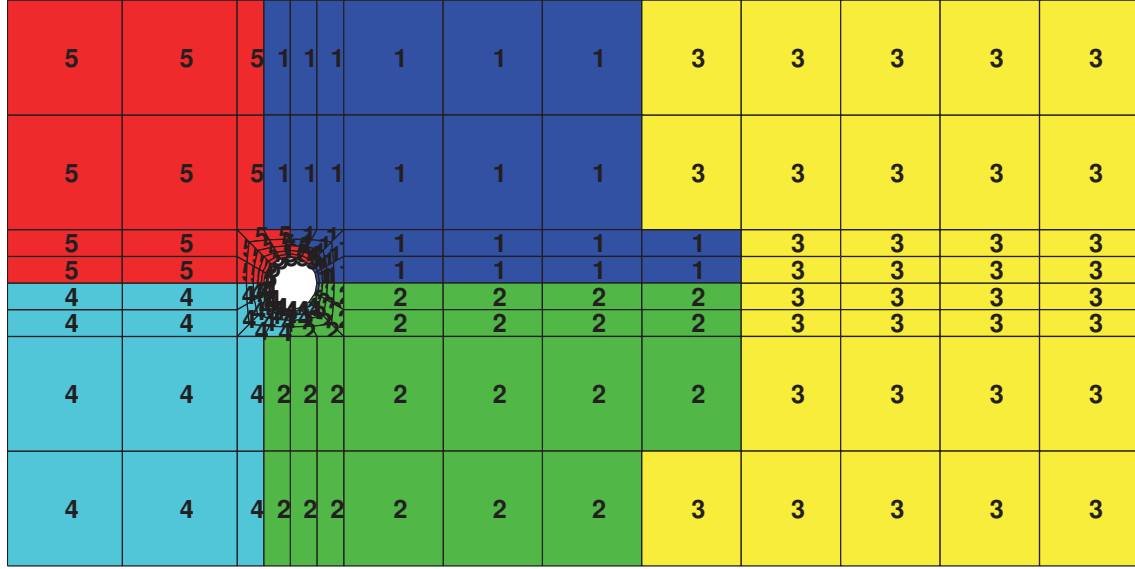
Figure 3.5: A two-dimensional spectral element mesh partitioned into 5 parts using recursive spectral bisection.

weights. Figure 3.6 shows the one dimensional velocity and pressure basis functions associated with a $\mathcal{P}_5$ quadrilateral spectral element. Figure 3.7 shows three different meshes for evaluating various integrals. The pressure mesh is used for evaluating integrals involving pressure basis functions. Mesh 2 is used for de-aliased integration of nonlinear terms. Mesh 1 is used for computing all other integrals. Mesh 1 and 2 used GLL (Gauss-Lobatto-Legendre) quadrature of appropriate order whereas the pressure mesh uses LG(Legendre-Gauss) quadrature.

The program `matrix.c` defines various matrix classes and related functions used by the program. Serial dense matrices and parallel sparse matrices are supported. A sparse matrix-vector product is custom coded whereas LAPACK and BLAS are used for dense matrix operations. The file `lpk_blas.c` provides the interface to external LAPACK and BLAS libraries.

The program `map2stdel.c` contains code for generating the internal spectral element mesh. First, nodes on the exterior of each cell are mapped to appropriate locations and a smooth interior nodal distribution is obtained by solving a Poisson equation with exterior node distribution as boundary condition. It also computes Jacobian's and other entities needed for local elemental operations like integration and differentiation.

The program `dss.c` contains functions for setting and effecting direct stiffness summation. The program `tens.c` contains functions that evaluate the effect of an operator on a vector. In this code, none of the operators are explicitly constructed. For quadrilateral and hexahedral spectral elements, these operators can be written as a tensor product (see Deville et al. [2002]). For a d-dimensional problem, the sum factorization technique can be used to evaluate these tensor product-vector multiplications in $O(n^{d+1})$ operations instead of the naive $O(n^{2d})$ operation count for a matrix of order n .

The GMRES (generalized minimal residual) solver for pressure and the PCG (preconditioned conjugate gradient) solver for the Helmholtz system are written in `gmres.c` and `pcg.c` respectively. The fractional
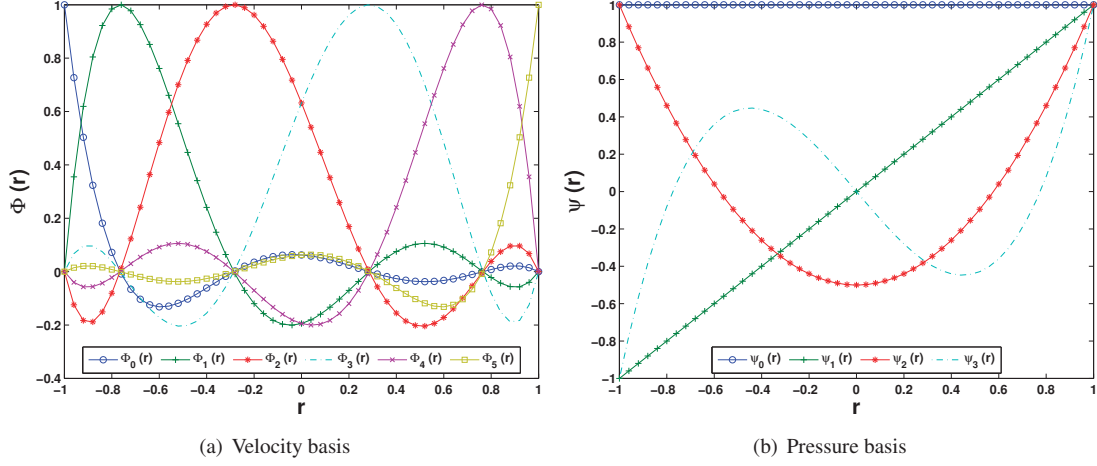
(a) Velocity basis   (b) Pressure basis

Figure 3.6: One-dimensional basis functions for $\mathcal{P}_5 - \mathcal{P}_3$ spectral element formulation.

step method is implemented in `navier_stokes.c`. The program `coarse.c` contains functions for building the coarse pressure matrix. The direct parallel solver for the coarse pressure problem is coded in `xxt.c`. The algebraic multigrid solver is coded in `amg.c`.

For meshes containing more than 100000 spectral elements, AMG solver needs to be used. A multi-threaded solver `setup_amg` is built for generating data needed for the AMG solver. In this case, first the coarse pressure matrix is built and written to a file. `setup_amg` is called to set up data needed for the AMG solver before running the spectral element solver.

Finally, the program `export.c` contains functions that perform input-output (IO) operations. We use MPI-IO for optimal IO performance. VisIt and Tecplot are used for visualization of results.

3.5 Algebraic multigrid solver

In this section, we describe in detail the algebraic multigrid solver used for the solution of the coarse problem.

3.5.1 Introduction

We consider the solution of the linear system

$$A\mathbf{x} = \mathbf{b}, \tag{3.43}$$

where A is a sparse symmetric positive definite $n \times n$ matrix using fixed point iteration method. Using the initial guess $\mathbf{x}^{\textbf{init}}$ and a symmetric positive definite smoother $C = B^{-1}$, the iterative solution method can be written as

$$\mathbf{x}^0 = \mathbf{x}^{init}, \tag{3.44}$$
$$\mathbf{x}^{m+1} = \mathbf{x}^m + C(b - A\mathbf{x}^m), \tag{3.45}$$

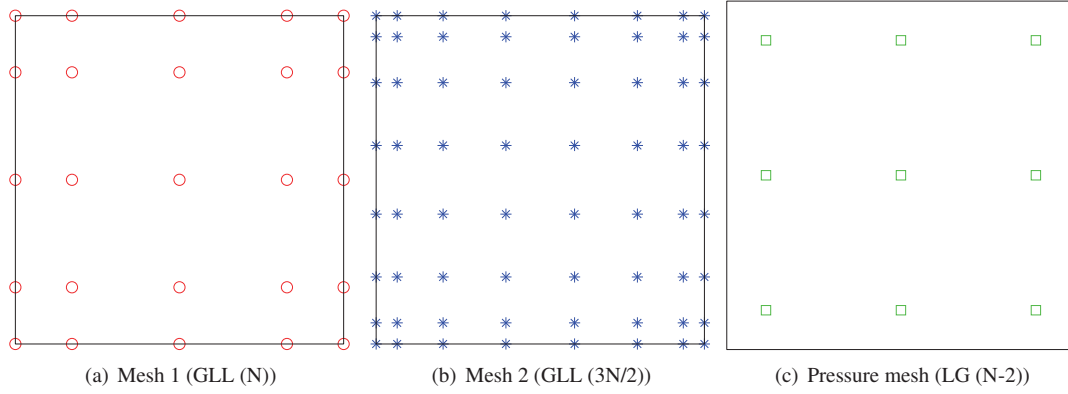(a) Mesh 1 (GLL (N)) (b) Mesh 2 (GLL (3N/2)) (c) Pressure mesh (LG (N-2))

Figure 3.7: Quadrature points for velocity mesh.

with the corresponding error

$$\mathbf{e}^{m+1} = (I - CA)\mathbf{e}^m = (I - CA)^m \mathbf{e^0}. \tag{3.46}$$

In general C can be allowed to be singular as is the case with the coarse-grid correction step of the algebraic multigrid method. The convergence of this algorithm is controlled by the spectral radius of the matrix $(I - CA)$. We consider the generalized eigenvalue problem

$$A\mathbf{z}_k = \lambda_k B\mathbf{z}_k, \tag{3.47}$$

where $\mathbf{z}_k$ are the orthonormal eigenvectors, λ_k are the eigenvalues and B is scaled so that $0 < \lambda_1 \leq \lambda_2 \leq \cdots \leq \lambda_n \leq 1$. Using $\mathbf{e}^m = \sum_k \hat{\mathbf{e}}_k{}^m \mathbf{z}_k$, it follows from equation (3.46) that

$$\hat{\mathbf{e}}_k{}^m = (1 - \lambda_k)^m \hat{\mathbf{e}}_k{}^0, \qquad 1 \leq k \leq n. \tag{3.48}$$

We can see that the smoother is effective at reducing the high-wavenumber error components whereas it is slow at reducing the low-wavenumber error components.

The basic idea of the multigrid method is to combine a smoother, which is effective at reducing the high-wavenumber error with a coarse-grid correction to target the low-wavenumber error components. A typical multigrid algorithm consists of three steps. The first step is smoothing, which is effective at reducing the high-wavenumber error. The second step involves restriction of the residual to the coarse level and computation of the coarse-level correction. The third step involves interpolation of the coarse correction to the fine level. This could be accompanied by further post smoothing. An L-level multigrid algorithm can be completely characterized by the coarsening algorithm, smoother C_l, and the prolongation operator P_l at each level. Defining the two-level multigrid error propagation matrix at the coarsest level $M_{tg,L}$, as

$$E_{tg,L} = (I_L - C_L A_L)^{m_{u,L}} (I_L - P_L A_{L+1}^{-1} P_L^T A_L)(I_L - C_L A_L)^{m_{d,L}}, \tag{3.49}$$

and the two-level multigrid error progagation matrix at level k, $k < L$, as

$$E_{tg,k} = (I_k - C_k A_k)^{m_{u,k}} (I_k - P_k(I - E_{tg,k+1}^{\gamma_k}) A_{k+1}^{-1} P_k^T A_k)(I_k - C_k A_k)^{m_{d,k}}, \tag{3.50}$$

35

a multigrid iteration can be written as

$$\mathbf{x} - \mathbf{x}_{i+1} = E_{mg}(\mathbf{x} - \mathbf{x}_i), \qquad (3.51)$$

where the multigrid error propagation matrix $E_{mg} = E_{tg,0}$, can be computed recursively. Here $A_0 = A$, $A_{k+1} = P_k^T A_k P_k$ is the coarse matrix at each level, $m_{d,k}$, $m_{u,k}$ are the number of pre- and post-smoothing iterations, respectively, at each level, and γ_k is the number of lower-level multigrid iterations made at each level. The convergence rate of the multigrid method is determined by the spectral radius of E_{mg}, $\rho(E_{mg})$. While convergence analysis of the entire multigrid algorithm is quite complicated, algorithms built from efficiently constructed two-level multigrid algoritms with small $\rho(E_{tg,k})$ results in multigrid algorithm with good overall convergence properties.

3.5.2 Two-level multigrid

We now look at the two-level multigrid iteration. We start by decomposing the variables into n_c coarse variables ("C-variables") and n_f fine variables ("F-variables"). The matrix A and the prolongation matrix P can be written in block form as

$$A = \begin{bmatrix} A_{ff} & A_{fc} \\ A_{cf} & A_{cc} \end{bmatrix}, P = \begin{bmatrix} W \\ I \end{bmatrix}. \qquad (3.52)$$

Here, W is the $n_f \times n_c$ matrix consisting of interpolation weights.

A two-level multigrid iteration can be written as

$$\mathbf{x} - \mathbf{x}_{i+1} = E_{tg}(\mathbf{x} - \mathbf{x}_i), \qquad (3.53)$$

where

$$E_{tg} = (I - BA)^{m_u}(I - PA_C^{-1}P^T A) \qquad (3.54)$$

is the two-level error propagation matrix. Here B is a smoother and $A_c = P^T A P$ is the coarse matrix. In this case, we only use a post-smoother. The convergence rate of this two-level method is determined by the spectral radius of E_{tg}, $\rho(E_{tg})$.

Following Lottes [2011] using the hierarchial basis

$$T = \begin{bmatrix} I & W \\ & I \end{bmatrix}, \hat{A} = T^T A T = \begin{bmatrix} A_{ff} & \hat{A}_{fc} \\ \hat{A}_{cf} & A_c \end{bmatrix}, \hat{\mathbf{b}} = T^T \mathbf{b}, \mathbf{x} = T\hat{\mathbf{x}}, \qquad (3.55)$$

the linear system (3.43) can be transformed to

$$\begin{bmatrix} A_{ff} & \hat{A}_{fc} \\ \hat{A}_{cf} & A_c \end{bmatrix} \begin{bmatrix} \hat{\mathbf{x}}_f \\ \hat{\mathbf{x}}_c \end{bmatrix} = \begin{bmatrix} \hat{\mathbf{b}}_f \\ \hat{\mathbf{b}}_c \end{bmatrix}, \qquad (3.56)$$

where $\hat{A}_{fc} = A_{ff}W + A_{fc}$ and $A_c = P^T A P$. The prolon,gation and smoother matrices transform to

$$\hat{P} = T^{-1}P = \begin{bmatrix} 0 \\ I \end{bmatrix}, \qquad (3.57)$$

$$\begin{aligned} \hat{B} &= T^{-1}BT^{-T} = \begin{bmatrix} \hat{B}_{ff} & \hat{B}_{fc} \\ \hat{B}_{cf} & \hat{B}_{cc} \end{bmatrix} \\ &= \begin{bmatrix} B_{ff} - B_{fc}W^T - WB_{cf} + WB_{cc}W^T & B_{fc} - WB_{cc} \\ B_{cf} - B_{cc}W^T & B_{cc} \end{bmatrix}, \end{aligned} \qquad (3.58)$$

36

respectively, where

$$T^{-1} = \begin{bmatrix} I & -W \\ 0 & I \end{bmatrix}. \tag{3.59}$$

The choice of weights $W = A_{ff}^{-1} A_{fc}$ is ideal and decouples the fine and coarse problem. However in this case the weight matrix W is full and is avoided. The error propagation matrix is

$$\hat{E}_{tg} = (I - \hat{B}\hat{A})^{m_u}(I - \hat{P}A_C^{-1}\hat{P}^T\hat{A}) = T^{-1}E_{tg}T. \tag{3.60}$$

We can see that E_{tg} and $\hat{E}_{tg}$ have identical spectra. The quality of the interpolation is defined by

$$\gamma = \| A_{ff}^{1/2} F A_c^{-1/2} \|, \tag{3.61}$$

where $F = W - (-A_{ff}^{-1}A_{fc})$. The coarse system, $A_c\hat{\mathbf{x}}_c = \hat{\mathbf{b}}_c$, is solved first. This needs to be solved recursively if it is not the coarsest level. The fine system, $A_{ff}\hat{\mathbf{x}}_f = \hat{\mathbf{b}}_f - \hat{A}_{fc}\hat{\mathbf{x}}_c$, is solved next.

Error estimates

$$Q = \begin{bmatrix} I & 0 \\ -A_c^{-1}\hat{A}_{fc}^T & I \end{bmatrix}, \tilde{A} = Q^T\hat{A}Q = \begin{bmatrix} S_f & 0 \\ & A_c \end{bmatrix}, \tag{3.62}$$

where

$$S_f = A_{ff} - \hat{A}_{fc}\hat{A}_c^{-1}\hat{A}_{fc}^T, \tag{3.63}$$

$$\tilde{P} = Q^{-1}\hat{P} = \begin{bmatrix} 0 \\ I \end{bmatrix}, \tag{3.64}$$

$$\begin{aligned} \tilde{B} &= Q^{-1}\hat{B}Q^{-T} = \begin{bmatrix} \tilde{B}_{ff} & \tilde{B}_{fc} \\ \tilde{B}_{cf} & \tilde{B}_{cc} \end{bmatrix} \\ &= \begin{bmatrix} \hat{B}_{ff} & \hat{B}_{ff}L^T + \hat{B}_{fc} \\ L\hat{B}_{ff} + \hat{B}_{cf} & L\hat{B}_{ff}L^T + L\hat{B}_{fc} + \hat{B}_{cf}L^T + \hat{B}_{cc} \end{bmatrix}, \end{aligned} \tag{3.65}$$

where $L = A_c^{-1}\hat{A}_{fc}^T$

$$Q^{-1} = \begin{bmatrix} I & \\ A_c^{-1}\hat{A}_{fc}^T & I \end{bmatrix}. \tag{3.66}$$

$$\tilde{E}_{tg} = (I - \tilde{B}\tilde{A})^{m_u}(I - \tilde{P}A_C^{-1}\tilde{P}^T\tilde{A}) = Q^{-1}\hat{E}_{tg}Q. \tag{3.67}$$

$$I - \tilde{P}A_c^{-1}\tilde{P}^T\tilde{A} = I - \begin{bmatrix} 0 & \\ & A_c^{-1} \end{bmatrix}\begin{bmatrix} S_f & \\ & A_c \end{bmatrix} = \begin{bmatrix} I & \\ & 0 \end{bmatrix} \tag{3.68}$$

$$\tilde{E}_{tg} = (I - \tilde{B}\tilde{A})\begin{bmatrix} I & \\ & 0 \end{bmatrix} = \begin{bmatrix} I - \tilde{B}_{ff}S_f & 0 \\ -\tilde{B}_{cf} & 0 \end{bmatrix} \tag{3.69}$$

$$\tilde{B}_{ff} = \hat{B}_{ff} = \begin{bmatrix} I & -W \end{bmatrix} B \begin{bmatrix} I & -W \end{bmatrix}^T \tag{3.70}$$

37

$$A = W - (-A_{ff}^{-1}A_{fc}) = A_{ff}^{-1}\hat{A}_{fc}, \tag{3.71}$$

$$\gamma = \|A_{ff}^{\frac{1}{2}}FA_c^{\frac{1}{2}}\|_2 = \sup_{\mathbf{v}\neq 0} \frac{\|F\mathbf{v}\|_{A_{ff}}}{\|\mathbf{v}\|_{A_c}} \tag{3.72}$$

$$\rho(E_{tg}) \leq 1 - (1 - \gamma^2)(1 - \rho_f) \tag{3.73}$$

$$\kappa_f = \kappa(D_{ff}^{\frac{1}{2}}A_{ff}D_{ff}^{\frac{1}{2}}) \tag{3.74}$$

$$\gamma = \|A_{ff}^{\frac{1}{2}}FA_c^{-\frac{1}{2}}\|_2 \tag{3.75}$$

$$\rho_f = \rho(I - \hat{B}_{ff}A_{ff}) \tag{3.76}$$

$$F = W - (-A_{ff}^{-1}A_{fc}), \hat{B}_{ff} = \begin{bmatrix} I & -W \end{bmatrix} B \begin{bmatrix} I & -W \end{bmatrix}^T \tag{3.77}$$

We now describe the smoothing, coarsening and interpolation steps in detail.

Smoother

We use a smoother of the form

$$B = \begin{bmatrix} B_{ff} & 0 \\ 0 & 0 \end{bmatrix} \tag{3.78}$$

for solving the fine system.

Coarsening

$$X = I - D_{ff}^{-\frac{1}{2}}A_{ff}D_{ff}^{-\frac{1}{2}}$$
$$\kappa_f = \kappa(I - X)$$

$$r_i = \mathbf{e}_I^T |X| \mathbf{1} \tag{3.79}$$

$$\kappa_f = \frac{1 + r_{max}}{1 - r_{max}} \text{ when } r_{max} < 1 \tag{3.80}$$

Interpolation

$$\gamma = \|A_{ff}^{\frac{1}{2}}FA_c^{-\frac{1}{2}}\|_2$$
$$\|A_{ff}^{\frac{1}{2}}FD\|_F$$

$$\text{minimize } tr(P^T AP) \text{ subject to } W\mathbf{u} = -A_{ff}^{-1}A_{fc}\mathbf{u} \tag{3.81}$$

$$X_i = R_i^T (R_i A_{ff} R_i^T)^{-1} R_i, \tag{3.82}$$

38

$$We_i = X_i(-A_{fc}e_i + u_i\lambda), \tag{3.83}$$

where

$$X\lambda = -A_{ff}^{-1}A_{fc}\mathbf{u} - \sum_{i=1}^{n_c} u_i X_i(-A_{fc}e_i), X = \sum_{i=1}^{n_c} u_i^2 X_i. \tag{3.84}$$

$$\frac{1}{2}(DA_{ff} + A_{ff}D) \approx X^{-1}, D = diag(d_j^{-1}), d_j = \sum_{i=1}^{n_c} u_i^2 e_j^T R_i^T R_i e_j. \tag{3.85}$$

$$\gamma = \|A_{ff}^{-\frac{1}{2}}\hat{A}_{fc}A_c^{-1}\|_2 \approx \|D_{ff}^{-\frac{1}{2}}\hat{A}_{fc}D_c^{-1}\|_2, \tag{3.86}$$

$$\|A\|_2^{2p} \leq \max_{i, w_i^{(r)} \neq 0} \frac{w_i^{(r+p)}}{w_i^{(r)}}, \mathbf{w}^{(r)} = (RR^T)^r \mathbf{1}, c_i = \sqrt{w_i^{(2)}/w_i^{(1)}}, \tag{3.87}$$

$$\gamma \approx \|D_{ff}^{-frac12}\hat{A}_{fc}D_c^{-1}\|_2 \leq c_{max}, c_{max} = \max_{1 \leq i \leq n_c} c_i. \tag{3.88}$$

Table 3.1: AMG setup for flow over 2d circular cylinder simulation, $t_{conv} = 0.1$, $\gamma_{targ} = 0.226$.

Level	N	N_f	N_c	N_c/N	ρ_f	m	γ	nnz(W)/nc	nnz(A_{ff})/nf
1	199	125	74	0.371	0.564	4	0.201	7.324	4.120
2	74	53	21	0.283	0.678	4	0.315	11.142	11.867
3	21	17	4	0.190	0.656	4	0.197	13.750	15.941
4	4	3	1	0.250	0.594	4	0.000	3.000	3.000

Table 3.2: AMG setup for flow over wall mounted cube simulation, $t_{conv} = 0.5$, $\gamma_{targ} = 0.541$.

Level	N	N_f	N_c	N_c/N	ρ_f	m	γ	nnz(W)/nc	nnz(A_{ff})/nf
1	18362	7972	10390	0.565	0.804	4	-	20.077	8.865
2	10390	6040	4350	0.418	0.614	4	-	50.152	144.717
3	4350	3000	1350	0.310	0.677	4	-	119.565	750.170
4	1350	1085	265	0.196	0.784	5	0.292	227.566	818.321
5	265	227	38	0.143	0.774	4	0.371	127.210	227.000
6	38	34	4	0.105	0.776	4	0.173	31.750	34.000
7	4	3	1	0.250	0.421	3	0.000	3.000	3.000

Table 3.3: AMG setup for 3d urban boundary layer array simulation, $t_{conv} = 0.5$, $\gamma_{targ} = 0.541$.

Level	N	N_f	N_c	N_c/N	ρ_f	m	γ	nnz(W)/nc	nnz(A_{ff})/nf
1	164604	81896	82708	0.502	0.844	3	-	11.856	9.719
2	82708	48966	33742	0.407	0.707	3	-	39.205	77.497
3	33742	23990	9752	0.289	0.746	3	-	101.838	485.489
4	9752	7413	2339	0.239	0.758	3	-	158.084	1084.056
5	2339	1902	437	0.186	0.777	3	0.531	202.924	1102.716
6	437	366	71	0.162	0.742	2	0.497	107.112	366.000
7	71	61	10	0.140	0.711	2	0.568	27.900	61.000
8	10	9	1	0.100	0.452	2	0.000	9.000	9.000

Chapter 4

Experimental results

4.1 Flow characteristic study tools.

Two-dimensional contour plots are used to present and compare the flow characteristics such as TKE, Reynolds stresses and mean velocities and are used to study the three-dimensional behavior of the turbulent flow in our regions of interest. Figure 4.1 shows a sample for a group of $x - z$ slices at different spanwise positions with the color indicating the mean streamwise velocity. Horizontal $x - y$ slices (S_z) and vertical $x - z$ slices (S_y) will be used in the discussion to depict various flow quantities; specifically, a combination of one S_y, and two S_z at different heights will be used.

According to Stull [1988] the region of the boundary layer directly above the mean height of the blocks is denoted as the 'wake layer' and the region beneath is called the 'urban canopy'. The region of large initial turbulence in the wake layer of the urban array is mostly due to the flow separation occurring at the leading edge of the upstream block (Martinuzzi and Havel [2000]). In this study each street area is divided into two main sub-regions; the 'lower layer' starts from ground level up to the mid-height of a block ($0 < z/H < 0.5$) and the 'upper layer' includes the upper half of each street ($0.5 < z/H < 1$). The region between two adjacent spanwise blocks is called the intersection. Figure 4.2(a) shows horizontal planes in the lower layer (red) at $z/H = 0.25$ and upper layer (red) at $z/H = 0.85$ as well as the intersection (purple). In addition a vertical slice (S_y) is chosen at the mid-span plane of each street ($y/W = 0$) shown as the green slice in Figure 4.2b. The combination of these three slices are used to investigate the complicated phenomena in the urban boundary layer investigated in this study. Four flow quantities are studied in each of these three slices: mean velocity (U_m, V_m and W_m), turbulent kinetic energy (TKE) and its components ($\overline{u'^2}$, $\overline{v'^2}$ and $\overline{w'^2}$) and Reynolds stress components ($-\overline{u'v'}$, $-\overline{u'w'}$ and $-\overline{v'w'}$).

4.2 Results

In this section, different flow characteristics are studied for four angle of incidence (AOI) values: $0°$, $15°$, $30°$ and $45°$. In order to simplify the evaluations, a street-to-street comparison is run for each angle of incidence (AOI) condition, and then, the effect of AOI on different streets is studied. The effects are discussed both in the lower layer (at $z/H = 0.25$) and upper layer ($z/H = 0.85$) slices as well as the center vertical slice ($y/W = 0$) .

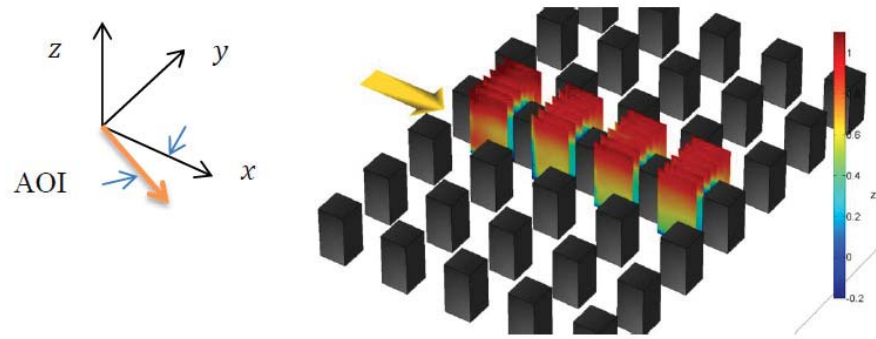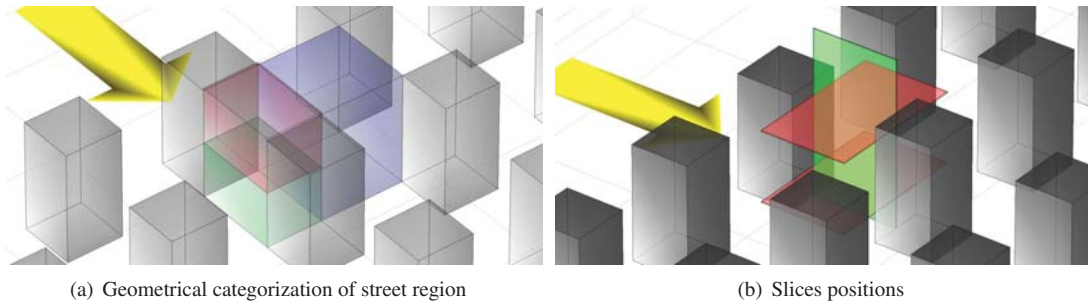Figure 4.1: Sample of a group of vertical slices showing streamwise mean velocity.

(a) Geometrical categorization of street region

(b) Slices positions

Figure 4.2: Regions under study.

4.2.1 Mean velocity

Contours in S_y slices

Streamwise mean velocity. All mean velocity magnitudes are normalized by U_H, which is the streamwise component of the mean free stream flow velocity at the height of a building ($H = 50$ mm). For AOI = $0°$, the S_y slice at mid-span ($y/W = 0$) for U_m shows the high-speed free-stream flow at the upper roof level ($z/H > 1.3$) in all streets (Figure 4.3). A strong velocity gradient ($\frac{\partial U}{\partial z}$) is detected in a thin layer near the roof level ($0.8 < z/H < 1.2$) for all streets. At lower values ($z/H < 0.8$), an approximately zero streamwise mean velocity is observed close to both the upstream and downstream buildings', with a slightly negative values observed in the central part of the streets. The contours shown in 4.3 show that for AOI = $15°$ the streamwise velocity distribution on the $x - z$ mid-span plane for all streets is very similar to AOI = $0°$ except for the upper roof level of the 2nd , 3rd and 4th streets in which the shear layer is observed in a larger region compared to AOI = $0°$. The changes of the distribution of the streamwise component of the mean velocity is considerable in transition from AOI = $15°$ to AOI = $30°$. The S_y slice for U_m/U_H shows that for AOI = $30°$ the streamwise velocity is always positive in the entire street at the mid-span of the streets. Moreover, there is a region of slightly positive streamwise velocity in the downstream half of the 1st and 2nd streets. Also, the thickness of the shear layer at the upper-roof level is thicker than AOI = $15°$, and grows in transition from the 1st to the 4th street. The thickness of the shear layer is even larger for AOI = $45°$: it is detectable in the range of $0.8 < z/H < 1.4$. Also, the streamwise velocity magnitudes at the upper-roof level are considerably smaller for AOI = $45°$ as compared to the smaller AOI conditions investigated.

(a) AOI = $0°$

(b) AOI = $15°$

(c) AOI = $30°$

(d) AOI = $45°$
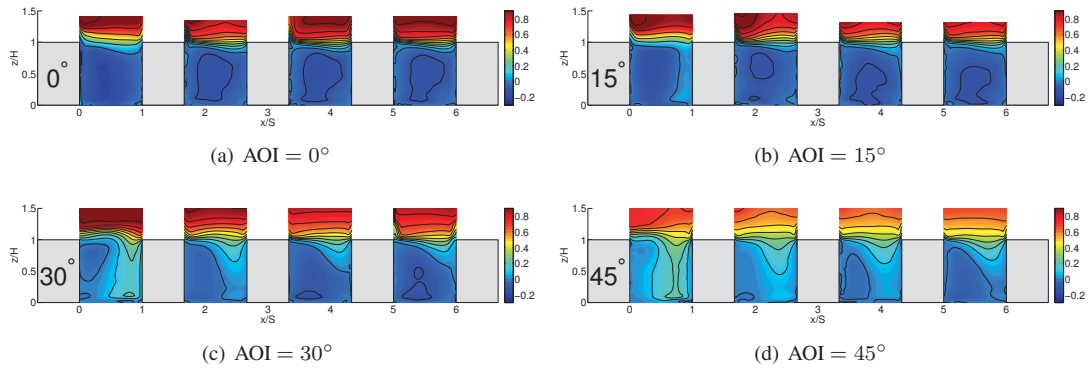
Figure 4.3: U_m/U_H in the S_y plane.

Spanwise mean velocity. The mean spanwise velocity distributions at the mid-span $x-z$ plane ($y/W = 0$) are shown in Figure 4.4. For AOI = $0°$, zero values for V_m/U_H are expected based on symmetry and a significant change is observed with increasing AOI. Higher magnitudes of V_m are observed in the streets near the downstream building. The magnitudes are greater in the 1st street as compared to the 2nd, 3rd and 4th. By increasing the AOI to $30°$ and $45°$, the spatial extent of the non-zero values of the velocity increase; however, the magnitudes show a gradual decrease. For the upper-roof region ($1.0 < z/H < 1.5$) the magnitude of the spanwise velocity increases from AOI = $0°$ to AOI = $45°$.

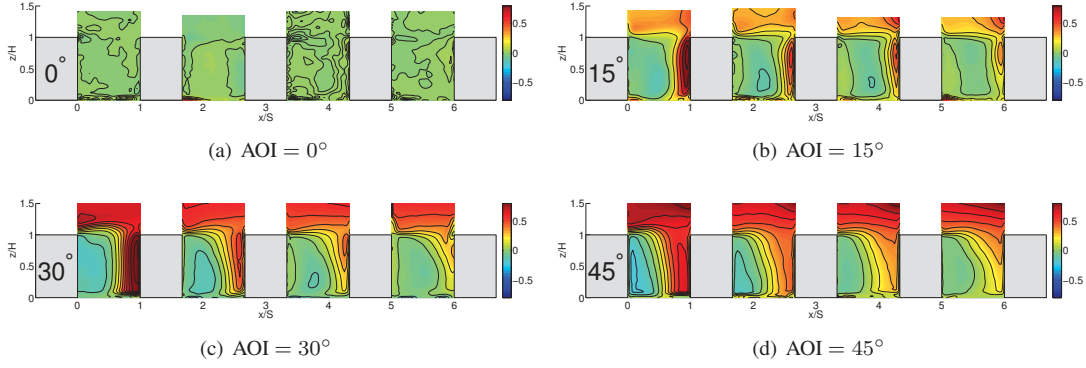(a) AOI = 0°   (b) AOI = 15°

(c) AOI = 30°   (d) AOI = 45°

Figure 4.4: V_m/U_H in the S_y plane.

Wall-normal mean velocity. The S_y slices of wall-normal mean velocity, W_m/U_H, contours (Figure 4.5) for AOI = 0° show that there are two main regions of wall-normal flow in all four streets: a negative (downward) flow close to the wall of the downstream building, and a positive (upward) flow close to the wall of the upstream building. For all four AOI values, the effect of the relatively strong flow separation off the first block is observed (see Martinuzzi and Havel [2004]). In transition from the 1st to the 4th street, the mean velocity magnitude of the downward flow near the downstream building increases but the mean velocity values of the upward flow near the upstream building are decreasing. This combination of the downward and upward flow regions within the streets is evidence of a single recirculation region within the street and is expected for the skimming flow regime.

(a) AOI = 0°   (b) AOI = 15°

(c) AOI = 30°   (d) AOI = 45°
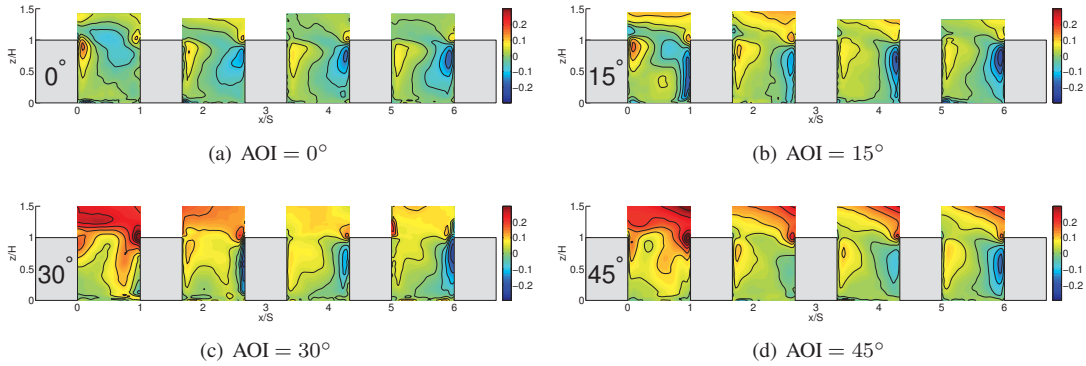
Figure 4.5: W_m/U_H in the S_y plane.

44

Contours in S_z slices

Streamwise mean velocity. The S_z slices at wall-normal heights of $z/H = 0.25$ and $z/H = 0.85$ are shown in Figure 4.6. For AOI = 0°, symmetric flow is observed with higher-speed U_m values in the intersections as expected. U_m values in the intersection are higher in the 1st street and decrease as the flow moves downstream. There is a region of zero U_m values close to the upstream and downstream buildings' walls and was observed for the S_y slices discussed above. Also there is an area of reverse flow at the center of the streets. This reverse flow together with the positive streamwise flow on the sides shows the existence of the legs of the classical arch vortex within the street region. The effect of AOI is clearly seen in the figures (note that the direction of the incoming flow is shown by the arrow on the first block). This changing distribution of mean flow results in a shift of the classical arch vortex and will be discussed in more detail later.

(a) AOI = 0°, $z/H = 0.25$

(b) AOI = 0°, $z/H = 0.85$

(c) AOI = 15°, $z/H = 0.25$

(d) AOI = 15°, $z/H = 0.85$

(e) AOI = 30°, $z/H = 0.25$

(f) AOI = 30°, $z/H = 0.85$

(g) AOI = 45°, $z/H = 0.25$

(h) AOI = 45°, $z/H = 0.85$
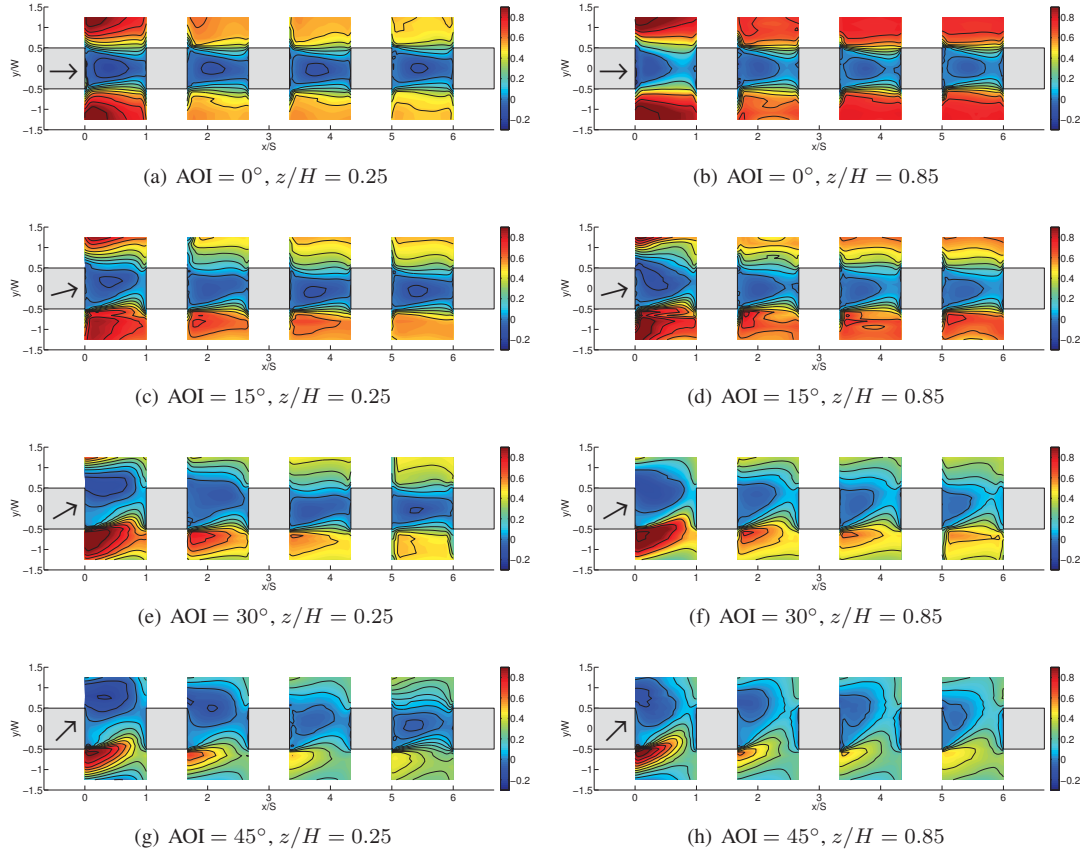
Figure 4.6: Streamwise mean velocity normalized by U_H in S_z slices at $z/H = 0.25$ and $z/H = 0.85$.

Spanwise and Wall-Normal mean velocity. The contours of the normalized spanwise (V_m/U_H) and Wall normal (W_m/U_H) components of the mean velocity are shown in Figures 4.7 and 4.8 respectively for two

45

horizontal planes in all four streets. Fairly symmetric results for AOI = 0° are observed along with a strong dependence on AOI. For example the spanwise channelling of the flow increases with increasing AOL is clearly seen in Figure 4.7. Also for the wall normal flow (4.8) increases in the upward flow for $y/W < 0$ 0 and downward flow for $y/W > 0$ are seen with increasing AOI: this effect is particularly apparent higher in the street at $z/H = 0.85$.

(a) AOI $= 0°$, $z/H = 0.25$

(b) AOI $= 0°$, $z/H = 0.85$

(c) AOI $= 15°$, $z/H = 0.25$

(d) AOI $= 15°$, $z/H = 0.85$

(e) AOI $= 30°$, $z/H = 0.25$

(f) AOI $= 30°$, $z/H = 0.85$

(g) AOI $= 45°$, $z/H = 0.25$

(h) AOI $= 45°$, $z/H = 0.85$
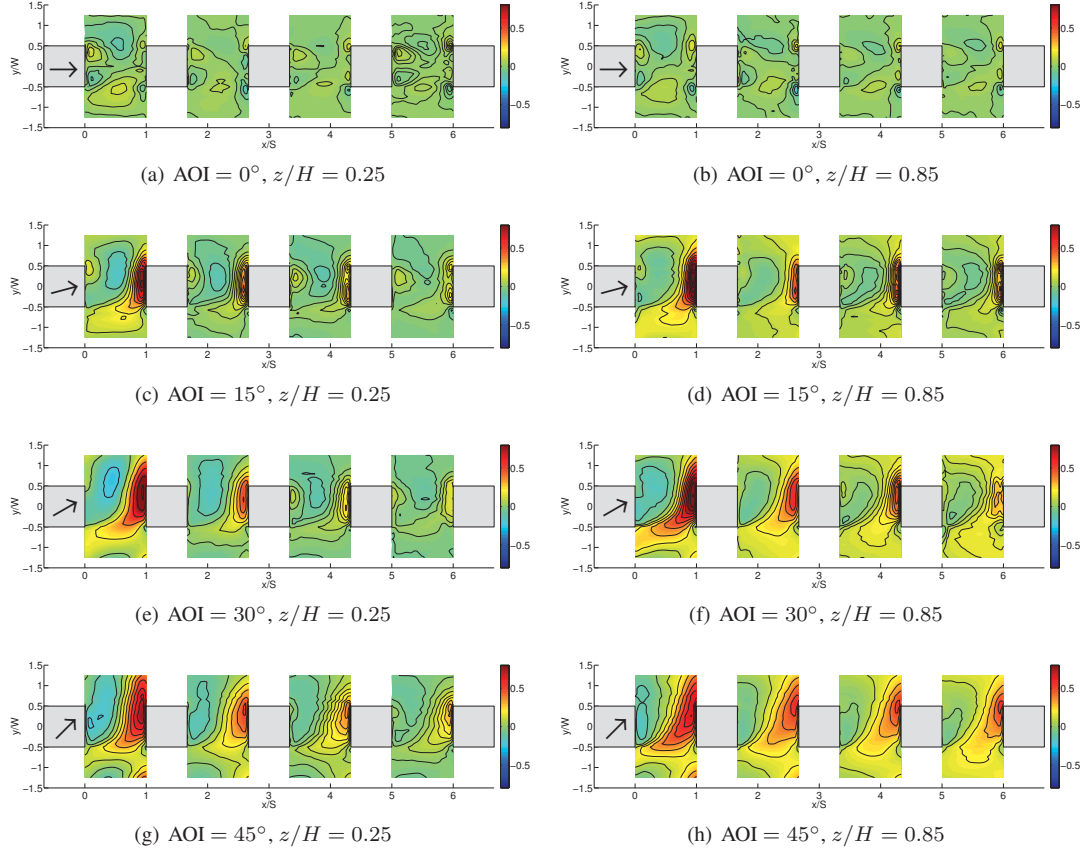
Figure 4.7: Spanwise mean velocity normalized by U_H in S_z slices at $z/H = 0.25$ and $z/H = 0.85$.

(a) AOI = $0°$, $z/H = 0.25$

(b) AOI = $0°$, $z/H = 0.85$

(c) AOI = $15°$, $z/H = 0.25$

(d) AOI = $15°$, $z/H = 0.85$

(e) AOI = $30°$, $z/H = 0.25$

(f) AOI = $30°$, $z/H = 0.85$

(g) AOI = $45°$, $z/H = 0.25$

(h) AOI = $45°$, $z/H = 0.85$
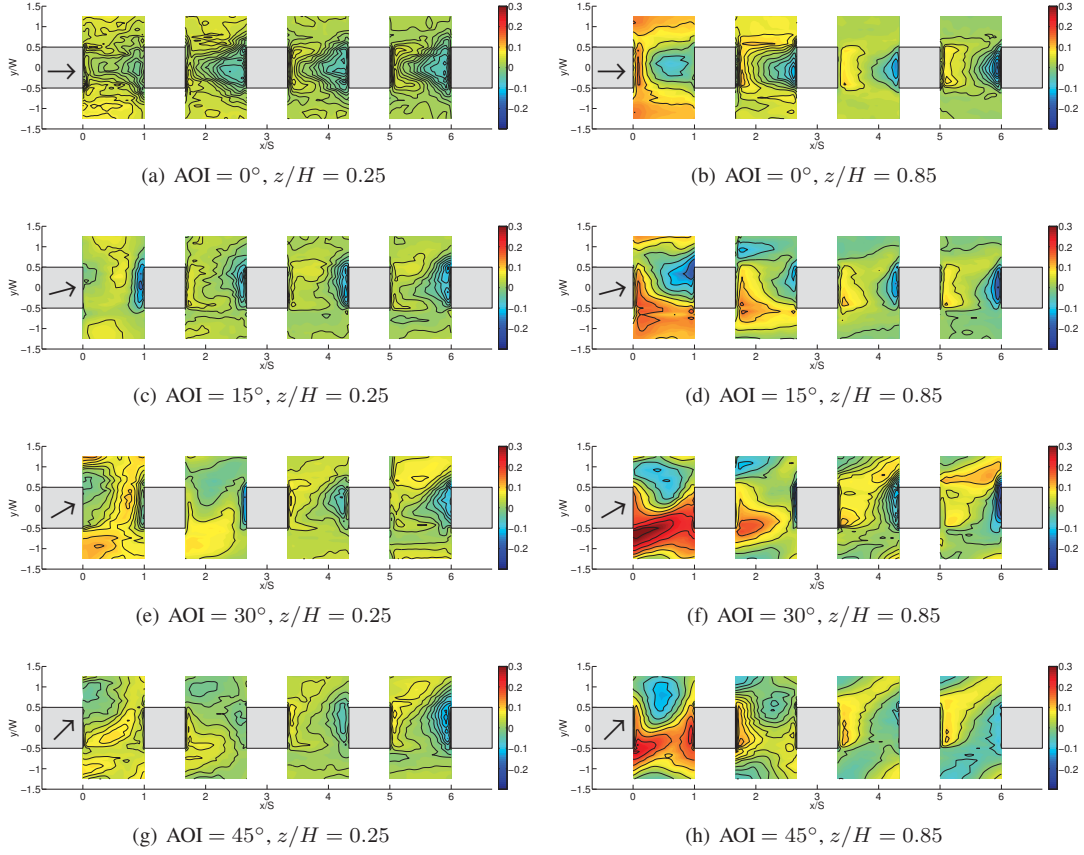
Figure 4.8: Wall normal mean velocity normalized by U_H in S_z slices at $z/H = 0.25$ and $z/H = 0.85$.

4.2.2 Turbulent kinetic energy

Turbulent kinetic energy (TKE), as defined by Equation 4.1, will be normalized by U_H^2 and will be denoted as TKE_H.

$$\text{TKE} = \frac{1}{2}\left(\overline{u'^2} + \overline{v'^2} + \overline{w'^2}\right), \tag{4.1}$$

where u', v', and w' are the fluctuating components of the velocity as defined using the classic Reynolds decomposition with the overbar representing time averaging. TKE_H is therefore:

$$\text{TKE}_H = \frac{\text{TKE}}{U_H^2},$$

Figures 4.9 and 4.10 show the dependence of the TKE_H with AOI in a vertical slice at midspan in the urban array at $y/W = 0$ for the four AOI cases investigated. Also included in the figures are the contributions of each of the three components of the fluctuating velocities ($\frac{1}{2}\,\overline{u'^2}$, $\frac{1}{2}\,\overline{v'^2}$ and $\frac{1}{2}\,\overline{w'^2}$) to the overall TKE with color indicating the magnitude of the normalized values. It is instructive to look at the relative magnitudes of the component contributions in the various regions of the urban array. For example, the high TKE levels just upstream of the downstream block are mainly due to the spanwise component of the fluctuation velocity for AOI = 0° and 15° as seen in Figure 4.9. In the separating shear layer near $z/H = 1$ the high TKE values are due to both the streamwise and spanwise components of the fluctuation velocities. The wall normal component ($\frac{1}{2}\,\overline{w'^2}/U_H^2$) contributes very little to the TKE in the street. As AOI increases to 30° and 45° (Figure 4.10) the overall levels of normalized TKE decrease because of the strong channelling of the overall flow but it is still observed that the main contribution to the shear layer at $z/H = 1$ is due to the streamwise and spanwise components and that the wall-normal component does not contribute significantly to the overall TKE at the midspan of the street.

The horizontal S_z contour slices (at $z/H = 0.25$) of TKE_H and the relative contributions of the fluctuating velocity components ($\frac{1}{2}\,\overline{u'^2}$, $\frac{1}{2}\,\overline{v'^2}$ and $\frac{1}{2}\,\overline{w'^2}$) are provided in Figures 4.11 and 4.12 for the four AOI values investigated. A slight asymmetry is observed in the TKE_H distribution in street 1 for AOI = 0°. Every effort was made to place the urban array in the wind tunnel at an AOI = 0°; however, a slight asymmetry is observed. Monnier et al. [2010] also reported a similar issue: they found that for even a very small deviation in AOI (= 0.5°) asymmetry in flow characteristics can be observed. The main contribution to the TKE in the intersections is from $\frac{1}{2}\,\overline{u'^2}$, for AOI = 0° and the contribution to TKE in the region just upstream of the downstream block is from the spanwise component $\frac{1}{2}\,\overline{v'^2}$. Again the contribution of the wall normal component $\frac{1}{2}\,\overline{w'^2}$, to the TKE is negligible in the entire street. As the AOI is increased to 30° and 45° the normalized TKE values decrease in the street overall. The contribution to the TKE in the intersections are not just due to $\frac{1}{2}\,\overline{u'^2}$, but also to the spanwise component $\frac{1}{2}\,\overline{v'^2}$.

4.2.3 Reynolds Shear Stress

The results for normalized $-\overline{u'w'}$ and $-\overline{u'v'}$ are shown in Figures 4.13 and 4.14 respectively. For the streamwise and wall-normal stress we choose to show vertical slices at mid span in Figure 4.13. For all four AOI values the largest magnitudes are due to the separating shear layer from the top surface of the block. Again due to the relative strong separation for street 1 and compared with the downstream streets the magnitudes of $-\overline{u'w'}$ decrease with downstream distance. The normalized $-\overline{u'v'}$ values are provided in horizontal planes at $z/H = 0.25$ in Figure 4.14. The expected distribution at AOI = 0° is observed; namely the sign of $-\overline{u'v'}$ is positive in the region $0 < y/H < 1$ and negative for $-1 < y/H < 0$. As AOI increases the streamwise-spanwise correlation distribution is significantly affected by the channeling effect due to the non zero AOI values.
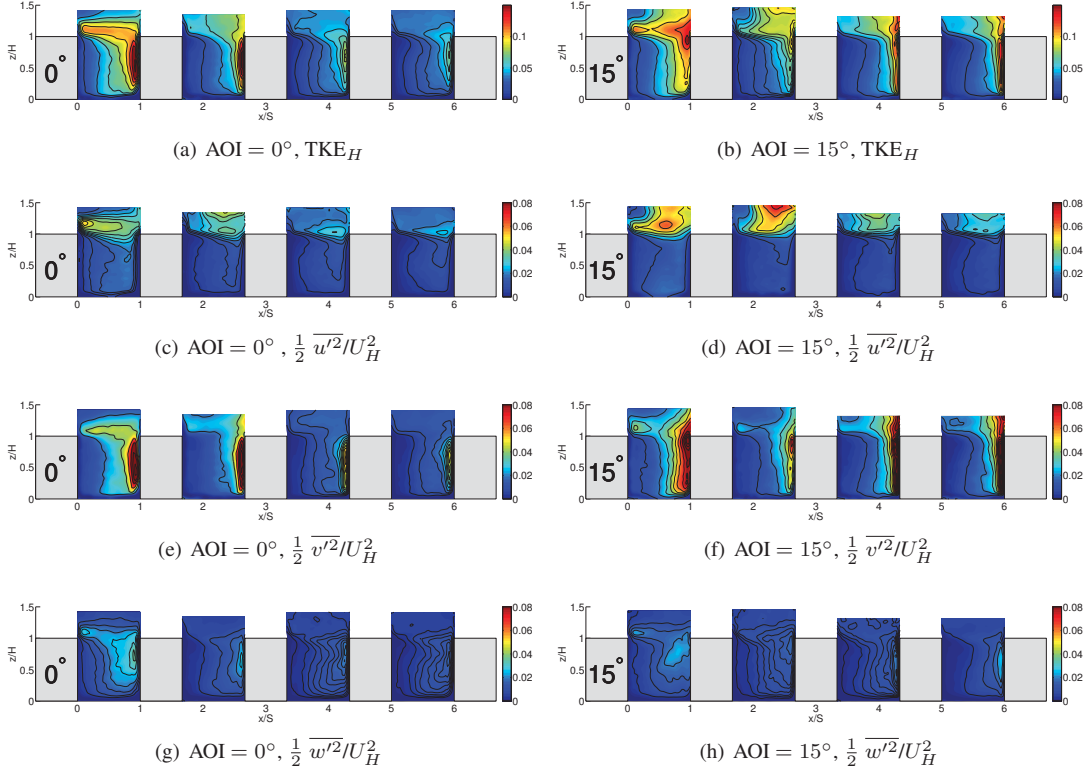
(a) AOI $= 0°$, TKE$_H$

(b) AOI $= 15°$, TKE$_H$

(c) AOI $= 0°$, $\frac{1}{2}\overline{u'^2}/U_H^2$

(d) AOI $= 15°$, $\frac{1}{2}\overline{u'^2}/U_H^2$

(e) AOI $= 0°$, $\frac{1}{2}\overline{v'^2}/U_H^2$

(f) AOI $= 15°$, $\frac{1}{2}\overline{v'^2}/U_H^2$

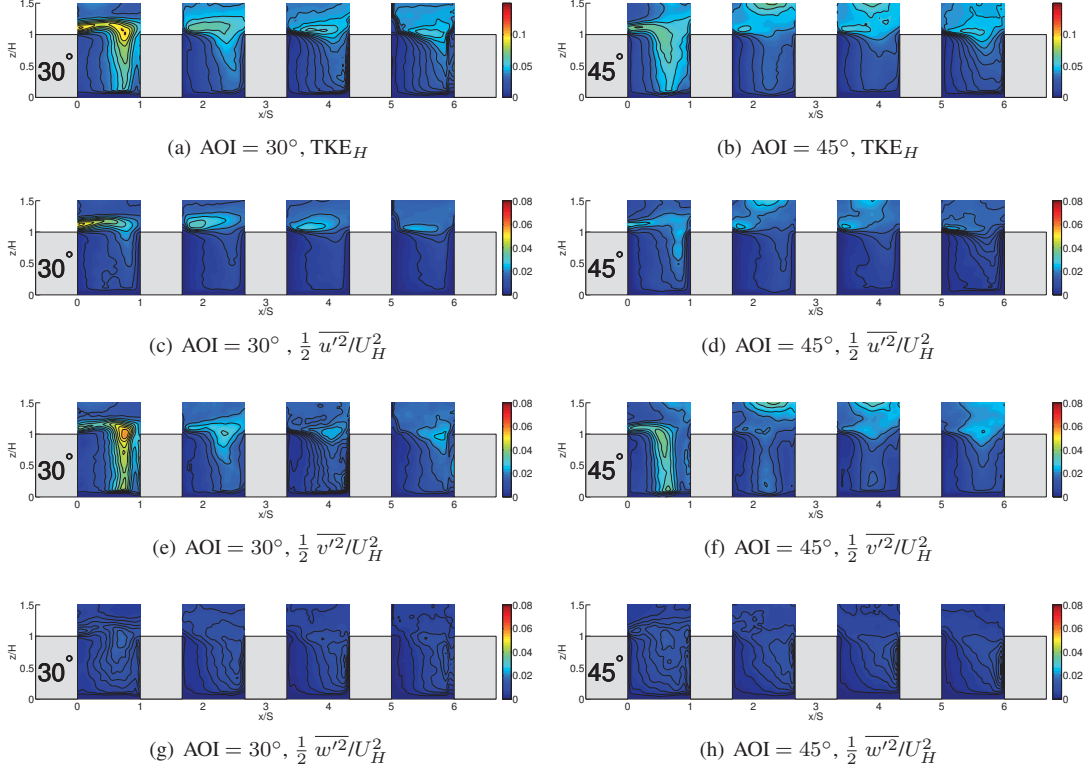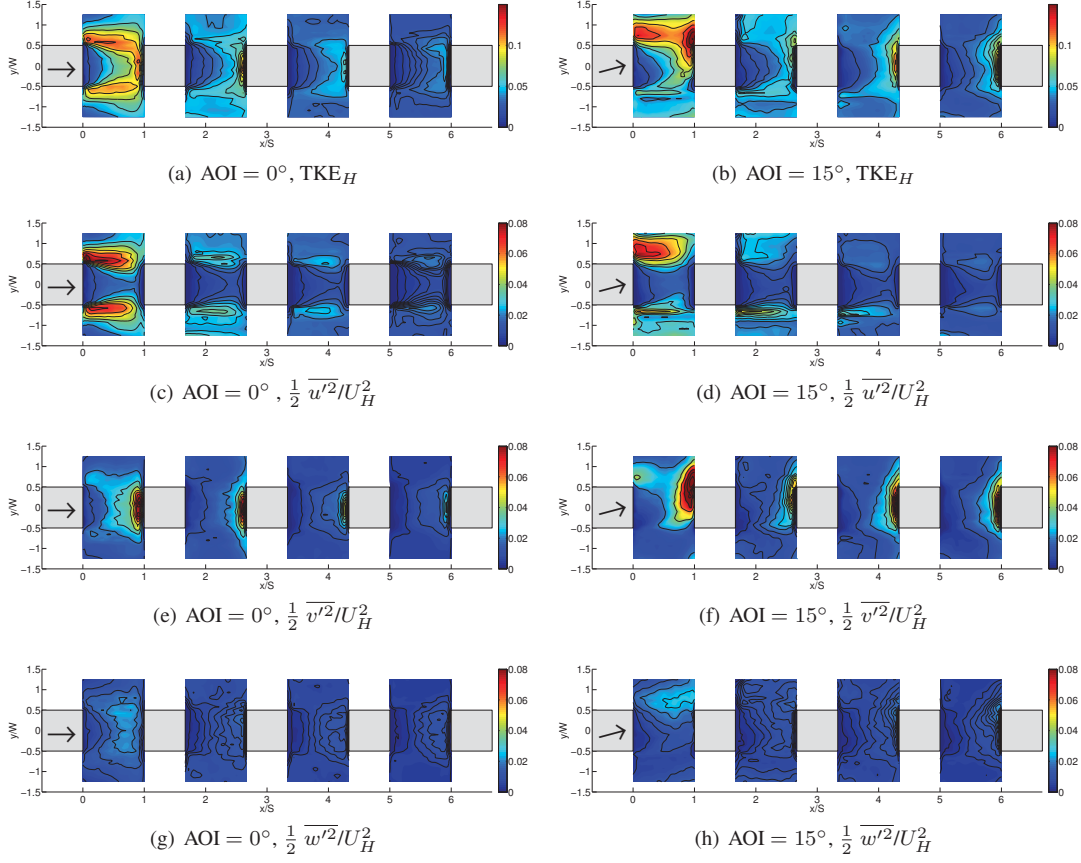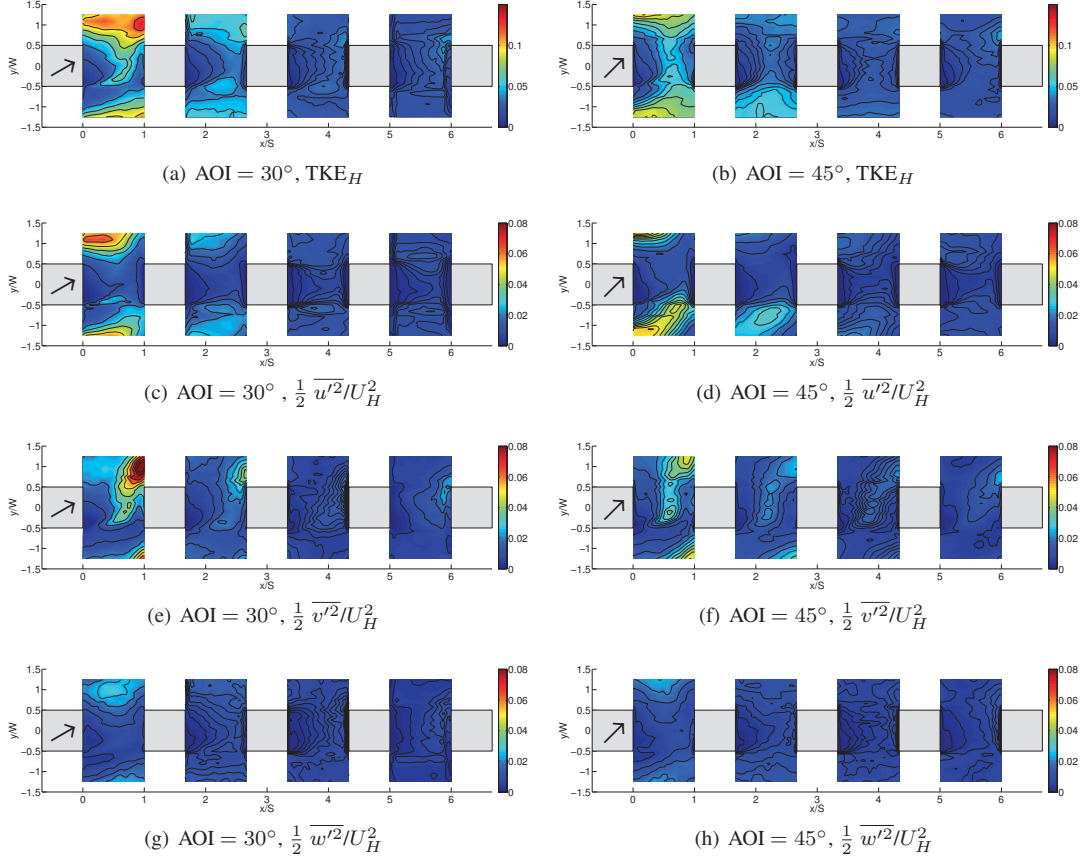(g) AOI $= 0°$, $\frac{1}{2}\overline{w'^2}/U_H^2$

(h) AOI $= 15°$, $\frac{1}{2}\overline{w'^2}/U_H^2$

Figure 4.9: TKE$_H$ and the contribution of fluctuating velocity components normalized by U_H^2, in S_y slices at $y/W = 0$ for AOI = 0° and AOI = 15°.

49

(a) AOI $= 30°$, TKE$_H$

(b) AOI $= 45°$, TKE$_H$

(c) AOI $= 30°$, $\frac{1}{2}\,\overline{u'^2}/U_H^2$

(d) AOI $= 45°$, $\frac{1}{2}\,\overline{u'^2}/U_H^2$

(e) AOI $= 30°$, $\frac{1}{2}\,\overline{v'^2}/U_H^2$

(f) AOI $= 45°$, $\frac{1}{2}\,\overline{v'^2}/U_H^2$

(g) AOI $= 30°$, $\frac{1}{2}\,\overline{w'^2}/U_H^2$

(h) AOI $= 45°$, $\frac{1}{2}\,\overline{w'^2}/U_H^2$

Figure 4.10: TKE$_H$ and the contribution of fluctuating velocity components normalized by U_H^2, in S_y slices at $y/W = 0$ for AOI $= 30°$ and AOI $= 45°$.

50

(a) AOI $= 0°$, TKE$_H$ (b) AOI $= 15°$, TKE$_H$

(c) AOI $= 0°$, $\frac{1}{2}\,\overline{u'^2}/U_H^2$ (d) AOI $= 15°$, $\frac{1}{2}\,\overline{u'^2}/U_H^2$

(e) AOI $= 0°$, $\frac{1}{2}\,\overline{v'^2}/U_H^2$ (f) AOI $= 15°$, $\frac{1}{2}\,\overline{v'^2}/U_H^2$

(g) AOI $= 0°$, $\frac{1}{2}\,\overline{w'^2}/U_H^2$ (h) AOI $= 15°$, $\frac{1}{2}\,\overline{w'^2}/U_H^2$

Figure 4.11: TKE$_H$ and the contribution of fluctuating velocity components normalized by U_H^2, in S_z slices at $z/H = 0.25$ for AOI $= 0°$ and AOI $= 15°$.

51

(a) AOI $= 30°$, TKE$_H$

(b) AOI $= 45°$, TKE$_H$

(c) AOI $= 30°$, $\frac{1}{2}\,\overline{u'^2}/U_H^2$

(d) AOI $= 45°$, $\frac{1}{2}\,\overline{u'^2}/U_H^2$

(e) AOI $= 30°$, $\frac{1}{2}\,\overline{v'^2}/U_H^2$

(f) AOI $= 45°$, $\frac{1}{2}\,\overline{v'^2}/U_H^2$

(g) AOI $= 30°$, $\frac{1}{2}\,\overline{w'^2}/U_H^2$

(h) AOI $= 45°$, $\frac{1}{2}\,\overline{w'^2}/U_H^2$

Figure 4.12: TKE$_H$ and the contribution of fluctuating velocity components normalized by U_H^2, in S_z slices at $z/H = 0.25$ for AOI $= 0°$ and AOI $= 15°$.

(a) AOI $= 0°$, $-\overline{u'w'}/U_H^2$

(b) AOI $= 15°$, $-\overline{u'w'}/U_H^2$

(c) AOI $= 30°$, $-\overline{u'w'}/U_H^2$

(d) AOI $= 45°$, $-\overline{u'w'}/U_H^2$
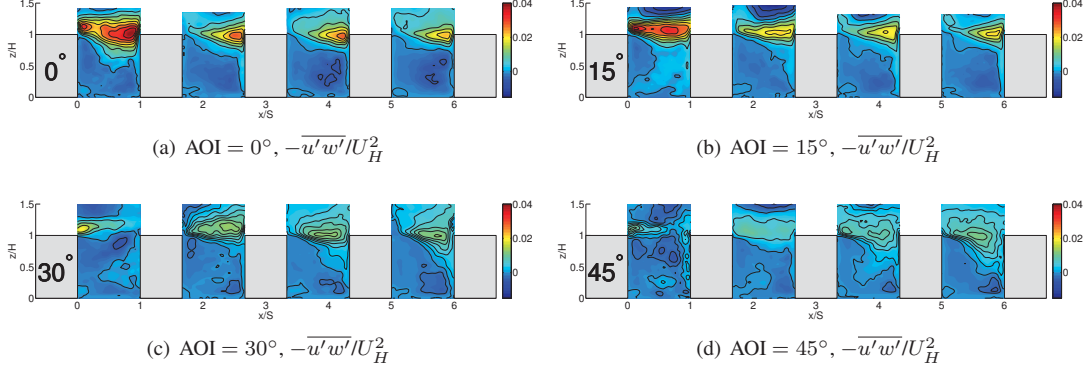
Figure 4.13: $-\overline{u'w'}$ normalized by U_H^2, in the S_y slice at $y/W = 0$ for AOI $= 0°$, $15°$, $30°$ and $45°$.

(a) AOI $= 0°$, $-\overline{u'v'}/U_H^2$

(b) AOI $= 15°$, $-\overline{u'v'}/U_H^2$

(c) AOI $= 30°$, $-\overline{u'v'}/U_H^2$

(d) AOI $= 45°$, $-\overline{u'v'}/U_H^2$
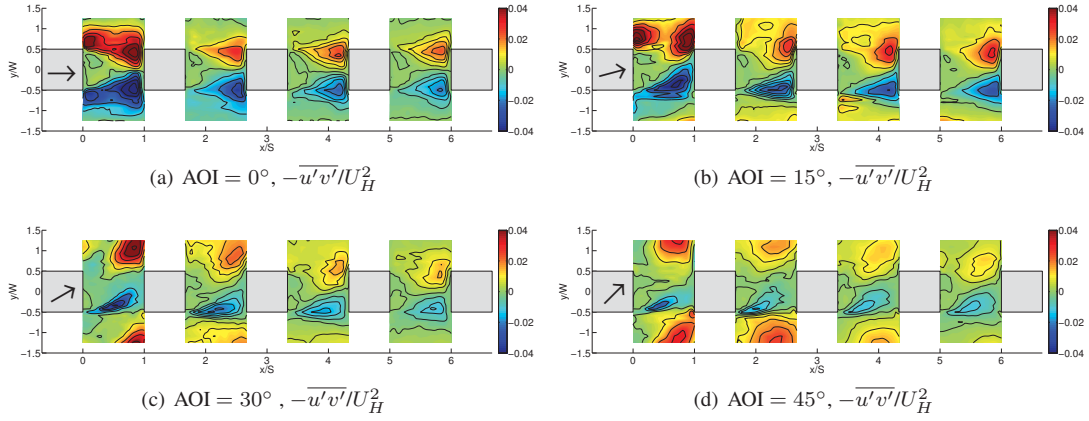
Figure 4.14: $-\overline{u'v'}$ normalized by U_H^2, in the S_z slice at $z/H = 0.25$ for AOI $= 0°$, $15°$, $30°$ and $45°$.

4.2.4 Arch Vortex

Sousa [2002] used the normalized angular momentum to locate the core of the vortical structures behind a single cuboid obstacle. This normalized angular momentum is a 3D implementation of Γ_1 as defined by Graftieaux et al. [2001]. Monnier et al. [2010] applied this method to the 3D data of SPIV in street canyons of an urban array model. Unlike the majority of coherent structures detection methods which use the velocity gradients in calculations, Γ_1 is an integral based quantity. Γ_1 is calculated as:

$$\Gamma_1(\boldsymbol{x}_P) = \frac{1}{\Omega} \int_{\boldsymbol{x} \in \Omega} \frac{(\boldsymbol{x} - \boldsymbol{x}_P) \times \boldsymbol{V}(\boldsymbol{x})}{|\boldsymbol{x} - \boldsymbol{x}_P||\boldsymbol{V}(\boldsymbol{x})|} d\boldsymbol{x}, \tag{4.2}$$

where $\boldsymbol{x}_P$ is the spatial location at which Γ_1 is computed, Ω is the spatial domain over which the integration is performed (typically a small subset of the entire data domain centered about $\boldsymbol{x}_P$) and $\boldsymbol{V}(\boldsymbol{x})$ is the velocity vector at $\boldsymbol{x}$. The quantity Γ_1 is therefore a vector quantity.

We are using the norm of Γ_1 to identify coherent structures in the urban array. The thresholds used to display isosurfaces of Γ_1 are selected as $\Gamma_1 = 0.4$ for AOI = 0° and 15°, $\Gamma_1 = 0.35$ for AOI = 30°, and $\Gamma_1 = 0.33$ for AOI = 45°. As shown in Figure 4.15, the arch vortex (also known as portal vortex, Kim and Baik [2004]) is easily observed in all streets for AOI = 0°. A reasonable symmetry with respect to the mid-span xz plane at $y/W = 0$ is observed, which is expected for a symmetrical geometry. This was investigated in several studies such as Monnier et al. [2010], Becker et al. [2002] and Kim and Baik [2004], employing different geometries. The latter study used the most similar geometry to the current work, with the geometrical ratios of $H/W = 1$ and $S/W = 1$ (compared with the present ratios of $H/W = 2$ and $S/W = 1.5$) but the results show a point of contrast in general inclination of the structures.

For AOI = 15° (Figure 4.16) the western leg in all four streets moves toward the northwestern corner of the street (moves closer to the blocks surface as compared with AOI = 0°) and the eastern leg moves downstream in the street without considerable transition in span. However, for the AOI = 30°, results presented in Figure 4.17, the eastern leg in the 1st and 2nd streets is located close to mid-span in the streets and the western leg is not entirely detectable within the street and intersection boundaries for the thresholds used. Also the leg may be outside of our data acquisition region. In the 3rd and 4th streets the entire structure is detected within the street region; however for the threshold used a continuous arch vortex in the upper layer of the 3rd and 4th streets is not observed. For AOI = 45° (Figure 4.18) the whole structure has a transition upstream in the streets as compared to AOI = 30° results. In all four streets only one leg of the arch (the eastern leg) is detectable within the street and intersection areas investigated in the study.
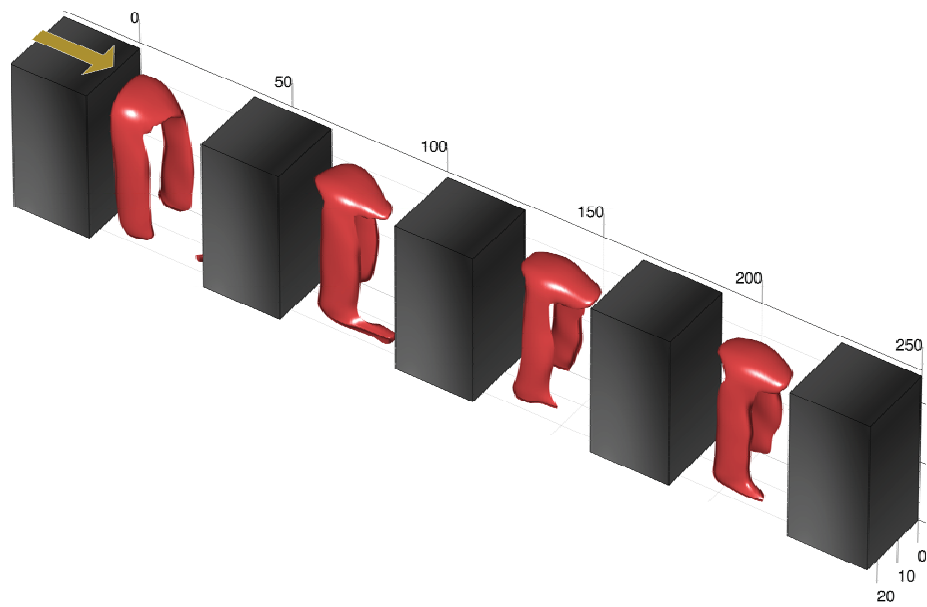
(a) Isometric view
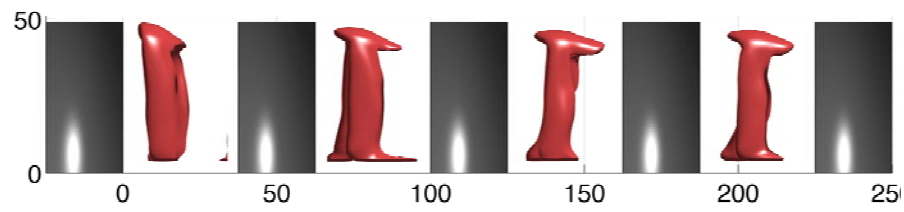
(b) Side view

(c) Top view

Figure 4.15: Arch vortex, using Γ_1 Iso-surfaces for AOI $= 0°$.
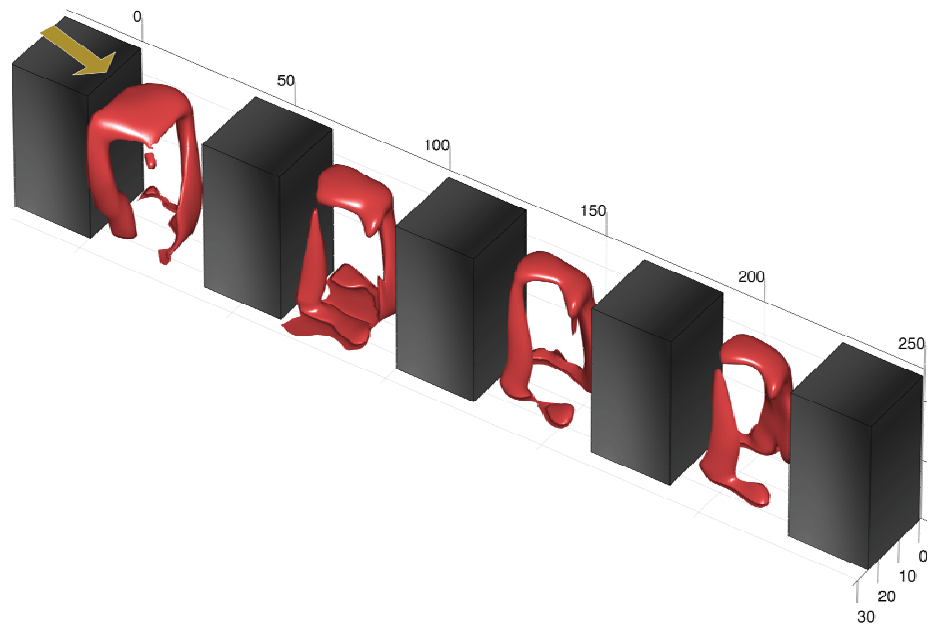
(a) Isometric view
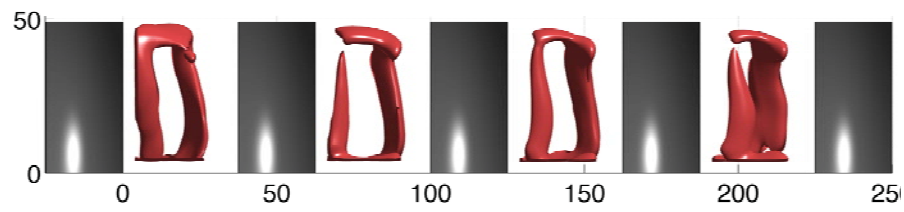
(b) Side view

(c) Top view

Figure 4.16: Arch vortex, using Γ_1 Iso-surfaces for AOI = 15°.

56
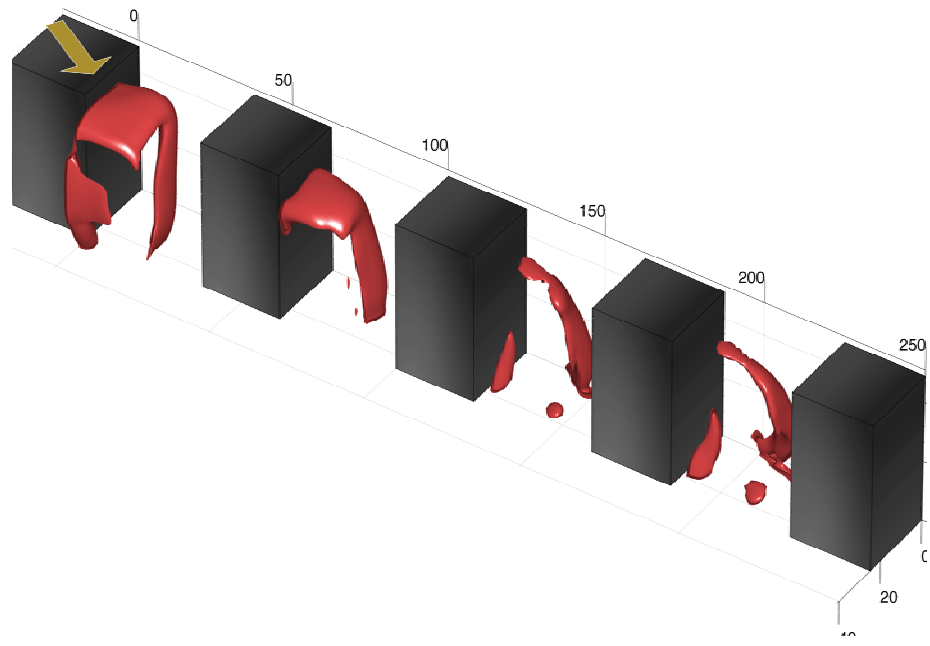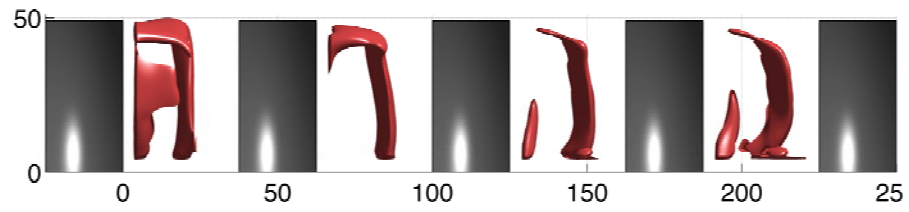
(a) Isometric view

(b) Side view

(c) Top view

Figure 4.17: Arch vortex, using Γ_1 Iso-surfaces for AOI = 30°.
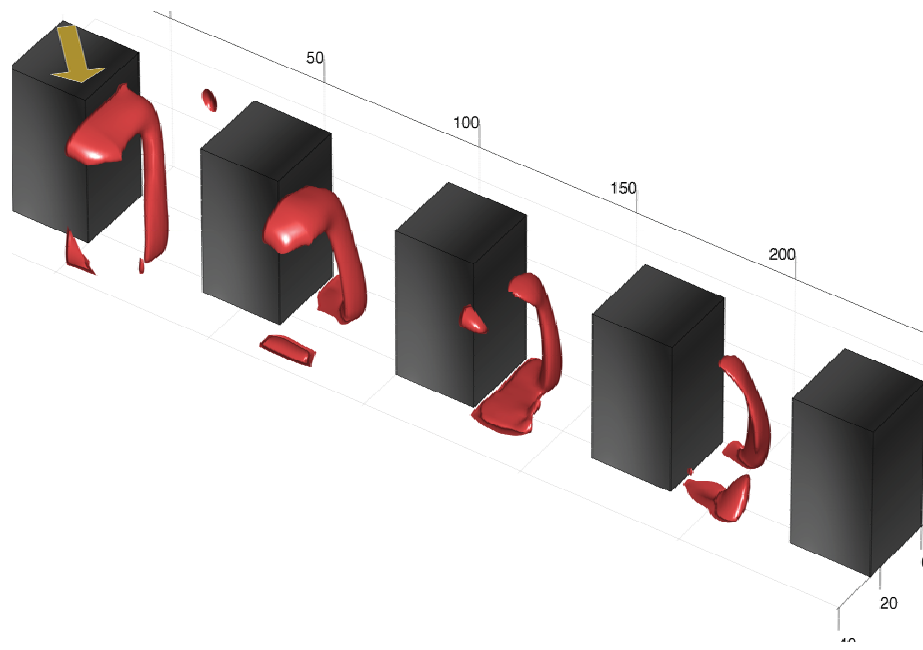
(a) Isometric view
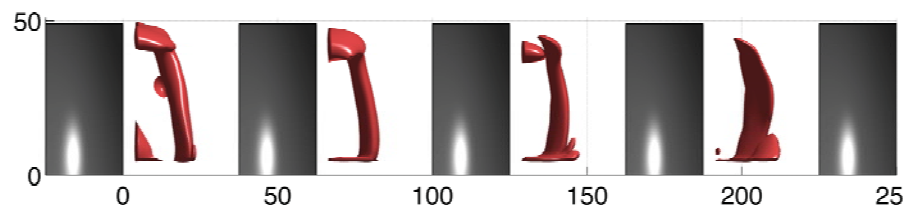
(b) Side view
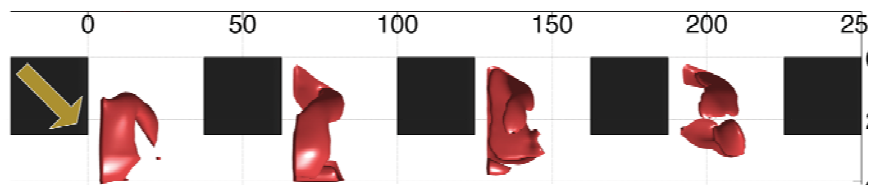
(c) Top view

Figure 4.18: Arch vortex, using Γ_1 Iso-surfaces for AOI $= 45°$.

Chapter 5

Numerical results

We start this chapter with a discussion of several code validation and test cases demonstrating accuracy and performance of our computer code. After that, the following sections describe simulation results for the urban boundary layer flow.

5.1 Code validation

5.1.1 Wannier Flow

Our first test case is the Wannier flow, a Stokes flow past a rotating cylinder next to a sliding wall. The schematic of the flow domain and streamlines are plotted in Figure 5.1. The solution can be described in terms of the cylinder radius (r), its angular velocity (ω), distance from the center of the cylinder to the moving wall (d) and the velocity of the wall (U). In this simulation a cylinder of radius $r = 0.25$ is centered at $(x_1, x_2) = (0, 0)$ and is rotating with an angular velocity $\omega = 2$. The wall is located at $d = 0.5$ and moves with velocity $U = 1.0$. The exact solution, originally derived by Wannier [1950] and Karniadakis and Sherwin [2005], can be written as:

$$u(x_1, x_2) = U - 2(a_1 + a_0 Y_1) \left[\frac{[s + Y_1]}{K_1} + \frac{s - Y_1}{K_2} \right] - a_0 ln \left(\frac{K_1}{K_2} \right)$$

$$- \frac{a_2}{K_1} \left[s + Y_2 - \frac{(s + Y_1)^2 Y_2}{K_1} \right]$$

$$- \frac{a_3}{K_2} \left[s - Y_2 + \frac{(s - Y - 2)^2 Y - 2}{K_2} \right], \tag{5.1}$$

$$v(x_1, x_2) = \frac{2x_1}{K_1 K_2} (a_1 + a_0 Y - 1)(K_2 - K_1) - \frac{x_1 a_2 (s + Y_1) Y_2}{K_1^2}$$

$$- \frac{x_1 a_3 (s - Y_1) Y_2}{K_2^2}, \tag{5.2}$$

where

$$s = d^2 - r^2,$$

$$\tau = \frac{d+s}{d-s}$$

$$a_0 = \frac{U}{ln(\tau)},$$

$$a_1 = -d\left(a_0 + \frac{1}{2}\frac{r^2\omega}{s}\right)$$

$$a_2 = 2(d+s)\left(a_0 + \frac{1}{2}\frac{r^2\omega}{s}\right),$$

$$a_3 = 2(d-s)\left(a_0 + \frac{1}{2}\frac{r^2\omega}{s}\right)$$

$$Y_1(x_2) = x_2 + d,$$

$$Y_2 = 2Y_1(x_2)$$

$$K_1(x_1, x_2) = x_1^2 + (s - Y - 1(x_2))^2,$$

$$K_2(x_1, x_2) = x_1^2 + (s - Y_1(x_2))^2$$
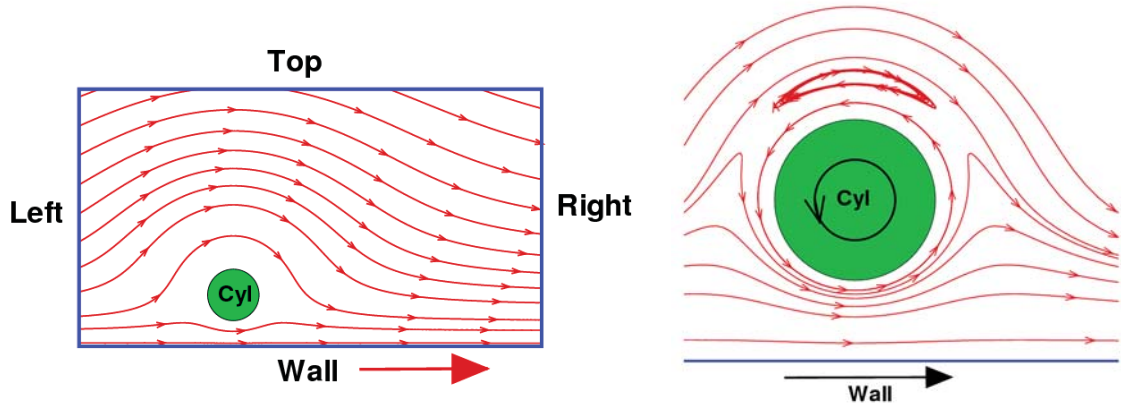
Figure 5.1: Schematic of Wannier flow.
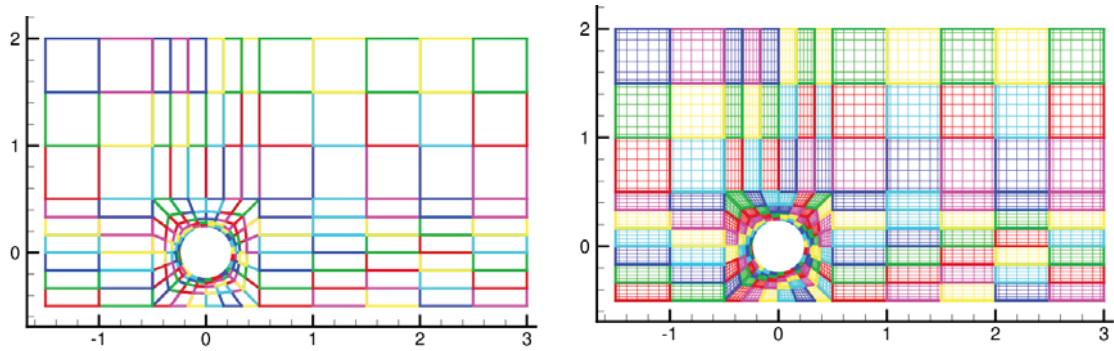
Figure 5.2: Mesh with 201 quadrilateral spectral elements.

The mesh used for the simulation is shown in Figure 5.2. The outer mesh is made of 201 quadrilateral spectral elements and the polynomial order is varied from 4 to 10 for this study.

60

Figure 5.3 plots the L_∞ and L_2 norms of error in velocity. The L_2 norms of error are normalized by the L_2 norms of the exact solution for each of the velocity components to obtain relative errors. We can see that the errors in both norms drop exponentially fast. At higher values of polynomial degree, the L_∞ errors are dominated by errors at points close to the cylinder wall whereas the L_2 error continues to drop exponentially.
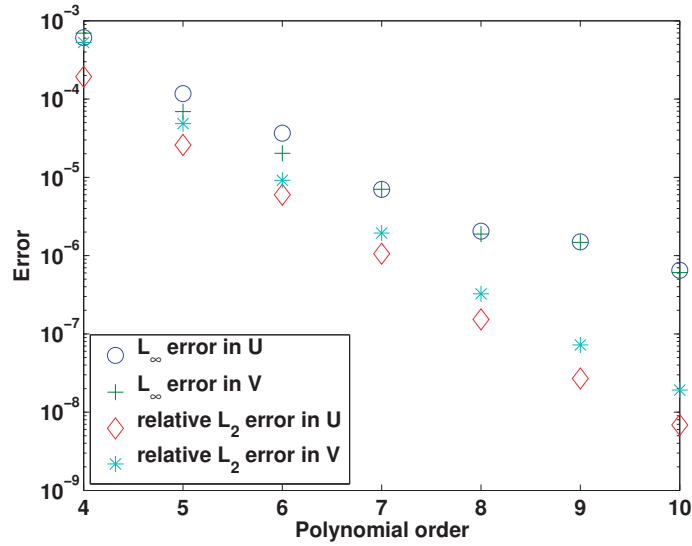
Figure 5.3: Convergence in L_∞ and L_2 norm as a function polynomial order for Wannier flow.

5.1.2 Kovasznay Flow

Our second test case is Kovasznay flow, a laminar, incompressible flow behind a two-dimensional grid. The exact solution, due to Kovasznay [1948], can be written as a function of Reynolds number (Re) as follows:

$$u(x,y) \quad = \quad 1 - e^{\lambda x} cos(2\pi y), \tag{5.3}$$

$$v(x,y) \quad = \quad \frac{\lambda}{2\pi} e^{\lambda x} sin(2\pi y), \tag{5.4}$$

where

$$\lambda = \frac{Re}{2} - \left(\frac{Re^2}{4} + 4\pi^2 \right)^{\frac{1}{2}}. \tag{5.5}$$

The schematic of the flow domain is shown in Figure 5.4. Dirichlet boundary conditions, obtained from the exact solution, are prescribed on all domain boundaries. Second-order time stepping is used and the solution is marched until it reaches a steady state. Various parameters used for the simulation are presented in Table 5.1. Figure 5.5 shows a typical mesh used for the simulation of Kovasznay flow. Figure 5.6 shows the steady-state streamlines obtained from the simulation. In Figure 5.7 we see that the L_∞ and L_2 norm of error both decrease exponentially as we increase the order of polynomial expansion (P). As in the earlier case, L_2 norms of error are normalized with the L_2 norm of the exact solution.
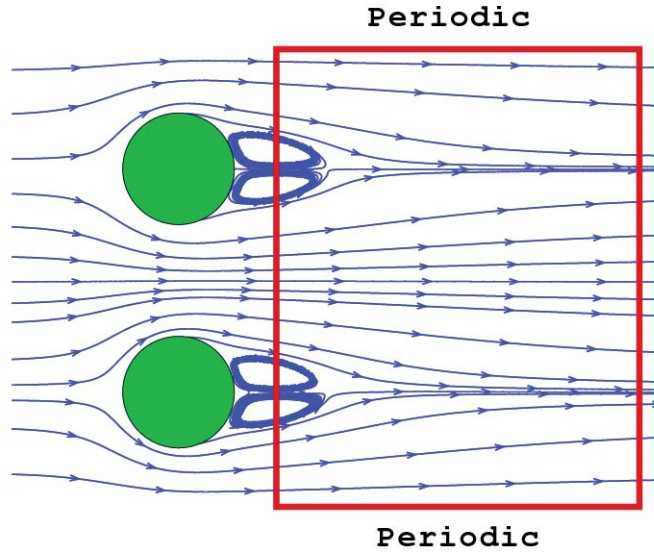
Figure 5.4: Schematic of Kovasznay flow.

Figure 5.8 plots the effect of streamwise domain size on solution accuracy when outflow boundary conditions are used at the right boundary. Initially, we can see that spectral convergence is obtained with increase in polynomial degree. After a certain point the error saturates as the error due to outflow boundary condition dominates numerical errors. This can be delayed by moving the outflow boundary further downstream. The simulation is also performed using a 3D mesh shown in Figure 5.9. Periodic boundary conditions are

Table 5.1: Parameters for Kovasznay flow simulation.

Parameter	Value
Re	40.0
Δt	0.001
N_{cells}	12
P	4-14
t_{order}	2

used in the third direction. As in the 2D case, Figure 5.10 shows exponential convergence with increase in polynomial order.
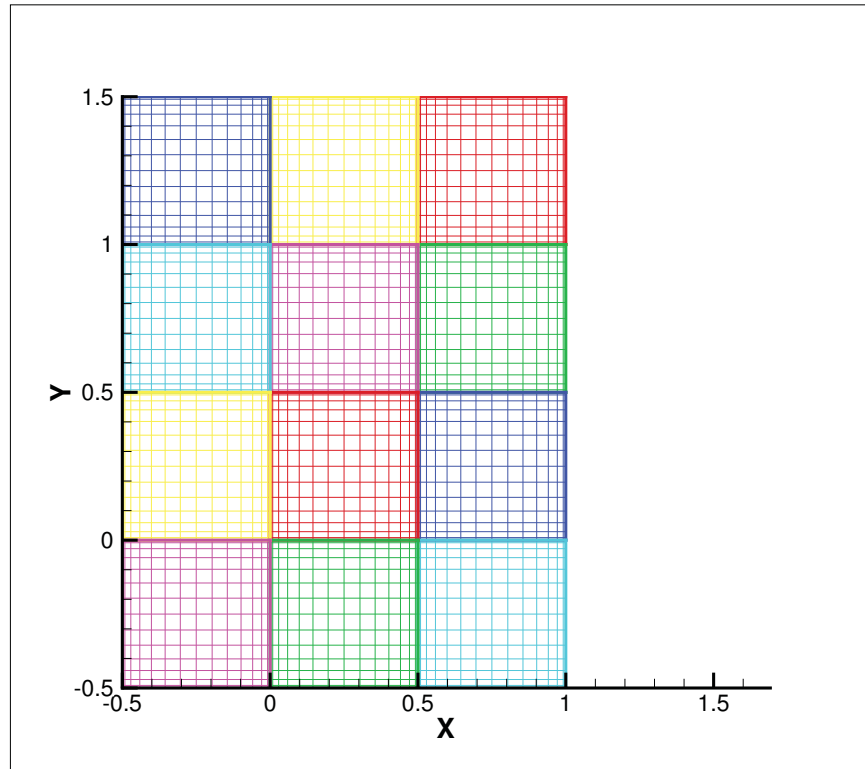
Figure 5.5: Mesh used for the simulation of steady state Kovasznay flow
($N_{cells} = 12$; P=14.).
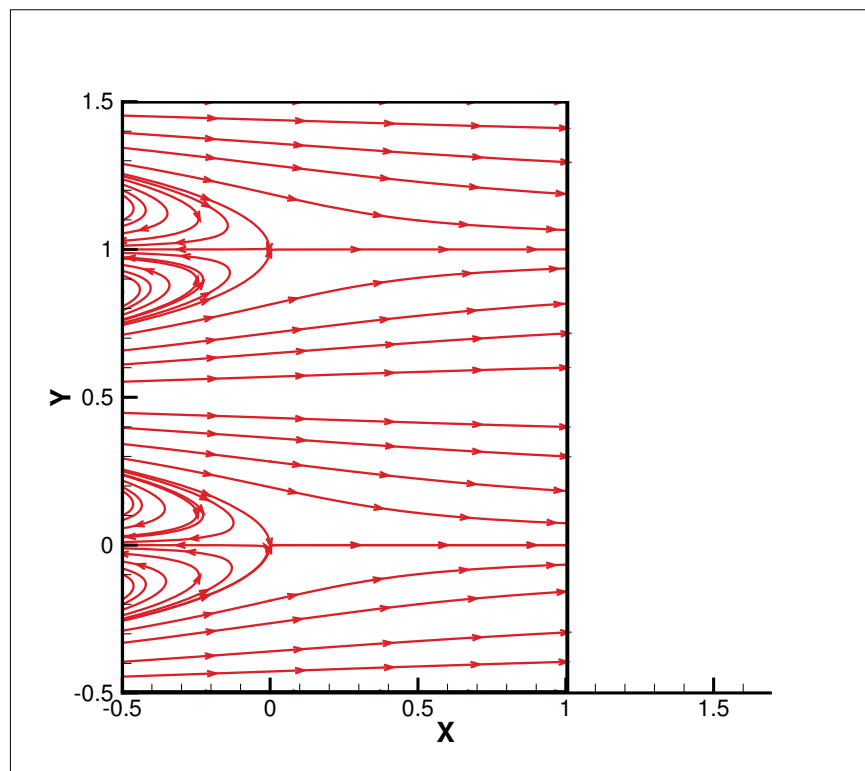
Figure 5.6: Streamlines for steady state Kovasznay flow.
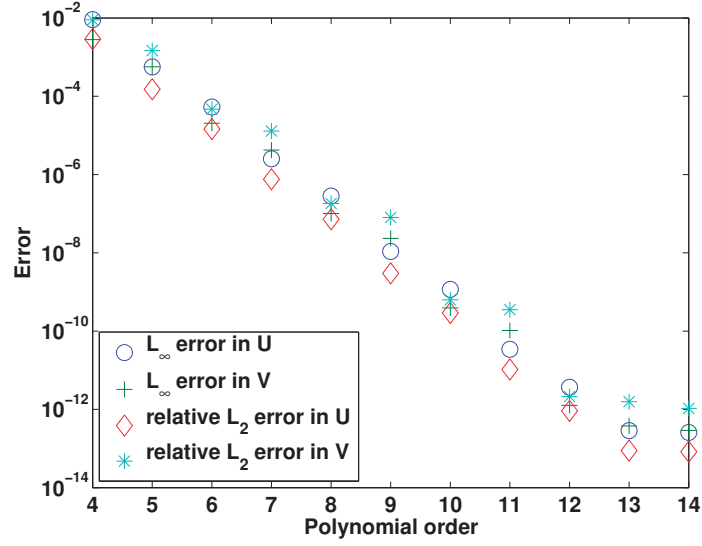
Figure 5.7: Convergence in L_∞ and L_2 norm as a function polynomial order for steady state Kovasznay flow at Reynolds number 40.

(a)

(b)
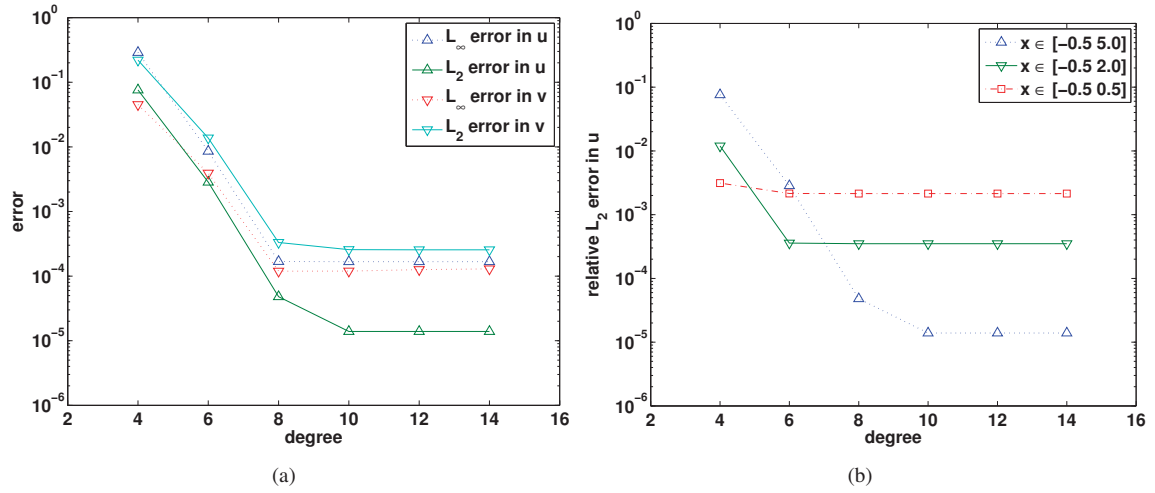
Figure 5.8: Study of effect of domain size on solution accuracy for 2d Kovasznay flow with outflow boundary condition prescribed on the right face. (a) L_∞ and L_2 errors in u and v as a function of polynomial order for domain $x \in [-0.5\ 5.0]$. (b) L_2 errors in u as a function of polynomial order for various domain sizes.
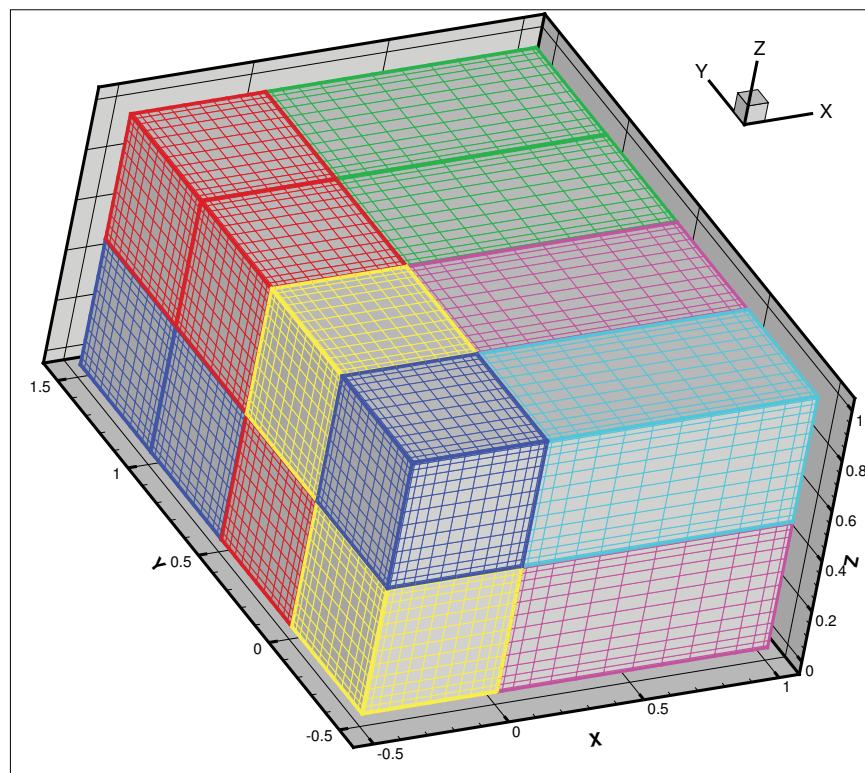
Figure 5.9: 3-d mesh used for Kovasznay flow simulation at Reynolds number 40.
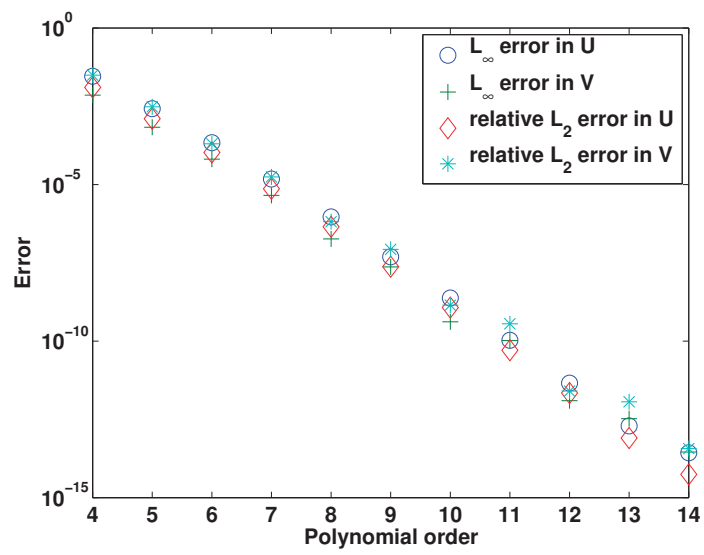
Figure 5.10: Convergence in L_∞ and L_2 norm as a function polynomial order for 3-d steady state Kovasznay flow at Reynolds number 40.

5.1.3 Orr-Sommerfeld problem

Our third test case is the simulation of the highly sensitive Orr-Sommerfeld problem. This involves computation of growth rates of small-amplitude Tollmien-Schlichting waves in the plane Poiseuille flow (Fischer [1997]). For this case, an accurate solution is available from linear stability theory. The domain and the mesh used for this simulation is shown in Figure 5.11. The domain consists of two walls separated by a distance $2h = 2$ and a streamwise length of $2\pi h$. Periodic boundary conditions are used in the streamwise direction and the flow is driven by a constant body force. The Reynolds number is given by $Re = \frac{U_c h}{\nu} = 7500$. Also shown is the perturbation stream function. The initial condition is the solution for the plane Poiseuille flow superimposed with a perturbation. Specifically, the initial condition is given by

$$u = 1 - y^2 + \epsilon \tilde{u}, \qquad (5.6)$$

$$v = \epsilon \tilde{v}. \qquad (5.7)$$

Here $(\tilde{u}, \tilde{v})$ correspond to the only unstable eigenfunction of the Orr-Sommerfeld equation with wave number unity at $Re = 7500$. We use $\epsilon = 10^{-5}$.

Linear stability theory predicts the energy of the perturbation

$$E(t) = \int_0^{2\pi} \int_{-1}^1 \left[(1 - y^2 - u)^2 + v^2 \right] \mathrm{d}y\, \mathrm{d}x, \qquad (5.8)$$

to grow as $\mathrm{e}^{2\omega t}$, where $\omega = 0.002234975649$. The relative error in growth rate is given by

$$error = \frac{1}{\omega} \left| \omega - \frac{1}{2t} ln\left(\frac{E(t + t_0)}{E(t_0)} \right) \right|. \qquad (5.9)$$

Table 5.2 shows the computed perturbation energy for various polynomial degrees. Figure 5.12 plots the temporal evolution of the perturbation and the computed growth rate for $P = 9$. In all cases, t_0 is chosen to be 1 sec after the start of the simulation. A second-order accurate time stepping scheme with a time step of $\Delta t = 0.003125$ is used for these simulations. For each of the cases, the relative error in growth rate is computed after $t = 50.28$ sec which corresponds to two periods of oscillation for the Tollmien-Schlichting waves. We can see that the computed value of the growth rate is in excellent agreement with the result from linear stability theory. We can also see spectral convergence as the polynomial degree is increased from 7 to 13. Once the polynomial degree is higher than 13, the temporal error corresponding to the time step size dominates the spatial error.
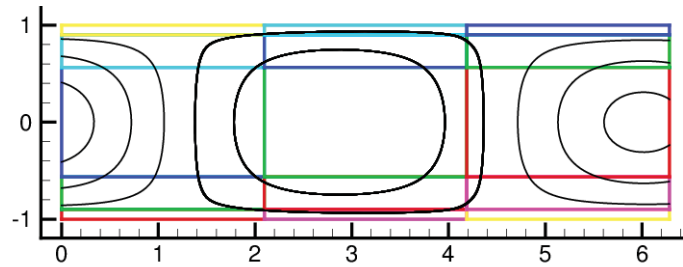
Figure 5.11: Domain and spectral element mesh used for the Orr-Sommerfeld simulation. Also shown is the stream function of the perturbation.
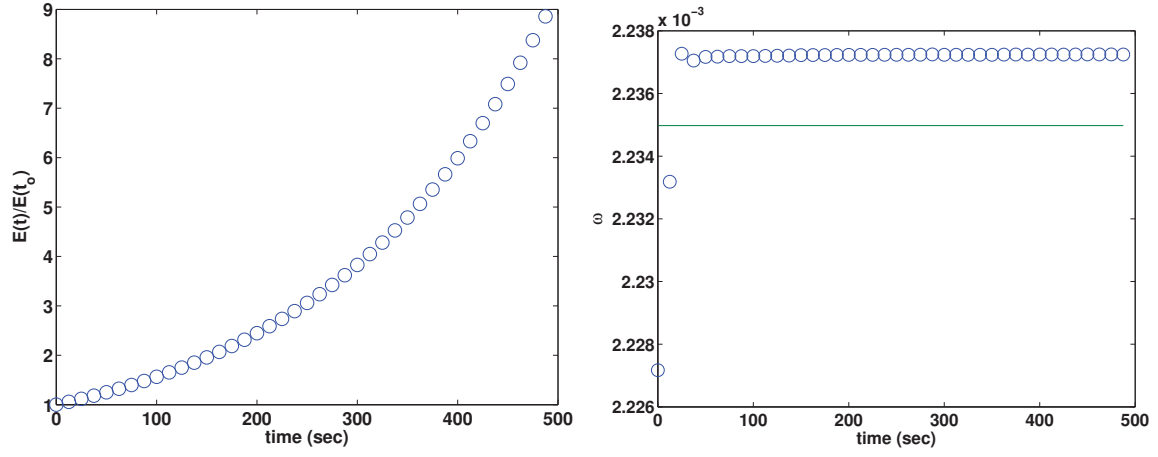
Figure 5.12: Temporal evolution of perturbation energy (left) and growth rate (right) for P=9, $\Delta t = 0.003125$.

Table 5.2: Spatial convergence, Orr-Sommerfeld problem: $N_{el} = 15$, $\Delta t = 0.003125$.

Degree	ω	error
7	2.293545188889385e-03	2.620589620991660e-02
9	2.237078145708761e-03	9.407246605581612e-04
11	2.234894879598453e-03	3.613882844038103e-05
13	2.234950158073417e-03	1.140546054491922e-05
15	2.234950158073417e-03	1.140546054491922e-05

5.1.4 Vortex shedding from circular cylinder

Our next test case is laminar flow past a circular cylinder in free stream. For $Re > 47$, vortex shedding is known to occur and a Von-Karman vortex street forms in the wake of the cylinder. This vortex shedding causes oscillating forces on the cylinder at a particular frequency, called the Strouhal frequency, and is of particular importance in engineering design. In our current study, we perform this experiment at various Reynolds numbers and compare the results with other simulations and experimental data. Strouhal number is used as a measure to compare the data.

The domain used for this simulation is shown in Figure 5.13. Also shown is the spectral element mesh used for the simulation at $Re = 100$. The mesh is further refined for higher Reynolds number cases. The diameter of the cylinder (d) is chosen as $d = 0.2828$. The center of the cylinder is located at $(x_1, x_2) = (1.5, 0.5)$. The domain starts at about 5 diameters upstream from the center of the cylinder and extends up to 16 diameters downstream from the center of the cylinder. Uniform inflow, $U_\infty = 1.0$, is prescribed at the inflow boundary and an outflow boundary condition is prescribed at the outflow boundary. Side boundaries are located at about 5 diameters from the center of the cylinder. A symmetry boundary condition is prescribed on these boundaries. The Reynolds number , $Re = U_\infty d/\nu$, is varied from 47 to 387. Figure 5.14 plots the instantaneous velocity and pressure contours at $Re = 100$.

Figure 5.15 compares the results of the simulation with 2D direct numerical simulations by Henderson [1997] and with the experiments of Williamson [1989]. The Strouhal numbers obtained at various Reynolds numbers are in good agreement with 2D simulations of Henderson at all Reynolds numbers considered in this study. They are also in good agreement with the experimental data for $Re < 190$ at which the 2D wake becomes unstable and bifurcates to a three-dimensional flow. Above this Reynolds number, three dimensional simulations are required to accurately resolve all flow features.
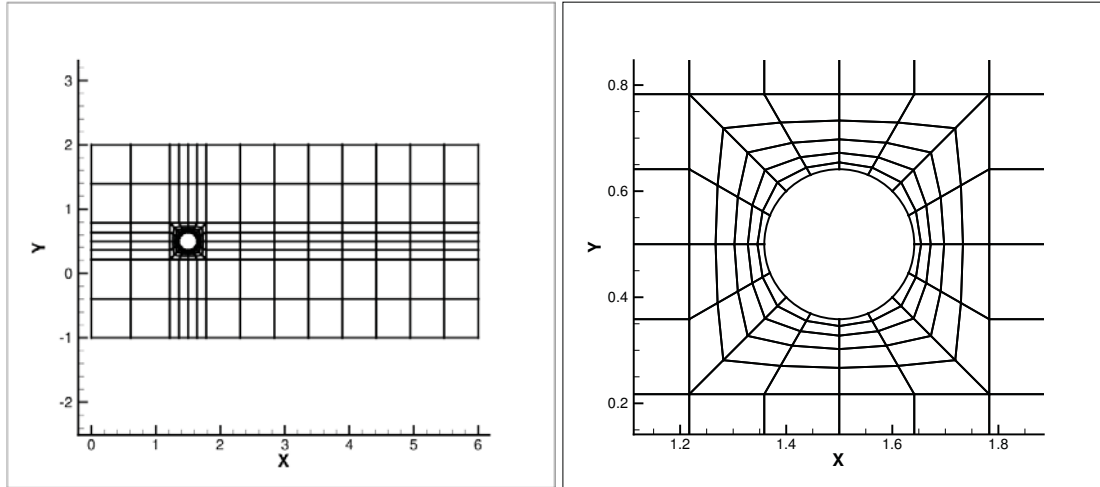
Figure 5.13: Spectral element mesh for simulation of vortex shedding from a circular cylinder at Re=100.

(a) U

(b) V
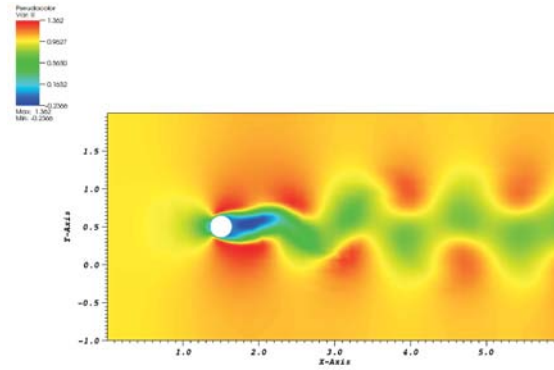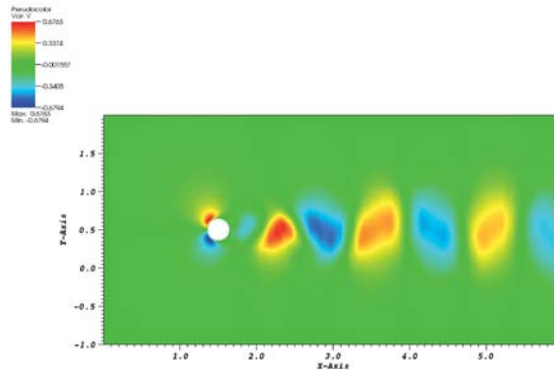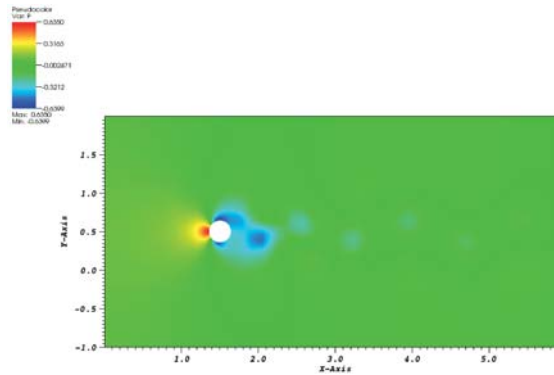
user: sriharshakandala
Thu Apr 3 20:40:46 2014

(c) Pressure

Figure 5.14: Instantaneous velocity and pressure contours at Re = 100.

72
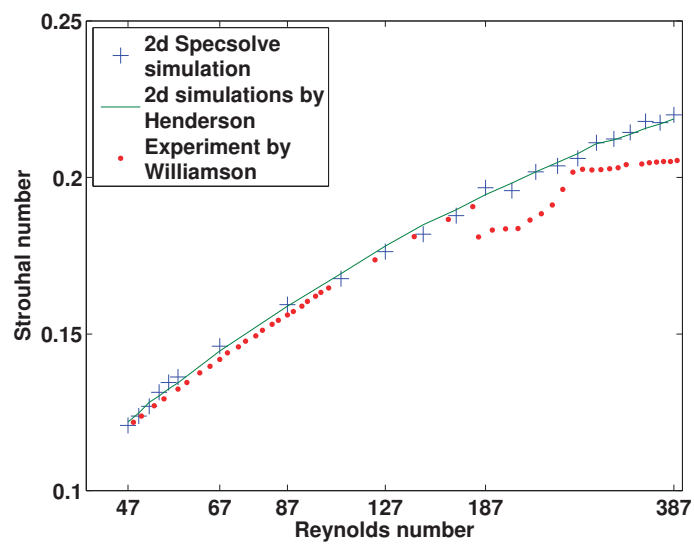
Figure 5.15: Comparison of variation of Strouhal number with Reynolds number.

5.1.5 Flow over a backward facing step

Our final test case is the three-dimensional laminar flow over a backward-facing step with an expansion ratio of 1:1.94. This is based on the experimental setup of Armaly et al. [1983] and was previously used in the numerical simulations of Couzy [1995], Biswas et al. [2004] and Shahbazi [2007]. The flow is characterized by three recirculation regions whose occurrence, location and size depends on the Reynolds number and expansion ratio of the step. In this study, we restrict ourselves to $Re < 400$ which has a single recirculation zone on the bottom wall directly at the base of the step.

The geometry and mesh used for the simulation is shown in Figure 5.16. The height of the downstream section, h, is chosen to be 1. The inflow is located $3h$ upstream of the expansion and the outflow is located $20h$ downstream of the expansion. The spanwise length is $9h$ with a wall on one side and symmetry boundary conditions on the opposite side. The inlet velocity profile is chosen to be the tensor product of a parabola (in the z-direction) and a Blasius boundary layer (in the y-direction). The Blasius velocity profile is characterized by the boundary layer thickness (δ) which represents the wall-normal distance at which the velocity attains 99% of the free-stream value. Specifically, the inlet velocity is given by

$$u = [15.08739(0.5149 - z)z]\, b(y), \tag{5.10}$$

$$v = 0.0, \tag{5.11}$$

$$w = 0.0. \tag{5.12}$$

The mesh consists of 682 spectral elements with with ninth-degree polynomial approximation within each element. Second-order time stepping with $\Delta = 0.0025$ is used. The simulation is continued until a steady-state solution is obtained. The simulation is carried out at Reynolds numbers 172 and 343. The recirculation zones for these Reynolds numbers are plotted in Figures 5.17 and 5.18. Figure 5.19 shows the variation of the length of the recirculation region with Reynolds number. We can see that the length of the recirculation zone increases with increase in Reynolds number. These results are in excellent agreement with earlier numerical simulations and with the experimental data.
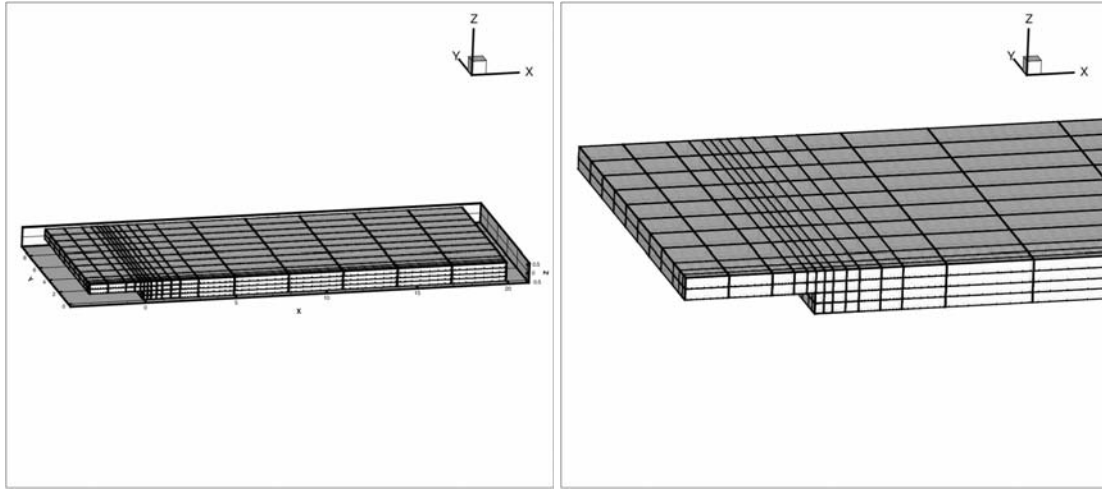
Figure 5.16: Spectral element mesh for simulation of flow over a backward facing step.
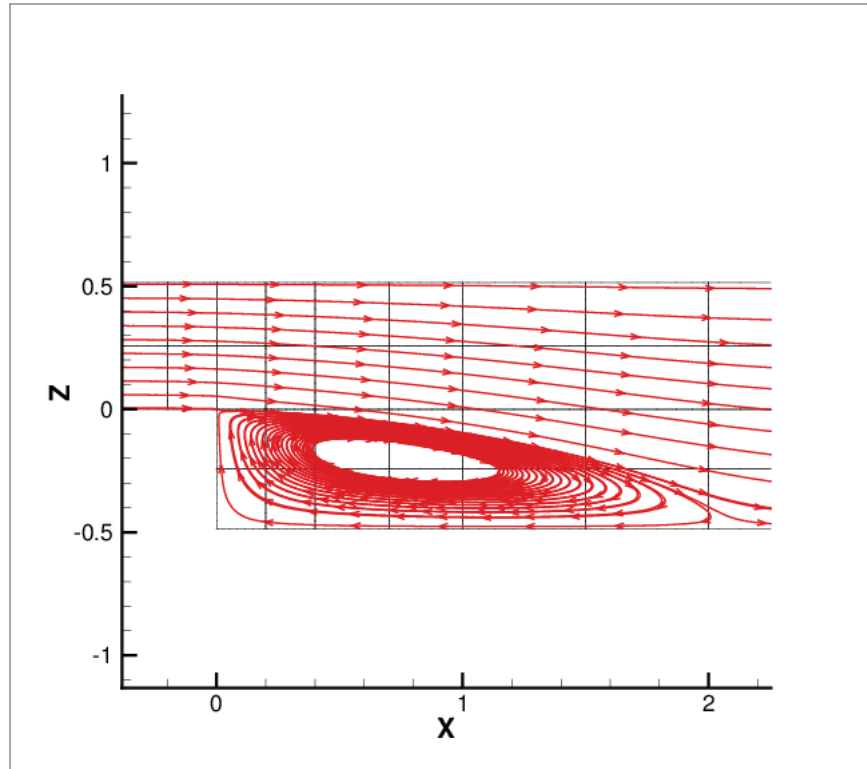
Figure 5.17: Flow pattern near the symmetry plane of the backward facing step for Re=172.
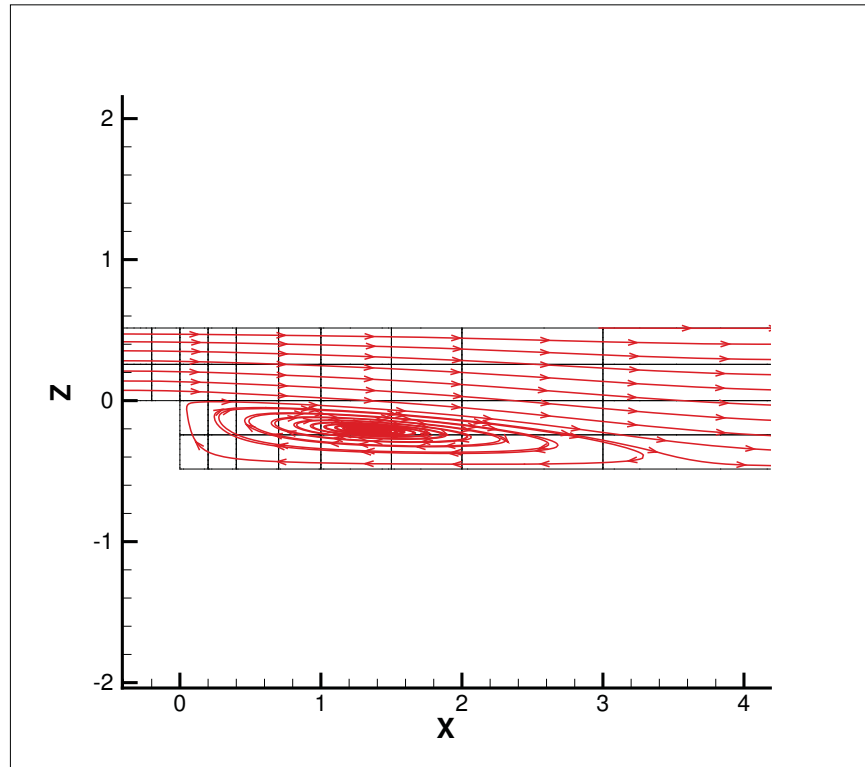
Figure 5.18: Flow pattern near the symmetry plane of the backward facing step for Re=343.
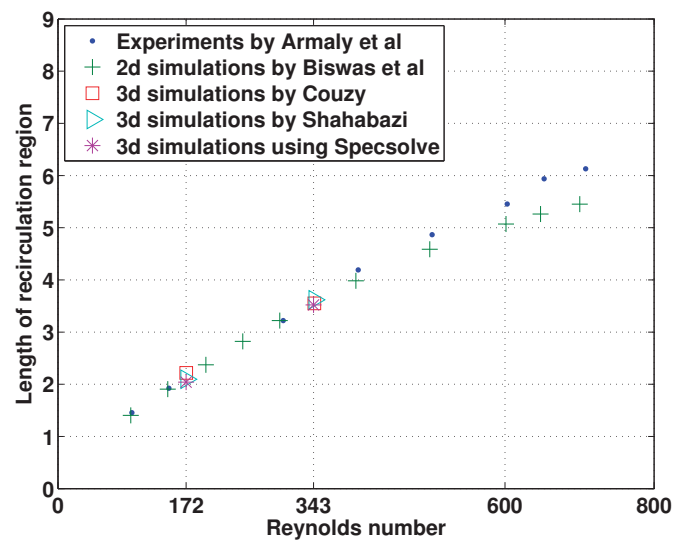
Figure 5.19: Variation of length of primary recirculation region with Reynolds number for flow over a backward facing step.

5.2 The urban boundary layer experiment

5.2.1 The urban boundary layer

The atmospheric boundary layer (ABL) is defined in (Stull [1988]) as the part of the troposphere that is directly influenced by the presence of the Earth's surface and responds to surface forcing with a time scale of about an hour or less. It consists of a succession of quasi-equilibrium boundary layers diffusing within older boundary layers in response to the forcing by frictional drag, terrain, heat transfer and pressure gradients. The lowest part of the ABL is called the surface layer. It extends to a height of about 150 m depending on the terrain. The surface layer over an urban area can be classified into three sublayers: the urban canopy layer, the roughness sublayer and the inertial sublayer (Britter and Hanna [2003]). This is schematically shown in Figure 5.20. In the urban canopy layer the flow at a specific point is directly influenced by the local obstacles, and in the roughness sublayer the flow is still adjusting to the effect of many obstacles.
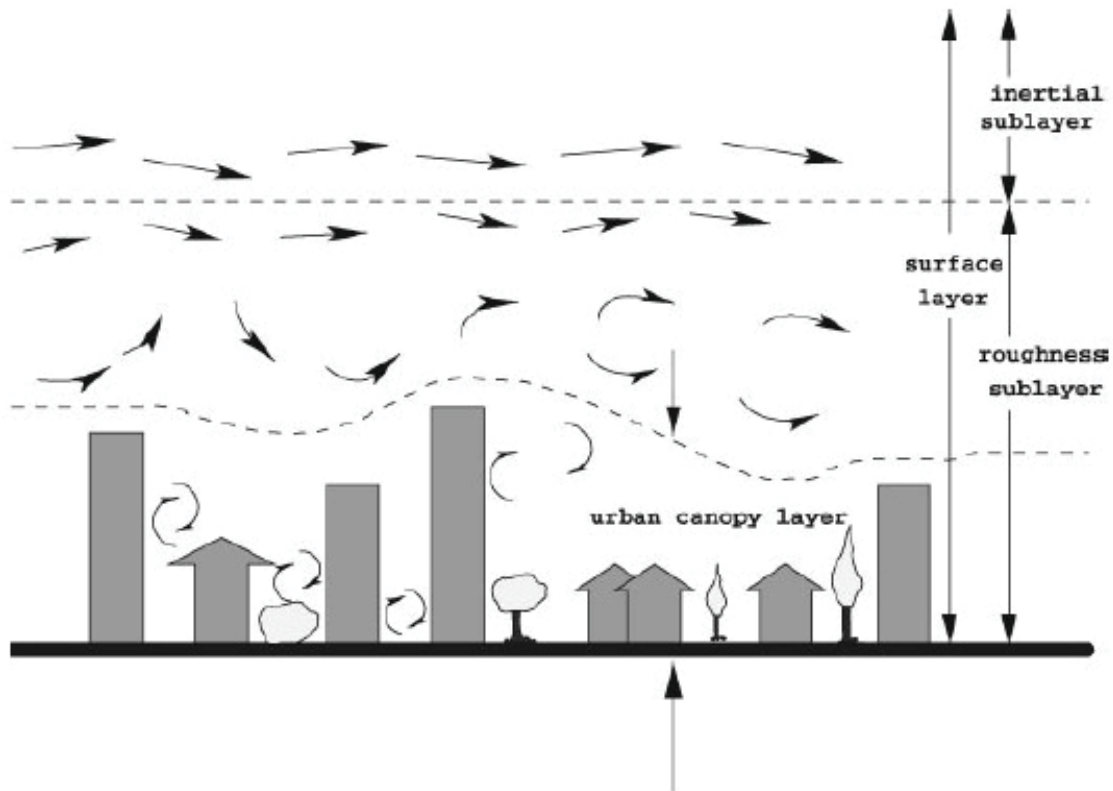
Figure 5.20: Schematic of Flow through and over an urban area (Grimmond and Oke [1999]).

The inertial sublayer is the area where the boundary layer has adapted to the integrated effect of the underlying surface. The mean velocity profile in this part can be represented by the log-law:

$$u = \left(\frac{u_*}{\kappa}\right) ln \left[\frac{z-d}{z_0}\right],$$ (5.13)

78

where u_* is the friction velocity, z is the elevation, κ is the von=Karman constant, z_0 is the surface roughness length and d is the surface displacement length. The last two parameters depend on the terrain, increasing with the roughness of the terrain. Various parameterizations for z_0 based on land-use were presented in the works by Stull [1988], Theurer [1999], Grimmond and Oke [1999] and Davenport [1965]. An alternative representation of velocity profile in the inertial layer widely used in wind profile modeling is through a power law

$$\frac{u}{u_\delta} = \left(\frac{y}{\delta}\right)^\alpha, \tag{5.14}$$

where u_δ is the mean velocity at $z = \delta$ and the exponent α depends on the roughness of the surface (Wang et al. [1996]). This can be reformulated as

$$\frac{u}{u_i} = \left(\frac{y}{y_i}\right)^\alpha, \tag{5.15}$$

where u_i is the velocity at a point $y = y_i$ in the inertial layer. The advantage of this power law is that it involves only one scaling parameter. While velocity profiles in the inertial layer can be satisfactorily described by either a power law or a log law with appropriately chosen parameters, flows inside urban canopies are in general three-dimensional and quite complex and are the focus of our current work.

Figure 5.21 shows a schematic of flow around a surface-mounted cube from Martinuzzi and Tropea [1993]. This is a fundamental building block for understanding flow characteristics in urban street canyons. In this case, a cube is placed in a fully-developed channel flow. The cube imposes a strong adverse pressure gradient on the flow causing boundary layer separation upstream of the cube. This causes the development of strong recirculation regions upstream and around the cube. The approach boundary layer vorticity rolls up into a *horse shoe vortex* which, along with the *arch vortex* located immediately behind the cube, is one of the most prominent features of this flow. A favorable pressure gradient diverts the flow upstream of the cube from the symmetry plane towards the sides. Shear layers separate on top and sides of the block. Behind the cube, there is a favorable pressure gradient from the sides to the symmetry plane causing the flow to reattach behind the block. Sousa [2002] studied the turbulent flow around a surface-mounted obstacle using two-dimensional three-component DPIV (Digital Particle Image Velocimetry). The out-of-plane velocity component was obtained by the use of continuity applied to two-dimensional velocity fields recorded in parallel planes. He noted that the use of swirling strength and normalized angular momentum to identify vortices is superior to traditional vorticity-based methods.

Becker et al. [2002] investigated the effect of wind direction, aspect ratio, Reynolds number, and the boundary layer type on flow structures around a single obstacle. This work extends the arch vortex topology proposed by Martinuzzi and Tropea [1993] to non-zero angle of attack. They noticed that increasing the angle of attack caused a dislocation of one of the footprints of the vortex until it switched to the top of the obstacle at an angle of $60°$. They found no fundamental difference in the vortex structure for various boundary layers and found that the length of the recirculation region decreased for rougher incoming boundary layers.

Additional complexities arise when an object is placed in the wake of another object. Based on the reattachment length of the wake behind the isolated object (in the absence of objects downstream) and the downstream spacing of the second object, the flow can be broadly classified into three different regimes. Figure 5.22 shows the classification into isolated roughness, wake interference and skimming flow regimes based on the canyon aspect ratio (Oke [1988]). Here, we use the words "canyon" and "streets" interchangeably. The canyon aspect ratio is defined as the ratio of spacing between the blocks to the height of the block ($\frac{S}{H}$). This work is 2D in nature and assumes infinite width of the street canyon. When the canyon aspect ratio is small ($\frac{S}{H} < 1.5$), the majority of the flow skims over the canyon with vortices trapped within the

canyon. This is called the *skimming flow regime*. When the objects are spaced further apart but not too far ($1.5 < \frac{S}{H} < 8 - 9$), the downstream object "sees" the wake of the upstream object. This is called the *wake interference regime*. Finally, when the canyon aspect ratio is larger ($\frac{S}{H} > 8 - 9$) the individual elements act as isolated roughness elements and the interaction of the flows induced by the buildings is negligible. This is called the *isolated roughness regime*. ? have studied the effect of street canyon aspect ratio on flow characteristics using a water tunnel experiment. Laser Doppler anemometry is used for measuring velocity. They noticed that similar regimes were found even when the width of the street is finite.
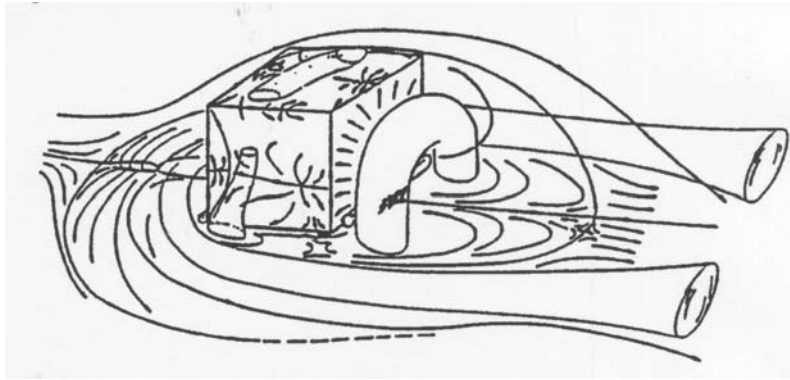
Figure 5.21: Schematic of Flow around a surface mounted cube (Martinuzzi & Tropea [1993]).
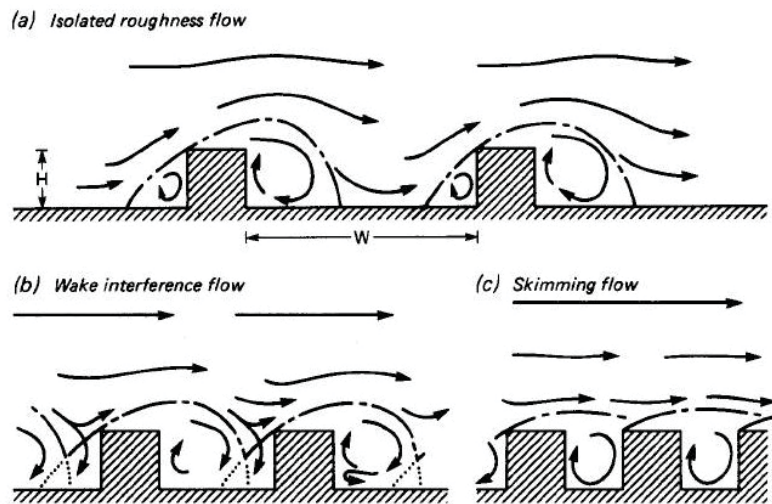
Figure 5.22: Schematic illustrating (a) isolated roughness (b) wake interference and (c) skimming flow regimes in an urban street canyon by Oke [1988].

The MUST (Mock Urban Setting Test) experiment (Biltoft [2001]) is a scaled urban dispersion experiment performed at Dugway proving grounds, Utah in 2001. The objective was to overcome the scaling and measurement limitations of laboratory experiments and characterize difficulties presented by real urban set-

tings. A 10×12 array of containers was used to represent an urban domain with symmetric characteristics. Continuous tracer releases were generated with propylene as a tracer gas, and concentrations were measured using fast response photo-ionization detectors. Gailis [2004] conducted a wind tunnel dispersion study of the MUST array. This study was intended to bridge some of the gaps between laboratory and full-scale outdoor trials. Yee et al. [2006] compared the field experiment to both a 1:50-scale wind tunnel and 1:205-scale water channel simulation. The study notes that while the behavior of plume dispersion is qualitatively the same in all studies, appropriately scaled water-channel simulations were able to reproduce qualitatively the results of the full-scale field experiments better than wind-tunnel experiments.

Monnier et al. [2010] has investigated the three-dimensional flow through an urban-type array consisting of rows of cuboid plexiglas blocks in a laboratory-modeled neutrally stratified atmospheric boundary layer using SPIV (stereoscopic particle image velocimetry). A typical domain used in the experiment is shown in Figure 5.23. The domain can be defined in terms of width of the block (W), height of the block (H) and spacing between the blocks (S). The SPIV technique is used to acquire velocity data in vertical planes in between the blocks. In this experiment, the effect of stream-wise spacing between adjacent rows defining the two different flow regimes (wake interference and skimming flow regimes) as well as the effect of the incident angle of the approaching boundary layer are studied. Dominant mechanisms responsible for transport and dispersion were quantified.

While earlier work in this area is primarily based on field measurements and wind tunnel experiments, rapid increase in computing power and development of highly scalable parallel algorithms to harness this power is making numerical simulations a tool of choice. Earliest numerical simulations in this area modeled flow in an archetypal street canyon which is basically a turbulent shear flow above a rectangular cavity with mean flow perpendicular to the axis of the street canyon. While 2D simulations assumed infinite street width, 3D simulations used periodic boundary conditions in the spanwise direction. Baik and Kim [1999] modeled flow and pollution in a 2D street canyon using a 2D $\kappa - \epsilon$ turbulence model . Their code used a finite volume method with a staggered grid. A power-law velocity profile is used as an inlet boundary condition at the top of the upstream building. They studied the flow patterns in a street canyon for various street canyon aspect ratios. Kim and Baik [2004] performed 3D numerical simulations of flow within an array of cube using a renormalization group $\kappa - \epsilon$ scheme. They investigated the effect of angle of incidence on flow structures and classified the flow in three regimes based on the angle of incidence. Liu et al. [2004] performed large eddy simulations of flow in a model urban street canyon using the Smagorinsky subgrid scale model. They investigated the effect of street canyon aspect ratio on flow structures and pollutant transport within the street canyon. Shah and Ferziger [1997] studied flow over a surface mounted cube using a large eddy simulation. A second-order finite volume code was used. Data from large-eddy simulations of channel flow at comparable Reynolds number is used to generate boundary conditions upstream of the cube. Camelli and Lohner [2006] studied flow and dispersion patterns in realistic urban areas like the Tyson's corner area in Fairfax, and the Madison Square Garden area in New York City using VLES (Very Large Eddy Simulation). They used a finite element code with a dynamic Smagorinsky LES model. Tseng et al. [2006] studied flow and dispersion through a model of downtown using large eddy simulation. Their code uses a pseudo-spectral method in the horizontal directions and a second-order accurate central difference scheme in the vertical direction. The presence of bluff bodies is modeled using an immersed boundary method. A Lagrangian dynamic LES (large eddy simulation) model (Bou-Zeid et al. [2005]) is used for modeling sub-grid scale stresses.

In this section, we present the results of the spectral element simulation of flow in a model urban street canyon. The domain used in this simulation consists of a 5×7 array of blocks and is similar to that used in the work of Monnier et al. [2010]. The inflow velocity profile is prescribed based on data provided from the hot-wire measurements and the flow upstream of the array is accurately resolved. Low pass filtering is used for stabilizing the simulation. No LES model is used.

In section 5.2.2 the results for the $0°$ AOI (angle of incidence) case, where the approaching boundary layer is normal to the array of blocks, are presented in detail. These results are compared with experimental data. Some preliminary results for $15°$ AOI are presented in section 5.2.3.
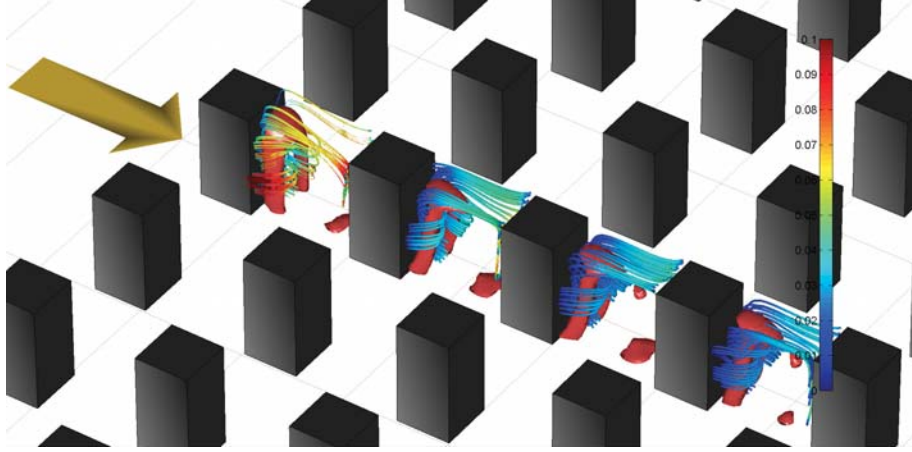

Figure 5.23: Array of cuboid plexiglas blocks used in the experiment by Monnier et al. [2010].

5.2.2 Numerical simulation of the urban boundary layer at zero angle of incidence

Description of numerical simulation and comparison with experimental data

The model of the urban street canyon used in the current study is shown in figure 5.24. It consists of a 5×7 array of blocks. Each block is 1 unit long ($L = 1$), 1 unit wide ($W = 1$) and 2 units high ($H = 2$), respectively. The spanwise and streamwise spacing between blocks is 1.5 units ($S = 1.5$). The wind direction is normal to the array ($AOI = 0°$). The domain used for our numerical simulation is shown in figure 5.25. The domain consists of a single row of blocks and periodic boundary conditions prescribed in the spanwise direction.The Reynolds number (Re_H), based on block height and inlet velocity at block height, is $Re_H = U_H H/\nu = 6283$. The domain used for the simulation is shown in figure 5.25. The domain consists of a single row of blocks and periodic boundary conditions are used in the spanwise direction. The inflow boundary is located 10 block widths upstream of the first block and the outflow boundary is located 40 block widths downstream of the last block. A symmetry boundary is condition is used on the top and is located at 17 block widths above the bottom wall. Inlet velocity profiles obtained from the hot-wire data provide the inlet boundary conditions for the simulation.

Three different simulations were carried out with the objective of studying the effects of grid resolution.

The first simulation uses a mesh of 15488 hexahedral spectral elements with a degree-6 polynomial approximation within each spectral element. This corresponds to about 5.3 million degrees of freedom. This mesh is shown in Figure 5.26. Third-order time stepping is used. The backward difference scheme is used for diffusion terms and extrapolation is used for nonlinear terms. De-aliasing and low pass filtering is used for stabilizing the simulation. No turbulence modeling is used. We have used the Nek5000 code for this simulation.
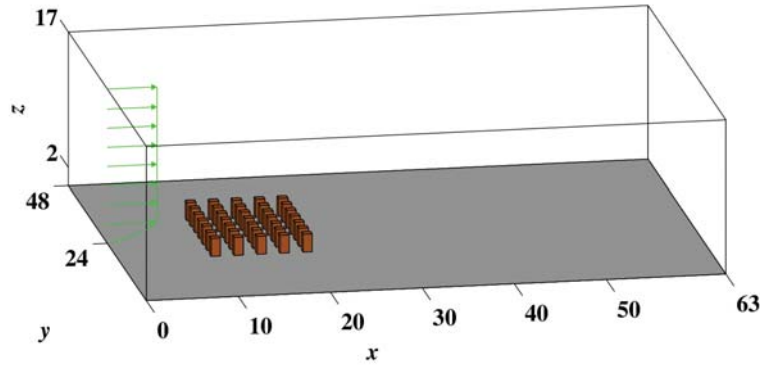
Figure 5.24: A typical urban street canyon.
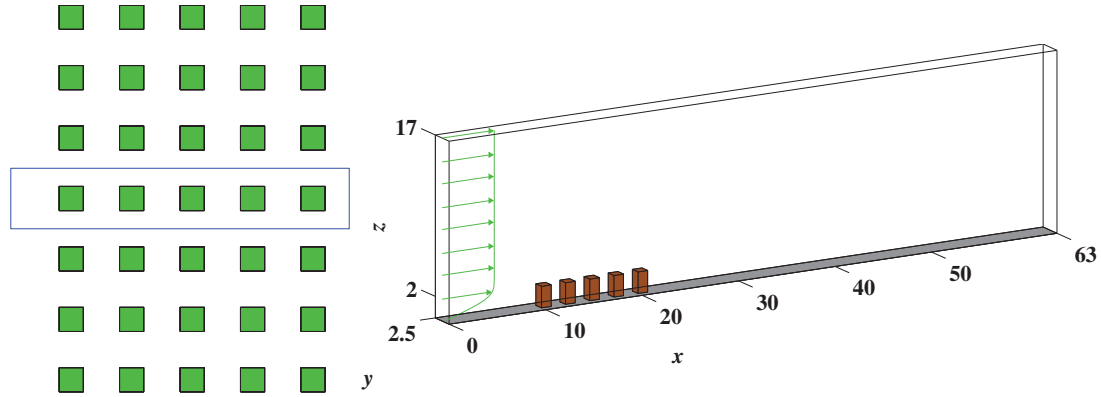
Figure 5.25: Domain used for the simulation of the urban boundary layer experiment.

The second simulation uses a mesh of 45748 hexahedral spectral elements with a degree-6 polynomial approximation within each spectral element. This corresponds to about 15.6 million degrees of freedom. This mesh is shown in Figure 5.27. Second-order time stepping is used. The backward difference scheme is used for diffusion terms and extrapolation is used for nonlinear terms. De-aliasing and low pass filtering is used for stabilizing the simulation. Steady inflow boundary condition is used for this case. This simulation is performed using *Specsolve*.

The third simulation uses a mesh of 88688 spectral elements with a degree-6 approximation within each spectral element. This mesh is shown in Figure 5.28. This corresponds to about 30.4 million degrees of freedom.
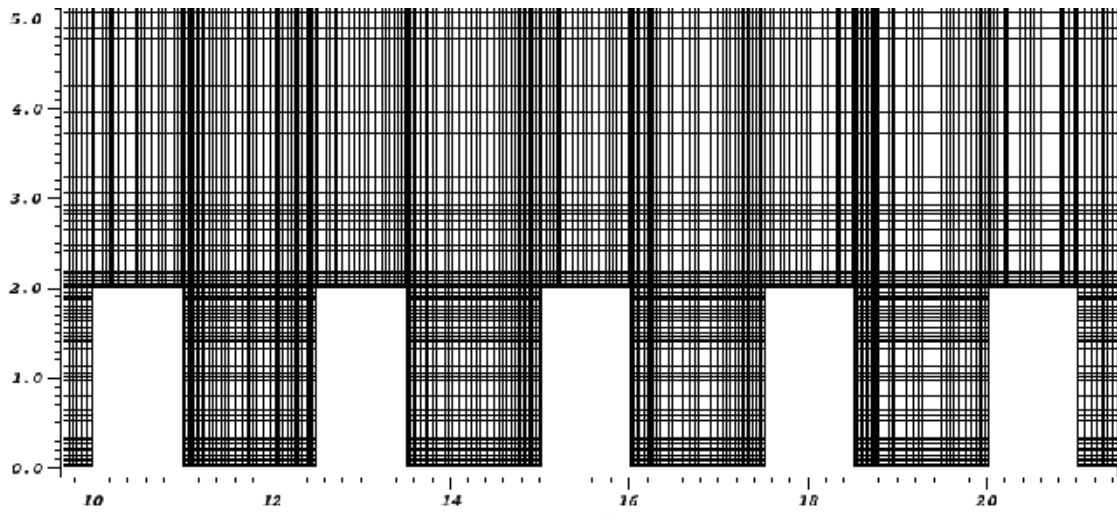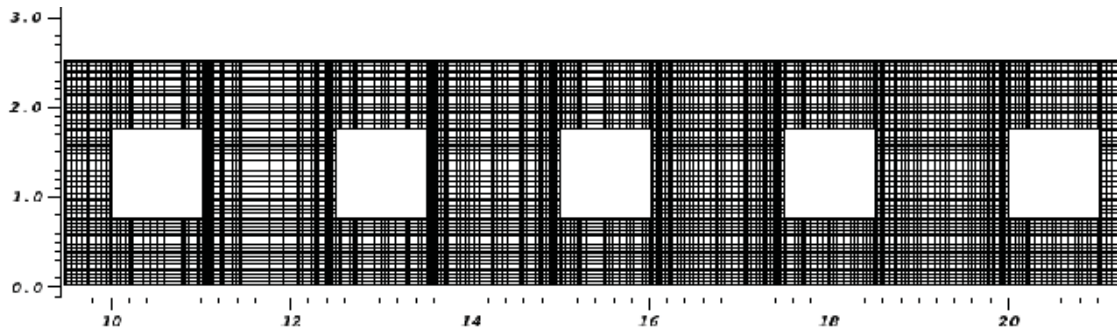
83

(a) Slice of mesh along y=1.25 plane

(b) Slice of mesh along z=0.5 plane
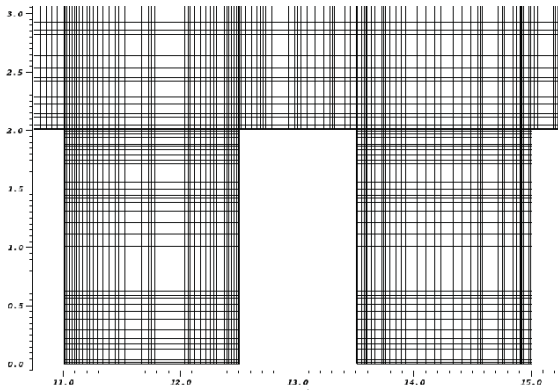
(c) Closeup of mesh along y=1.25 plane
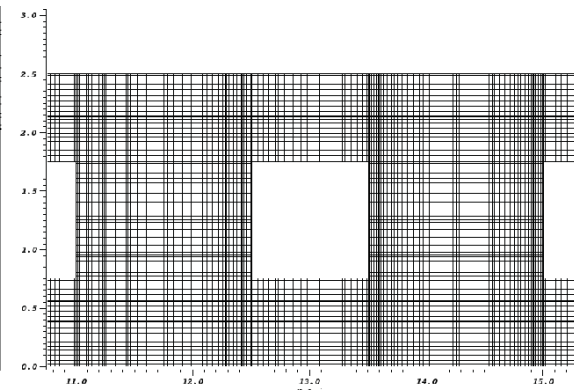
(d) Closeup of mesh along z = 0.5 plane

Figure 5.26: 15488 element hexahedral mesh for simulations 1.
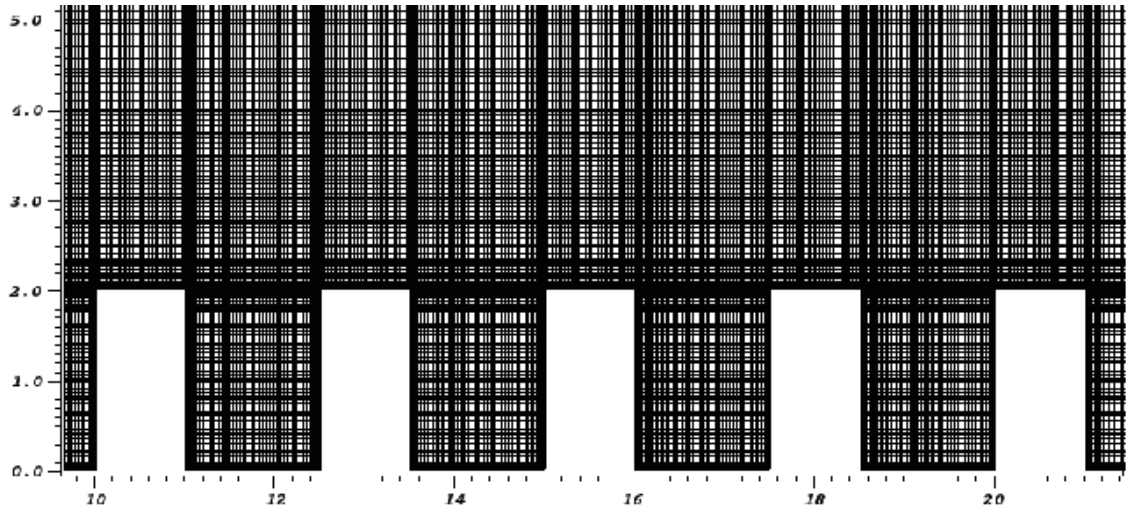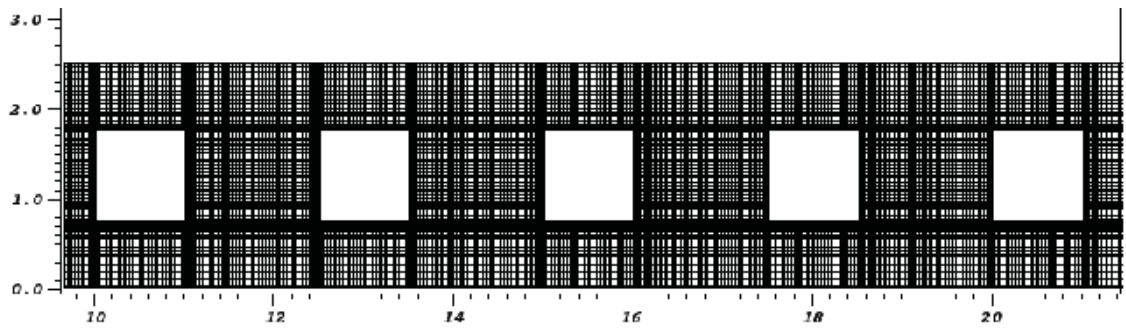
84

(a) Slice of mesh along y=1.25 plane.

(b) Slice of mesh along z=0.5 plane.
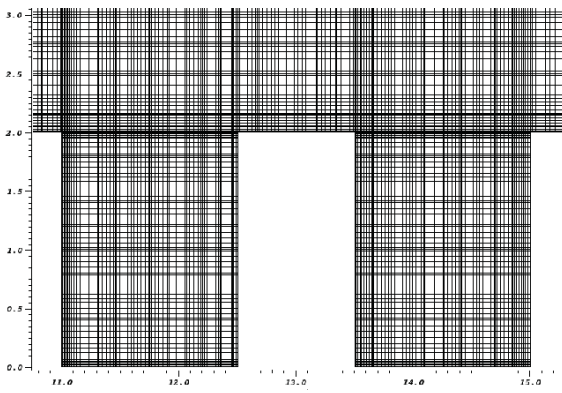
(c) Closeup of mesh along y=1.25 plane.
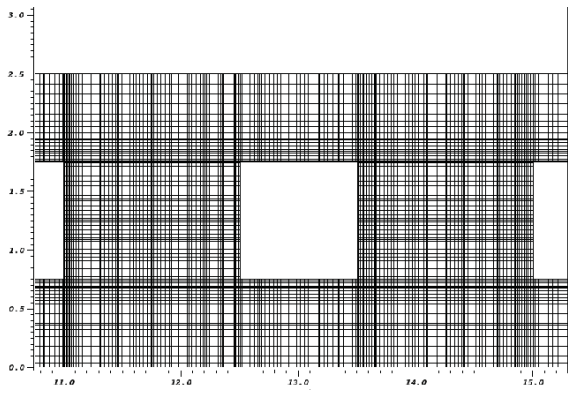
(d) Closeup of mesh along z=0.5 plane.

Figure 5.27: 45748 element hexahedral mesh for simulation 2.
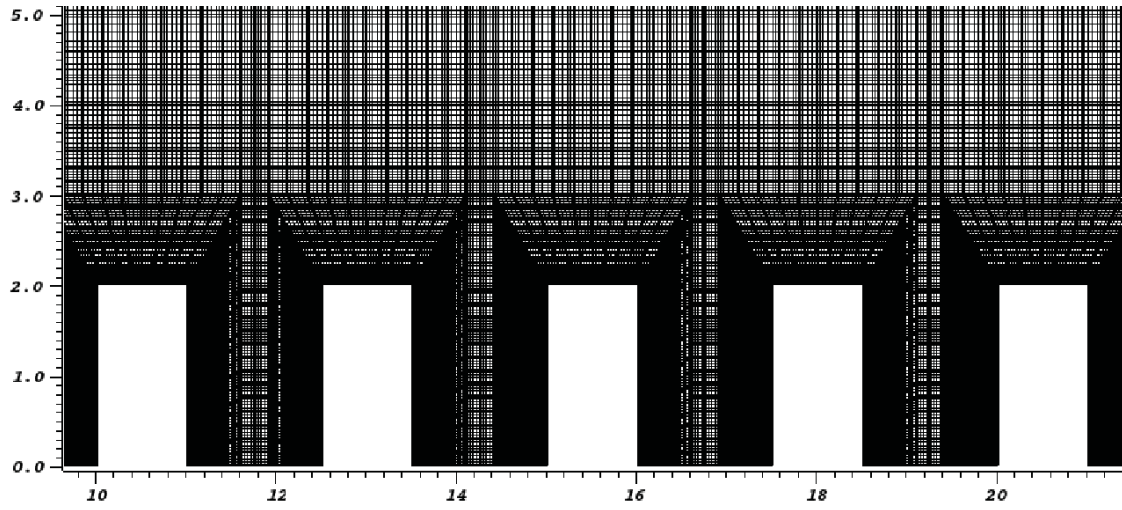
(a) Slice of mesh along y=1.25 plane
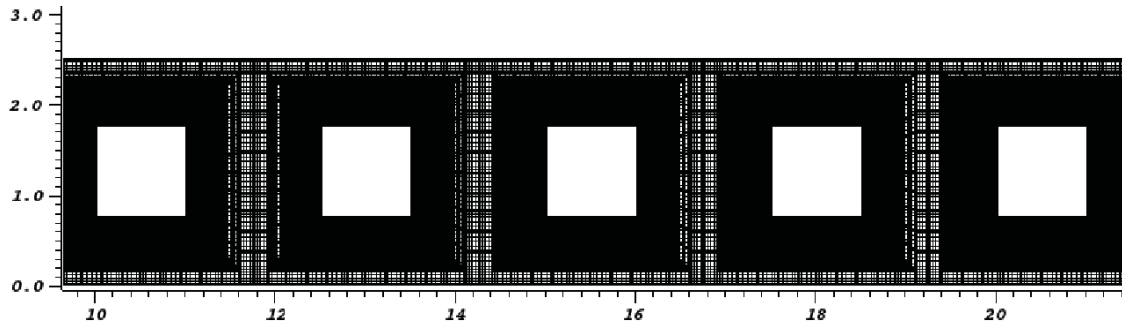
(b) Slice of mesh along z=0.5. plane
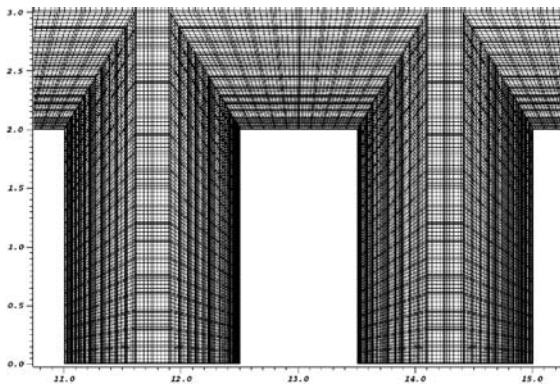
(c) Closeup of mesh along y=1.25. plane
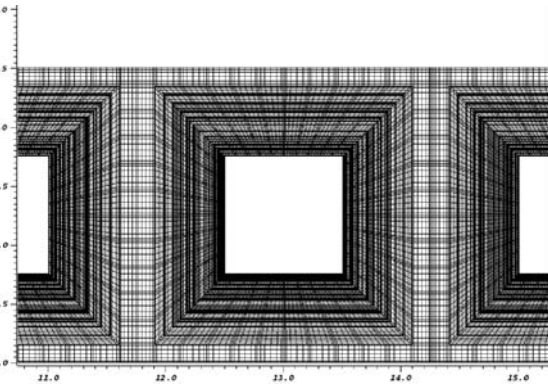
(d) Closeup of mesh along z=0.5. plane

Figure 5.28: 88688 element hexahedral mesh for simulation 3.

86

We compare the simulation results with PIV data obtained from the experiment in street 2. Comparisons are made along the planes $x = 0.75$, $y = 1.25$ and $z = 0.5$. Figures 5.29, 5.30 and 5.31 compare the mean velocity, rms velocity and Reynolds stress between the simulation and PIV data in the vertical plane $x = 0.75$. We can see that there is good agreement between simulation data and PIV data. Figures 5.32, 5.33 and 5.34 compare the mean velocity, rms velocity and Reynolds stress between the simulation and PIV data in the vertical plane $y = 1.25$. In this case, one can notice a significant improvement in W and TKE prediction between simulation 1 and simulation 2. This tells us that the mesh used for simulation 1 is not fine enough to resolve the flow features. There is only little improvement between simulation 3 and simulation 2. In general, all simulations seem to over-predict the magnitude of W upstream of the third block. Figures 5.35, 5.36 and 5.37 compare the mean velocity, rms velocity and Reynolds stress between the simulation and PIV data on plane $z = 0.5$. Figure 5.38 plots the first 4 POD (proper orthogonal decomposition modes) for U, V and W. Overall, we can see that there is good agreement between simulation and PIV data. From the data obtained from the grid resolution study, we can see that meshes two and three are fine enough to resolve all flow features. We think the comparison can be further improved by using more accurate inflow boundary conditions. Finally, Figure 5.39 presents the scaling results for simulation 3. We notice the parallel efficiency of 71.46% as the number of processors is increased from 252 (120710 degrees of freedom per processor) to 504(60360 degrees of freedom per processor). These tests are performed on the Kraken supercomputer at NICS (National institute for computational sciences) through an XSEDE startup allocation.
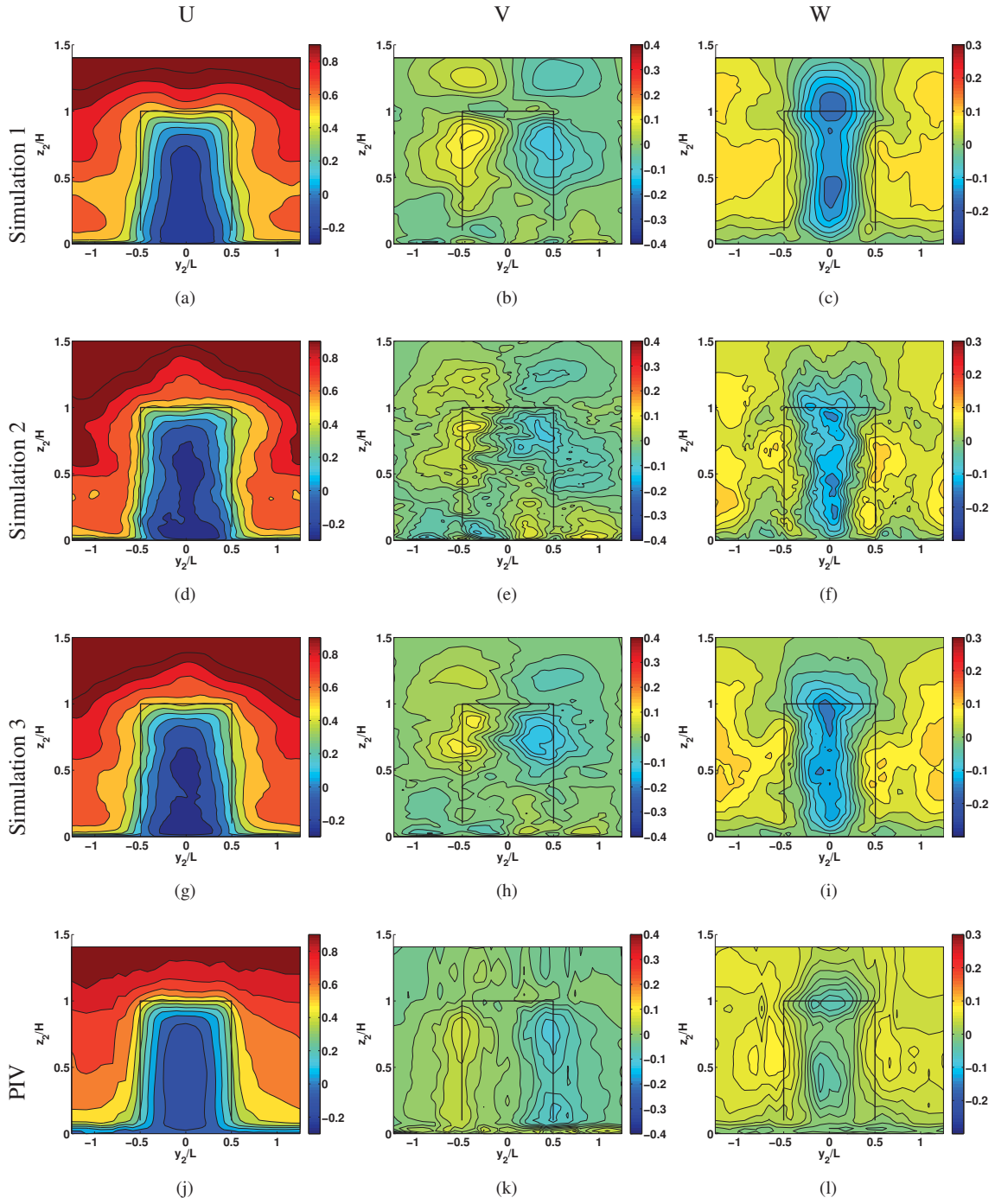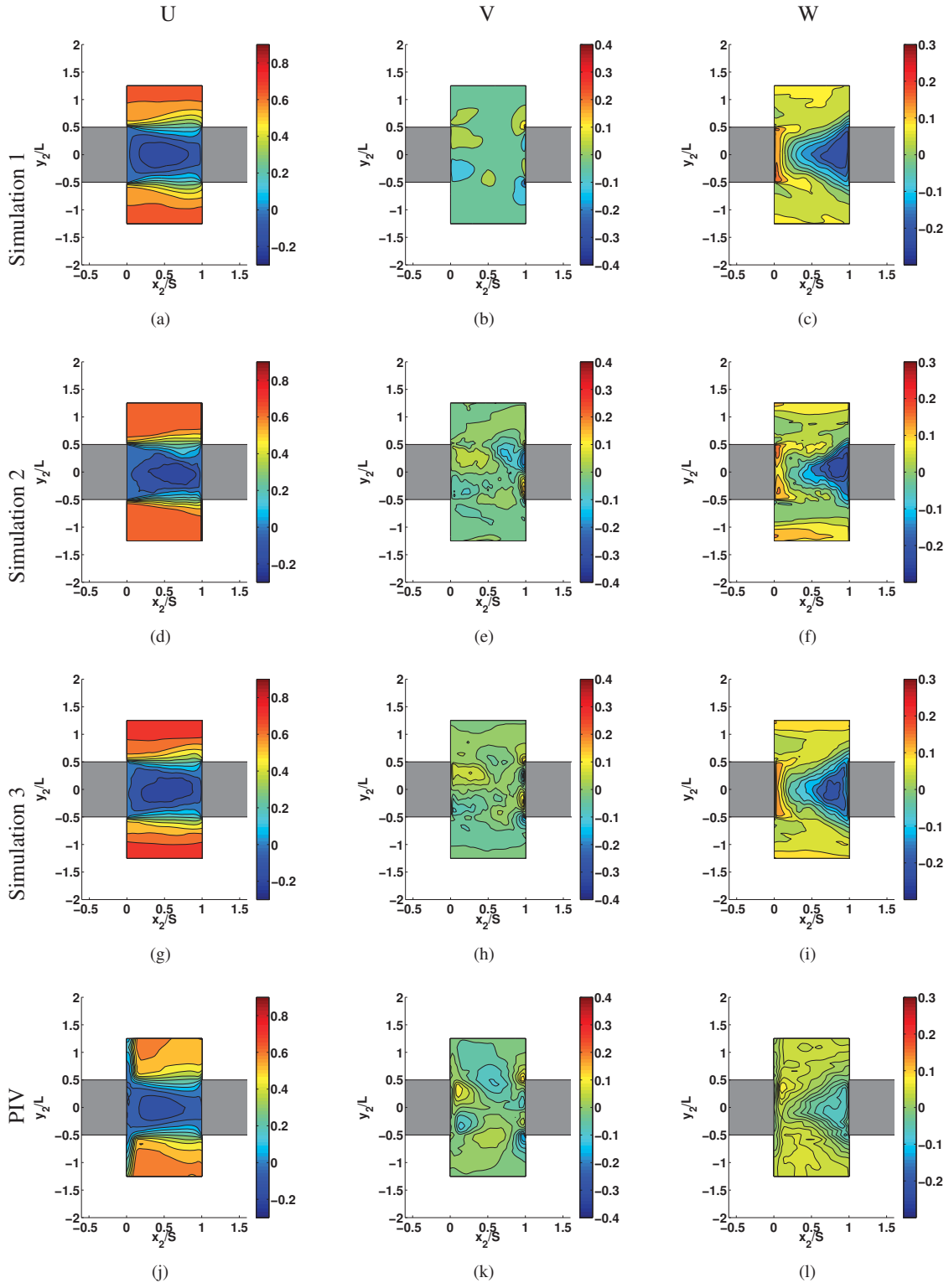
Figure 5.29: Comparison of mean velocity contours between spectral element simulations and PIV data on vertical plane X = 0.75.
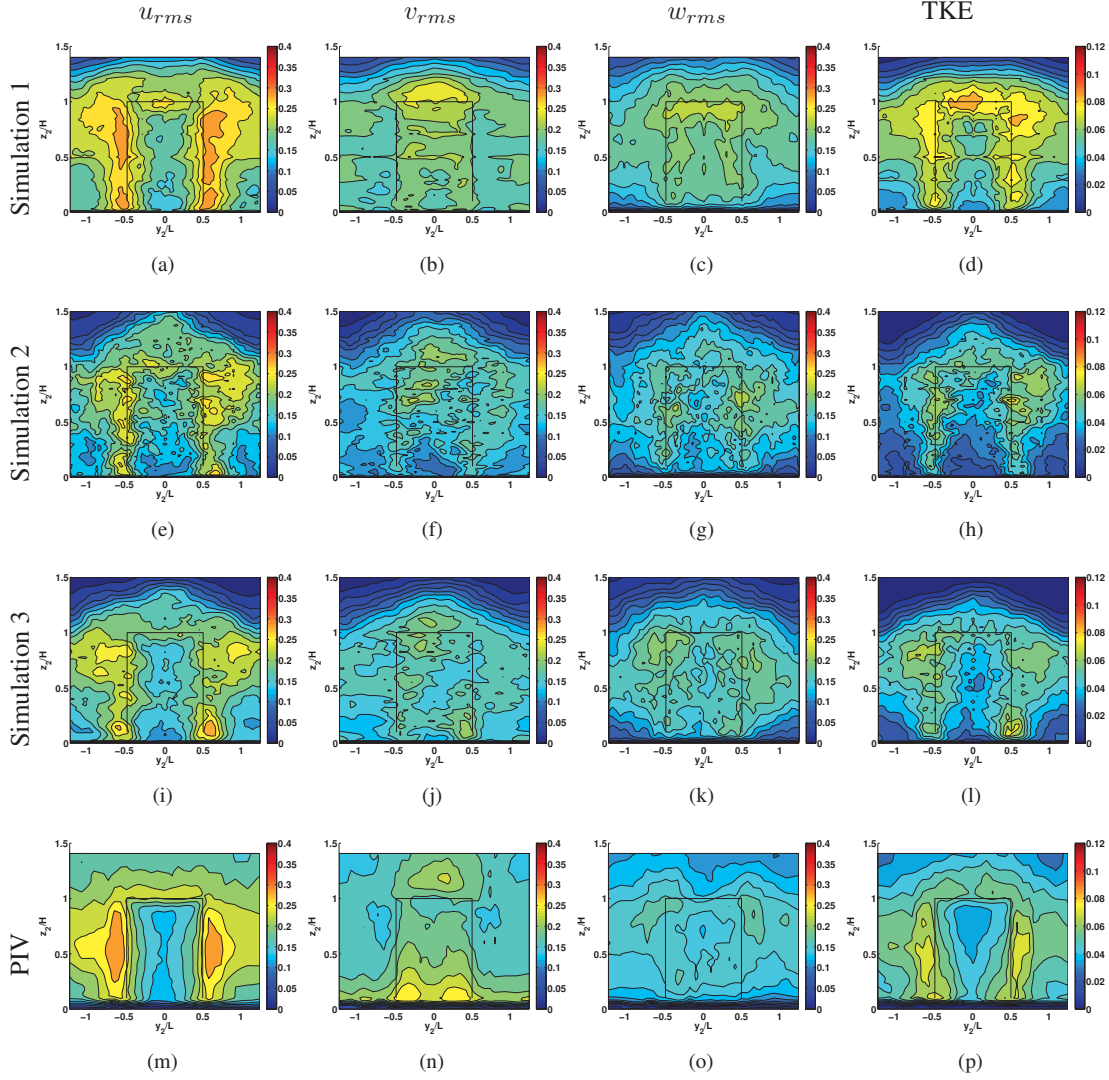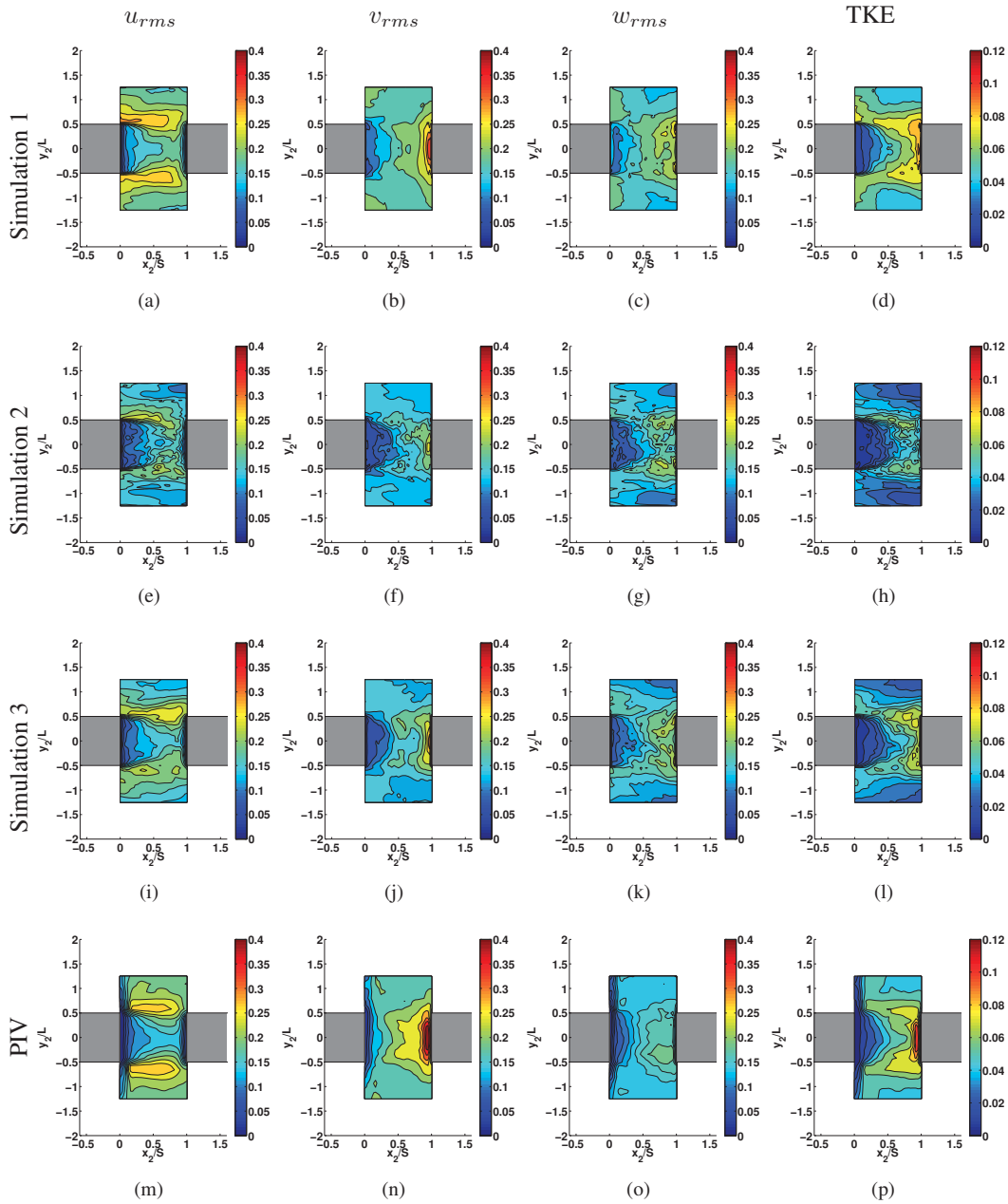
Figure 5.30: Comparison of root mean square velocity and turbulent kinetic energy contours between spectral element simulations and PIV data on vertical plane X = 0.75.
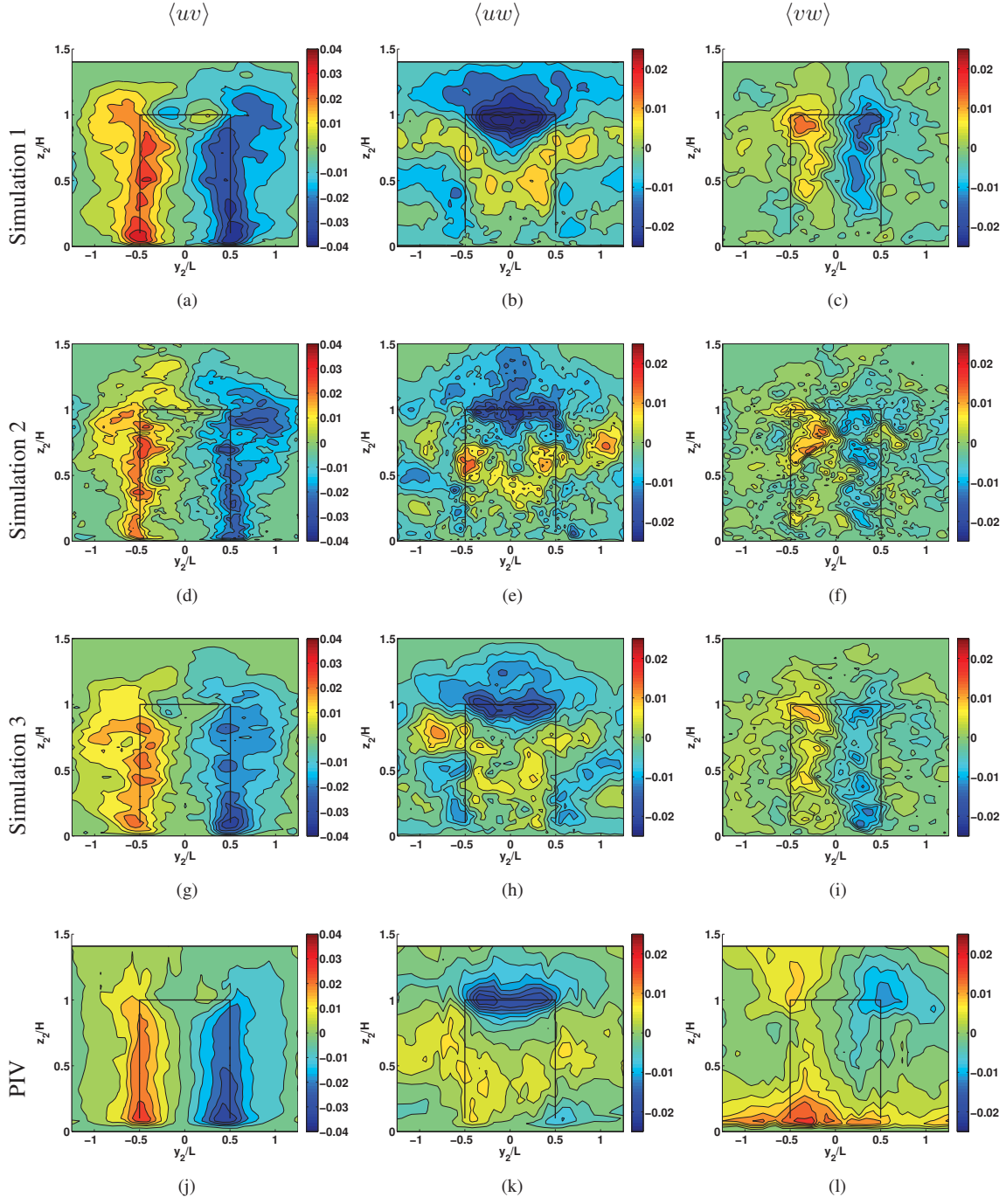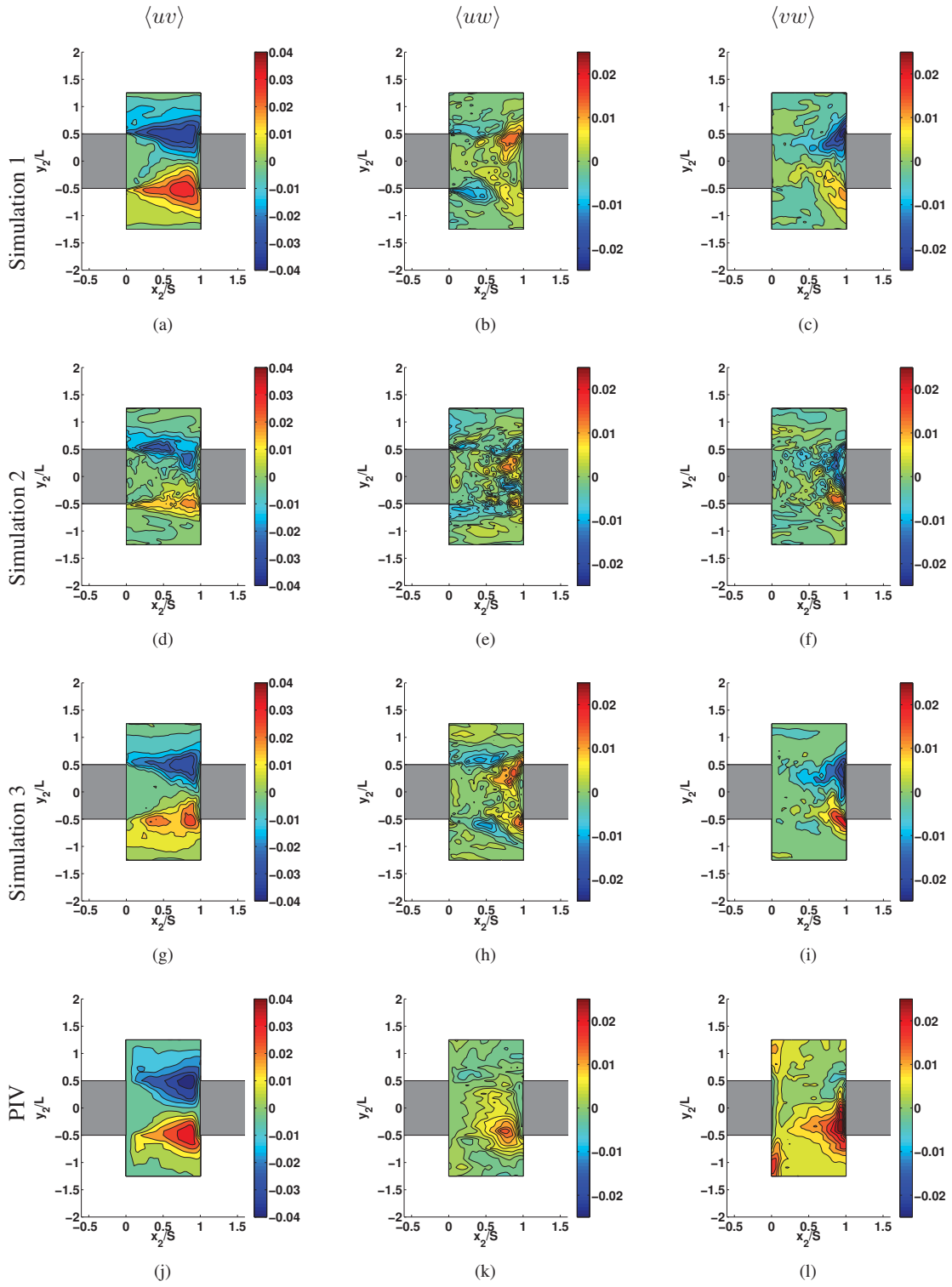
Figure 5.31: Comparison of Reynolds stress data between spectral element simulations and PIV data on vertical plane X = 0.75.
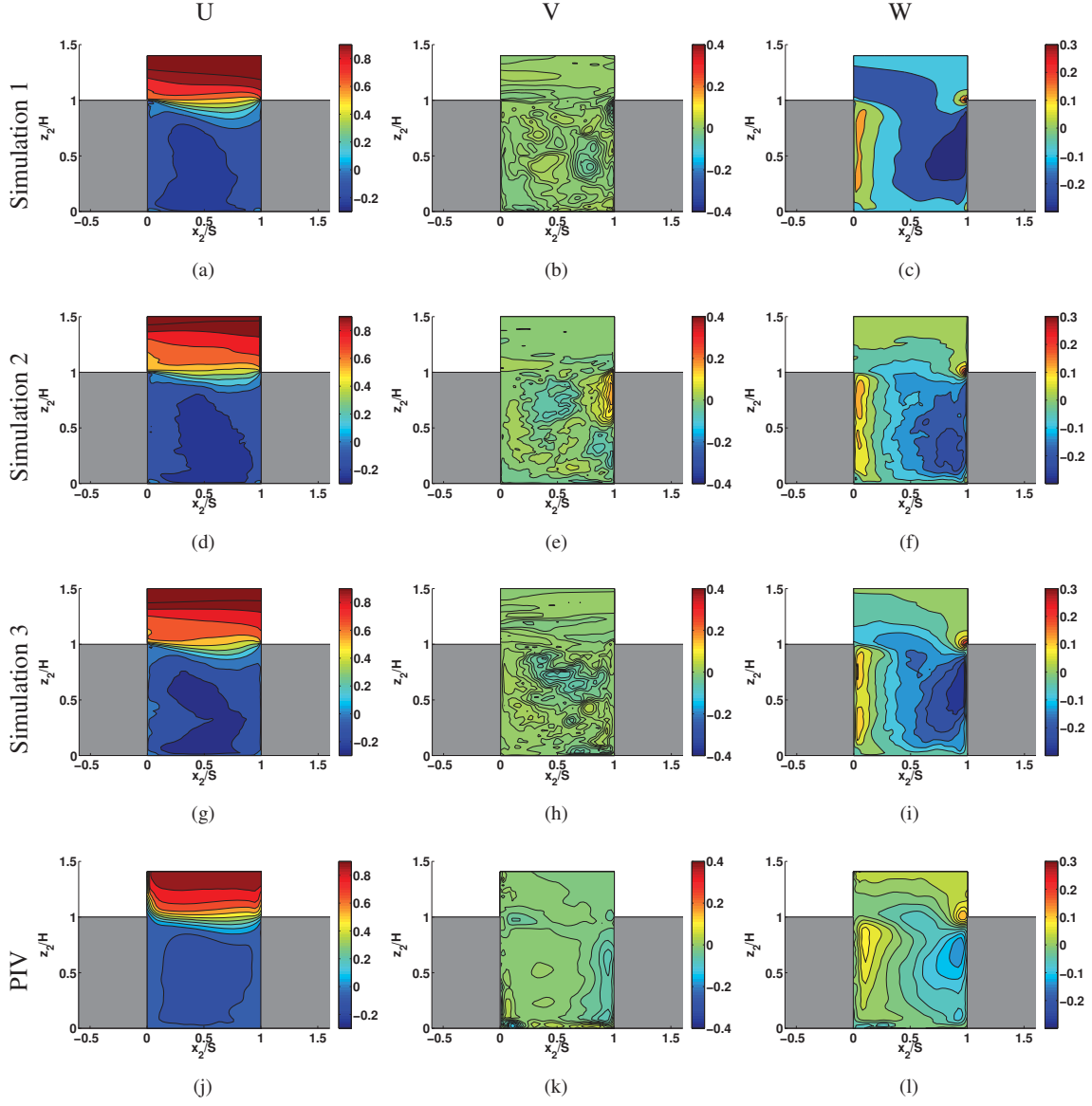
Figure 5.32: Comparison of mean velocity contours between spectral element simulations and PIV data on vertical plane Y = 1.25.
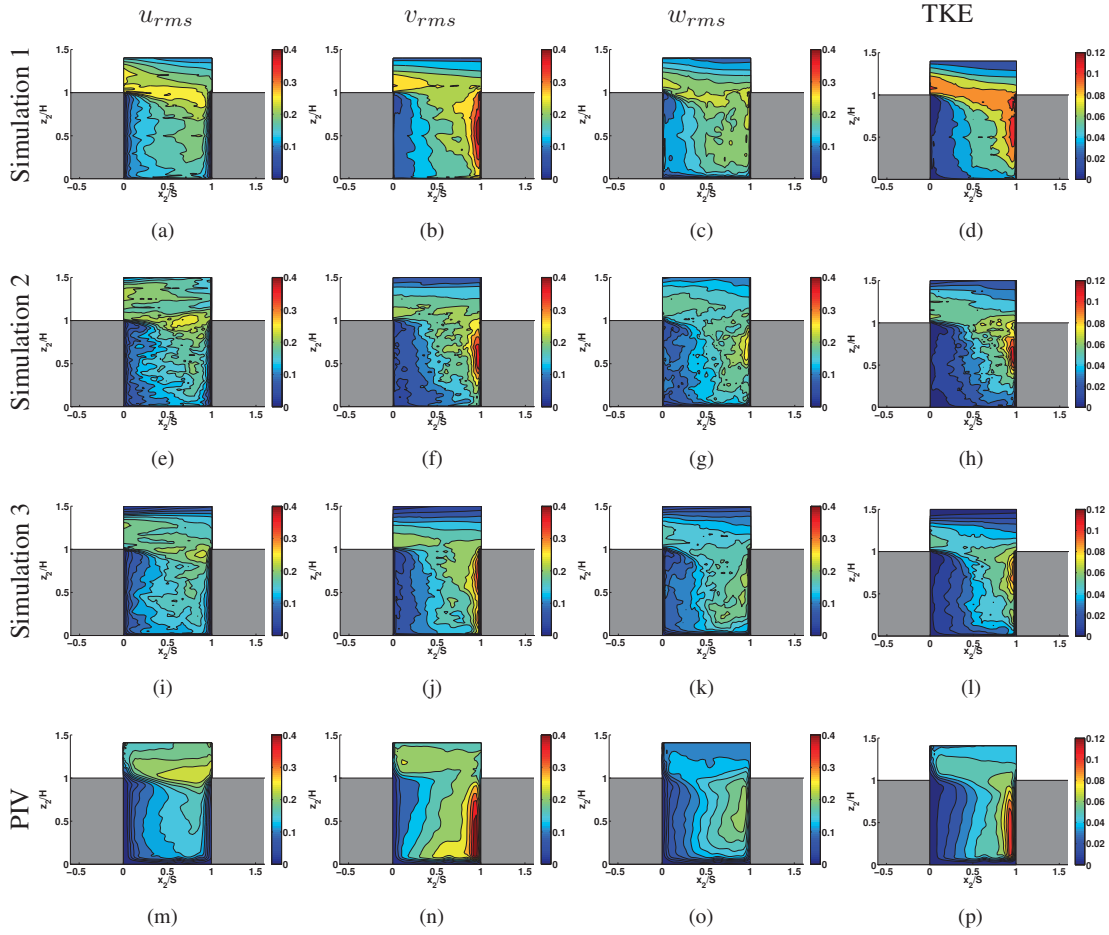
Figure 5.33: Comparison of root mean square velocity and turbulent kinetic energy contours between spectral element simulations and PIV data on vertical plane Y = 1.25.
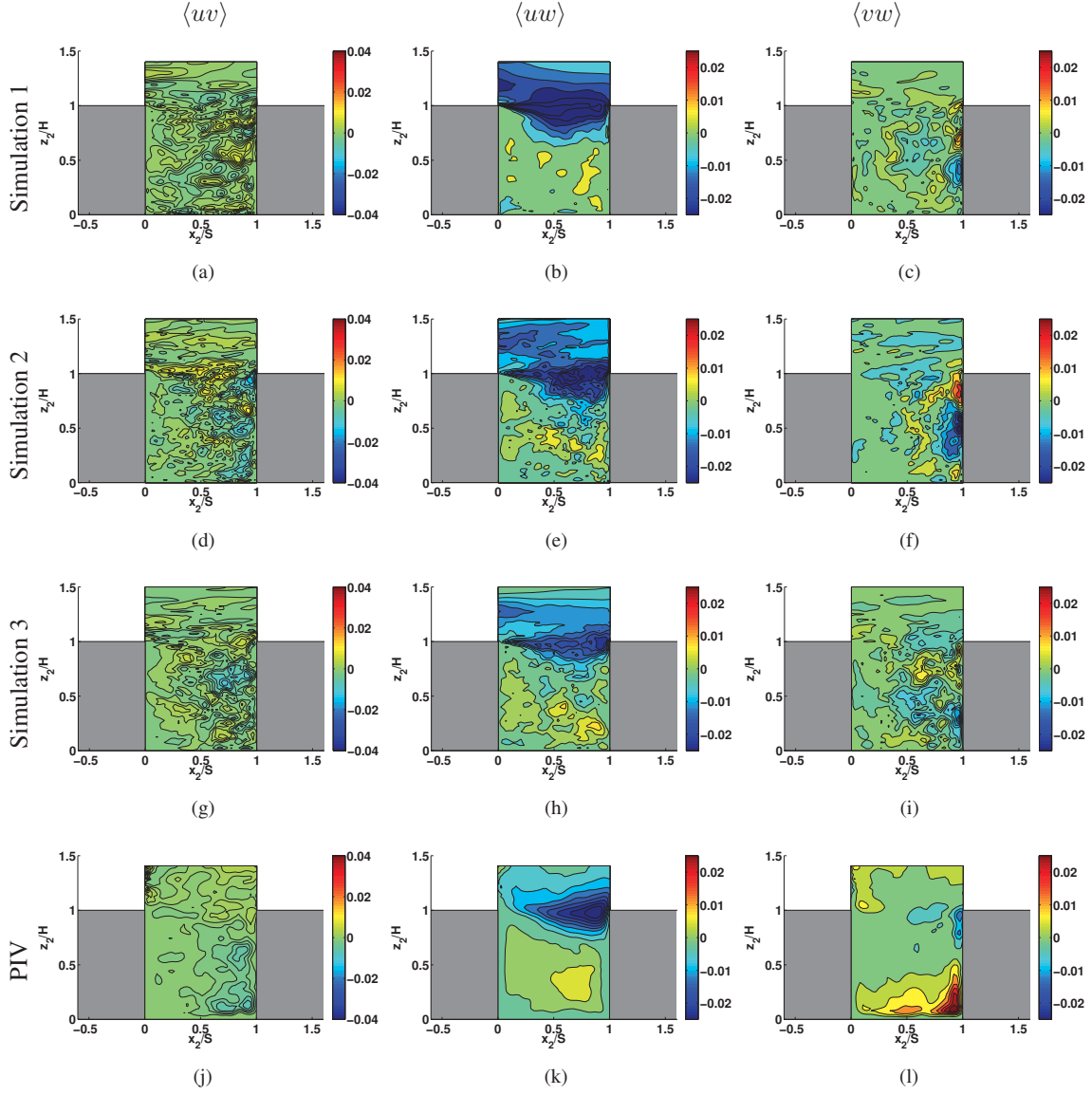
Figure 5.34: Comparison of Reynolds stress data between spectral element simulations and PIV data on vertical plane Y = 1.25.

Figure 5.35: Comparison of mean velocity contours between spectral element simulations and PIV data on vertical plane Z = 0.5.

Figure 5.36: Comparison of root mean square velocity and turbulent kinetic energy contours between spectral element simulations and PIV data on vertical plane $Z = 0.5$.

Figure 5.37: Comparison of Reynolds stress data between spectral element simulations and PIV data on vertical plane Z = 0.5.
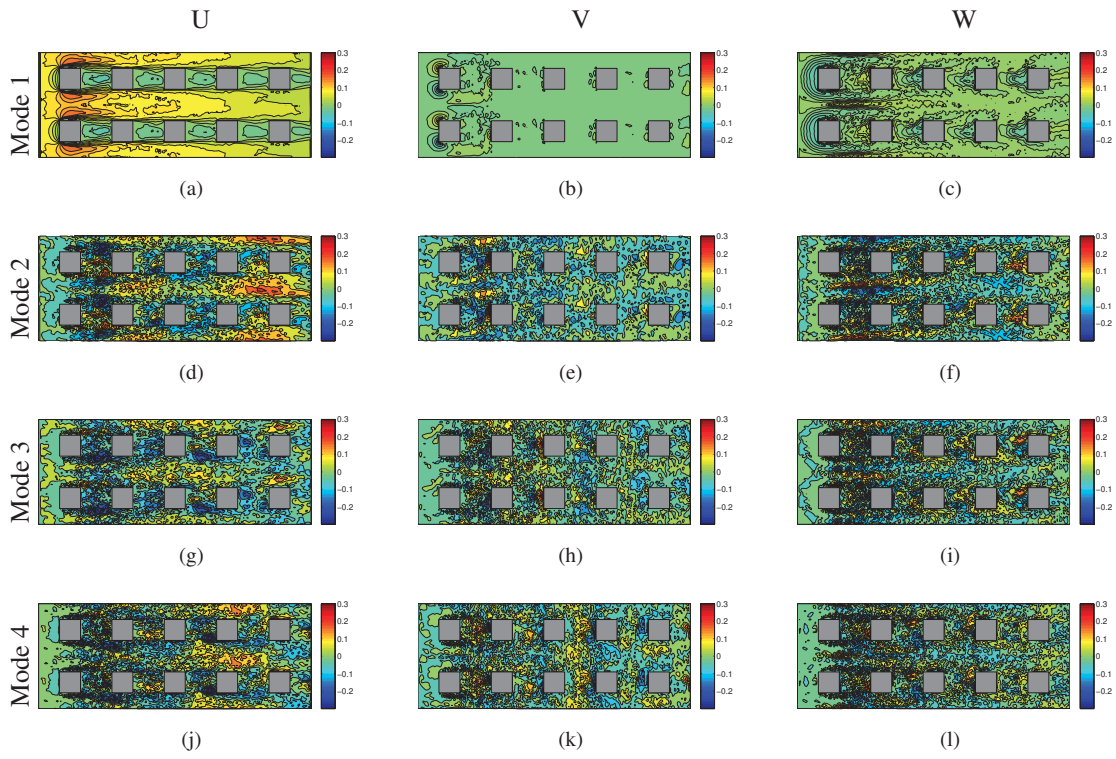
Figure 5.38: First four POD modes.
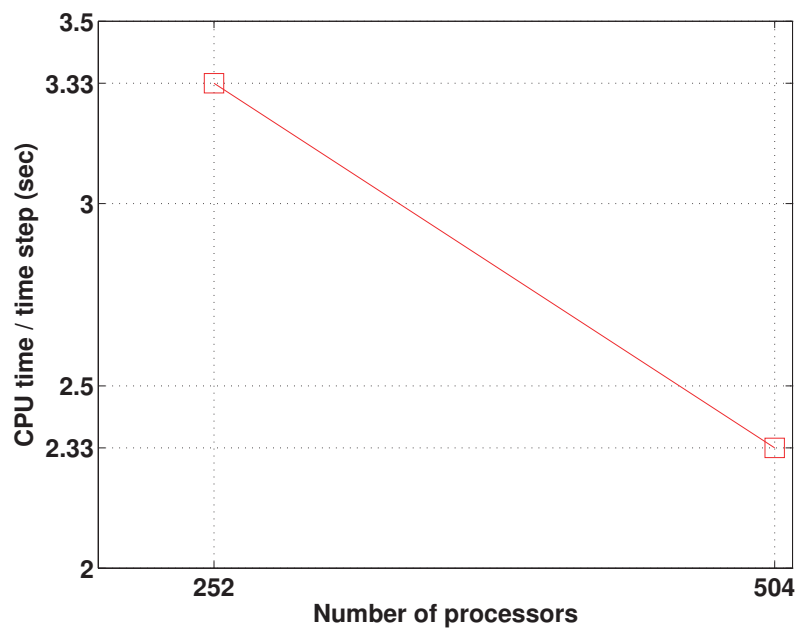
Figure 5.39: Scaling results for simulation 3 on NICS kraken.

Results and analysis

In this section, we present the results of the simulation. We define the coordinates $x_s = x - 11.0$, $y_s = y - 1.25$ and $z_s = z$. We use data along the slices $S_{y_1}(y = 1.25, y_s = 0.0, \frac{y}{h} = 1.25)$, $S_{z_1}(z = 0.5, z_s = 0.5, \frac{z}{h} = 0.25)$ and $S_{z_2}(z = 1.7, z_s = 1.7, \frac{z}{h} = 0.85)$ for our analysis. All statistics presented in this section are computed based on 80 seconds of data sampled at 50 Hz.

Figure 5.40 plots the mean velocity profiles along the midspan slice S_{y_1} for all four streets. The contour for U shows that the flow separates from the top of the first block and seems to reattach to the top of the second block. The region $\frac{Z}{H} > 1.3$ seems to be relatively unperturbed by the presence of the array. A strong streamwise velocity gradient exits in the shear layer region $0.8 < \frac{Z}{H} < 1.3$. The magnitude of U is significantly lower within the street and includes regions of reverse flow. Since the flow is symmetric along the mid-span plane, the spanwise component of velocity is negligible in this plane. The contour for W shows a strong downward draft on the windward side of each street and an upward draft on the leeward side of each street. These contours indicate the presence of a single large recirculation region for streets 2 through 4 which is expected for the skimming flow regime. A notable exception is street 1 which shows two large counter-rotating recirculation zones.

Figures 5.41 and 5.42 plot the mean velocity profiles along slices S_{z_1} and S_{z_2} respectively. In both cases, the magnitude of streamwise velocity is greatest at $\frac{y}{W} = 0$ and $\frac{y}{W} = 2.5$ respectively. We can also notice that the magnitude of this velocity decreases consistently as we move from street 1 to street 4. A region of reverse flow exists near the center of each street on slice S_{z_1}. The contour of V on slice S_{z_1} shows fluid being ejected from the street near the edges of the upstream block. This pattern is consistent with the structure of the leg of a an arch vortex. The contours for W on slices S_{z_2} indicate a strong downdraft in the windward region of each street and an updraft in the leeward region of each street consistent with earlier observations. Also noticeable is the decrease in the magnitude of the downward and upward drafts as we move from street 1 to street 4. Similar patterns are observed for S_{z_1} for streets 2 through 4. However the W velocity contour on slice S_{z_2} seems to indicate a second counter-rotating recirculation zone close to the wall consistent with the earlier observations.
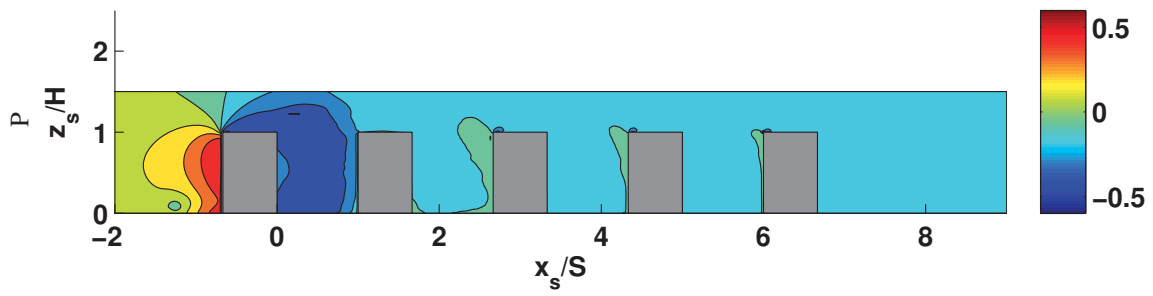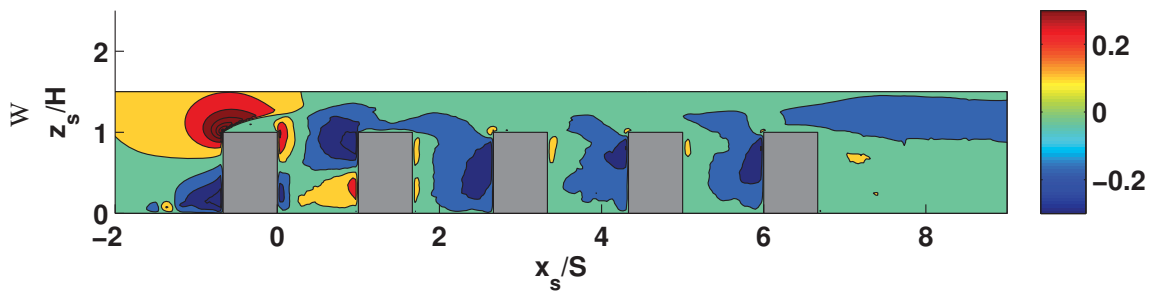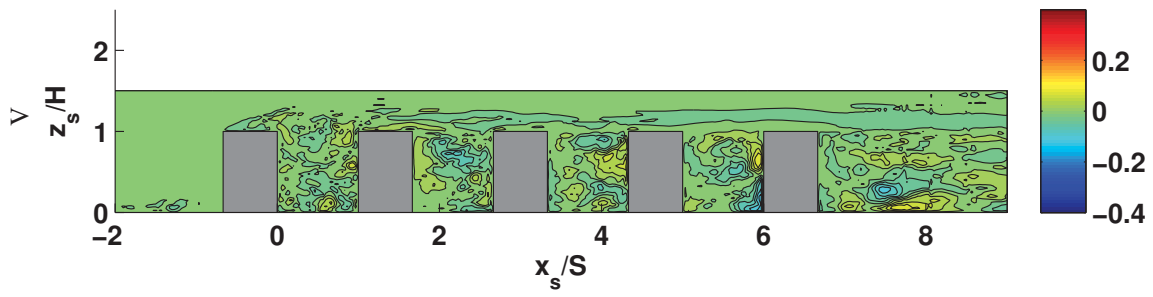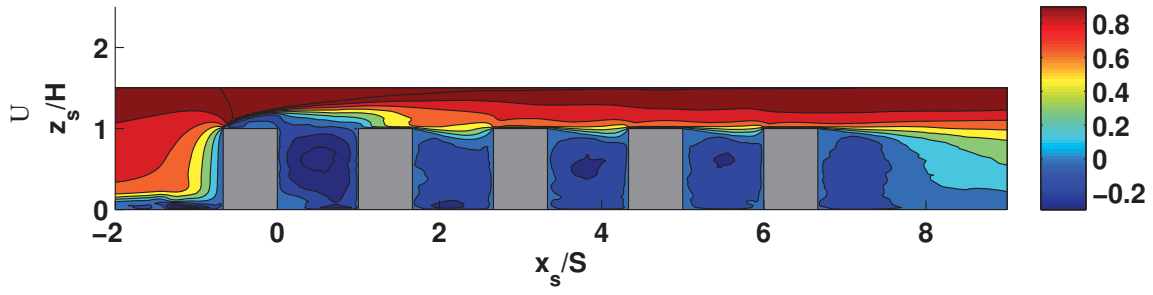
Figure 5.40: Mean velocity and pressure contours on slice S_{y_1}.

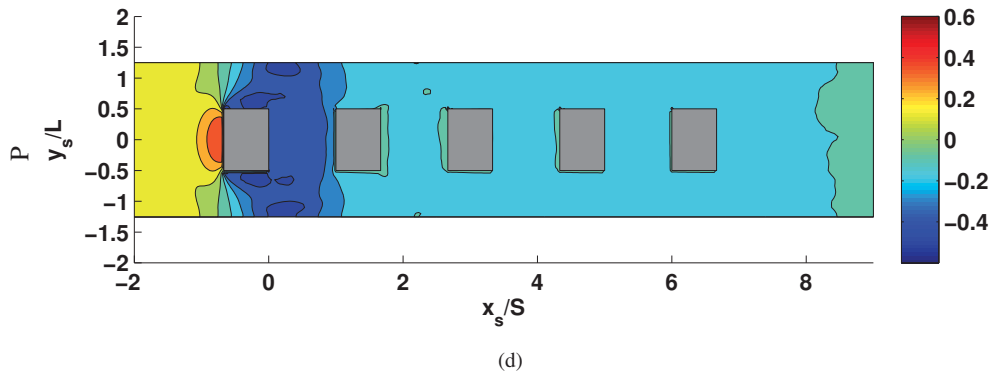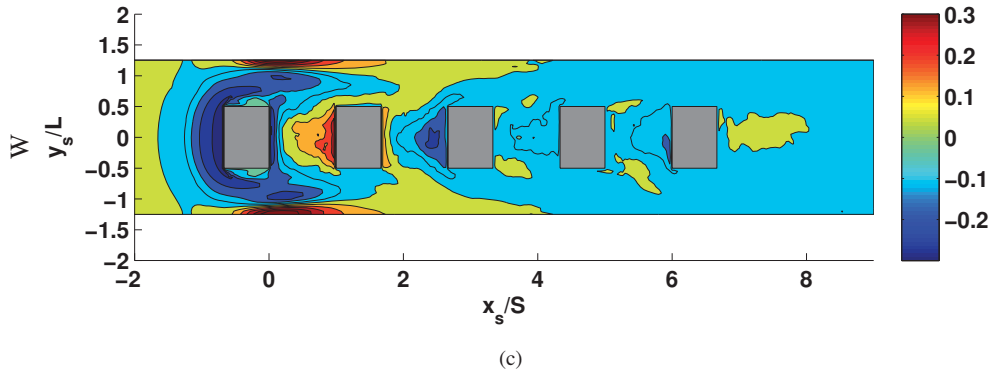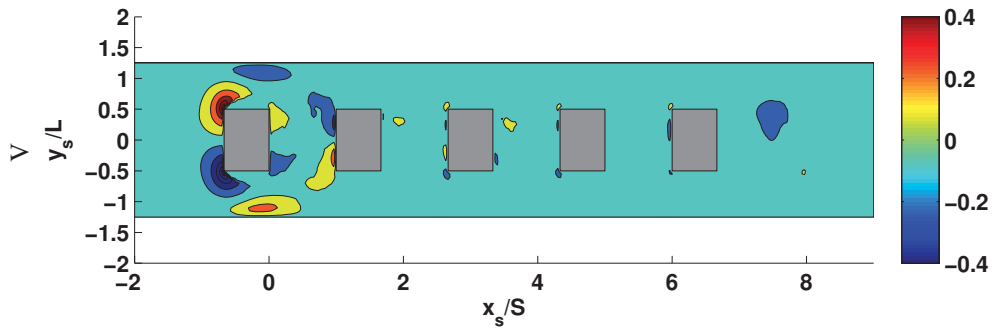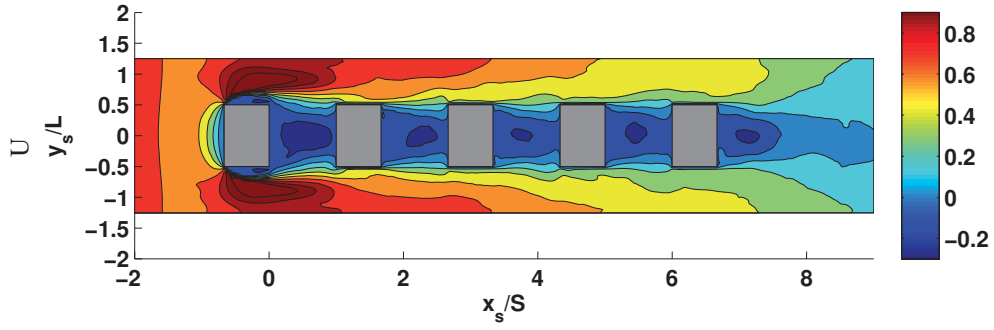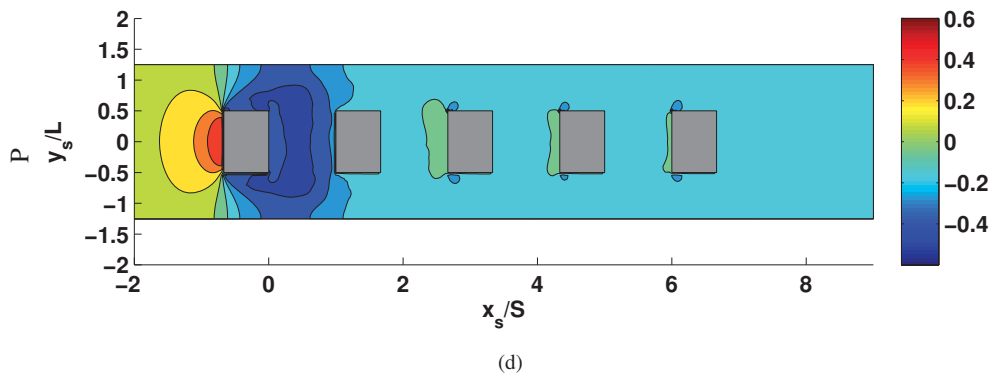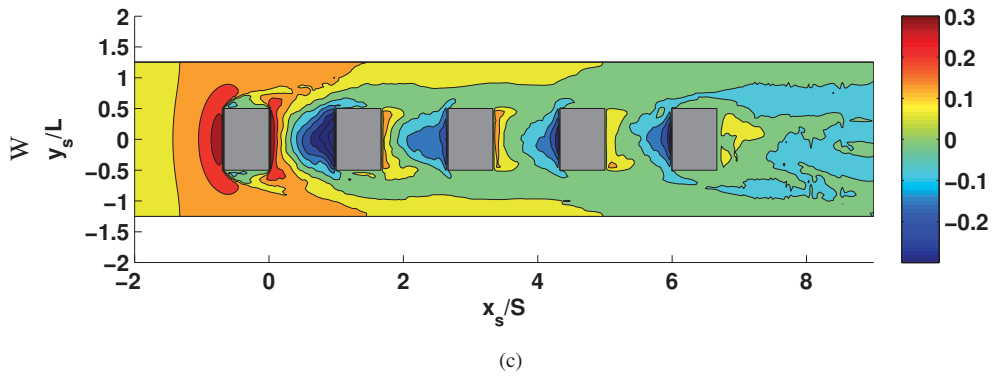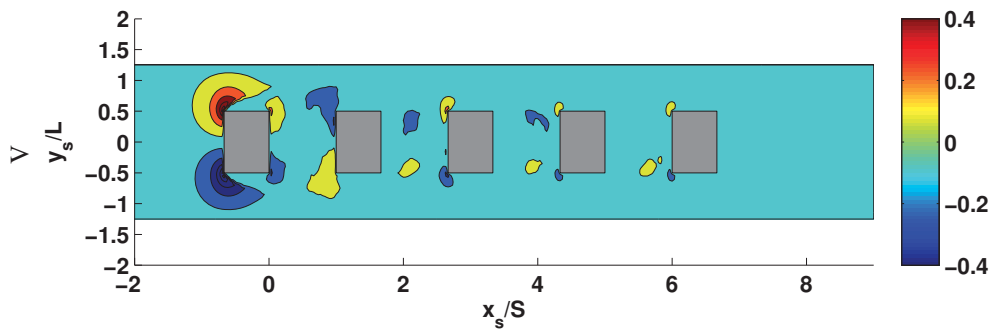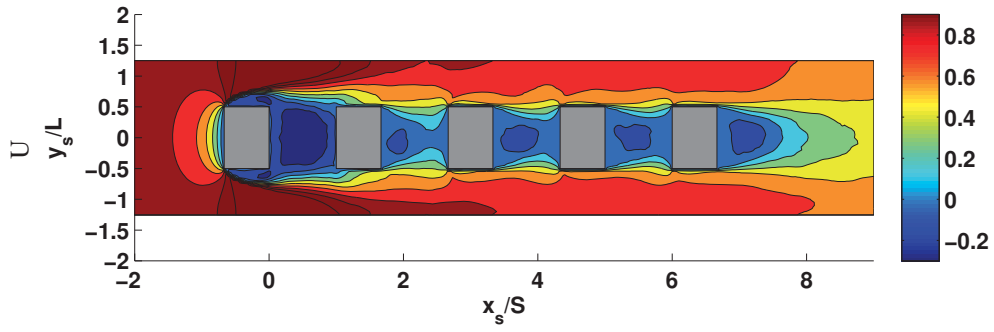Figure 5.41: Mean velocity and pressure contours on slice S_{z_1}.
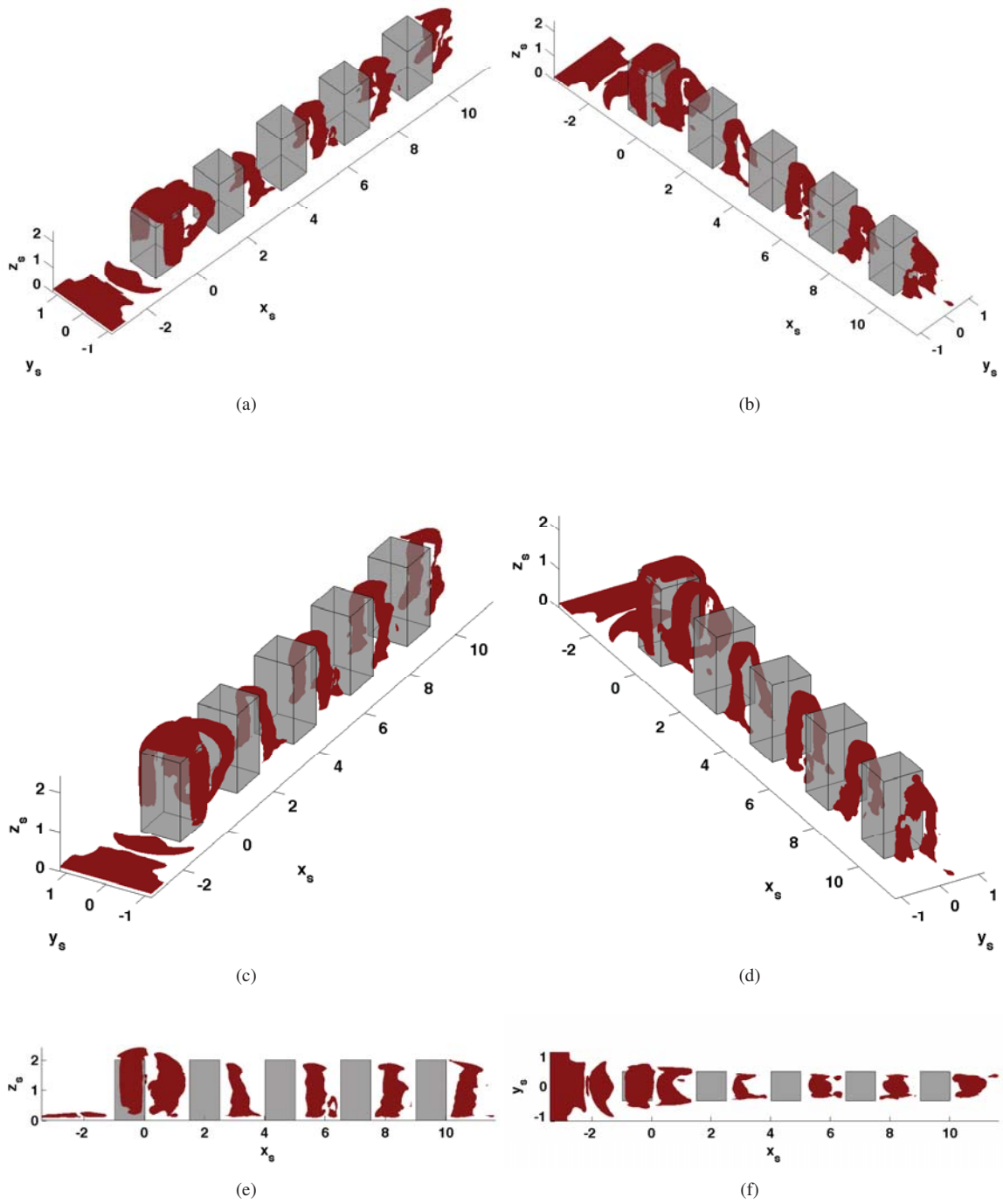
Figure 5.42: Mean velocity and pressure contours on slice S_{z_2}.

Figure 5.43 plots the iso-contours of Γ_1 (Eq. 4.2) indicating the locations of cores of arch vortices in the urban street canyon for $0°$ angle of incidence. A threshold value of 0.4 is used for generating these plots. We can see that for zero angle of incidence, arch vortices are located symmetrically with respect to slice S_{y_1}. We can also notice the horse-shoe vortex in front of the first block and vortices on top and sides of the first block.

Figure 5.43: Isocontours of Γ_1 as defined in Chapter 4 (Eq. 4.2) indicating the locations of cores of arch vortices in the urban street canyon for $0°$ angle of incidence.

Figure 5.44 plots the u_{rms}, v_{rms}, w_{rms} and turbulent kinetic energy contours on slice S_{y_1} for all four streets. We can see that the intensity of turbulent kinetic energy is high in the roof shear layer region and in the windward side of each street just upstream of the downstream block. There is a steady decrease in the magnitude of the turbulent kinetic energy as we move from street 1 to street 4. In the shear layer, the primary contribution to the turbulent kinetic energy comes from the streamwise component(u_{rms}) of velocity fluctuations with a smaller contribution from the wall normal component (w_{rms}). On the windward side of the street, the spanwise component of velocity fluctuations (v_{rms}) is the major contributor to the turbulent kinetic energy with a minor contribution from the wall normal component (w_{rms}) of fluctuating velocity.

Figures 5.45 and 5.46 plot the contours of u_{rms}, v_{rms}, w_{rms} and turbulent kinetic energy on slices S_{z_1} and S_{z_2} respectively. In this case, the intensity of turbulent kinetic energy is high in the side shear layers and on the windward side of each street. The intensity of turbulent kinetic energy decreases rapidly as we move from street 1 to street 4. The streamwise component of velocity fluctuations (u_{rms}) is the major contributor to turbulent kinetic energy in the side shear layers whereas the spanwise component of velocity fluctuations (v_{rms}) is the biggest contributor to turbulent kinetic energy in the windward side of of each street.

Finally, Figures 5.47, 5.48 and 5.49 plot contours of Reynolds stresses on slices S_{y_1}, S_{z_1} and S_{z_2} respectively. On slice S_{y_1} the $<uw>$ component of the Reynolds stress tensor is dominant in the top shear layer. The Reynolds stresses are small in other regions. On slices S_{z_1} and S_{z_2}, the $<uv>$ component of the Reynolds stress tensor is dominant in the side shear layers. The strength of the shear layer decreases steadily as we move from street 1 to street 4.
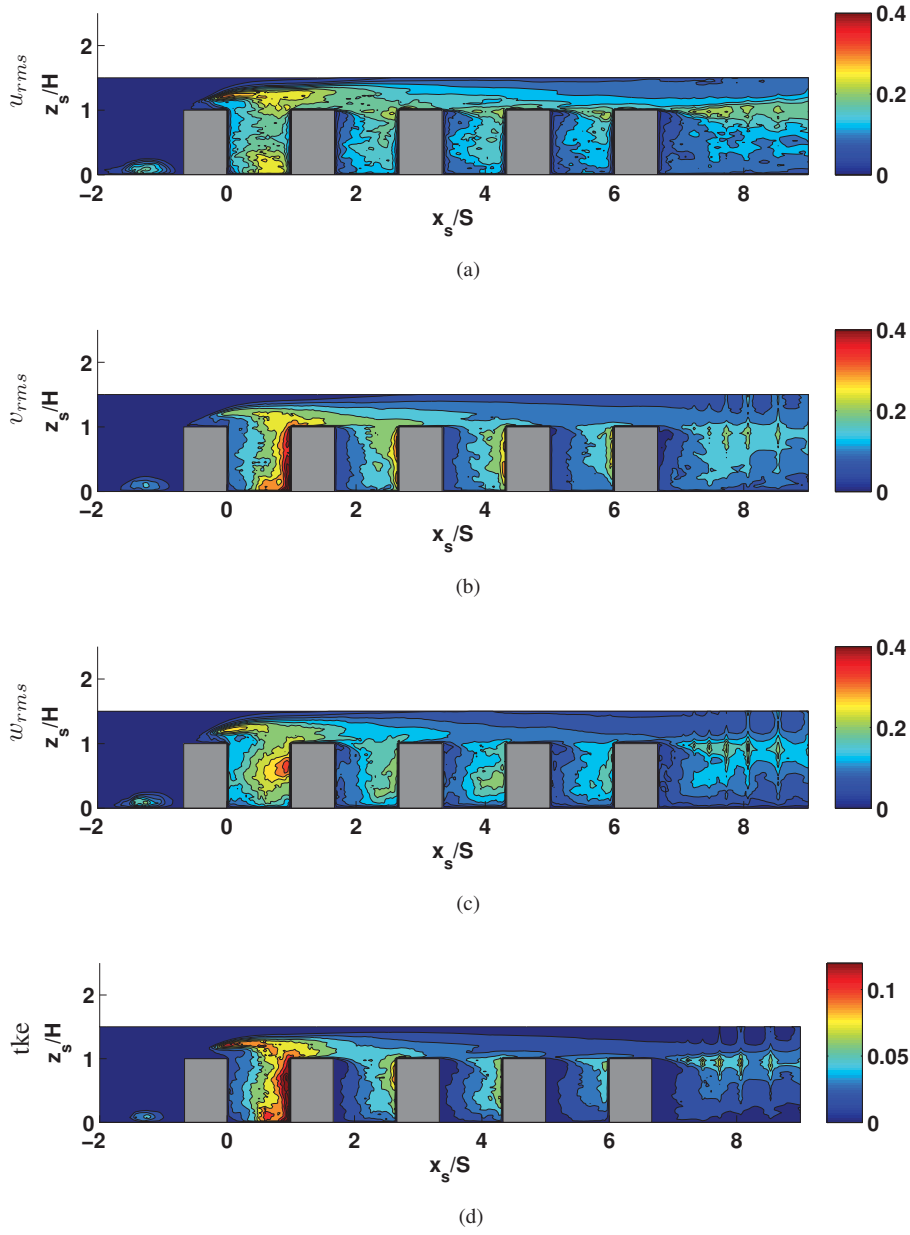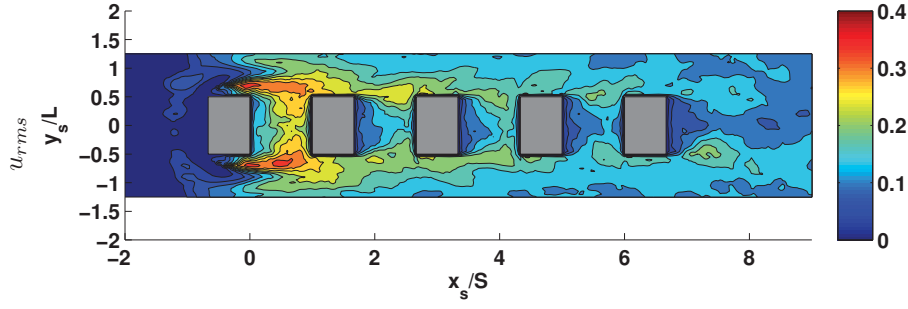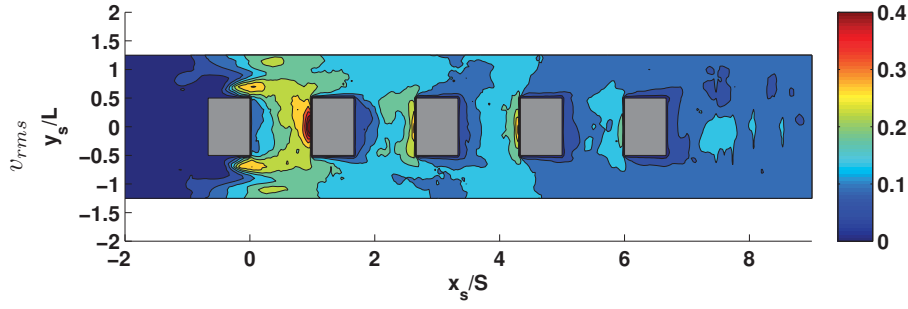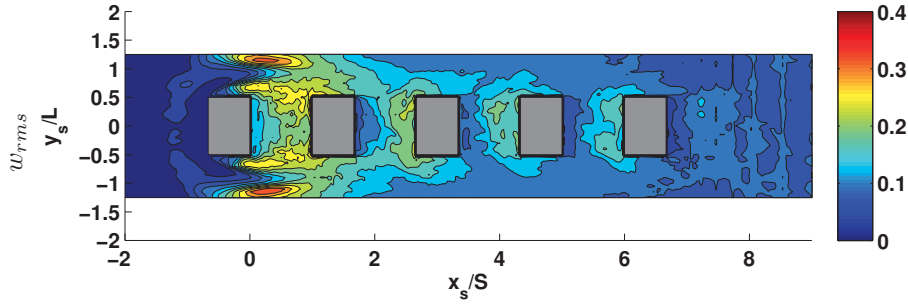
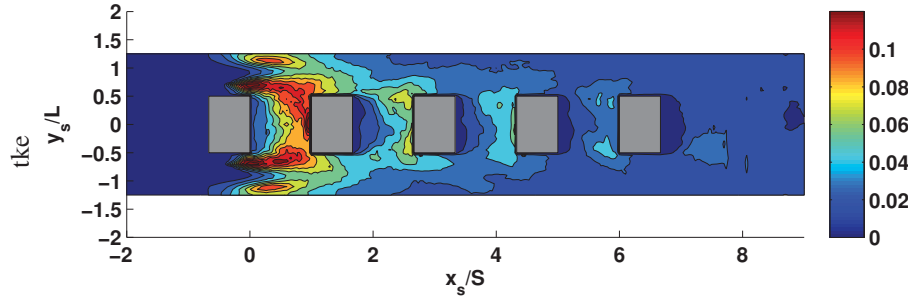Figure 5.44: u_{rms}, v_{rms}, w_{rms} and turbulent kinetic energy contours on slice S_{y_1}.

106
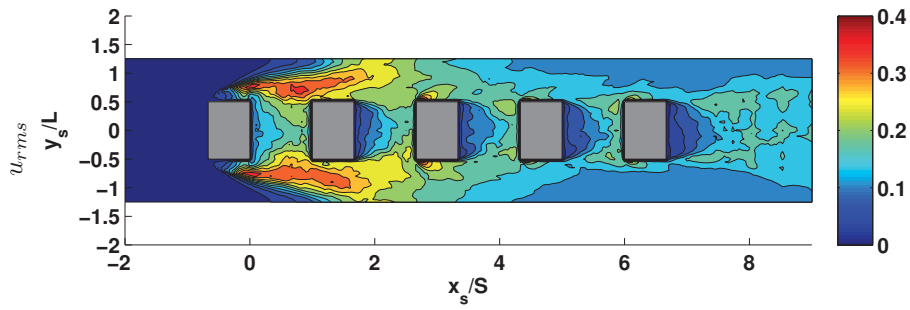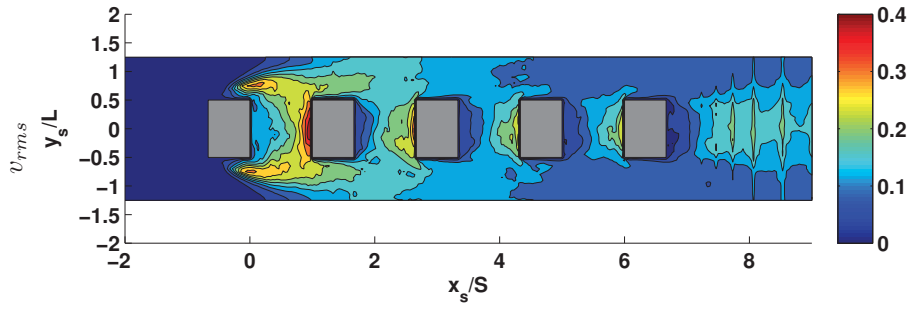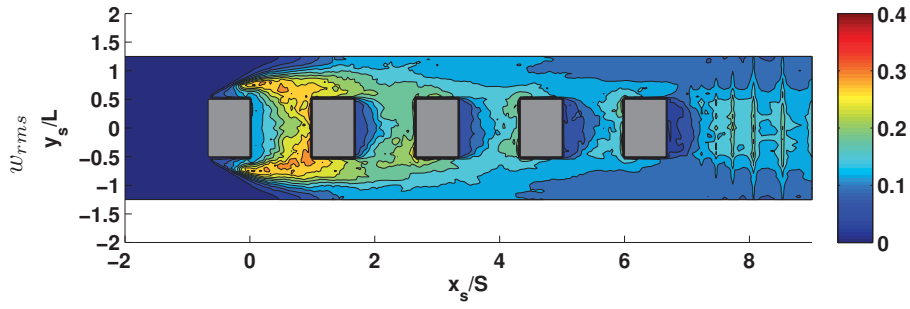
Figure 5.45: u_{rms}, v_{rms}, w_{rms} and turbulent kinetic energy contours on slice S_{z_1}.
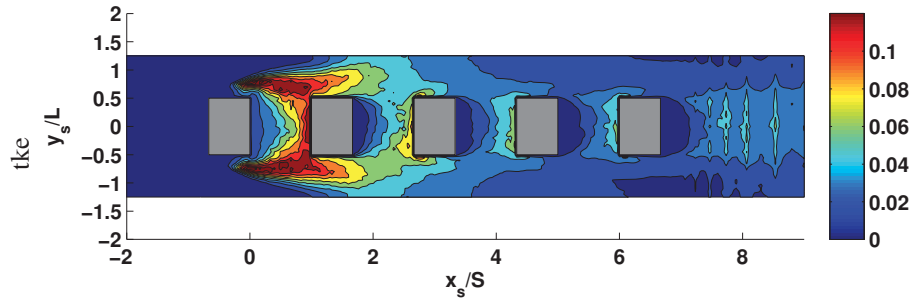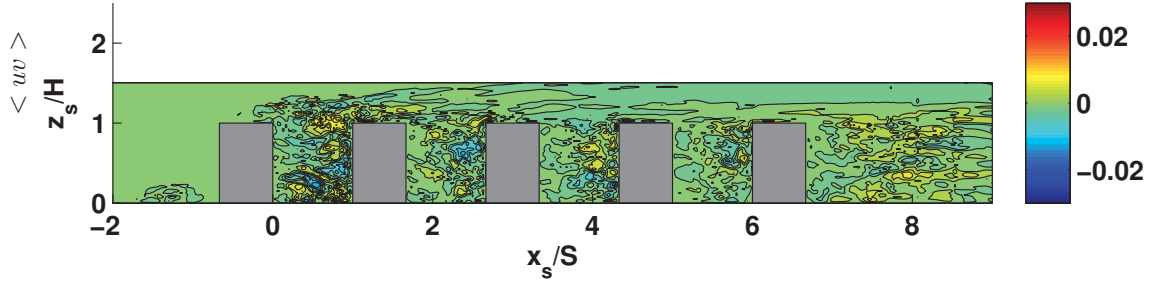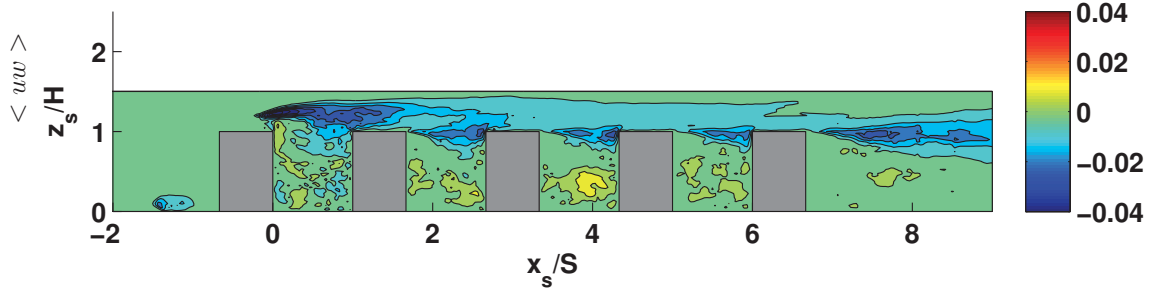
Figure 5.46: u_{rms}, v_{rms}, w_{rms} and turbulent kinetic energy contours on slice S_{z_2}.
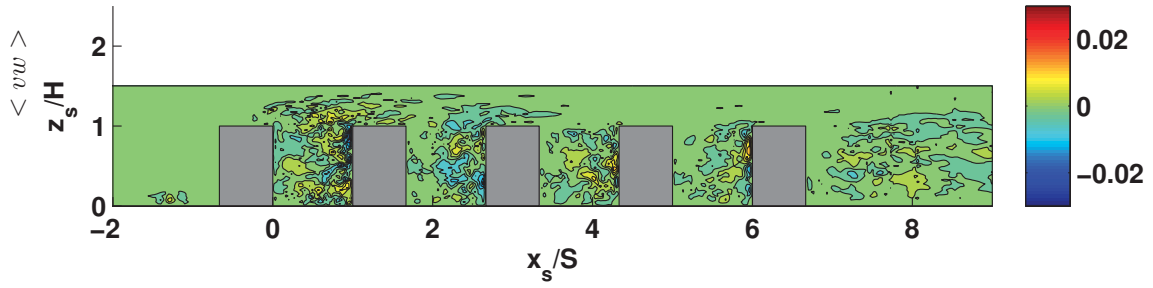
Figure 5.47: Contours of $\langle uv \rangle$, $\langle uw \rangle$ and $\langle vw \rangle$ on slice S_{y_1}.

Figure 5.48: Contours of $\langle uv \rangle$, $\langle uw \rangle$ and $\langle vw \rangle$ on slice S_{z_1}.

110

Figure 5.49: Contours of $\langle uv \rangle$, $\langle uw \rangle$ and $\langle vw \rangle$ on slice S_{z_2}.

111

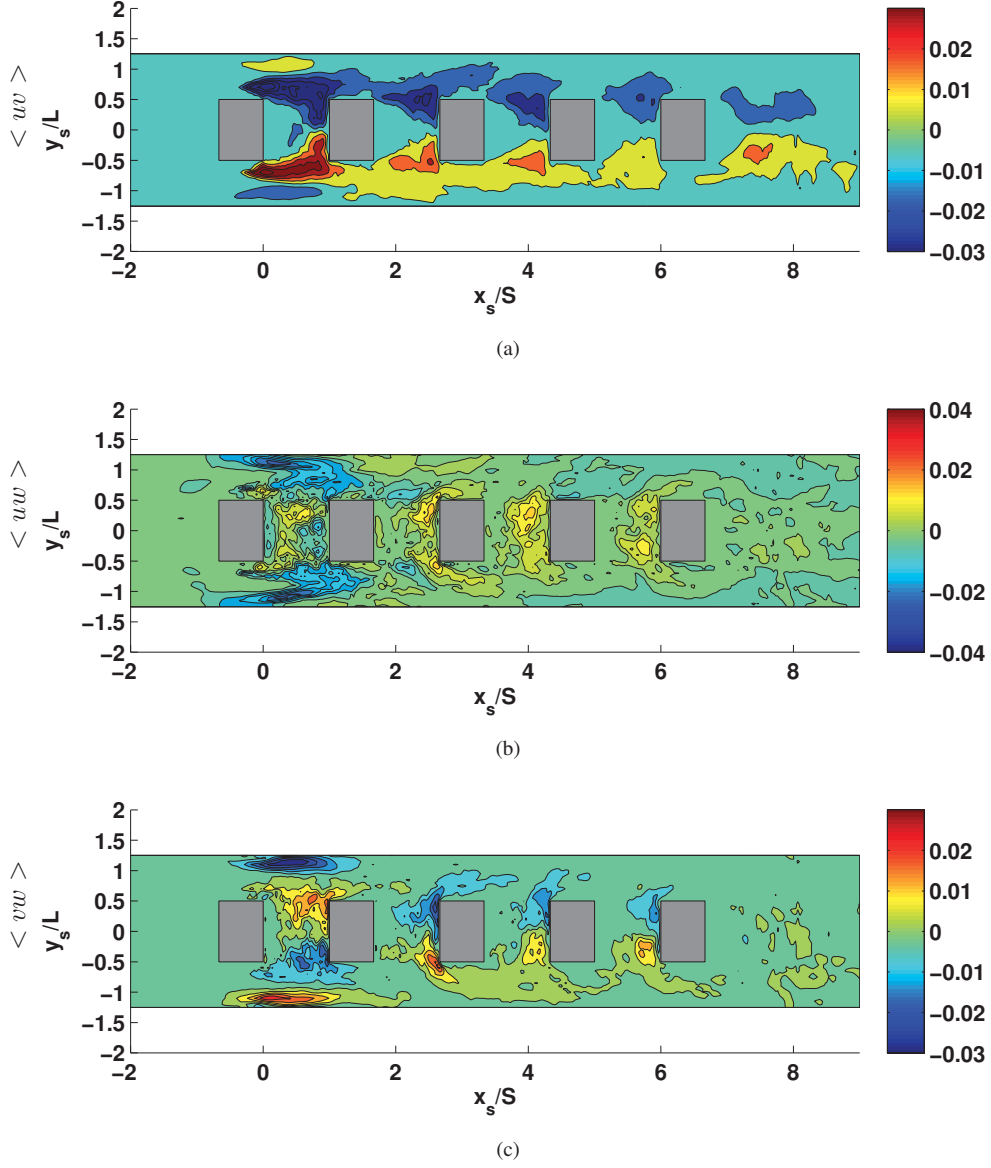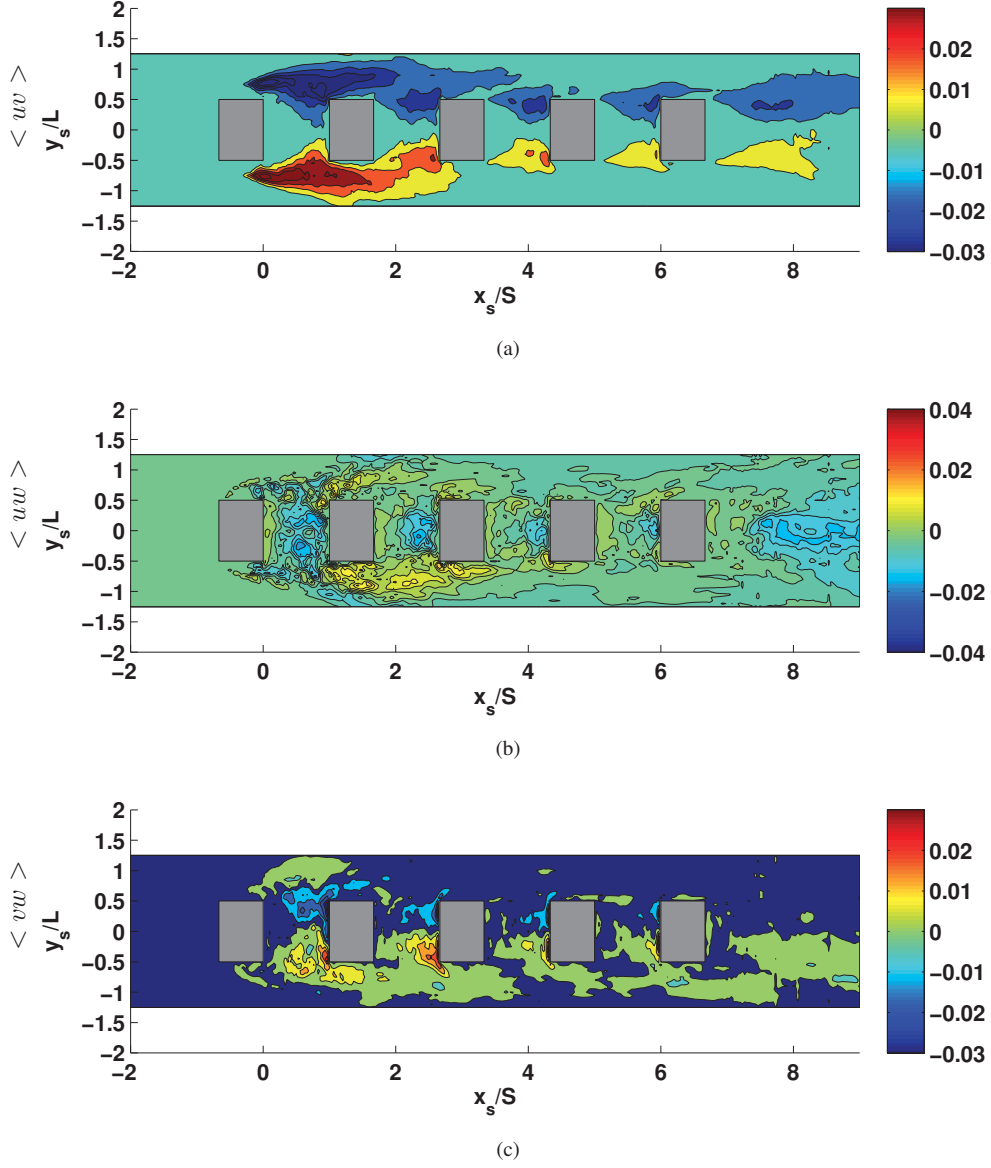### 5.2.3 Numerical simulation of the urban boundary layer at $15°$ angle of incidence

For this simulation, the domain consists of the full 7×5 array of blocks with $H/W = 2$, $S/W = 1.5$. The flow is incident at an angle of $15°$ to the array. The Reynolds number (Re_H), based on block height and inlet velocity at block height, is $Re_H = U_H H/\nu = 6283$. The inflow boundary is located approximately 10 block widths upstream of the first block and the outflow boundary is located 40 block widths downstream of the last block. A symmetry boundary is condition is used on the top and is located at 17 block widths away from the bottom wall. A wall boundary condition is used in the spanwise direction. These walls are about 16 block widths away from the outermost block. Inlet velocity profiles obtained from the hotwire data provide the inlet boundary conditions for the simulation. 152936 spectral elements with an eighth-order approximation within each spectral element are used for this simulation. This corresponds to about 111 million degrees of freedom. The backward difference scheme is used for diffusion terms and extrapolation is used for nonlinear terms. De-aliasing and low pass filtering is used for stabilizing the simulation. This simulation is run on the MIRA supercomputer at ALCF. 8192 cores with two threads per core are used for this simulation. This corresponds to 16384 processors. The code scales to about 10,000 degrees of freedom per processor. A cross-section of the mesh used for this simulation is shown in figure 5.50. This simulation is still in progress and the statistics presented here are based on 6.2 seconds sampled at 20 Hz. While this sample size is not sufficient to compute good quality statistics, we can see some of the basic changes in flow structure for non-zero angle of incidence.

Figure 5.51 plots the mean velocity profiles along the midspan slice S_{y_1} for all four streets. The contour for U shows that the size of the shear layer region is larger for this case compared to $0°$ angle of incidence. The contour for spanwise velocity V is significantly different from the $0°$-angle of incidence case. We can see a strong channeling effect in the windward region of each street. The flow is from the positive y-axis to the negative y-axis. The contour for W shows a downward draft on the windward side of each street and an upward draft on the leeward side of each street. This is similar to the $0°$-angle of incidence case.
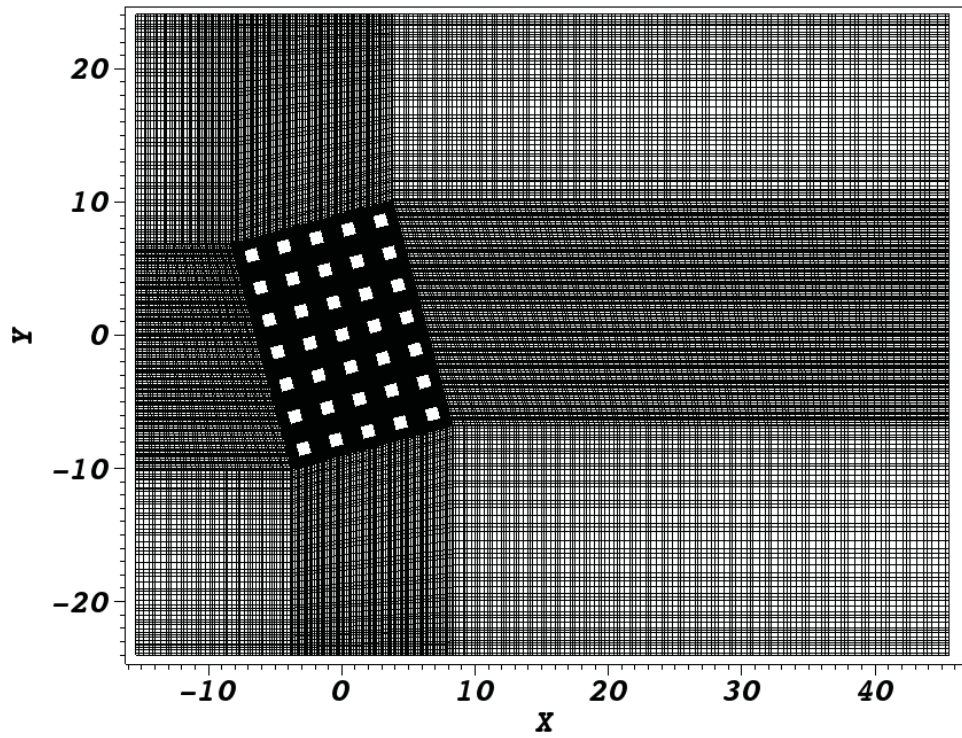
(a)

Figure 5.50: Cross-section of mesh along slice S_{z_1} .
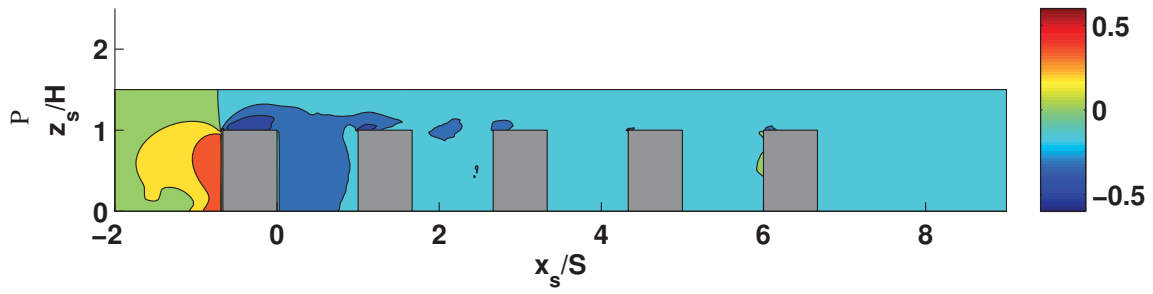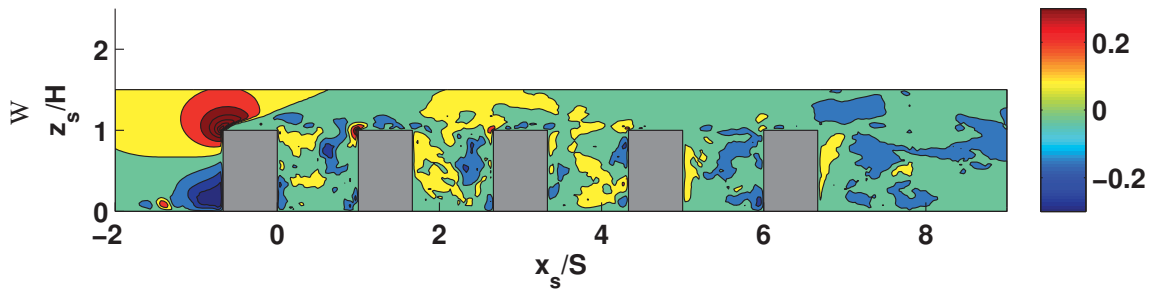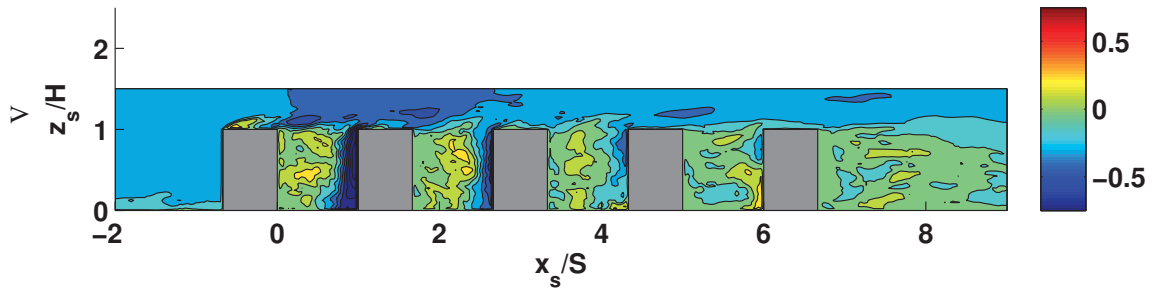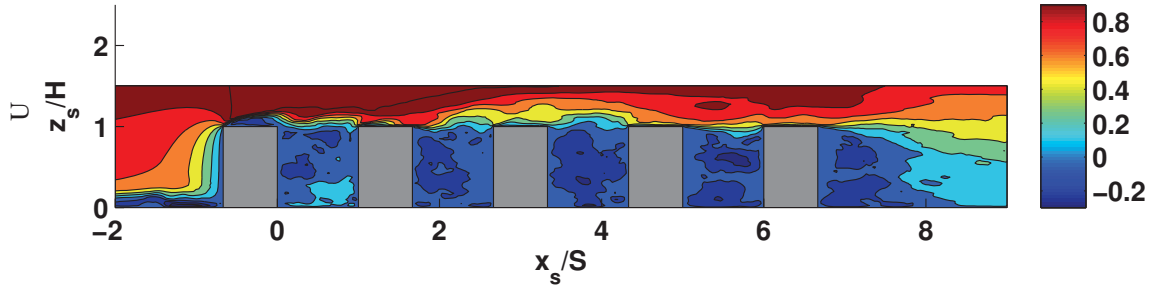
Figure 5.51: Mean velocity and pressure contours on slice S_{y_1} for $15°$ angle of incidence.

Figures 5.52 and 5.53 plot the mean velocity profiles along slices S_{z_1} and S_{z_2} respectively. In both cases, the streamwise velocity distribution loses symmetry with respect to slice S_{y_1}. The spanwise velocity component V is strong in the windward region of the street and its magnitude reduces from street 1 to street 4. This loss of symmetry is also noticed for the W component.

Figure 5.52: Mean velocity and pressure contours on slice S_{z_1} for $15°$ angle of incidence.

Figure 5.53: Mean velocity and pressure contours on slice S_{z_2} for $15°$ angle of incidence.

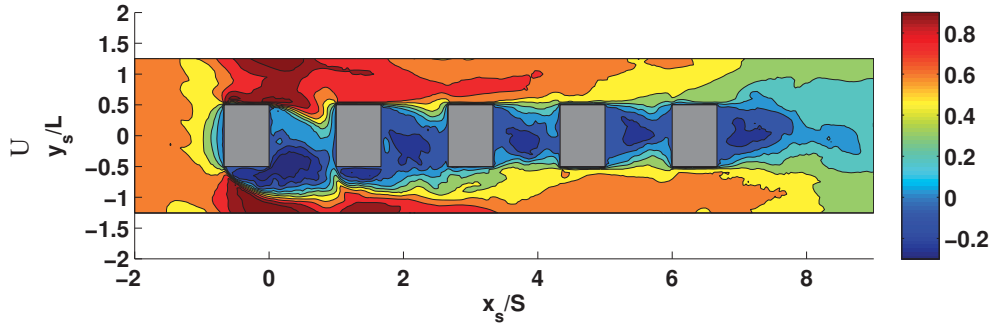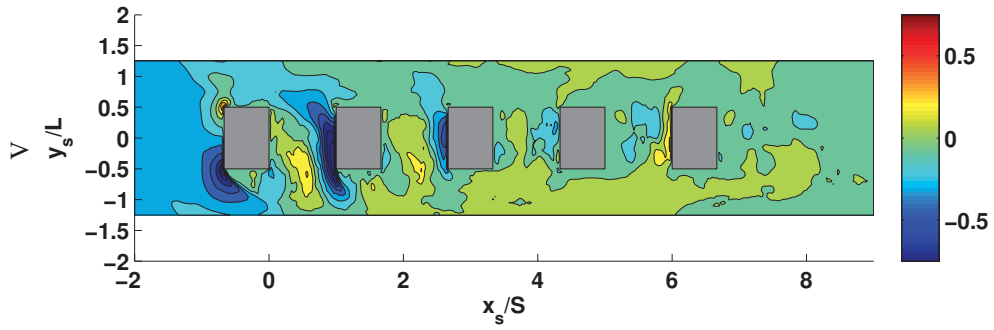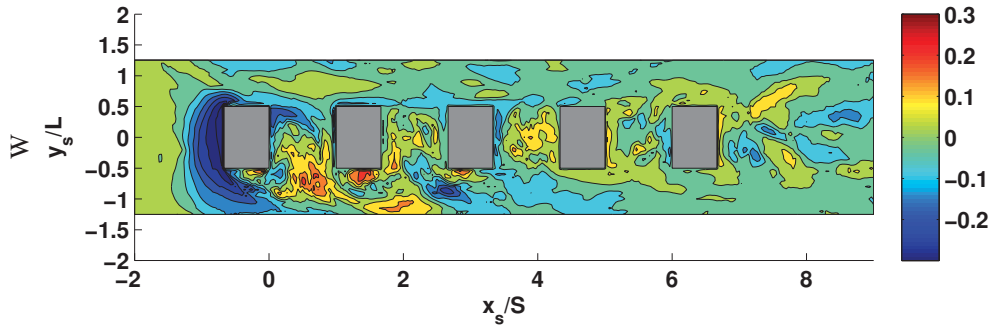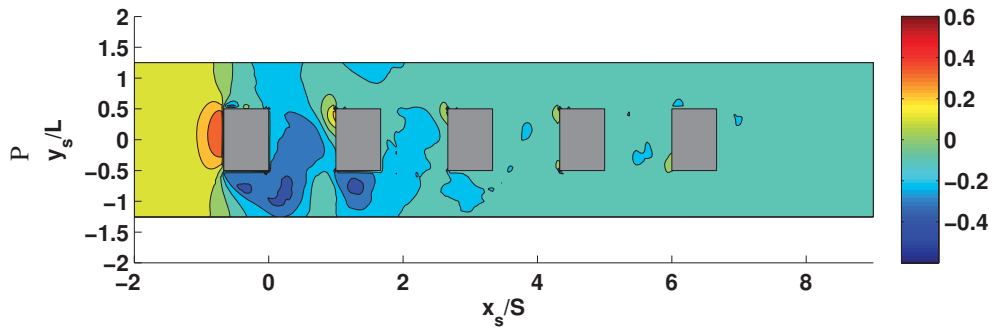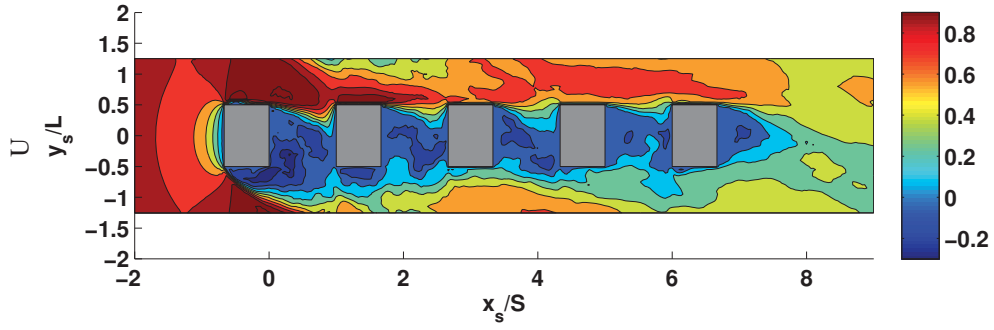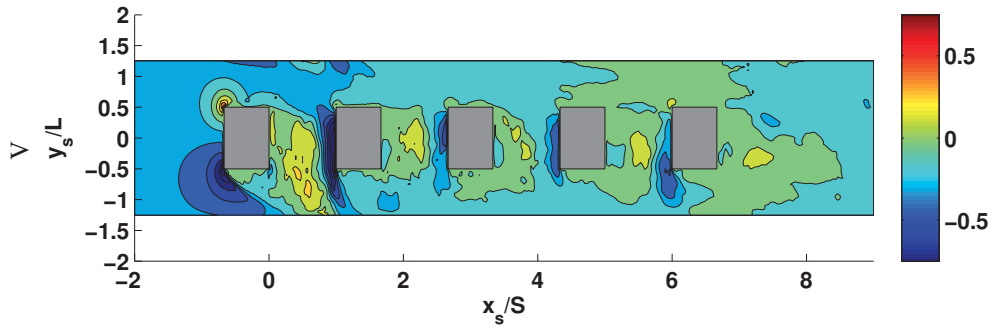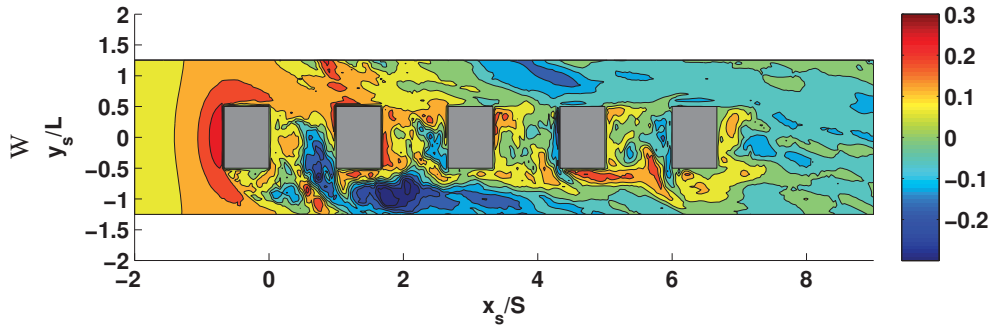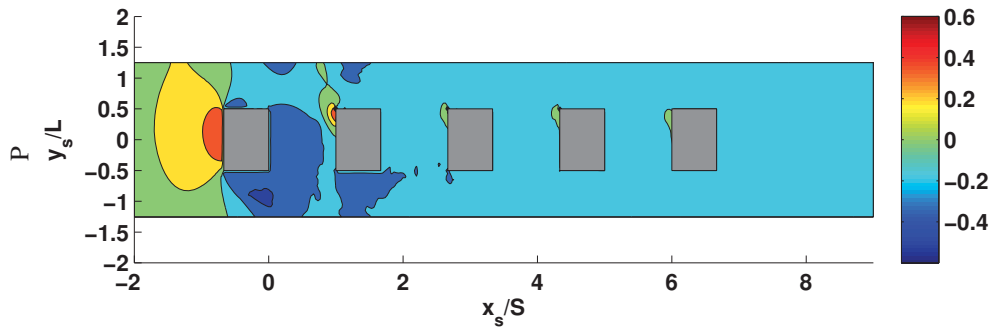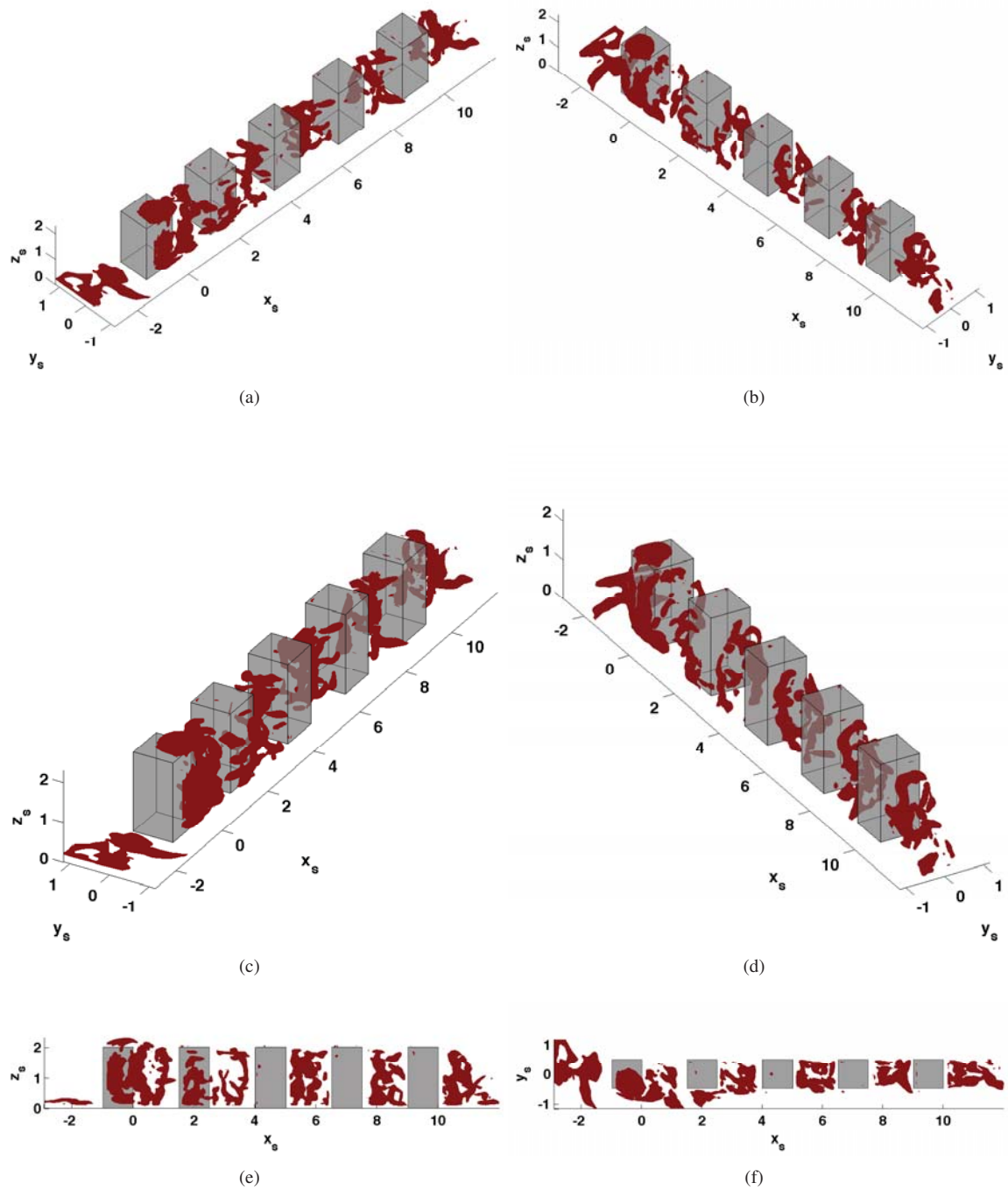Figure 5.54: Isocontours of Γ_1 as defined in Chapter 4 (Eq. 4.2) indicating the locations of cores of arch vortices in the urban street canyon for $15°$ angle of incidence.

Chapter 6

Discussion

6.1 Arch vortex

6.1.1 Comparison experimental and numerical results

Figure 6.1 presents a side-by-side comparison of the arch vortices represented by iso-surfaces of Γ_1 from the experimental results presented in Chapter 4 and from the numerical results presented in Chapter 5 for the AOI of $0°$. In both cases the arch vortices are well captured and the best agreement between experimental and numerical results is observed in streets 3 and 4.

6.1.2 Arch vortex core location dependence on street and angle of incidence

Three-dimensional Γ_1 iso-surfaces presented earlier provide general information about the location of the vortical structures; however to more precisely present comparisons regarding the location of the arch vortex legs, we focus on the maximum of Γ_1 which represents the actual center of vortical structures. To illustrate this, Γ_1 contours are presented in Figure 6.2 with the velocity vector field superimposed for the AOI of $0°$ case in the first street. The data are presented in an S_z plane at $z/H = 0.5$. The maxima of Γ_1 are shown as magenta stars on top of the Γ_1 contours. The detection of the maximum Γ_1 corresponds well with the center of the vortices shown with the 2D vector field in the displayed S_z plane. The accuracy of this core detection method which is defined based on the data acquisition grid dimensions, is 1 mm in the x direction and 2.5 mm in span (y).

In Figure 6.3, we use the same vortex core location detection technique but we now present a contour of the TKE instead of Γ_1 in order to illustrate the spatial connection between the arch vortex and the regions dominated by the turbulence. Figure 6.3 presents the vortex core locations for all four streets and the four AOI cases investigated. We also extract the actual angle of the arch vortex structure with respect to an axis aligned with the y-axis, depicted by the magenta lines. A summary of these angles is given in Table 6.1. Figure 6.3(a) shows that for AOI = $0°$, the arch vortex moves downstream from street 1 to street 4. For AOI = $0°$ the arch vortex angle with respect to the street should be equal to zero in each street. The variation in the measured angles for all four streets, listed in Table 6.1, arises from the slight asymmetry in the incoming flow triggering a channeling effect which is known to be strong even for small AOIs (see Monnier et al. [2010]). For $15°$ AOI, see Figure 6.3(b), the arch vortices are significantly tilted within the streets. Both legs are still within the region resolved with the SPIV measurements. It can be seen that one leg is leaving
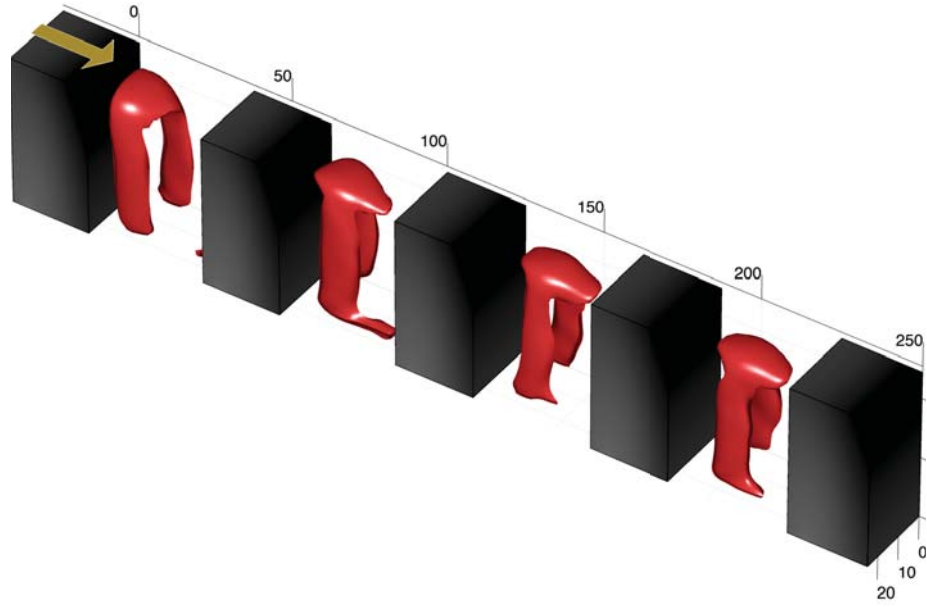
(a) Experimental
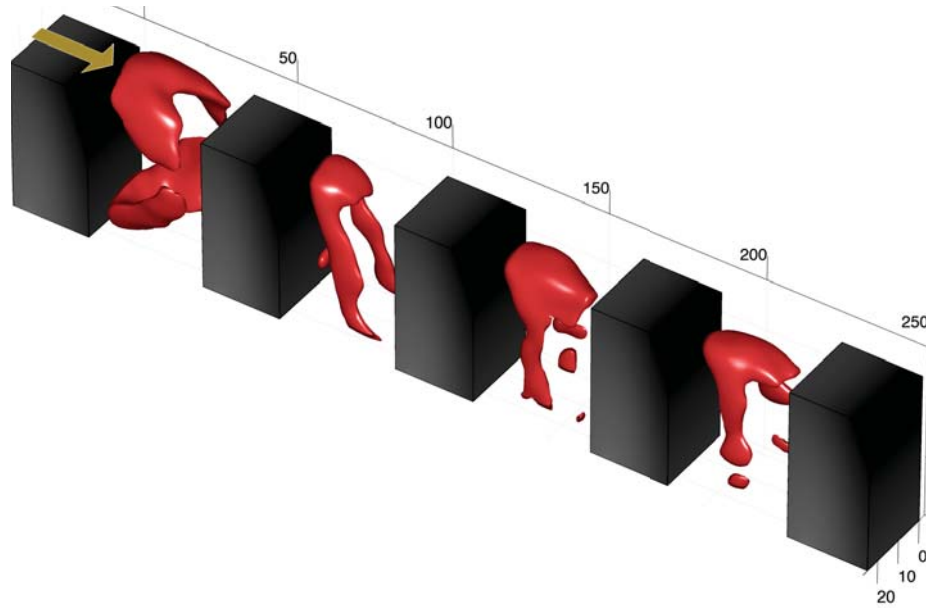
(b) Numerical

Figure 6.1: Arch vortex, using Γ_1 Iso-surfaces for AOI = 0° for both experimental and numerical results.

120

Figure 6.2: Mean velocity vector field (black vectors), Γ_1 magnitude contour background, vortex core locations (magenta stars), xy slice at $z/H = 0.5$.

the region directly behind the first block in street 1 ($-0.5 < y/w < 0.5$) and entering the intersection. For streets 2 to 4, both legs are still lying in the $-0.5 < y/w < 0.5$ region. As the angle is increased to $30°$, Figure 6.3(c), a single leg is captured within streets 1 and 2. The second leg, if it exists, would most likely have moved out of the region resolved in our measurements. This is a point that we will be able to address in the near future with a numerical simulation of this case. Within streets 3 and 4, both legs are captured within the $-0.5 < y/w < 0.5$ region. The angle of the arch vortex with respect to the street is larger than for the $15°$ AOI configuration, as can be seen in Table 6.1. Finally, for the $45°$ AOI, a single leg is captured in each street. Again, our assumption is that a second leg would exist in the region not resolved by our measurements.

A comparison between experimental and numerical results is presented in Figure 6.4. The agreement between the two is fairly good in streets 2, 3 and 4. Differences in the location of the arch vortex are observed in street 1 but the TKE distribution is very similar in both data sets. Apart from street 1, the angle of the arch vortex with respect to the street obtained from the numerical simulation is very comparable to the experimental results, see Table 6.1.

Table 6.1: Arch horizontal axis inclination (φ) in degree at z/H=0.5.

	Street #	1st	2nd	3rd	4th
Numerical	AOI=0°	20.0°	-3.5°	-2.9°	9.5°
Experimental	AOI=0°	4.5°	-10.2°	2.6°	-3.0°
	AOI=15°	29.6°	39.7°	37.9°	29.8°
	AOI=30°	-	-	50.2°	51.9°
	AOI=45°	-	-	-	-

(a) AOI $= 0°$

(b) AOI $= 15°$

(c) AOI $= 30°$

(d) AOI $= 45°$

Figure 6.3: Mean velocity vector field (black vectors), TKE magnitude contour background, vortex core locations (magenta stars), xy slice at $z/H = 0.5$.
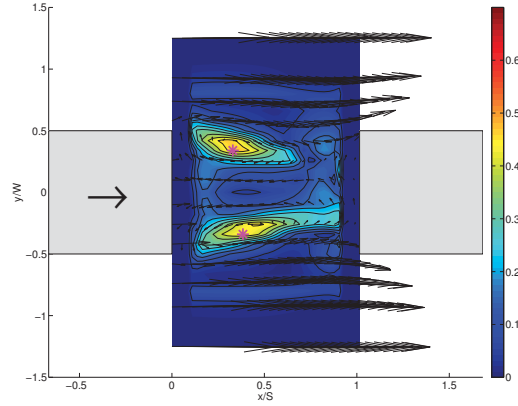

(a) AOI $= 0°$, experimental
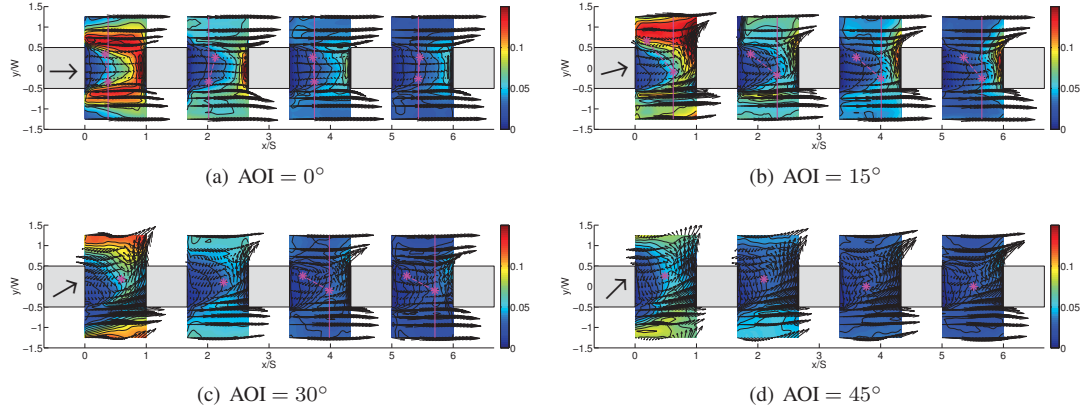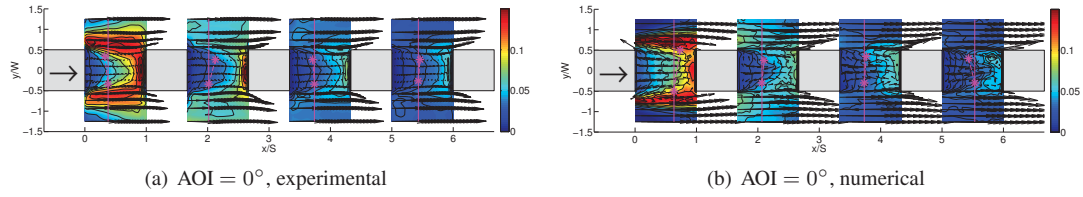
(b) AOI $= 0°$, numerical

Figure 6.4: Mean velocity vector field (black vectors), TKE magnitude contour background, vortex core locations (magenta stars), xy slice at $z/H = 0.5$ for both experimental and numerical results for AOI $= 0°$.

6.2 Turbulence characteristics of the gusts within the streets

In this section, we are focusing our attention on the probability density functions (PDFs) associated with the fluctuating part of the velocity field (u', v' and w'). From the experimental data, we extract the instantaneous velocity components, u', v' and w' from the SPIV snapshots at two specific positions in space which are chosen for their large contribution to the overall TKE. The first position is depicted in Figure 6.5(a) as a black square in an xy slice at $z/H = 0.25$ and its coordinates are $x/S = 0.5$, $y/W = -0.5$ and $z/H = 0.25$. Similarly, the second position is shown in Figure 6.5(b) in an x-z slice with coordinates equal to $x/S = 0.5$, $y/W = 0$, $z/H = 1$. These two locations are closely connected with the shear layers forming off the top and sides of the buildings where significant contributions to the TKE are observed. Also included in the figures are probability density functions of the gusts; that is, the PDFs of the individual fluctuating velocity components (normalized by U_H) at the position in space indicated by the black square. Since the choice of the black square was based on the relatively high level of TKE, we expect large gust amplitudes in the corresponding PDFs. It is worth noting here that instantaneous gust magnitudes can reach reach between 20% to 40% of the incoming wind velocity as normalized by the roof level U_H as shown in the plots. Also included in these plots are the three correlation coefficients, R_uv, R_uw and R_vs which give an indication of the coupling between the different gust components.

Figure 6.6 presents a comparison of the gust PDFs in street 3 for the four AOIs investigated. In addition to the PDFs, a Gaussian curve was fitted to each PDF and the corresponding mean, μ, and standard deviation, σ for each fluctuating velocity component are shown along with the three correlation coefficients. Comparing the PDFs of u', v' and w' for all four AOIs, it can be seen that the overall distribution of the gust is not noticeably affected by the wind direction. The only significant difference is observed in street 4 where the correlation coefficient R_{uv} drops from about 0.6 to 0.2 indicating a decoupling of the streamwise and spanwise gusts. The overall similarity of the gust profiles in the x-y slice at $z/H = 0.25$ is most likely due to the fact that this area of the street is more shielded from the incoming wind.

When looking at the second location, at roof level of the blocks, the effect of the AOI is more evident as shown by the results given in Figure 6.7. At an AOI of $0°$, the u' component PDF has a larger $\sigma_{u'} = 0.20$ as compared with the v' or w' distributions. As the AOI is increased, the spanwise v' component distribution gets wider and eventually becomes larger than its u' counterpart. In addition, the PDFs are getting more skewed as AOI is increased. The roof-level region is much more sensitive to the wind direction as compared with the location closer to the ground discussed above. In terms of correlation coefficients between any two gust components, the R_{uw} is dominant for the $0°$ AOI case. As the AOI is increased, the streamwise gust gains correlation with the other two gust components. By $45°$, the dominant correlation coefficient is R_{uv} but both R_{uw} and R_{vw} are also significantly larger. The wind direction has the effect of redirecting the gust and redistributing the gusts in all three directions with a significant coupling between the different components.

We now perform a side-by-side comparison of PDFs between the experimental data and the numerical data. Figure 6.8 presents such a comparison for the first two streets at the $x/S = 0.5$, $y/W = -0.5$, $z/H = 0.25$ location (near the ground) for the $0°$ AOI while Figure 6.9 presents the same comparison for streets 3 and 4. Apart from some differences in street 1, both the standard deviations of the fluctuating velocity components and the correlation coefficients are very close between the experimental and numerical results, indicating that the turbulent characteristics of the flow field are well captured by the numerical simulation. This last point is also true when comparing the gust PDFs at the second location (at roof level) as is illustrated by Figures 6.10 and 6.11.
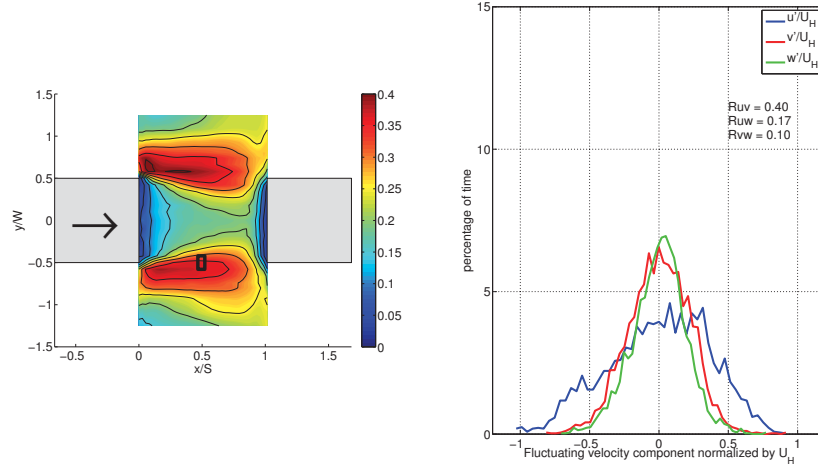
(a) xy slice at $z/H = 0.25$ showing u_{rms} contours and a sample of gust probability density function based on data extracted from a point at $(x/S = 0.5, y/W = -0.5, z/H = 0.25)$
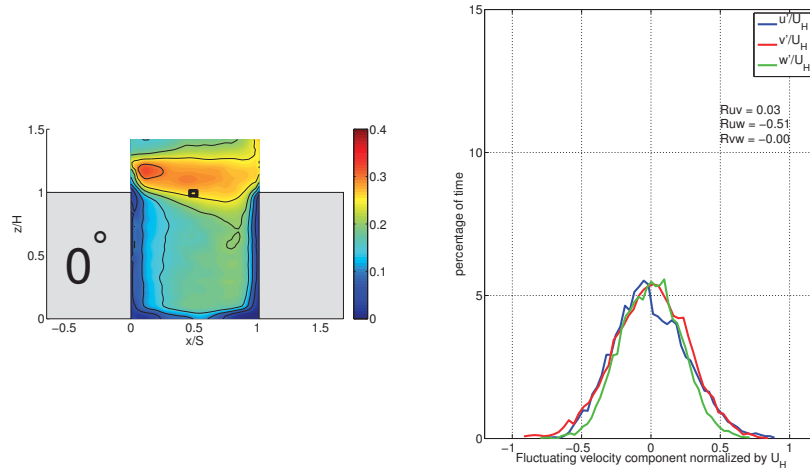
(b) xz slice at $y/W = 0$ showing u_{rms} contours and a sample of gust probability density function based on data extracted from a point at $(x/S = 0.5, y/W = 0, z/H = 1)$

Figure 6.5: Spatial locations (black squares) used to extract gusts probability density functions
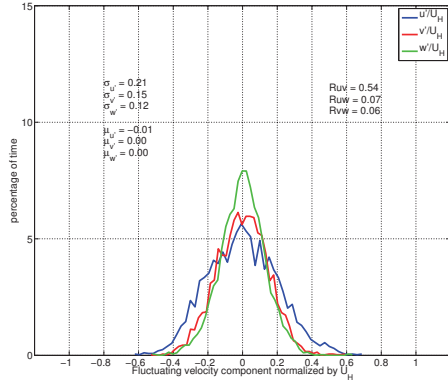
(a) AOI $= 0°$, experimental results in street 3
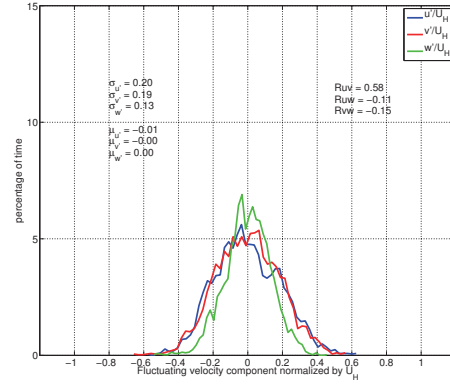
(b) AOI $= 15°$, experimental results in street 3
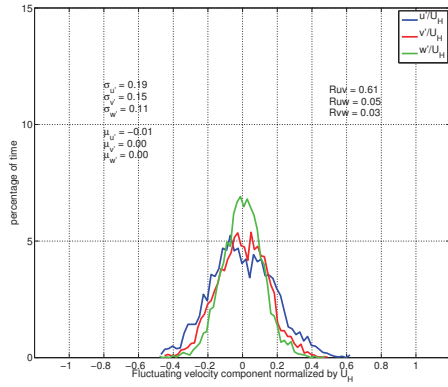
(c) AOI $= 30°$, experimental results in street 3
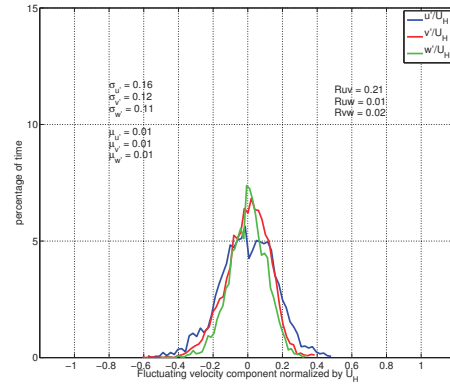
(d) AOI $= 45°$, experimental results in street 3

Figure 6.6: PDFs of gusts at a specific point in the street: $(x/S = 0.5, y/W = -0.5, z/H = 0.25)$ for all 4 AOIs.
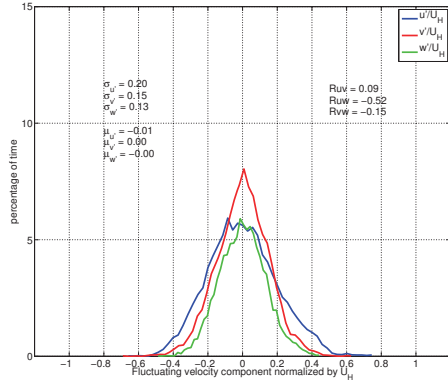
(a) AOI $= 0°$, experimental results in street 3
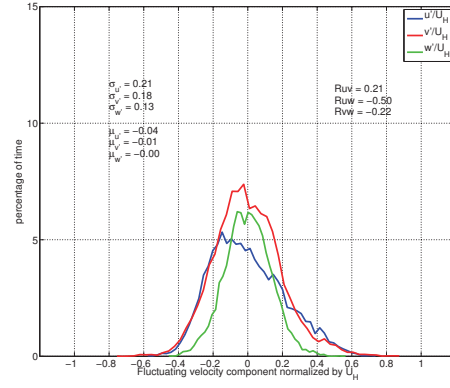
(b) AOI $= 15°$, experimental results in street 3
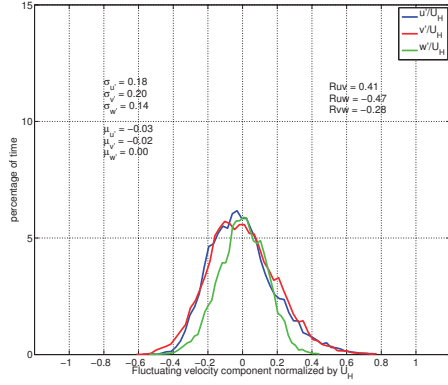
(c) AOI $= 30°$, experimental results in street 3
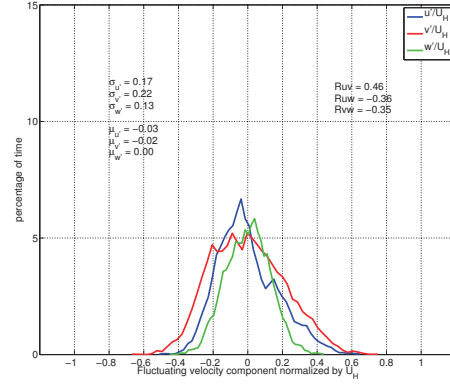
(d) AOI $= 45°$, experimental results in street 3

Figure 6.7: PDFs of gusts at a specific point in the street: ($x/S = 0.5$, $y/W = 0$, $z/H = 1$) for all 4 AOIs.
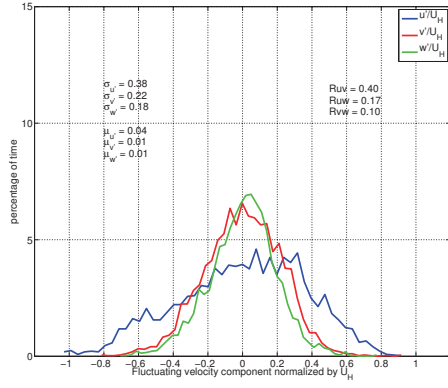
(a) AOI $= 0°$, experimental results in street 1
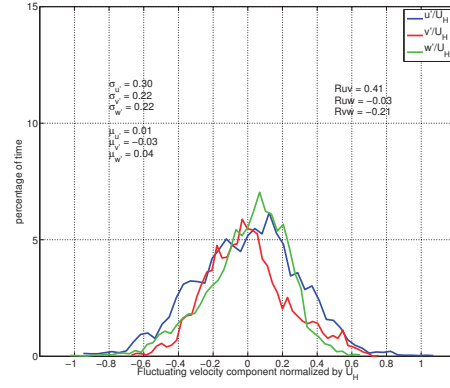
(b) AOI $= 0°$, numerical results in street 1
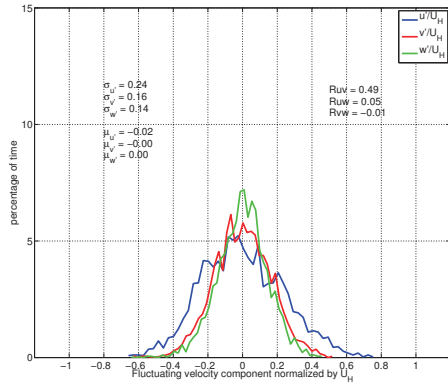
(c) AOI $= 0°$, experimental results in street 2
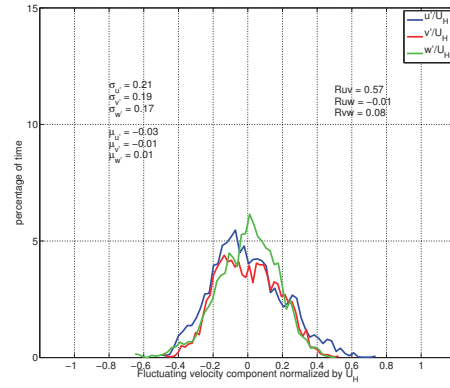
(d) AOI $= 0°$, numerical results in street 2

Figure 6.8: PDFs of gusts at a specific point in the street: ($x/S = 0.5$, $y/W = -0.5$, $z/H = 0.25$)
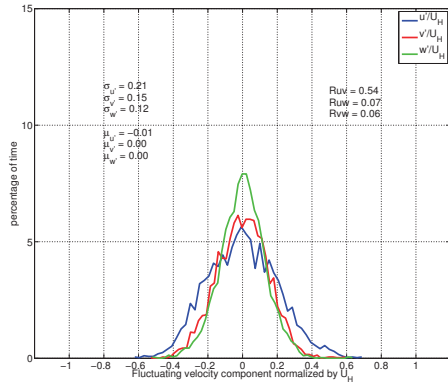
127

(a) AOI $= 0°$, experimental results in street 3

(b) AOI $= 0°$, numerical results in street 3

(c) AOI $= 0°$, experimental results in street 4

(d) AOI $= 0°$, numerical results in street 4

Figure 6.9: PDFs of gusts at a specific point in the street: ($x/S = 0.5$, $y/W = -0.5$, $z/H = 0.25$)
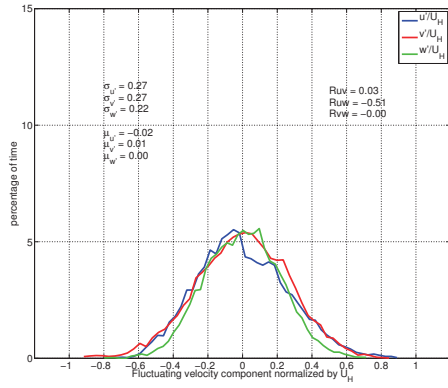
(a) AOI = 0°, experimental results in street 1
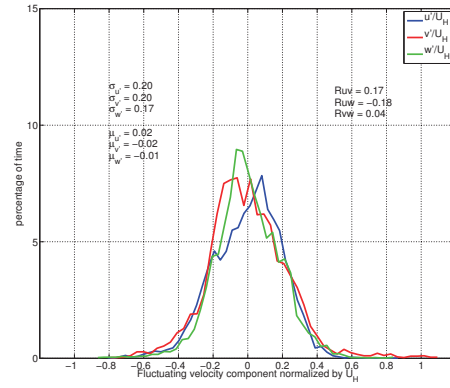
(b) AOI = 0°, numerical results in street 1
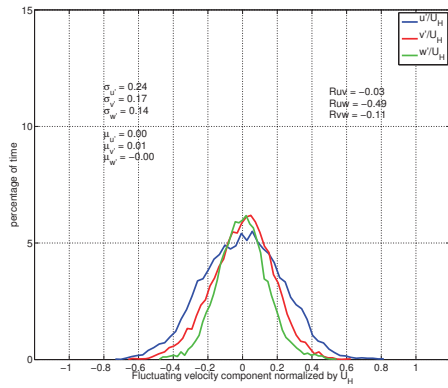
(c) AOI = 0°, experimental results in street 2
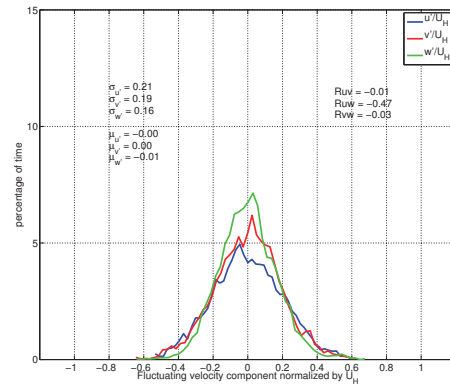
(d) AOI = 0°, numerical results in street 2

Figure 6.10: PDFs of gusts at a specific point in the street: ($x/S = 0.5$, $y/W = 0$, $z/H = 1$)
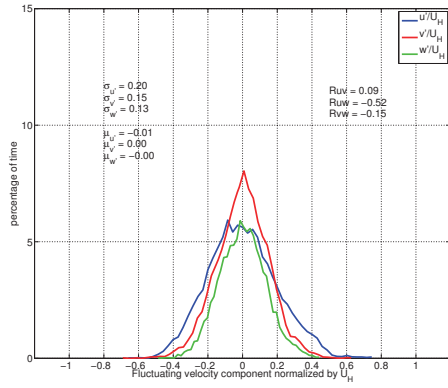
(a) AOI $= 0°$, experimental results in street 3
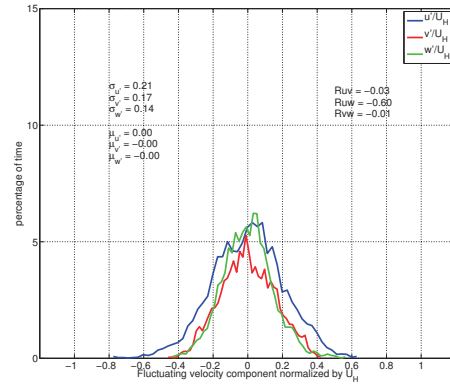
(b) AOI $= 0°$, numerical results in street 3
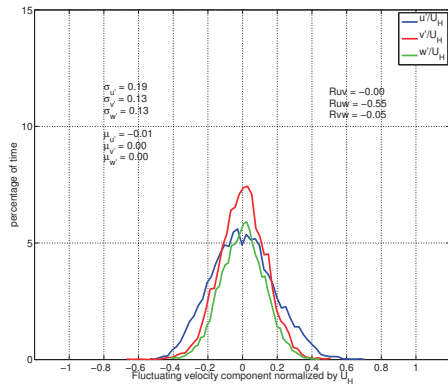
(c) AOI $= 0°$, experimental results in street 4
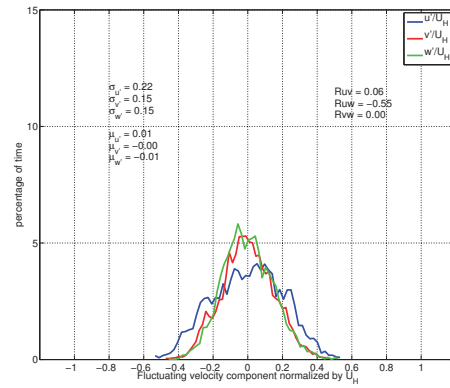
(d) AOI $= 0°$, numerical results in street 4

Figure 6.11: PDFs of gusts at a specific point in the street: ($x/S = 0.5$, $y/W = 0$, $z/H = 1$)

6.3 Connection between arch vortices and high turbulence areas

In this section, we are looking at the arch vortex location with respect to regions of high turbulence (large u_{rms}, v_{rms} or w_{rms}). To do so, we are presenting 3D iso-surfaces of Γ_1, u_{rms} and v_{rms} in Figure 6.12. The experimental data are presented in street 1 for the four AOIs investigated. The thresholds used to plot the regions of high turbulence are selected as 75% of the local maximum of u_{rms} and v_{rms} within the street. For the $0°$ AOI, see Figure 6.12(a), the two regions of large u_{rms} are essentially due to the shear layers formed off the sides of the blocks with the arch vortex being "trapped" between these two regions. Similarly, the region of large v_{rms} observed near the windward face of the downstream block is located downstream of the arch vortex. The large spanwise fluctuations associated with v_{rms} are observed in the middle of the street in the spanwise direction ($y/W = 0$) which is also between the legs of the arch vortex. The arch vortex is surrounded by regions of high turbulence but its core sits in a low turbulence area. As the AOI is increased to $15°$, see Figure 6.12(b), the arch vortex is tilted with respect to the street axis. The regions of high turbulence are also redistributed around the arch vortex. The spanwise turbulence region is shifted and again aligned with the middle of the two legs of the arch vortex. For the $30°$ AOI, see Figure 6.12(c), the picture is very similar to the $15°$ case. In the $45°$ AOI case, the trend is similar but an additional region of high spanwise turbulence appears due to the side shear layer with the arch vortex still sitting in the low turbulence region.

Comparing the experimental results with the numerical results, see Figure 6.13, the same trends are observed. The main difference lies in the shape of the arch vortex which partly explains the difference observed in the fluctuating velocity PDFs presented in the previous section.
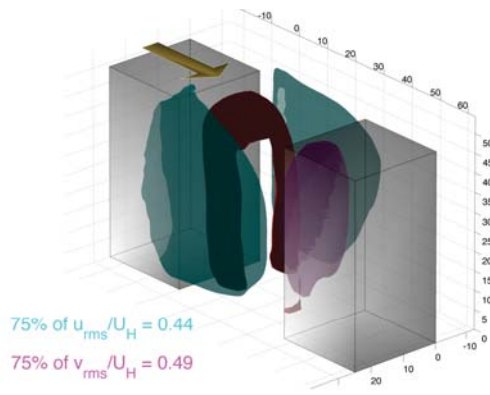
(a) AOI $= 0°$
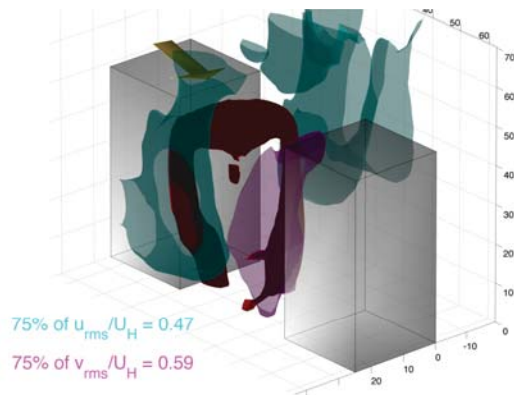
(b) AOI $= 15°$
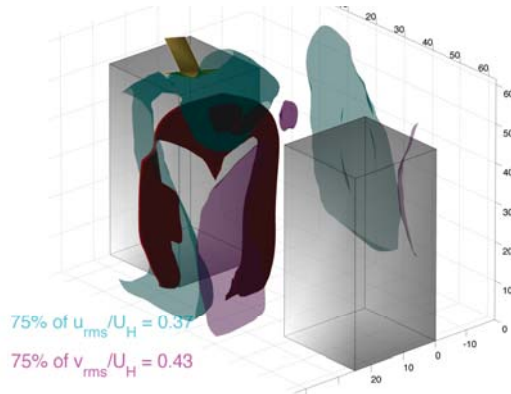
(c) AOI $= 30°$
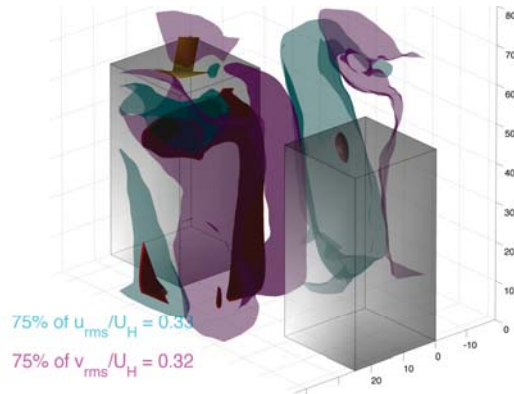
(d) AOI $= 45°$

Figure 6.12: Arch vortex and regions of high u_{rms} and v_{rms}.

(a) AOI $= 0°$, experimental

(b) AOI $= 0°$, numerical
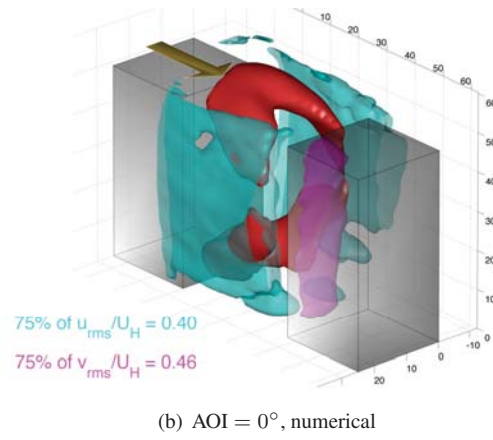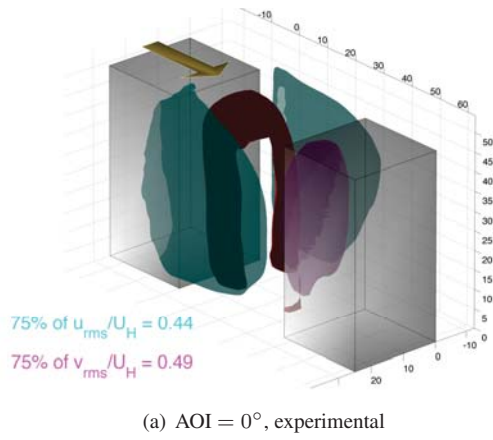
Figure 6.13: Arch vortex and regions of high u_{rms} and v_{rms} for both experimental and numerical results.

Chapter 7

Conclusions

7.1 Experiment

In this study, a scaled urban environment model is simulated in a low-speed wind tunnel. Stereoscopic particle image velocimetry (SPIV) was used to provide three-dimensional velocity data in the urban streets to achieve a thorough spatial map of the mean and turbulent flow. Contour slices and iso-surfaces are the tools used to document the complex flow in four consecutive streets within the urban array. Additionally, the effect of the incoming wind direction on the flow characteristics was studied for incidence angles of $0°$ to $45°$.

The channelling of the flow down the streets is easily seen by the results for the non-zero incidence angles of $15°$, $30°$ and $45°$. The channelling of the flow is also reflected in the tilting of the arch vortex. For the $0°$ case the arch vortex in street 1 is located relatively close to the upstream building and its vertical axis is almost perpendicular to the ground. Further downstream in the array the arch vortex is observed to tilt (around the spanwise coordinate) in the downstream direction. Γ_1 was used to locate the core locations of the arch vortex legs in the horizontal streamwise-spanwise plane at a wall-normal position of $z/H = 0.5$. These results show that there is also an effect of AOI on the tilting of the arch vortex around the streamwise coordinate.

The TKE results for all four AOI cases investigated illustrate that the flow through the array seems to reach an equilibrium condition in as little as 3 to 4 streets. The turbulence levels from street 1 to 2 were shown to decrease significantly with smaller decreases from street to street after that. Regarding the effect of AOI on the turbulence levels it is observed that the TKE level increases slightly from AOI=$0°$ to AOI=$15°$ and then decreases as the AOI increases to $30°$ and $45°$. By decomposing the TKE into its three components it is shown that the streamwise $(\overline{u'^2})$ and spanwise $(\overline{v'^2})$ fluctuating components are more significant than the wall-normal $(\overline{w'^2})$ component. The relationship between the turbulence and gust magnitudes was investigated by looking at the probability density functions for all three velocity components in regions corresponding to high TKE. Gust magnitudes as large as 20–40% of U_H in all three velocity components are common for all cases considered. The correlations between the gust components were also studied and it was found that lower in the street the correlations between the streamwise and spanwise gusts, (R_{uv}), were dominant for all four AOI cases and the two other cross correlations (spanwise/wall-normal (R_{vw}) & streamwise/wall-normal (R_{uw})) were negligible. At higher wall-normal positions in the array $(z/H = 1)$ the R_{vw} & R_{uw} correlations increased as compared with the lower $z/H = 0.25$ condition. At $z/H = 1$ for AOI = $0°$ the R_{uv} correlation is negligible whereas the correlation between the streamwise and wall-normal

gusts (R_{uw}) is relatively large. As AOI increases at this $z/H = 1$ position R_{uw} decreases as AOI increases and for AOI values of $30°$ and $45°$ all three correlations are significant.

Overlaying the arch vortex structures with the TKE components reveals that the vortex cores are located in regions of relatively low turbulence but surrounded by high-turbulence regions. For AOI = $0°$ the high u_{rms} regions are due to the shear layers from the sides of the building. Similarly, the region of large v_{rms} observed near the windward face of the downstream block is located downstream of the arch vortex. As the incidence angle is increased the arch vortex is tilted with respect to the street axis with the regions of high turbulence being redistributed around the arch vortex. In addition the region of large v_{rms} values is shifted and again aligned with the middle of the two legs of the arch vortex.

7.2 Numerical

As part of this project, a high-order accurate incompressible Navier-Stokes solver capable of performing high fidelity simulations of flows of engineering interest was built. The physical problem to be tackled here required a solver which is highly scalable, supports complex geometries and has low dispersion and diffusion errors.

We therefore developed *Specsolve*, a scalable spectral element solver. The solver is coded in C++ and uses the MPI (Message Passing Interface) library for communication. It exploits the object-oriented features of C++ and uses dynamic memory allocation for optimal memory usage. The code is mostly self-contained and the only external dependencies are the standard LAPACK and BLAS libraries. It supports meshes generated by general-purpose mesh generators like CUBIT and GAMBIT. An efficient mesh partitioner, based on parallel recursive spectral bisection algorithm, is built for generating high quality mesh partitions.

The solver uses the $\mathcal{P}_N - \mathcal{P}_{N-2}$ formulation for spatial discretization of velocity and pressure. Velocity is represented within each spectral element using a tensor product of Lagrangian basis functions based on GLL (Gauss-Lobatto-Legendre) nodes and C^0 continuity is enforced between adjacent spectral elements. Pressure within each spectral element is represented using a tensor product of one-dimensional Legendre polynomials of appropriate order and inter-element continuity is not explicitly enforced. A semi-implicit scheme, which treats the Stokes operator implicitly and the nonlinear term explicitly, is used for temporal integration. A fractional step scheme with second-order temporal accuracy is used to decouple velocity and pressure. This requires the solution of a Helmholtz system for each component of velocity and consistent Poisson equation for pressure at each time step. While the Helmholtz system can be solved efficiently using the Jacobi preconditioned conjugate gradient method, the solution of the consistent Poisson equation remains the principal bottleneck in the numerical solution of the Navier-Stokes equations.

To address this, a multilevel strategy was implemented to build a scalable solver for pressure. The deflation approach is used to decompose pressure into fine and coarse components. An FDM-based block-Jacobi preconditioner is used for efficient solution of the fine pressure problem. A parallel direct solver and a state-of-the-art algebraic multigrid solver are implemented to solve the coarse pressure problem. The parallel direct solver is used for meshes with less than 10^5 spectral elements whereas the algebraic AMG solver is used for larger mesh sizes. A multi-threaded C++ code was built for setting up the data needed for the AMG solver.

The solver was tested for accuracy on various benchmark problems. Two-dimensional test cases comprised Wannier flow, Kovasznay flow, vortex shedding from a circular cylinder at various Reynolds numbers, and the highly sensitive Orr-Sommerfeld problem. Three-dimensional test cases include the three-dimensional Kovasznay flow and the flow over a backward-facing step at $Re = 172$ and $Re = 343$. In all cases, the results are in excellent agreement with the corresponding exact solutions predicted by theory and

experimental data.

Additional issues arise when high-order solvers are used outside their traditional realm of simulating canonical flows. Typically, most flows of engineering interest occur in relatively complex domains and it is fairly common to have outflow boundaries. In addition, it is generally impractical to have highly resolved meshes throughout the flow domain. Simulating high Reynolds number flow generally requires a stabilization method in the absence of LES models, or exorbitantly high mesh resolutions and an outflow boundary condition that can handle energy influx to the domain caused by strong vortices exiting at the outflow boundary. At high Reynolds numbers, our solver uses filter-based stabilization and supports a turbulent outflow boundary condition to stabilize the flow at the outflow boundary.

Our solver was used to simulate flow in a model urban street canyon. The domain consists of an array of blocks, typical of a modern urban environment, placed in the wind tunnel. The Reynolds number based on block height (H) and inlet velocity at block height (U_H) is $Re_H = \frac{U_H H}{\nu} = 6283$. The simulation results are in good agreement with the PIV data generated from the experiments and demonstrate the fitness of the solver for production use.

7.3 Future work

Our immediate objectives are as follows:

- Further improve the comparison between experiments and simulation for the urban street canyon simulation. This would involve using more accurate inflow boundary conditions.

- Study the effect of angle of attack on flow in the urban street canyon. This would involve simulating the entire three dimensional array as opposed to simulating a single row of blocks.

- Extend this work from wind tunnel scale to field scale. This would require implementation of robust LES models Bou-Zeid et al. [2005] which work with marginally resolved grids which only resolve the upper edge of the inertial layer.

- Further improve the scalability of the solver.

136

Bibliography

R. Adrian. Twenty years of particle image velocimetry. *Experiments in Fluids*, 39:159–169, 2005.

R. Adrian and C.S. Yao. Pulsed laser technique application to liquid and gaseous flows and the scattering power of seed materials. *Applied optics*, 24(1):44–52, 1985.

K. Ahmad, M. Khare, and K. Chaudhry. Model vehicle movement system in wind tunnels for exhaust dispersion studies under various urban street configurations. *Journal of Wind Engineering and Industrial Aerodynamics*, 90:1051–1064, 2002.

B.F. Armaly, F. Durst, J.C.F. Pereira, and B. Schönung. Experimental and theoretical investigation of backward-facing step flow. *J. Fluid Mech.*, 121:473–496, 1983.

J.J. Baik and J.J. Kim. A numerical study of flow and pollutant dispersion characteristics in urban street canyons. *Journal of Applied Meteorology*, 38:1576–1589, 1999.

S. Becker, H. Lienhart, and F. Durst. Flow around three-dimensional obstacles in boundary layers. *Journal of Wind Engineering and Industrial Aerodynamics*, 90:265–279, 2002.

S. Belcher and O. Coceal. Scaling the urban boundary layer. *COST 715 Workshop on Urban Boundary Layer Parameterisations, Zurich, 10 pp*, 2001.

C.A. Biltoft. Customer report for Mock Urban Setting Test. *DPG Document No. WDTC- FR-01-121, West Desert Test Center, U.S. Army Dugway Proving Ground, Dugway, Utah, 58 pp.*, 2001.

G. Biswas, M. Breuer, and F. Durst. Backward-facing step flows for various expansion ratios at low and moderate reynolds numbers. *J. Fluids Eng.*, 126:362–374, 2004.

R.F. Blackwelder and J.H. Haritonidis. Scaling of the bursting frequency in turbulent boundary layers. *Journal of Fluid Mechanics*, 132:87–103, 1983.

E. Bou-Zeid, C. Meneveau, and M.B. Parlange. A scale-dependent lagrangian dynamic model for large eddy simulation of complex turbulent flows. *Phys. Fluids.*, 17, 025105, 2005.

R. Britter and S.R. Hanna. Flow and dispersion in urban areas. *Annual Review of Fluid Mechanics*, 35: 469–96, 2003.

D. Calluaud and L. David. Stereoscopic particle image velocimetry measurements of the flow around a surface-mounted block. *Experiments in Fluids*, 36:53–61, 2004.

F. Camelli, R. Lohner, and S. Hanna. VLES study of flow and dispersion patterns in heterogeneous urban areas, 14 pp. *44th AIAA Aerospace Sciences Meeting and Exhibit*, 2006.

F.E. Camelli and R. Lohner. Vles study of flow and dispersion patterns in heterogeneous urban areas. *44th AIAA Aerospace Sciences Meeting and Exhibit 9-12 January 2006, Reno, Nevada*, 2006.

I.P. Castro and G. Robins. The flow around a surface-mounted cube in uniform and turbulent streams. *Journal of Fluid Mechanics*, 79:307–335, 1977.

I.P. Castro, H. Cheng, and R. Reynolds. Turbulence over urban-type roughness: Deductions from wind-tunnel measurements. *Boundary-Layer Meteorology*, 118:109–131, 2006.

H. Cheng and I.P. Castro. Near wall flow over urban-like roughness. *Boundary-Layer Meteorology*, 104(2): 229–259, 2002. doi: 10.1023/A:1016060103448.

A. Christen, R. Vogt, and M. Rotach. Profile measurements of selected turbulence characteristics over different urban surfaces. *Fourth International Conference on Urban Air Quality, Prague*, 25–27:408–411, 2003.

O. Coceal and S. Belcher. A canopy model of mean winds through urban areas. *Quarterly Journal of the Royal Meteorological Society*, 130:1349–1372, 2004.

O. Coceal, T. Thomas, I.P. Castro, and S.E. Belcher. Mean flow and turbulence statistics over groups of urban like cubical obstacles. *Boundary-Layer Meteorology*, 121:491–519, 2006.

W. Couzy. *Spectral Element Solution Discretization of the Unsteady Navier-Stokes Equations and Its Iterative Solution on Parallel Computers*. Swiss Federal Institute of Technology, Lausanne, 1995.

A.G. Davenport. The relationship of wind structures to wind loading. *Wind Effects on Buildings and Structures, Proceedings of the Conference held at the National Physical Laboratory, Symposium No. 16, Teddington, Middlesex*, pages 54–102, 1965.

M.O. Deville, P.F. Fischer, and E.H. Mund. *High-order methods for incompressible fluid flow*. Cambridge Monographs on Applied and Computational Mathematics, Cambridge University Press, 2002.

A. Dobre, S. Arnold, R. Smalley, J. Boddy, J.F. Barlow, A.S. Tomlin, and S.E. Belcher. Flow field measurements in the proximity of an urban intersection in London, UK. *Atmospheric Environment*, 39:4647–4657, 2005.

S. Dong, G.E. Karniadakis, and C. Chryssostomidis. A robust and accurate outflow boundary conditions for incompressible flow simulations on severely-truncated unbounded domains. *J. of Comp. Phys.*, 261: 83–105, 2014.

R.E. Drubka, J. Tan-atichat, and H.M. Nagib. Analysis of temperature compensating circuit for hot-wires and hot-films. *DISA information*, 22:5–14, 1977.

I. Eliasson, B. Offerle, and C. Grimmond. Wind fields and turbulence statistics in an urban street canyon. *Atmospheric Environment*, 40:1–16, 2006.

R. Eskridge and S. Trivikrama Rao. Turbulent diffusion behind vehicles: experimentally determined turbulence mixing parameters. *Atmospheric Environment (1967)*, 20(5):851–860, 1986.

P. Fischer and J. Mullen. Filter-based stabilization of spectral element methods. *C. R. Acad. Sci. Paris*, 261: 265–270, 2001.

P.F. Fischer. Parallel multi-level solvers for spectral element methods. *Int. Conf. on Spectral and High-Order Methods 95, Houston, TX, edited by A. V. Ilin and L. R. Scott (Houston Journal of Mathematics, 1996)*, 1996.

P.F. Fischer. An overlapping schwarz method for spectral element solution of the incompressible navier-stokes equations. *J. of Comp. Phys.*, 133:84–101, 1997.

R. Gailis. Wind tunnel simulations of the Mock Urban Setting Test - experiment procedures and data analysis, 63 pp. *Australian Government - Department of Defence, DSTOTR1532*, 2004.

V. Garbero, P. Salizzoni, and L. Soulhac. Experimental study of pollutant dispersion within a network of streets. *Boundary-Layer Meteorology*, 136(3):457–487, 2010.

Y. Gayev and E. Savory. Influence of street obstructions on flow processes within urban canyons. *Journal of Wind Engineering and Industrial Aerodynamics*, 82:89–103, 1999.

L. Graftieaux, M. Michard, and N. Grosjean. Combining PIV, POD and vortex identification algorithms for the study of unsteady turbulent swirling flows. *Measurement Science and Technology*, 12:1422–1429, 2001.

C.S.B. Grimmond and T.R. Oke. Aerodynamic properties of urban areas derived from analysis of surface form. *Journal of Applied Meteorology*, 38:1262–1292, 1999.

C. Gromke and B. Ruck. Influence of trees on the dispersion of pollutants in an urban street canyon–experimental investigation of the flow and concentration field. *Atmospheric Environment*, 41:3287–3302, 2007.

C. Gromke and B. Ruck. On the impact of trees on dispersion processes of traffic emissions in street canyons. *Boundary-Layer Meteorology*, 131:19–34, 2009.

C. Gromke, R. Buccolieri, S. Di Sabatino, and B. Ruck. Dispersion study in a street canyon with tree planting by means of wind tunnel and numerical investigations-evaluation of CFD data with experimental data. *Atmospheric Environment*, 42:8640–8650, 2008.

H. Gunes, S. Sirisup, and G. Karniadakis. Gappy data: To krig or not to krig? *Journal of Computational Physics*, 212:358–382, 2006.

T. Gunnarsson. Implementation of the counter-jet technique for modeling of atmospheric surface layers in the IIT environmental wind tunnel. Master's thesis, Illinois Institute of Technology, Chicago, IL, 1974.

A. Hagishima, J. Tanimoto, and K. Nagayama. Aerodynamic parameters of regular arrays of rectangular blocks with various geometries. *Boundary-Layer Meteorology*, 132:315–337, 2009.

J. Hang, Y. Li, M. Sandberg, R. Buccolieri, and S. Sabatino. The influence of building height variability on pollutant dispersion and pedestrian ventilation in idealized high-rise urban areas. *Building and Environment*, 56:346–360, 2012.

R.D. Henderson. Nonlinear dynamics and pattern formation in turbulent wake transition. *J. Fluid Mech.*, 352:65–112, 1997.

H.J. Hussein and R.J. Martinuzzi. Energy balance for turbulent flow around a surface mounted cube placed in a channel. *Physics of Fluids*, 8:764–780, 1996.

G.E. Karniadakis and S.J. Sherwin. *Spectral/hp Element Methods for CFD*. Numerical Mathematics and Scientific Computation, Oxford University Press, 2005.

P. Kastner-Klein and M. Rotach. Mean flow and turbulence characteristics in an urban roughness sublayer. *Boundary-Layer Meteorology*, 111:55–84, 2004.

P. Kastner-Klein, R. Berkowicz, and E.J. Plate. Modelling of vehicle-induced turbulence in air pollution studies for streets. *International Journal of Environment and Pollution*, 14(1-6):496–507, 2000.

P. Kastner-Klein, E. Fedorovich, and M. Rotach. A wind tunnel study of organised and turbulent air motions in urban street canyons. *Journal of Wind Engineering and Industrial Aerodynamics*, 89:849–861, 2001.

R. Kellnerova, J. Kukacka, K. Jurcakova, V. Uruba, and Z. Janur. Piv measurement of turbulent flow within a street canyon: Detection of coherent motion. *Journal of Wind Engineering and Industrial Aerodynamics*, 104–106:302–313, 2012.

J. Kim and J. Baik. Urban street-canyon flows with bottom heating. *Atmospheric Environment*, 35:3395–3404, 2001.

J. Kim and J. Baik. Effects of inflow turbulence intensity on flow and pollutant dispersion in an urban street canyon. *Journal of Wind Engineering and Industrial Aerodynamics*, 91:309–329, 2003.

J. Kim and J. Baik. A numerical study of the effects of ambient wind direction on flow and dispersion in urban street canyons using the RNG k-epsilon turbulence model. *Atmospheric Environment*, 38:3039–3048, 2004.

A. Kovar-Panskus, P. Louka, J. Sini, E. Savory, M. Czech, A. Abdelqari, P.G. Mestayer, and N. Toy. Influence of geometry on the mean flow within urban street canyons–a comparison of wind tunnel experiments and numerical simulations. *Water, Air, and Soil Pollution: Focus*, 2:365–380, 2002a.

A. Kovar-Panskus, L. Moulinneuf, E. Savory, A. Abdelqari, J-F. Sini, J-M. Rosant, A. Robins, and N. Toy. A wind tunnel investigation of the influence of solar-induced wall-heating on the flow regime within a simulated urban street canyon. *Water, Air, and Soil Pollution: Focus*, 2:555–571, 2002b.

L.I.G. Kovasznay. Laminar flow behind a two-dimensional grid. *Proc. Cambridge Philos. Soc.*, 44:58–62, 1948.

S. Krajnovic and L. Davidson. Flow around a three-dimensional bluff body. *9th International Symposium on Flow Visualization, Heriot-Watt Univeristy, Edinburgh, 10 pp*, 2000.

A. Lecerf, B. Renou, D. Allano, A. Boukhalfa, and M. Trinit. Stereoscopic PIV: validation and application to an isotropic turbulent flow. *Experiments in Fluids*, 26:107–115, 1999.

X. Li, D. Leung, C. Liu, and K. Lam. Physical modeling of flow field inside urban street canyons. *Journal Of Applied Meteorology and Climatology*, 47:2058–2067, 2008.

C.H. Liu, M.C. Barth, and D.Y.C. Leung. Large-eddy simulation of flow and pollutant transport in street canyons of different building-height-to-street-width ratios. *Journal of Applied Meteorology*, 43:1410–1424, 2004.

J. Lottes. Independent quality measures for symmetric algebraic multigrid components. *ANL/MCS-P1820-0111*, 2011.

H. Louhichi, T. Fournel, J. Lavest, and H. Ben Aissia. Camera self-calibration in Scheimpflug condition for air flow investigation. *Advances in Visual Computing, LCNS*, 4292:891–900, 2006.

P. Louka, S. Belcher, and R. Harrison. Modified street canyon flow. *Journal of Wind Engineering and Industrial Aerodynamics*, 74-76:485–493, 1998.

P. Louka, S. Belcher, and R. Harrison. Coupling between air flow in streets and the well-developed boundary layer aloft. *Atmospheric Environment*, 34:2613–2621, 2000.

P. Louka, G. Vachon, J.F. Sini, P. Mestayer, and J.M. Rosant. Thermal effects on the airflow in a street canyon - Nantes'99 experimental results and model simulations. *Water, Air, and Soil Pollution: Focus*, 2: 351–364, 2002.

R. MacDonald, S. Carter Schofield, and P. Slawson. Physical modelling of urban roughness using arrays of regular roughness elements. *Water, Air and Soil Pollut: Focus*, 2:541–554, 2002.

R.J. Martinuzzi and B. Havel. Turbulent flow around two interfering surface-mounted cubic obstacles in tandem arrangement. *Journal of Fluids Engineering*, 122:24–31, 2000.

R.J. Martinuzzi and B. Havel. Vortex shedding from two surface-mounted cubes in tandem. *International Journal of Heat and Fluid Flow*, 25:364–372, 2004.

R.J. Martinuzzi and C. Tropea. The flow around surface-mounted, prismatic obstacles placed in a fully developed channel flow. *Journal of Fluids Engineering*, 115:85–92, 1993.

P. Mestayer, J.F. Sini, and M. Jobert. Simulation of the wall temperature influence on flows and dispersion within street canyons. *Transactions on Ecology and the Environment*, 6:109–116, 1995.

B. Monnier, B. Neiswander, and C. Wark. Stereoscopic particle image velocimetry measurements in an urban-type boundary layer: Insight into flow regimes and incidence angle effect. *Boundary-Layer Meteorology*, 135:243–268, 2010.

N. Murray and L. Ukeiley. An application of Gappy POD. *Experiments in Fluids*, 42:79—91, 2007. doi: 10.1007/s00348-006-0221-y.

H. Nagib, M. Morkovin, J. Yung, and J. Tan-atichat. On modeling of atmospheric surface layers by the counter-jet technique. *AIAA J*, 14(2):185–190, 1974.

M. Nielsen. Turbulent ventilation of a street canyon. *Environmental Monitoring and Assessment*, 65:389–396, 2000.

T.R. Oke. Street design and urban canopy layer climate. *Energy and Buildings*, 11:103–113, 1988.

A.T. Patera. A spectral element method for fluid dynamics - laminar flow in a channel expansion. *Journal of Computational Physics.*, 54:468–488, 1984.

J. Blair Perot. An analysis of the fractional step method. *J. of Comp. Phys.*, 108:51–58, 1993.

E.J. Plate. *Aerodynamic Characteristics of Atmospheric Boundary Layer*. United States Atomic Energy Commission, 192 pp, Oak Ridge, TN, 1971.

M. Princevac, J. Baik, X. Li, H. Pan, and S. Park. Lateral channeling within rectangular arrays of cubical obstacles. *Journal of Wind Engineering and Industrial Aerodynamics*, 98:377–385, 2010.

S. Rafailidis. Influence of building areal density and roof shape on the wind characteristics above a town. *Boundary-Layer Meteorology*, 85:255–271, 1997.

M. Raffel, C.E. Willert, and J. Kompenhans. *Particle Image Velocimetry: A Practical Guide*. Springer-Verlag Berlin Heidelberg, New York, NY, third edition, 1998.

R.T. Reynolds and I.P. Castro. Measurements in an urban-type boundary layer. *Experiments in Fluids*, 45 (1):141–156, 2008. doi: 10.1007/s00348-008-0470-z.

P.J. Richards, R.P. Hoxey, and L. Short. Wind pressures on a 6m cube. *Journal of Wind Engineering & Industrial Aerodynamics*, 89:1553–1564, 2001.

P.J. Richards, R.P. Hoxey, B.D. Connell, and D.P. Lander. Wind-tunnel modelling of the silsoe cube. *Journal of Wind Engineering & Industrial Aerodynamics*, 95:1384–1399, 2007.

A. Robins and I.P. Castro. A wind tunnel investigation of plume dispersion in the vicinity of a surface mounted cube – II. the concentration field. *Atmospheric Environment (1967)*, 11:299–311, 1977.

M. Rotach. Profiles of turbulence statistics in and above an urban street canyon. *Atmospheric Environment*, 29(13):1473–1486, 1995.

K.B. Shah and J.H. Ferziger. A fluid mechanicians view of wind engineering: Large eddy simulation of flow past a cubic obstacle. *Journal of Wind Engineering*, 67 & 68:211–224, 1997.

K. Shahbazi. *A Parallel High-Order Discontinuous Galerkin Solver For the Unsteady Incompressible Navier-Stokes Equations in Complex Geometries*. University of Toronto, Toronto, 2007.

S. Soloff, R. Adrian, and Z.C. Liu. Distortion compensation for generalized stereoscopic particle image velocimetry. *Measurement Science and Technology*, 8(12):1441–1454, 1997.

J.M.M. Sousa. Turbulent flow around a surface-mounted obstacle using 2D-3C DPIV. *Experiments in Fluids*, 33:854–862, 2002.

R.B. Stull. *An Introduction to Boundary Layer Meteorology*. Kluwer Academic Publishers, Dordrecht, The Netherlands, first edition, 1988.

H. Takimoto, A. Sato, S. Onomaura, J. Barlow, R. Moriwaki, A. Inagaki, and M. Kanda. Particle image velocimetry measurements of turbulent flow within outdoor and indoor urban scale models and flushing motions in urban canopy layers. *Boundary-Layer Meteorology*, 140:295–314, 2011.

W. Theurer. Typical building arrangements for urban air pollution modelling. *Atmos. Environ.*, 33:4057–4066, 1999.

Y. Tseng, C. Meneveau, and M.B. Parlange. Modeling flow around bluff bodies and predicting urban dispersion using large eddy simulation. *Environ. Sci. Technol.*, 40:2653–2662, 2006.

H.M. Tufo. Fast parallel direct solvers for coarse grid problems. *J. Parallel and Distributed Computing*, 61:151–177, 2001.

H. Uehara, S. Murakami, S. Oikawa, and S. Wakamatsu. Wind tunnel experiments on how thermal stratification affects flow in and above urban street canyons. *Atmospheric Environment*, 34:1553–1562, 2000.

Z.Y. Wang, E.J. Plate, M. Rau, and R. Keiser. Scale effects in wind tunnel modelling. *Journal of Wind Engineering and Industrial Aerodynamics*, 61:113–130, 1996.

G.H. Wannier. A contribution to the hydrodynamics of lubrication. *Q. Appl. Math.*, 8:1, 1950.

S. Watkins, M. Abdulrahim, M. Thompson, M. Shortis, B. Loxton, R. Segal, C. Bil, and J. Watmuff. An overview of experiments on the dynamic sensitivity of MAVs to turbulence. *AIAA Paper 2009-5906*, 2009.

S. Watkins, S. Ravi, and B. Loxton. The effect of turbulence on the aerodynamics of low reynolds number wings. *Engineering Letters*, 18:6 pp., 2010.

C.H.K. Williamson. Oblique and parallel modes of vortex shedding in the wake of a circular cylinder at low reynolds numbers. *J. Fluid Mech.*, 206:579627, 1989.

S. Xie, Y. Zhang, L. Qi, and X. Tang. Spatial distribution of traffic-related pollutant concentrations in street canyons. *Atmospheric Environment*, 37(23):3213–3224, 2003.

X. Xie, Z. Huang, J. Wang, and Z. Xie. The impact of solar radiation and street layout on pollutant dispersion in street canyon. *Building and environment*, 40:201–212, 2005.

X. Xie, C. Liu, D. Leung, and M. Leung. Characteristics of air exchange in a street canyon with ground heating. *Atmospheric Environment*, 40:6396–6409, 2006.

E. Yee, R.M. Gailis, A. Hill, T. Hilderman, and D. Kiel. Comparison of wind-tunnel and water-channel simulations of plume dispersion through a large array of obstacles with a scaled field experiment. *Boundary-Layer Meteorology*, 121:389–432, 2006. doi: 10.1007/s10546-006-9084-2.

S.A. Zaki, A. Hagishima, J. Tanimoto, and N. Ikegaya. Aerodynamic parameters of urban building arrayswith random geometries. *Boundary-Layer Meteorology*, 138:99–120, 2011.

1.

1. Report Type

Final Report

Primary Contact E-mail

Contact email if there is a problem with the report.

Rempfer@iit.edu

Primary Contact Phone Number

Contact phone number if there is a problem with the report

312-567-3189

Organization / Institution name

Illinois Institute of Technology

Grant/Contract Title

The full title of the funded effort.

Characterization and Low-Dimensional Modeling of Urban Fluid Flow

Grant/Contract Number

AFOSR assigned control number. It must begin with "FA9550" or "F49620" or "FA2386".

FA9550-11-1-0056

Principal Investigator Name

The full name of the principal investigator on the grant or contract.

Dietmar Rempfer

Program Manager

The AFOSR Program Manager currently assigned to the award

Douglas R. Smith

Reporting Period Start Date

05/02/2011

Reporting Period End Date

04/30/2014

Abstract

This report describes work that was done under AFOSR Contract Number FA9550-11-1-0056, studying the structure of a model urban boundary layer flow. The model geometry consisted of a set of plexiglass blocks, and the flow around this geometry was studied both experimentally as well as computationally. For the experiment, a Stereoscopic Particle Image Velocimetry (SPIV) method was developed that allows for a three-dimensional description of this urban flow, and helps gain insight into the characteristic flow structures in the streets and canyons of our model urban geometry. On the computational side, a new spectral-element code was developed that was demonstrated to produce accurate results, and can scale to thousands of processors on large high-performance computing systems. Good agreement between the experiment and computation was demonstrated.

Most notably, wind tunnel experiments were performed at a number of different angles of incidence, providing for the first time a detailed overview of the effect of wind direction on the flow structures in the urban geometry. Valuable information about the flow structures are presented. The effects of incidence angles from 0 to 45 degrees of the incoming flow with

respect to the urban array are investigated. A major observation from this work is that a strong channeling effect is observed for all incidence angles and is in agreement with that observed in other investigations for as little as 4 degrees. This channeling significantly affects the turbulence distribution within the array, the correlations between the various gust components and the structures responsible for contaminant transport.

Distribution Statement

This is block 12 on the SF298 form.

Distribution A - Approved for Public Release

Explanation for Distribution Statement

If this is not approved for public release, please provide a short explanation. E.g., contains proprietary information.

SF298 Form

Please attach your SF298 form. A blank SF298 can be found here. Please do not spend extra effort to password protect or secure the PDF, we want to read your SF298. The maximum file size for SF298's is 50MB.

AFD-070820-035.pdf

Upload the Report Document. The maximum file size for the Report Document is 50MB.

FinalReport_final-PRT.pdf

Upload a Report Document, if any. The maximum file size for the Report Document is 50MB.

Archival Publications (published) during reporting period:

Changes in research objectives (if any):

Change in AFOSR Program Manager, if any:

Extensions granted or milestones slipped, if any:

AFOSR LRIR Number

LRIR Title

Reporting Period

Laboratory Task Manager

Program Officer

Research Objectives

Technical Summary

Funding Summary by Cost Category (by FY, $K)

	Starting FY	FY+1	FY+2
Non-Military Government Personnel Costs			
In-house Contractor Costs			
Travel (Be Specific)			
Training (Be Specific)			
Supplies			
Other Expenses (Be Specific)			
Total Resource Requirements			

Report Document

Appendix Documents

2. Thank You

E-mail user